Cranfield University

Maria del Mar Salinas-Ruiz

Development of a rubber toughened epoxy adhesive loaded with carbon nanotubes, for aluminium – polymer bonds

School of Applied Sciences

PhD

Cranfield University

School of Applied Sciences
Department of Materials – Composites Centre

PhD Thesis

Academic Year 2008-2009

Maria del Mar Salinas-Ruiz

Development of a rubber toughened epoxy adhesive loaded with carbon nanotubes, for aluminium – polymer bonds

Supervisor: Professor Ivana K. Partridge

June 2009

This thesis is submitted in partial fulfilment of the requirements for the Degree of Doctor of Philosophy

Abstract

This thesis describes the formulation of a ternary thermosetting adhesive which consists of a diglycidyl ether of bisphenol-A (DGEBA) epoxy resin cured with 3,3'-diamino diphenyl sulphone (3,3'-DDS) hardener and modified through the addition of carboxyl-terminated butadiene-acrylonitrile (CTBN) rubber and multi-walled carbon nanotubes (MWCNTs). Processing implications of the novel adhesive in the film form are considered in order to manufacture bonded specimens for characterisation of the adhesive performance in structural joints. The ternary blend which represents the novel adhesive formulation is also characterised in bulk form.

The cure kinetics behaviour of the novel ternary blend is investigated using differential scanning calorimetry which shows 10% reduction in the total reactivity, and therefore reduced final crosslinking density, with the addition of the carbon nanotubes. A cure kinetics model is developed for the novel ternary thermoset. From characterisation of cast samples, a toughening effect of the phase separated rubber particles is observed, from 144 to 317 J/m^2, with a further increase to 551 J/m^2 in the presence of the carbon nanotubes. In the absence of rubber, the nanotubes alone produce a minimal effect upon the thermo-mechanical and mechanical characteristics of the resin. The morphology of the cured material is affected by the presence of the nanoparticles, resulting in the reduction of the mean rubber particle size from 3μm to below 1μm. The electrical conductivity of the cured resin samples is found to increase by six orders of magnitude, up to 3.6 x10^{-3} S/m in the ternary blend for a low carbon nanotube concentration of 0.3 wt%.

DCB and ELS tests are used to study the performance of the novel adhesive in a joint configuration. The adhesive joint strength is dependent on the substrate type as well as on the surface preparation. The novel adhesive is also examined under fatigue in a 'bonded crack retarder' application.

A mi padre y a mi madre,
en la tierra y en el cielo.

Acknowledgements

First and foremost I would like to express my sincere gratitude to my supervisor, Professor Ivana Partridge. You provided me with many helpful suggestions, important support when I needed it most and constant encouragement during the course of this work. I am immensely proud of being your first PhD girl. I also wish to express my appreciation to Professor Phil Irving who directed the project in which this research was involved and set a valuable managerial example.

Special thanks are due to Dr. Alex Skordos for the many hours spent searching for carbon nanotubes under the microscope and for taking intense academic interest in this study as well as providing valuable suggestions.

Special gratitude goes to Dr. David Ayre for his valuable instructions and suggestions throughout this work. Sincere thanks are extended to Dr. Denis Cartié for his support during the BCR project and his guidance in carrying out and presenting experimental work. My keen appreciation goes to Jim for his invaluable assistance with the manufacturing work and the many irrelevant but fanatical discussions.

To Dr. James Lander, my exceptional English proofreader and Dr. Douglas Figueroa-Gordon for provided me unflinching encouragement and support and to all the friends I have made at Cranfield. I would like to express my heartfelt thanks to my Mexican friends, Adriana, Isidro and Itzel for always letting me feel my Latin culture.

To Rosa, Juan Antonio, Jorge, Abuelos, Jan, Keith, Jono, Chris and Mark for their support and affection. Lastly and most importantly, to James, por el amor, apoyo y comprensión que acompañan mis días.

Contents

List of figures **1**

Nomenclature **15**

Abbreviations **19**

1. General introduction **21**

Thesis overview 22

2. Structural epoxy adhesives to meet today's challenge **25**

2.1 Overview of adhesives for aircraft structures 26

2.1.1 Adhesives vs. alternative joining methods 26

2.1.2 Reducing internal stresses 27

2.1.3 Making adhesives conductive 29

2.1.4 'Bonded crack retarders' in aircraft structures 29

2.2 Adhesion Overview 30

2.2.1 Epoxy adhesive toughening 32

2.2.2 Reactive liquid rubber: in detail 33

2.2.2.1 Stress fields around rubber particles 34

2.2.2.2 Matrix plastic yielding and particle cavitation 34

2.3 Effect of adhesive bond thickness 37

2.4 Use of nanotechnology in structural adhesives 41

2.4.1.1 Mechanics of nanoparticle toughening 42

2.5 Why use carbon nanotubes in structural adhesives? 44

2.5.1 CNTs as mechanical reinforcement in epoxy resins 46

2.5.1.1 Considerations for manufacturing CNT – polymer composites for mechanical reinforcement 47

2.5.2 CNTs to assist conductivity and damage monitoring in epoxy resins 50
2.5.2.1 Considerations for manufacturing CNT – polymer composites for conductivity and damage monitoring 51
2.5.3 CTE control 52
2.5.4 Processing control via rheological additives 53
2.5.5 Special consideration: galvanic corrosion 54
2.6 Cure of ternary thermosetting systems 56
2.6.1 Cure kinetics modelling of thermosetting systems 57

3. Materials 59
3.1 Raw materials 60
3.1.1 Epoxy resin – hardener system 60
3.1.2 Toughener 60
3.1.3 Carbon nanotubes 62
3.1.4 Carbon nanofibres 63
3.2 Veils 64
3.3 Commercial adhesives 66
3.3.1 FM® 94K modified epoxy film 66
3.3.2 FM® 1515-3M film adhesive 66
3.3.3 Araldite® 420 A/B 67
3.4 Substrates 67
3.4.1 Glass-fibre reinforced plastic (GFRP) 67
3.4.2 Aluminium alloy 68

4. Manufacturing: constraints, design and methodology 71
4.1 Designing the formulation 72
4.1.1 Glass transition temperature requirement 72
4.1.2 Selection of the "control" epoxy – hardener system 74
4.1.3 Carbon nanotubes as fillers 75
4.1.3.1 Selection of carbon nanotube forms 75
4.1.3.2 Selection of carbon nanotube concentration 77
4.1.4 Toughener 77
4.1.4.1 Selection of toughener form 77

4.1.4.2 Selection of toughener concentration 80
4.1.5 Novel adhesive formulation finalised 81
4.2 Processing 81
4.2.1 Dispersion of carbon nanotubes into epoxy resin 82
4.2.1.1 Study of dispersion: Optical microscopy and SEM 85
4.2.2 Degassing of resins: preparation for final mixing 87
4.2.3 Mixing of the constituents 89
4.2.4 Casting 90
4.2.5 Filming 92
4.2.5.1 Importance of the veil 92
4.2.5.2 Filming process 93
4.2.5.3 Films obtained 95
4.2.5.4 Improving adhesion through the use of a surface primer 97
4.2.6 Alternative processing routes considered 98
4.2.6.1 Spraying CNTs onto adhesive surface 98
4.2.6.2 Targeting nanofillers at the adhesive-substrate interface 99
4.3 Specimen preparation 101
4.3.1 Cast specimens 101
4.3.1.1 Dynamic mechanical thermal analysis (DMTA) specimens 102
4.3.1.2 Thermal mechanical analysis (TMA) specimens 103
4.3.1.3 Fracture specimens: 3 point bending 103
4.3.1.4 Flexural specimens 106
4.3.1.5 Compression specimens 107
4.3.1.6 Electrical conductivity specimens 107
4.3.2 Adhesively bonded specimens 108
4.3.2.1 Manufacture of GFRP plates 108
4.3.2.2 Preparation of bonding surfaces 110
4.3.2.3 DCB test coupons 111
4.3.2.4 ELS coupons 118
4.3.2.5 Bonded Crack Retarder (BCR) structure 119

5. Test methods 127
5.1 Resin characterisation: cure study 128

5.1.1 Determination of T_g by MDSC 129
5.2 Resin characterisation: cast specimens 130
5.2.1 Post-cure analysis by DMTA 130
5.2.2 Determination of CTE by TMA 132
5.2.3 Fracture testing: determination of K_{IC} and G_{IC} 133
5.2.4 Flexure testing: determination of E_f 137
5.2.5 Compressive test: determination of σ_{yc} 138
5.2.6 Electrical conductivity measurement 141
5.3 Adhesive characterization: bonded specimens 142
5.3.1 Flexure testing 142
5.3.2 Mode I: Double cantilever beam (DCB) tests 143
5.3.3 Mode II: End loaded split (ELS) test 146
5.3.4 Fatigue delamination test 150

6. Characterisation of ternary resin blends 157
6.1 Cure study of the resin blends 158
6.1.1 Effect of carbon nanotube addition on CRN cure 158
6.1.2 Modelling the cure of the CRN formulation 160
6.2 Thermo-mechanical properties 165
6.2.1 Glass transition temperature, T_g 165
6.2.2 Post-cure analysis and $T_{g\infty}$ 167
6.2.3 Coefficient of thermal expansion, CTE 169
6.3 Mechanical properties 170
6.3.1 Fracture toughness, K_{IC} and fracture energy, G_{IC} 170
6.3.2 Flexural modulus, E_f 172
6.3.3 Compression yield stress, σ_{yc} 173
6.4 Electrical conductivity 175
6.5 Structure-property relationships 177

7. Characterisation of adhesives in bonded specimens 183
7.1 Flexural modulus of substrates 184
7.2 Mode I adhesive fracture energy 184

7.2.1 Unsupported films: contribution of each constituent in the adhesive joint 185
7.2.2 Selecting the veil for the novel adhesive film 187
7.2.3 CNTs contribution to the novel adhesive film 189
7.2.4 Targeting nanofillers at the adhesive-substrate interface 191
7.2.5 Novel adhesive film against commercially available adhesive films 194
7.2.6 Adhesion: GFRP vs. Aluminium alloy 197
7.2.7 Comparison between resin and joint fracture with reference to plastic-zone models 201
7.3 Mode II adhesive fracture energy 204
7.3.1 CNTs contribution to the novel adhesive film 205
7.3.2 Targeting nanofillers at the adhesive-substrate interface 207
7.3.3 Novel adhesive film compared against commercially available adhesive films 209
7.4 Fatigue crack propagation 211

8. Overall discussion 219
8.1 Literature outlook of carbon nanotubes in epoxy resins 220
8.2 Design and manufacture of the novel adhesive film 222
8.3 Effects of carbon nanotubes on an epoxy / CTBN system 224
8.4 Reinforcement or conductivity – the way forward? 226

9. Conclusions and suggestions for further work 231
9.1 Conclusions 232
9.2 Suggestions for further work 233
9.2.1 Improving the filming process 233
9.2.2 Improving interfacial adhesion 234
9.2.3 Further work on the novel adhesive formulation 237
9.2.4 Further work on bonded joints 239

Appendix A – 3PB fracture testing – Correction factors and data analysis 242

Appendix B – DCB test correction factors 244

Appendix C – ELS test correction factors..... 245

List of figures

Figure 2.1 – Airbus A380 which employs structural adhesives to join many parts of the primary structure [8] 26

Figure 2.2 – Structural adhesives in aircraft subjected to bonding and in-service temperatures 27

Figure 2.3 – Bonded crack retardation concept 30

Figure 2.4 – Mechanisms of adhesion involves in bonding metal to metal and metal to composite; (a) adsorption and (b) mechanical interlocking [28] 31

Figure 2.5 – Stress field generated around a rubber particle embedded in the epoxy matrix 34

Figure 2.6 – Fracture deformation processes of a rubber toughened epoxy adhesive, modified from [39] 35

Figure 2.7 – Optical microscopy image of the perpendicular section to the fracture surface of a rubber-modified epoxy system. Shear bands (at low angles) and stretched rubber particles appear bright under polarized light [33] 36

Figure 2.8 – Scanning electron microscopy (SEM) image of a rubber modified epoxy resin, showing cavitation of the particles on the fracture surface [40] 37

Figure 2.9 – Simple elastic-plastic model for deformation zone at adhesive crack tip [42] 38
Figure 2.10 – Schematic representation of plane-stress and plane-strain deformation zones developed at the crack tip, modified from [43] 39
Figure 2.11 – Relationship between $G_{IC\,\mathrm{JOINT}}$, plastic-zone shape and degree of constraint in the joint due to bond thickness, modified from [42] 40
Figure 2.12 – TEM micrographs of epoxy resin containing (A) multi-walled carbon nanotubes [4] and (B) silica nanoparticles [62] 42
Figure 2.13 – SEM micrograph of the fracture surface of epoxy resin containing 9.6 vol% of nanosilica – Voids with nanoparticles are circled [62] 44
Figure 2.14 – SEM micrograph of the fracture surface of epoxy resin containing functionalised carbon nanotubes. The shear-bands around the agglomerates indicate plastic matrix deformation but there is no clear indication of void nucleation as claimed [63] 44
Figure 2.15 – TEM micrographs of (A) single-walled CNTs (SWCNTs) [65], (B) double-walled CNTs (DWCNTs) [65] and (C) multi-walled CNTs (MWCNTs) [67] 45
Figure 2.16 – Schematic of the carbon nanotube functionalisation process [4] 48
Figure 2.17 – Mini-calender (three-roll mill) purchased by the Composites Centre at Cranfield University for the dispersion of carbon nanotubes in thermoset matrices 50
Figure 2.18 – Carbon nanotubes for lightning protection in composite aircraft structures [85] 51
Figure 2.19 – Hysteresis obtained for thixotrope adhesive additives [91] 53

Figure 2.20 – Aluminium and carbon nanotubes in the galvanic series in flowing sea water, modified from [97] 55
Figure 3.1 – Chemical structures of the epoxy resin MY750 [118], hardener and catalyst..... 61
Figure 3.2 – Chemical structures of the toughener materials used in this work; reactive CTBN 1300x8 [122] and chemical bonds between molecules in the CTBN-epoxy adduct 62
Figure 3.3 – SEM images of the NC-7000 multi-walled carbon nanotubes as supplied 63
Figure 3.4 – SEM images of the PR-24-XT-LHT-OX carbon nanofibres, as supplied 64
Figure 3.5 – Polyester (F0826) and nylon (A1050) reinforcing veils used in the manufacture of supported adhesive films..... 65
Figure 3.6 – Polyester veil (F0826) with magnification of the woven architecture 65
Figure 3.7 – Nylon veil (A1050) with magnification of the honeycomb architecture 65
Figure 4.1 – Overview of the development process for the novel adhesive formulation 73
Figure 4.2 – General trends of adhesive properties related to temperature or molecular mobility [133]..... 74
Figure 4.3 – MB1215-00 multi-walled carbon nanotubes-epoxy masterbatch at room temperature..... 76
Figure 4.4 – “Lumpy” adhesive film obtained by using ground epoxy-CTBN adduct 78

Figure 4.5 – SEM micrographs of fracture surfaces for epoxy-rubber adduct formulations containing solid CTBN at 5 wt% (A & B) and liquid CTBN at 10 wt% (C & D) 79
Figure 4.6 – Supported novel adhesive film containing 5 wt% of CTBN rubber and 0.3 wt% of MWCNTs 81
Figure 4.7 – Dispermat CN10-F2 high shear rotational mixer 83
Figure 4.8 – Closed system used for studying the carbon nanotubes sonication process [94] 83
Figure 4.9 – Branson S-450D ultrasonic cell disruptor / homogenizers [139] 84
Figure 4.10 – Recordings from the sonication process showing (A) energy applied to the system and temperature of the mix and (B) evolution of resistivity and temperature of the resistivity cell 85
Figure 4.11 – Optical images of the carbon nanotubes-epoxy mixture subjected to sonication showing (1) before sonication, (2) middle of the sonication process and (3) end of the sonication process 86
Figure 4.12 – SEM micrographs of fracture surfaces containing 0.3wt% of carbon nanotubes and 5wt% of CTBN rubber showing (1) non-sonicated sample and (3) fully sonicated sample 87
Figure 4.13 – Degassing technique developed for highly viscous systems 89
Figure 4.14 – Casting of specimens showing (A) glass plate and steel mould, (B) covering the glass plate with coated glass cloth, (C) glass plate and steel mould assembled and secured using heat resistant tape and (D) poured adhesive pastes 91
Figure 4.15 – Casting mould after the curing process 91

Figure 4.16 – Veil architectures showing the open hole dimensions for polyester veil (A) and nylon veil (B) 92
Figure 4.17 – Lab-scale 'filming-line' 93
Figure 4.18 – Filming process 94
Figure 4.19 – Shaping the adhesive films 95
Figure 4.20 – Unsupported adhesive films showing (A) CRN; (B) CN; (C) CR and (D) C 96
Figure 4.21 – Supported CRN films showing (A) nylon veil version and (B) polyester veil version 96
Figure 4.22 – Polyester veil supported CR film 97
Figure 4.23 – Priming the GFRP substrate surfaces before bonding 97
Figure 4.24 – Adhesive joint structure divided into five regions [9] 98
Figure 4.25 – Proposed idea of spraying carbon nanotubes directly onto adhesive surface 99
Figure 4.26 – Bonding sequence of the structure with CF films at the interfaces 100
Figure 4.27 – Unsupported CF film 101
Figure 4.28 – Buehler precision saw (left) and Buehler Metaser Motopol 12 polisher (right) 102
Figure 4.29 – DMTA specimen dimensions (mm) 102
Figure 4.30 – TMA specimen dimensions (mm) 103
Figure 4.31 – SENB test specimen diagram 103
Figure 4.32 – Tapping system used to generate the natural pre-crack on the SENB specimen 105

Figure 4.33 – SENB specimens from the C formulation (A) and the CRN formulation (B) 105
Figure 4.34 – Flexural test specimen diagram 106
Figure 4.35 – Flexural specimens, showing the C formulation (A) and the CRN formulation (B) 106
Figure 4.36 – Compression specimen dimensions (mm) 107
Figure 4.37 – DC and AC conductivity measurement specimen dimensions (mm) 107
Figure 4.38 – DC and AC conductivity specimens for the different adhesive formulations 108
Figure 4.39 – Lay-up and peel ply placement on the bonding side of the plates 109
Figure 4.40 – Preparing the autoclave for curing the plates 109
Figure 4.41 – Cured GFRP plates showing (A) a shiny surface and (B) a matt surface obtained when using a peel ply 110
Figure 4.42 – SEM micrographs showing the resulting composite surface after the removal of the peel ply 110
Figure 4.43 – Position of crack starter film in a single adhesive film bonded delamination test coupon 113
Figure 4.44 – Manufacturing the bonded panels 114
Figure 4.45 – Panel layout for bonded GFRP testing coupons (dimensions in mm) ... 115
Figure 4.46 – DCB test coupon geometry for GFRP substrates (dimensions in mm) 116
Figure 4.47 – Panel layout for bonded aluminium alloy testing coupons (dimensions in mm) 117

Figure 4.48 – DCB test coupon geometry for aluminium alloy substrates (dimensions in mm) 118
Figure 4.49 – ELS test coupon geometry for GFRP substrates (dimensions in mm) .. 119
Figure 4.50 – Aluminium alloy plate 'as received' for the Bonded Crack Retarders study 120
Figure 4.51 – Priming the BCR structure substrates before bonding 121
Figure 4.52 – BCR structure before bonding 121
Figure 4.53 – Bonding sequence of the BCR structure 122
Figure 4.54 – BCR structure after bonding 123
Figure 4.55 – BCR structure (dimensions in mm) 124
Figure 5.1 – Schematic of a typical DSC cell [155] 128
Figure 5.2 – Determination of the T_g from the MDSC trace of heat capacity vs. temperature 129
Figure 5.3 – DMTA (Gabo Qualimeter GmbH, Germany) with close-up of the incorporated measurement system 130
Figure 5.4 – Determination of the T_g from the tan δ vs. temperature curve (schematic) 131
Figure 5.5 – TMA (TA Instruments 2940) with details of the enclosed measurement system 132
Figure 5.6 – Determination of the mean coefficient of linear thermal expansion α 133
Figure 5.7 – Three point loading arrangement at the end of fracture testing 134
Figure 5.8 – Calculation of indentation correction 135
Figure 5.9 – Use of travelling microscope to determine notch depth 136
Figure 5.10 – Force vs. displacement curve for a notched test specimen 136

Figure 5.11 – Three point loading arrangement at the end of flexure testing 138

Figure 5.12 – Compression arrangement by using the compression cage 139

Figure 5.13 – Typical stress vs. strain curves for compression 140

Figure 5.14 – In-house setup for DC conductivity measurements..... 141

Figure 5.15 – DCB test arrangement..... 143

Figure 5.16 – GFRP DCB specimen arrangement with bonded loading blocks 144

Figure 5.17 – Aluminium DCB specimen with loading holes drilled through the loading arms 144

Figure 5.18 – Typical DCB test load vs. deflection curves testing from the insert and from the mode I pre-crack..... 145

Figure 5.19 – ELS test arrangement..... 147

Figure 5.20 – ELS test arrangement diagram 147

Figure 5.21 – A typical ELS test load vs. deflection curve with crack propagation markers 149

Figure 5.22 – Olympus OmniScan® MX with the phased array (PA) module..... 151

Figure 5.23 – Probes attached to the crack horizontal centreline 151

Figure 5.24 – Schematic representation of the experimental setup (Electrical potential technique)..... 152

Figure 5.25 – Fatigue test arrangement 153

Figure 5.26 – Pre-cracking length for the fatigue test..... 154

Figure 5.27 – Xantrex XPD Programmable DC Power Supply and Keithley 2000 Multimeter 154

Figure 6.1 – Heat flow vs. temperature for the dynamic cure of the CR and the CRN formulations..... 158

Figure 6.2 – Heat flow vs. cure time for the CR and CRN formulations at 120ºC 159

Figure 6.3 – Degree of cure vs. cure time for the CR and CRN formulations at 120ºC 160

Figure 6.4 – Superposition of dynamic and isothermal DSC reaction rate vs. conversion for the CRN formulation 161

Figure 6.5 – Cure kinetics model fit – Evolution of degree of cure with time for the CRN isothermal experiments 164

Figure 6.6 – Cure kinetics model fit – Evolution of degree of cure with temperature for a 2.5ºC/min CRN dynamic experiment 165

Figure 6.7 – DMTA traces from measurements made on the C, the CR, the CN and the CRN post-cured formulations 167

Figure 6.8 – Thermo-mechanical curves obtained for cured samples of the CR and the novel formulation, CRN 169

Figure 6.9 – Optical micrographs of the fracture surfaces of the formulations (A) C, (B) CR, (C) CN and (D) CRN 172

Figure 6.10 – Flexural stress vs. flexural strain for the C and the CRN formulations 173

Figure 6.11 – Compression curves for the C and the CRN formulations 174

Figure 6.12 – AC conductivity spectra for all the formulations, C, CR, CN and CRN. The close-up graph at the bottom shows detail of the response of CN and CRN at the higher frequencies 176

Figure 6.13 – SEM micrographs of cryo-fracture surfaces (A) CN and (B) etched CRN 178

Figure 6.14 – SEM micrographs of three-point bending room temperature fracture surfaces of CR at two magnifications 179
Figure 6.15 – SEM micrographs of etched cryo-fracture surfaces at two magnifications (A) and (B) CR; (C) and (D) CRN..... 180
Figure 6.16 – Fracture energy, G_{IC} and electrical conductivity of the formulations employed 181
Figure 7.1 – Mode I R-curves for the unsupported adhesive films 185
Figure 7.2 – Mode I R-curves for CRN supported films with polyester (GFRP-P-CRN) and nylon veil (GFRP-N-CRN)..... 187
Figure 7.3 – Mode I load vs. displacement curves for CRN supported films with polyester (GFRP-P-CRN) and nylon veil (GFRP-N-CRN) 188
Figure 7.4 – Fracture surfaces of the CRN formulation with nylon veil, GFRP-N-CRN (left) and polyester veil, GFRP-P-CRN (right)..... 189
Figure 7.5 – Mode I R-curves for the CRN and the CR formulations with polyester veil..... 190
Figure 7.6 – Fracture surfaces of the CR formulation with polyester veil, GFRP-P-CR 191
Figure 7.7 – Mode I R-curves for GFRP-P-CR and GFRP-U-CF / P-CR 192
Figure 7.8 – Mode I load vs. displacement curves for GFRP-U-CF / P-CR adhesive system 192
Figure 7.9 – 'Fibre bridging' in the GFRP-U-CF / P-CR joint 194
Figure 7.10 – Mode I R-curves for GFRP-P-CRN and the commercially available adhesive films, GFRP-FM94 and GFRP-FM15 195

Figure 7.11 – Mode I load vs. displacement curves for GFRP-P-CRN and the commercially available adhesive films, GFRP-FM94 and GFRP-FM15 195
Figure 7.12 – Fracture surfaces images of the mixed mode failed GFRP-FM94 (left) and the cohesive mode failed GFRP-FM15 (right) 197
Figure 7.13 – Mode I R-curves for the P-CRN to GFRP & the P-CRN to Al 198
Figure 7.14 – Fracture surface images of GFRP-P-CRN (top) and Al-P-CRN (bottom) 198
Figure 7.15 – Mode I R-curves for the Al-P-CRN and the commercially available adhesive films, Al-FM 94 and Al-FM15 199
Figure 7.16 – Photographs of micro-cracking in the adhesive layer from ELS testing of an epoxy adhesive film - The vertical black lines are drawn 1mm apart [153] 205
Figure 7.17 – Mode II R-curves for the CRN and the CR formulations with polyester veil 206
Figure 7.18 – Mode II R-curves for the GFRP-P-CR and the GFRP-U-CF / P-CR joints 208
Figure 7.19 – Fracture surface images of GFRP-U-CF / P-CR system 209
Figure 7.20 – Mode II R-curves for the GFRP-P-CRN and the commercially available adhesive films 210
Figure 7.21 – Crack length vs. number of cycles and close-up for the Al without straps, the Al with straps bonded with FM® 94K and the Al with straps bonded with the novel adhesive film 212

Figure 7.22 – Crack growth rate vs. crack length for the Al without straps, the Al with straps bonded with FM® 94K and the Al with straps bonded with the novel adhesive film..... 213
Figure 7.23 – Fracture surfaces images for the Al structure with FM® 94K adhesive film after fatigue crack propagation 214
Figure 7.24 – Fracture surfaces images for the Al plate reinforced with the use of the novel adhesive film (P-CRN) after fatigue crack propagation 215
Figure 7.25 – Scans of fatigue crack growth test with the FM® 94K adhesive after failure 216
Figure 7.26 – Scans of fatigue crack growth test with the novel adhesive film, a) before and b) after failure..... 217
Figure 8.1 – Illustrations of the atomic structure of (a) armchair and (b) ziz-zag carbon nanotubes [51]..... 221
Figure 8.2 – Industrial adhesive film manufacturing line [216]..... 223
Figure 8.3 – SEM micrograph of the NC-7000 multi-walled carbon nanotubes as supplied, showing a highly-entangled structure 224
Figure 8.4 – SEM micrographs of etched fracture surfaces of CR formulation..... 226
Figure 8.5 – SEM micrographs of etched fracture surfaces of CRN formulation 226
Figure 8.6 – Possible morphology change in the thermosetting ternary blend with an increase in the rubber concentration..... 228
Figure 8.7 – TEM micrographs of an epoxy-thermoplastic system containing 2 wt % of carbon black showing selective localisation of the nanoparticles between the two phases [217]..... 229

Figure 9.1 – SEM micrographs of mode I fracture surfaces for (A) the novel adhesive film joint GFRP-P-CRN and (B) the commercial adhesives film joint GFRP-FM94 233
Figure 9.2 – Proposal for the manufacture of adhesive films 234
Figure 9.3 – Fracture surfaces of the mixed mode failed GFRP-FM94 (left) and the cohesively failed Al-FM94 (right) 236
Figure 9.4 – SEM micrographs of the GFRP surface prior to bonding (A) before ultrasonication and (B) after ultrasonication 237

Nomenclature

a	Crack length
A	Cross-sectional area of the specimen
a_0	Initial crack length
A_1, A_2	Pre-exponential factors for the curing reaction
a_C	Calculated crack length
a_n	Machined crack
$a_{pre\text{-}cracking}$	Crack length after pre-cracking test
C	Compliance
C	Parameter of chemically to diffusion controlled reaction transition
C_0	Load line compliance
$C_{0+5\%}$	Load line compliance increased by 5 %
C_Q	Deformation factor
D	Diffusion limitations parameter
dyn	Dynamic conditions
$d\alpha/dt$	Reaction rate
E_1, E_2	Activation energies
E_f	Flexural modulus of elasticity
eq.	Equivalent (for concentrations)
est	Estimated data
exp	Experimental data
f	Geometry calibration factor
F	Applied force
f	Frequency
F	Large deflection correction
F_{max}	Maximum applied force

F_Q	Applied force at the initiation of crack growth in the 3PB test
G_{IC}	Critical strain energy release rate (or delamination toughness) for Mode I
$G_{IC\ \mathrm{BULK}}$	Fracture energy of the bulk adhesive
$G_{IC\ \mathrm{JOINT}}$	Fracture energy of the adhesive in the joint
G_{IIC}	Mode II critical strain energy release rate (or delamination toughness)
h	Specimen thickness
iso	Isothermal conditions
k_1, k_2	Rate constants for the curing reaction
K_{IC}	Critical stress intensity factor or fracture toughness for Mode I
l	Specimen length
L	Span
l_0	Specimen length at room temperature
L_0	Gauge length of the test specimen
m, n	Cure kinetics model exponent
MAX/5%	Maximum load of the curve or intersection point of a $C_{0+5\%}$ slope line with the load vs. displacement curve
N	Load block correction
N	Number of fatigue cycles
n	Number of experimental points
NL	Onset of non-linearity on the load vs. displacement curve
P	Load
phr	Concentration of parts per hundred parts of resin
R	Electrical resistance
R	Loading stress ratio for fatigue test
R	Universal gas constant
r_{Iy}	Crack tip plastic zone radius
s	Displacement
t	Bond thickness
T	Temperature
T_g	Glass transition temperature
$T_{g\infty}$	Glass transition temperature of fully cured material
t_i	Bond thickness at i point

t_m	Bond thickness at maximum $G_{IC\,\mathrm{JOINT}}$
v	Poisson's ratio
V	Voltage
VIS	Onset of visually recognizable crack growth on the edge of the delamination specimen on the load vs. displacement curve
vol%	Concentration of volume percentage
w	Specimen width
W_{B}	Energy to break
wt%	Concentration of weight percentage
Z^*	Complex impedance
α	Fractional conversion or degree of cure
Δ	Mode I delamination crack length correction
Δ_{clamp}	Clamping correction for the ELS test
Δ_{II}	Mode II delamination length correction
ε_c	Compressive strain
ε_{yc}	Compressive strain at yield
θ_x	Rotation of the beam at any point x along the cracked region
σ	Electrical conductivity
σ_c	Uniaxial compression stress
σ_{yc}	Uniaxial compression yield stress
σ_{yt}	Uniaxial tensile yield stress
ΔH	Total enthalpy of the curing reaction
α	Coefficient of linear thermal expansion
α_{cT}, α_{c0}	Linear parameter of chemically to diffusion controlled reaction transition
δ	Deflection (or displacement)
ϕ	Energy calibration factor

Abbreviations

3,3'- DDS	3,3'- diamino diphenyl sulphone
3PB	3 point bend (test)
AC	Alternating current
ACZ	Adherend + Cohesive zone
AHEW	Amine hydrogen equivalent weight
ASTM	American Society for Testing and Materials
BCR	Bonded crack retarder
BF_3-MEA	Boron trifluoride-monoethylamine
BSI	British Standard Institute
C	Control formulation
CBT	Corrected beam theory
CBTE	Corrected beam theory with effective crack length
CF	Control plus carbon nanofibre formulation
CFRP	Carbon-fibre reinforced plastic
CN	Control plus carbon nanotube formulation
CNF	Carbon nanofibre
CNT	Carbon nanotube
CR	Control plus rubber formulation
CRN	Control plus rubber plus carbon nanotube formulation
CTBN	Carboxyl-terminated butadiene-acrylonitrile
CTE	Coefficient of thermal expansion
CVD	Chemical vapour deposition
DC	Direct current
DCB	Double cantilever beam (mode I delamination test method)
DGEBA	Diglycidyl ether of bisphenol-A

DMTA	Dynamic mechanical thermal analysis
DSC	Differential scanning calorimetry
DWCNT	Double-walled carbon nanotube
EEW	Epoxide equivalent weight
E-glass	Electrical grade glass
ELS	End loaded split (mode II delamination test method)
FM15	Commercial adhesive FM® 1515-3M
FM94	Commercial adhesive FM® 94K
GFRP	Glass-fibre reinforced plastic
GLARE	Glass-reinforced fibre metal laminate
ID	Identification
ISO	International Standards Organisation
LEFM	Linear elastic fracture mechanics
MDSC	Modulated differential scanning calorimetry
MEK	Methyl ethyl ketone
MWCNT	Multi-walled carbon nanotube
N	Nylon veil
P	Polyester veil
PEI	Polyetherimide
PmPV	Poly(m-phenylenevinylene-co-2,5-dioctoxy-p-phenylenevinylene)
PTFE	Poly(tetrafluoroethylene)
RE	Relative error
R-curve	Resistance curve
SEM	Scanning electron microscopy
SENB	Single edge-notched bending
SSA	Specific surface area
SWCNT	Single-walled carbon nanotube
TEM	Transmission electron microscopy
TMA	Thermal mechanical analysis
U	Unsupported
UD	Unidirectional

Chapter 1

General introduction

This thesis describes the formulation of a ternary thermosetting blend, consisting of a difunctional epoxy resin modified through the addition of a reactive liquid rubber and multi-walled carbon nanotubes.

The objective of the present study is the identification of possible means of minimising the thermal residual stresses created during cure of adhesively bonded aluminium-composite joints. These typically occur in current aerospace structures.

The ternary thermosetting formulation is intended to provide a novel, 120ºC cure adhesive in film form. This work aims to identify the critical parameters, relating to processability and performance, in producing this structural adhesive.

Commercial multi-walled carbon nanotubes have been shown to contract under thermal loading [1,2] and it is therefore believed that including them in the adhesive will produce a reduction in the Coefficient of Thermal Expansion (CTE) of the resin. This effect has been observed in poly(vinylidene fluoride) containing single-walled carbon nanotubes [3]. The CTE reduction has the potential to reduce the residual stresses in

bonded structures. Furthermore, carbon nanotubes have the potential to improve the mechanical, physical and electrical properties of the polymer. They exhibit an exceptionally high aspect ratio in combination with low density, as well as high strength and stiffness, which make them a strong candidate for the reinforcement of polymeric materials [4].

Traditionally, the issue of brittleness of highly crosslinked thermosetting matrices has been addressed with the incorporation of reactive liquid rubber. The formation of a heterogeneous material consisting of an epoxy matrix with embedded rubber particles provides a fracture toughness improvement. The combination of toughened systems of this type with carbon nanotubes has the potential to create thermoset matrices with superior mechanical properties.

Finally, multi-walled carbon nanotubes are highly conductive making them excellent candidates for the production of conductive polymer composites capable of dissipating electrostatic charge or shielding devices from electromagnetic radiation [5].

Thesis overview

A background to structural epoxy adhesives, an overview of the mechanisms of adhesion and matrix toughening and the adhesive specifications for aircraft structures is given in Chapter 2. Special attention is given to the use of nanotechnology in structural adhesives with a focus on carbon nanotubes.

The full range of materials utilised in this study is detailed in Chapter 3. The raw materials for the formulation of the adhesive compositions are described here along with the veils used to reinforce the adhesives. Two commercial adhesive films, selected as a reference for the performance of the developed adhesives, are also introduced. Two different substrate materials for manufacturing mechanical test specimens are detailed.

The full design process of the novel adhesive composition is described in Chapter 4. The contribution of each constituent in the adhesive formulation can only be fully

understood through the production of different adhesive variants, created by separating out the constituents. Special attention is given to the preparation of the various films and cast samples and to the manufacture of bonded specimens and structures for mechanical testing.

Chapter 5 details the methodologies for the full range of experimental tests carried out for this work. These include the thermo-mechanical and electrical characterisation of cast specimens and mechanical tests on laboratory scale Double Cantilever Beam (DCB) and End Loaded Split (ELS) specimens. Lastly, a fatigue delamination test on a larger Bonded Crack Retarder (BCR) structure is detailed.

The results obtained from the characterisation of the ternary resin blend are presented in Chapter 6. These include the cure kinetics behaviour of this novel adhesive formulation and the effects of the carbon nanotubes on the cure. The thermo-mechanical, mechanical and electrical properties of the novel ternary resin blend, in the solid state, are presented along with the contribution of each constituent on these properties.

Bonded specimens are used to characterise the performance of the novel adhesive. Chapter 7 examines the contribution of each constituent in the formulation to the mechanical response and the effect of the use of reinforcing veils in the films. Attention is given to the comparison between the cast sample toughness values obtained in Chapter 6 and those achieved from DCB testing of the bonded specimens. This chapter includes the results obtained from fatigue testing of the BCR structure.

The penultimate chapter gives a critique of the key details within this study. An assessment of the shortcomings in the published work on carbon nanotubes in epoxy resins is given. Suggestions for improving the adhesive filming process as well as achieving greater interfacial adhesion are made. Discussion is focussed upon the effects of adding carbon nanotubes in terms of processing and resulting morphology.

Chapter 9 lists the main conclusions drawn from this work. The author gives her opinions on the most promising directions for future research on this attractive ternary blend of epoxy, reactive liquid rubber and carbon nanotubes.

Chapter 2

Structural epoxy adhesives to meet today's challenge

One of the commercial advancements in epoxy structural adhesives over the last two decades has been made in improving their toughness. Current discussion is focused on nanotechnology and how this may provide even more advanced products.

This chapter presents an overview of modern structural epoxy adhesives along with a more detailed account of the inclusion of rubber which is the dominant toughening agent for this type of adhesive. The term "structural" means that the polymerised (cured or hardened) adhesive possesses a relatively high modulus and strength so that a load-bearing joint is formed. The chapter introduces the 'Bonded Crack Retarders' concept which is the background of the PhD study. Finally, the motivations for incorporating carbon nanotubes into epoxy formulations are discussed.

2.1 Overview of adhesives for aircraft structures

2.1.1 Adhesives vs. alternative joining methods

Adhesive bonding offers several advantages over the traditional joining techniques of welding and riveting which are desirable in aircraft manufacturing. These include the ability of an adhesive to distribute the loading stresses evenly and to avoid introducing areas of stress concentration around rivets or bolt holes together with significant weight savings [6]. The use of structural adhesives in engineering applications is a major growth area. Figure 2.1 shows the new Airbus A380. In this aircraft, structural film adhesive is used in the GLARE fuselage panels as an integral part of the fibre-metal laminate and also in the vertical and horizontal tail planes, the ailerons, the wing centre box and in the engine nacelles [7].

Figure 2.1 – Airbus A380 which employs structural adhesives to join many parts of the primary structure [8]

2.1.2 Reducing internal stresses

One of the major considerations for aircraft structural materials is their ability to perform across a wide temperature range. In particular, structural aerospace adhesives are usually subjected to two thermal extremes; high temperatures associated with the hardening (curing) process and the sub-zero temperatures during high altitude cruise (see Figure 2.2). Aerospace grade structural adhesives are currently cured at temperatures in excess of 120ºC. This can be a drawback for aircraft manufacture as these adhesives are often used for the bonding of dissimilar materials, metal to composite, having approximately an order of magnitude difference in their coefficients of thermal expansion (CTE). A large CTE mismatch between the substrates and the adhesive is expected to lead to the development of damaging residual stresses in the structure [9,10]. In order to reduce the stress concentrations the use of an adhesive layer that possesses an intermediate CTE between that of the two substrates has proved particularly beneficial [11].

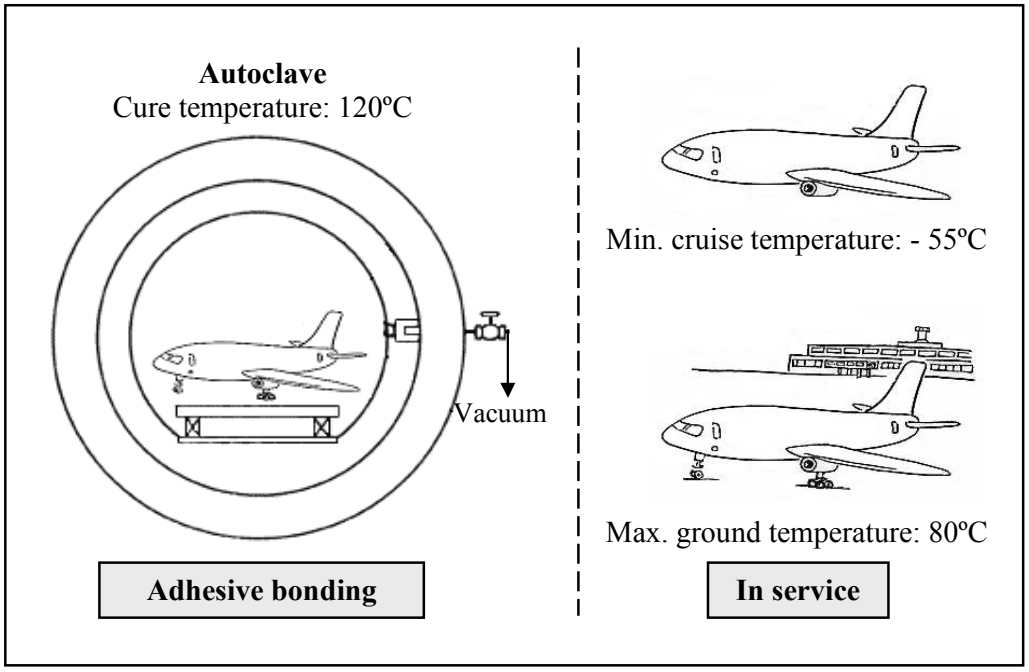

Figure 2.2 – Structural adhesives in aircraft subjected to bonding and in-service temperatures

Reduction and control of the residual stresses arising from manufacturing methods is an important issue in ensuring maximum bonded performance. Several methods to reduce

these thermal residual stresses by optimising the curing process have been developed [12,13]. These methods study the evolution of the adhesive visco-elastic properties during cure and apply different cooling and reheating cycles with the aim of minimising the adhesive shrinkage during cure. The result is the minimisation of the thermal residual stresses in the cured adhesive. However, these methods are not easy to use for large or complicated structures or in an industrial scenario. Another way to counteract the internal stresses is by introducing flexibilisers [10] in the formulation but their relatively low glass transition temperature and thermal endurance properties make them unsuitable for this purpose.

Reduction of the residual stresses can also be achieved through the adhesive formulation. Epoxy adhesives have a CTE that can be decreased and controlled by incorporation of a rigid and low CTE filler material. Typically, the filler is stiffer and has a coefficient of thermal expansion lower than the epoxy. This situation results in tensile stresses in the matrix and compressive stresses at the filler-matrix interface. To date, epoxy resins have been reinforced with quartz powder, alumina and silicon dioxide crystals observing that the residual stress between the filler and the epoxy decreased with increasing the amount of filler [14,15]. The fillers reduce the thermal shrinkage during service by bulk displacement of the resin with an inert compound which does not participate in the curing process [16].

Most high temperature adhesive systems incorporate metallic fillers, generally aluminium powder, to reduce the internal stresses due to thermal expansion [17]. However, high loading volumes increase viscosity to the point where the adhesive could not be easily applied or wet a substrate. For some base resins, filler loading values up to 200 parts per hundred parts of resin may be employed for matching the CTE of metal substrates. Moreover, metal fillers for high temperature adhesives must be carefully selected because of their possible effect on oxidation.

2.1.3 Making adhesives conductive

Future aerospace applications may require electrically conductive, polymer-based composites for static discharge, electrical bonding, interference shielding, primary and secondary power and current return through the structure [5,18,19]. Good electrical bonding of a joint is needed to assist in controlling and dissipating the build-up of electrostatic charge. Commercial adhesives are available which have been filled with high quantities (up to 60% by volume) of powdered silver, nickel or carbon black to achieve electrical conductivity. Unfortunately, such additives can deteriorate the mechanical properties, especially the elongation at break and toughness [18,20-22]. Toughness can be significantly decreased if the filler disbonds from the matrix and acts as a stress concentrator thus supplying the composite with potential sites for crack growth. However, strength and toughness can be improved depending on the filler content, morphology of the filler and resulting filler / matrix interactions in the cured adhesive.

2.1.4 'Bonded crack retarders' in aircraft structures

Trends in aircraft manufacture are towards the creation of integral structures via the use of carbon fibre polymer composite materials and in metals via manufacturing processes such as welding, casting and forging, rather than the traditional riveting. Unlike structures fabricated using mechanical fastening techniques, integral structures do not contain crack stoppers. They lack fail safety and regulators penalise such structures by imposition of extra design safety factors. The use of crack retarders, bonded to the integral structures to slow down or stop crack growth, can in principle overcome these difficulties (see Figure 2.3).

An in house project aimed to establish viable manufacturing routes and crack retardation performance of a range of composite straps adhesively bonded to a thick aluminium structure [23-25]. The focus of this study was the identification of possible means to minimise the thermal residual stresses induced during the adhesion of the composite straps. The formulation of a novel adhesive in this work concentrates on

trying to reduce these thermal residual stresses which are otherwise expected to limit the performance of such structures.

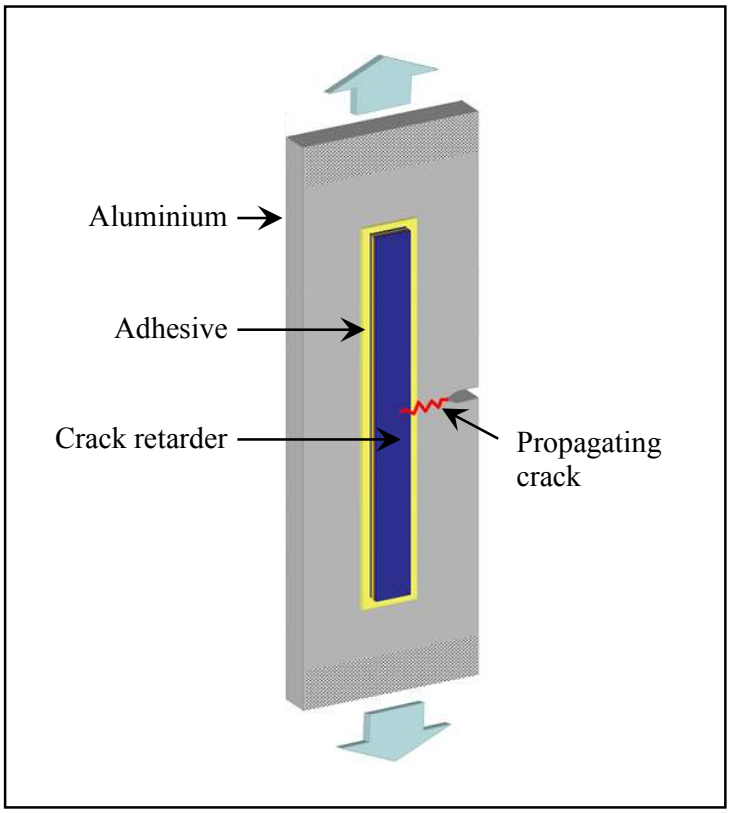

Figure 2.3 – Bonded crack retardation concept

2.2 Adhesion Overview

In the past thirty years the level of basic adhesion research has increased in accordance with the growing use of the technological applications. Despite this, a single unifying theory which adequately describes all adhesion phenomena is yet to be proposed. However, several basic models have been established. The mechanisms of adhesion can be classified into four areas: mechanical interlocking, diffusion, electronic and adsorption [26]. The adsorption and mechanical interlocking theories have been shown to be the most capable of explaining adhesion phenomena, particularly in the area of metal to metal and metal to polymer adhesion. Figure 2.4 presents these two mechanisms as diagrams. The adsorption theory states that adhesion results from

intimate intermolecular contact between two materials and involves surface forces that develop between the atoms in the two surfaces. The most common surface forces that form at the adhesive-substrate interface are Van der Waals forces. In addition, acid-base interactions and hydrogen bonds may also contribute to intrinsic adhesion forces. The mechanical interlocking theory of adhesion states that good adhesion occurs only when an adhesive penetrates into the pores, holes and crevices and other irregularities of the surface of a substrate and locks mechanically to the substrate. The adhesive must not only wet the substrate, but also have the right rheological properties to penetrate pores and openings in a reasonable time. The adhesive interlocks with the surface layers on both sides and provides a mechanical bond.

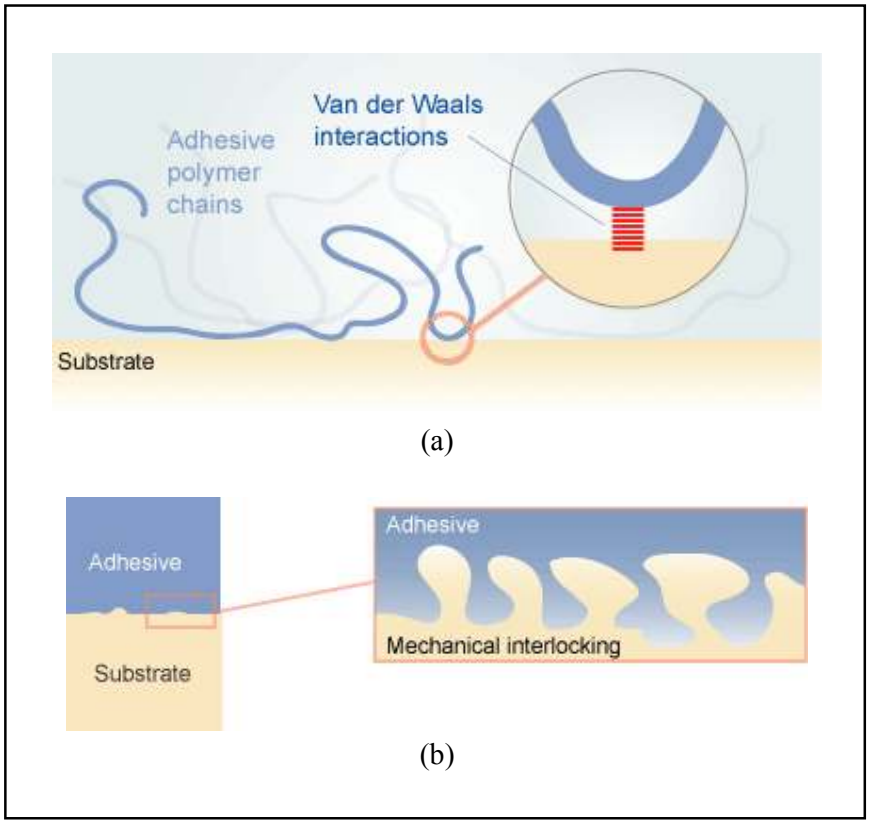

Figure 2.4 – Mechanisms of adhesion involves in bonding metal to metal and metal to composite; (a) adsorption and (b) mechanical interlocking [27]

Thermosetting epoxies are the oldest, most common and most diverse of the adhesive systems and can be used to join most engineering materials including metal, glass, composite and ceramic. Just as epoxies are the most common matrix for advanced

composites, epoxy adhesives are also the most effective for bonding them due to the chemical compatibility between the epoxy matrix in the composite and the epoxy resin in the adhesive [9].

Thermoset epoxy adhesives have the following advantages [26,28]:

- high strength and stiffness
- low level of creep under sustained load
- good tolerance to elevated temperatures
- good chemical resistance
- good gap filling properties
- low level of shrinkage on cure
- great formulation capability due to many types of base resins and curing agents that are available
- ability to cure under a wide range of conditions

2.2.1 Epoxy adhesive toughening

Epoxy resins cured with aromatic curing agents give a highly crosslinked adhesive matrix with many useful properties such as a high modulus and failure strength, low creep and good performance at elevated temperature [29,30]. However, the structure of such thermosetting adhesives also leads to one highly undesirable property in that they are relatively brittle, with a poor resistance to crack initiation and growth. Nevertheless, this problem can be overcome by toughening the adhesive system.

A variety of toughening agents have been used to modify epoxy adhesives without significantly affecting other properties of the base epoxy resin [29]. Generally these modifiers can be classified into three types:

- reactive liquid rubbers
- functionally terminated thermoplastics
- inorganic / core-shell particles

From the list above, the most successful method to toughen structural epoxy adhesives has been the incorporation of reactive liquid rubber, the most common being carboxyl-terminated butadiene-acrylonitrile (CTBN). One attraction of this method is that the liquid rubber is miscible in the uncured epoxy resin leading to a homogeneous solution. As the curing reaction proceeds, the molecular weight increases and phase separation occurs at some stage leading to the formation of a two-phase morphology where small rubber domains of a definite size and shape are formed. The domains cease growing at gelation and after cure is complete the adhesive consists of an epoxy matrix with embedded rubber particles [31-34].

Considerable work has shown that the separation of the elastomer into a separate phase is necessary for significant toughening to occur and to retain the bulk properties of the epoxy system [32,33]. Thus, particle size and distribution of the elastomer phase is very important. To obtain the desired phase separation and particle-size distribution, CTBN is usually pre-reacted (adducted) to the base epoxy resin. Adduction reduces the likelihood of early phase separation and maintains the solubility of the elastomer in the uncured resin system [31].

2.2.2 Reactive liquid rubber: in detail

Many different mechanisms have been proposed to explain the improved fracture toughness that may result with the formation of a secondary phase of dispersed rubber particles in an epoxy adhesive. Much of the dispute has concerned whether the rubbery particles or the epoxy matrix absorbs most of the energy [30]. However, it has been clearly established that plastic deformation of the epoxy matrix is the main source of energy dissipation and increased toughness [32,33,35]. Such enhanced plastic deformation arises from the interactions of the stress field ahead of a crack tip and the rubbery particles. The following section provides an overview of the stress field around the rubbery particles in the matrix and the deformation processes involved [30].

2.2.2.1 Stress fields around rubber particles

A rubber particle embedded in the matrix, which typically possesses a considerably lower shear modulus than the matrix, introduces a tensile stress concentration in the matrix. Furthermore, assuming that the particle is well bonded to the matrix, the local stress state at this point is one of triaxial tension (see Figure 2.5). This tension arises essentially because of the volume constraint represented by the bulk modulus of the rubber particle, which is comparable with that of the matrix. The low shear modulus of the rubber particle relative to the thermoset matrix, in spite of its comparable bulk modulus, is a consequence of the Poisson's ratio of the rubber being approximately 0.5; whilst that of the matrix is about 0.35. Thus, in contrast to a 'hole', which would produce a similar-size stress concentration, the rubbery particle can fully bear its share of the load across the crack front. This ability of the rubber particles to bear loads whilst functioning as stress concentrators can explain the observation that rubber particles are more effective for toughening the polymer, compared with 'holes'.

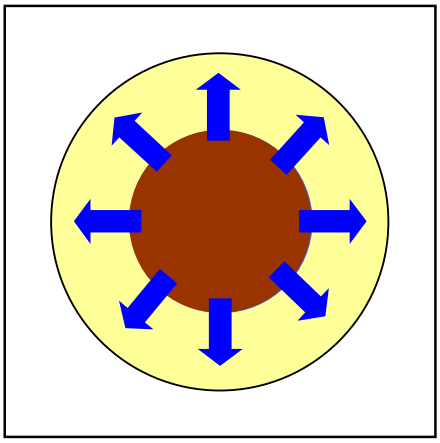

Figure 2.5 – Stress field generated around a rubber particle embedded in the epoxy matrix

2.2.2.2 Matrix plastic yielding and particle cavitation

The stress field associated with the rubber particles leads to the initiation of two important deformation processes, shear yielding and particle cavitation, shown in Figure 2.6, which can strongly interact [32,35-37].

The first of these deformation processes is the initiation and growth of multiple localised shear-yield deformations in the matrix [30]. The stress concentrations around the rubber particles act as initiation sites for the plastic shear deformation. During the deformation process, the shear stresses cause atoms or chains segments to slip past to each other. As a result, small elements of material in the yield zone change their shape without undergoing noticeable changes in volume. This phenomenon, even if it causes disturbances in the molecular packing, does not cause loss of cohesion. However, the plastic deformation is localised through the post-yield strain softening of the epoxy matrix and the fact that shear deformations initiate at one particle but terminate at another. The localised nature of the plastic shear bands, visible as furrows running at shallow angles and stretched rubber particles, is illustrated in Figure 2.7.

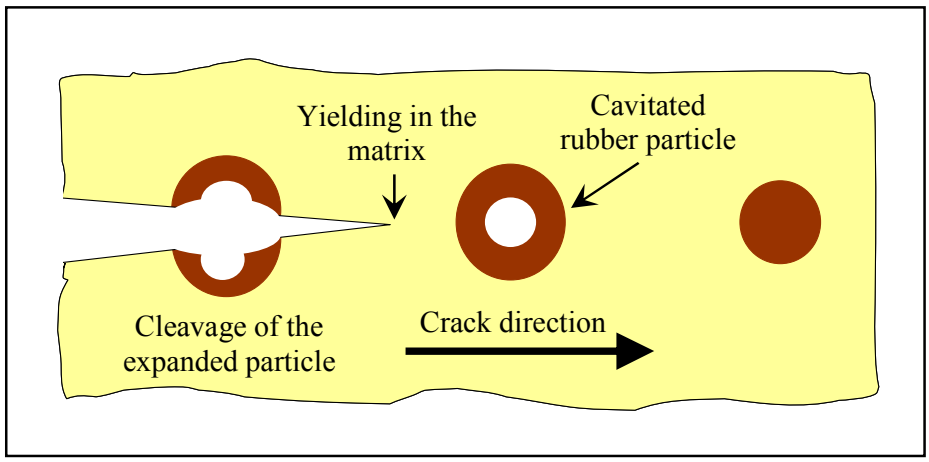

Figure 2.6 – Fracture deformation processes of a rubber toughened epoxy adhesive, modified from [38]

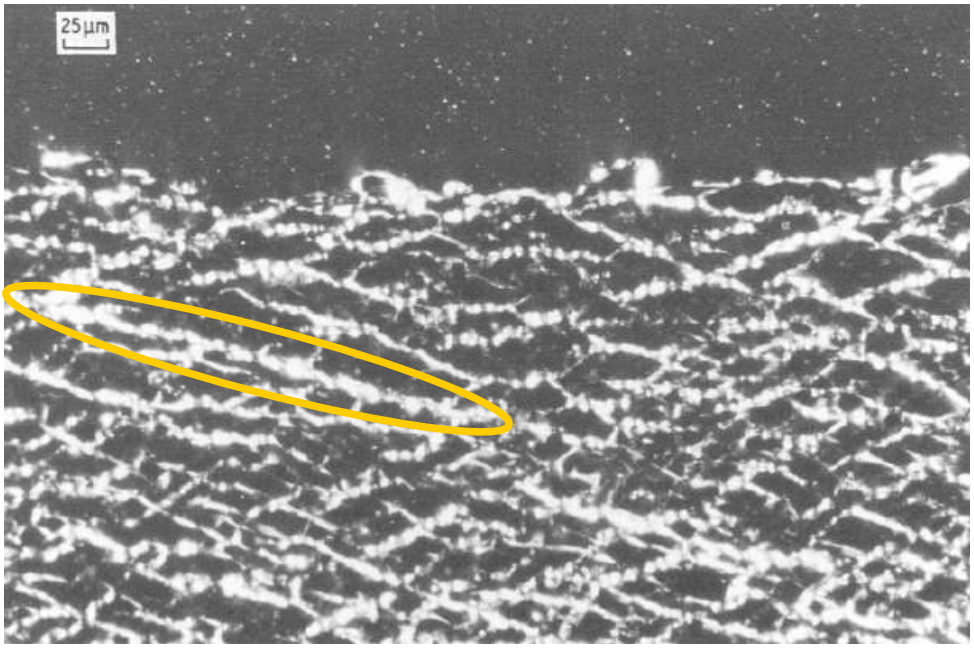

Figure 2.7 – Optical microscopy image of the perpendicular section to the fracture surface of a rubber-modified epoxy system. Shear bands (at low angles) and stretched rubber particles appear bright under polarized light [32]

The second major deformation process is cavitation of the rubber particles [30]. In considering this phenomenon, it is necessary to recall that an overall triaxial stress state (plane strain) usually exists ahead of the crack tip and produces dilation. These stresses are combined with the stresses that are induced in the particle by cooling after cure. As a result, the rubber is under high triaxial stresses and aims at releasing them to reach a lower energy state, which would be more stable. The way the rubber particles release these stresses is by forming a hole or cavity in the rubber particle. The formation of such a void in a rubber particle, termed cavitation, is clearly shown in Figure 2.8. The importance of the formation of such voids in the rubber particles ahead of the crack tip is not due to the energy that is associated with the formation of these voids. This is typically of little significance. Rather, after cavitation of the rubber particles, the matrix surrounding the rubber particle has more freedom to yield and deform (see Figure 2.6). After cavitation the shell of rigid polymer that is enclosing the rubber particle has the possibility to expand through biaxial extension, thus allowing the dimensions of the cavitated particle to increase. Nevertheless, it should be taken into account that yielding cannot develop infinitely around an isolated particle and therefore is limited.

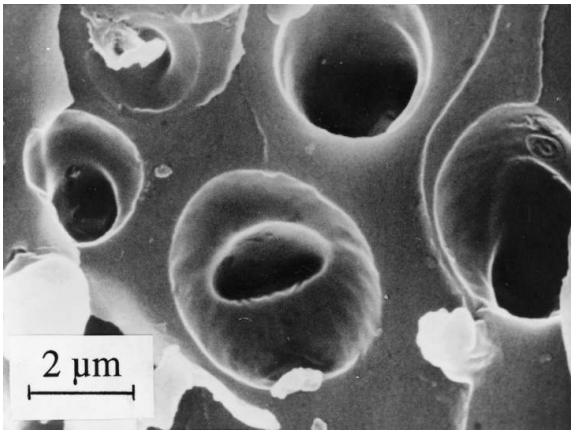

Figure 2.8 – Scanning electron microscopy (SEM) image of a rubber modified epoxy resin, showing cavitation of the particles on the fracture surface [39]

These two processes, matrix plastic yielding and particle cavitation, are responsible for the increase in toughness achieved when rubber particles are added to an epoxy resin to create a two-phase morphology [30].

2.3 Effect of adhesive bond thickness

The fracture of adhesive joints has been studied with considerable success by using the fracture mechanics approach [40]. In particular, adhesive joints with mode I crack growth (tensile loading perpendicular to the crack plane) have been well characterised. It has become clear that the plastic zone developed at the crack tip determines the crack resistance of the bonds. The adhesive joint fracture energy $G_{IC\ \mathrm{JOINT}}$, defined by the strain energy release rate, can be attributed to the size of this zone.

Previous works in literature have reported the attainment of a maximum value when they examined the variation of $G_{IC\ \mathrm{JOINT}}$ with the bond thickness. To interpret the occurrence of this maximum Kinloch and Shaw [41] employed an elastic-plastic model for the deformation zone surrounding the crack tip as shown in Figure 2.9. They claimed a maximum value of $G_{IC\ \mathrm{JOINT}}$ when the bond thickness (t_m) equals the diameter of crack tip plastic zone ($2r_{Iy}$).

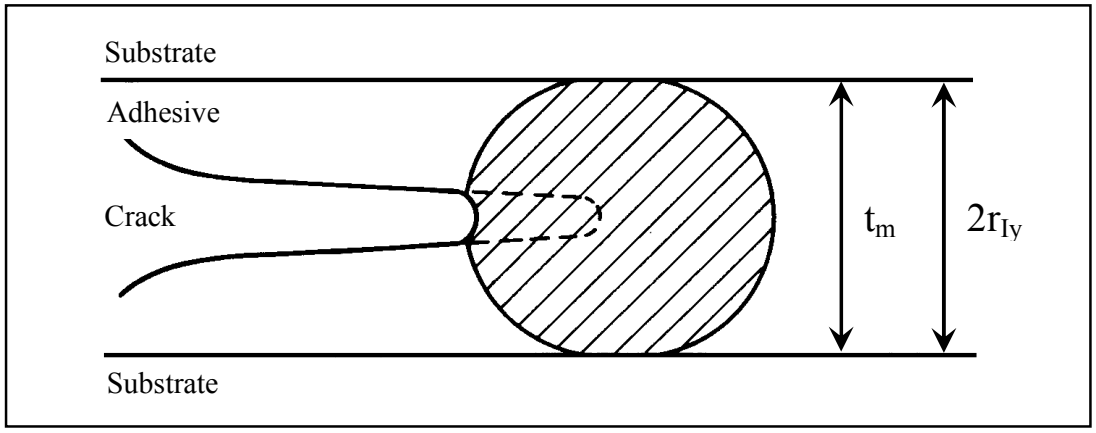

Figure 2.9 – Simple elastic-plastic model for deformation zone at adhesive crack tip [41]

The value of $2r_{Iy}$ and hence t_m, may be predicted from a fracture mechanics analysis, using bulk adhesive properties as follows [41]:

- Plane-stress condition:

$$r_{Iy} = \frac{1}{2\pi}\frac{E_f G_{IC\,BULK}}{\sigma_{yt}^2} \quad \text{..... (2.1)}$$

- Plane-strain condition:

$$r_{Iy} = \frac{1}{6\pi}\frac{E_f G_{IC\,BULK}}{\sigma_{yt}^2}\frac{1}{\left(1-\nu^2\right)} \quad \text{..... (2.2)}$$

Where:

E_f	is the flexural modulus of the bulk adhesive, in MPa
$G_{IC\,\mathrm{BULK}}$	is the fracture energy of the bulk adhesive, in J/m^2
ν	is the Poisson's ratio
σ_{yt}	is the uniaxial tensile yield stress, in MPa

When epoxy resins and more specifically rubber-modified epoxy are tested in uniaxial tension the material suffers brittle fracture prior to yielding. It is advisable to examine the yield behaviour by testing in uniaxial compression. The value of tensile yield stress, σ_{yt}, can be deduced from compression testing, since [41]:

$$\sigma_{yt} \approx 0.75\sigma_{yc} \quad \text{..... (2.3)}$$

Where:

σ_{yc} is the uniaxial compression yield stress, in MPa

Figure 2.10 shows an example of how the plane-stress and plane-strain zones are shaped in front of the crack tip.

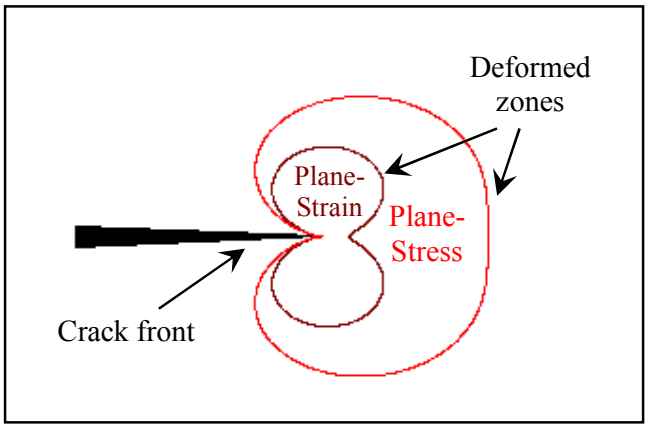

Figure 2.10 – Schematic representation of plane-stress and plane-strain deformation zones developed at the crack tip, modified from [42]

At the same time, research has compared the bulk and joint fracture, caused by the constraint imposed upon the adhesive layer when it is located between the substrates (see Figure 2.11) [41]. Essentially, the maximum volume of plastic deformation ahead of the crack tip in the adhesive layer occurs when the bond thickness equals the diameter of the plastic zone. Under this situation $G_{IC\ JOINT}$ is at its maximum value. $G_{IC\ JOINT}$ is lower than the maximum at smaller thickness due to restriction on the further development of the plastic zone. $G_{IC\ JOINT}$ is also lower than the maximum at larger thickness due to the decrease in degree of constraint reducing the length of the plastic-zone and hence reducing its volume. The degree of constraint is also a function of joint width.

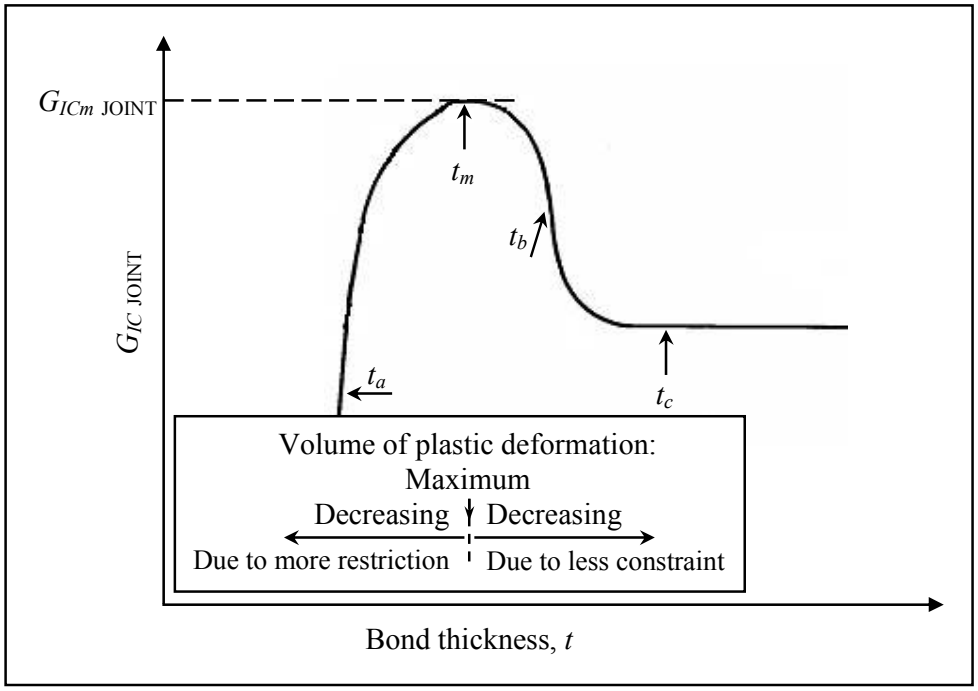

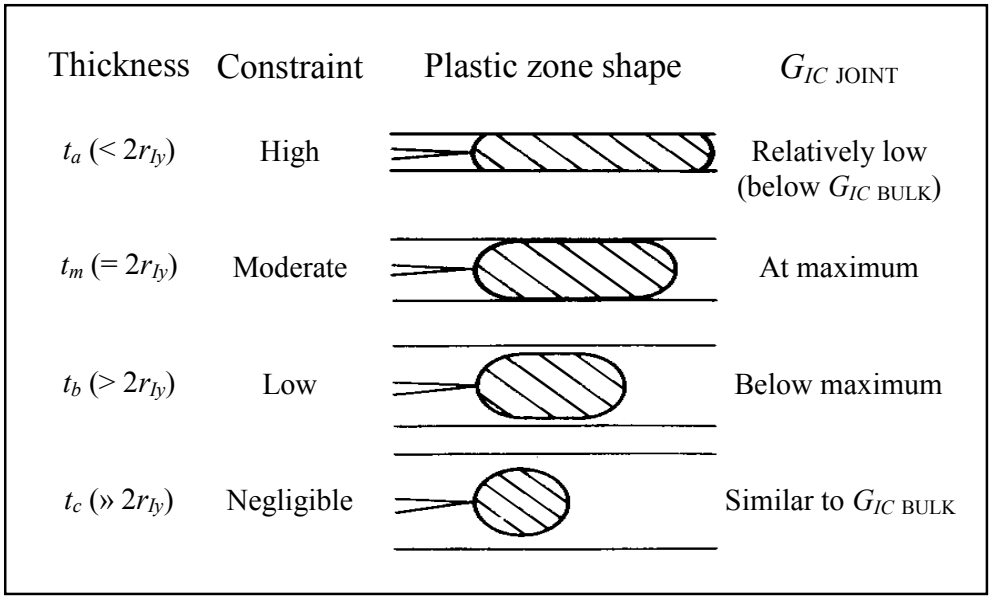

Figure 2.11 – Relationship between $G_{IC\,\mathrm{JOINT}}$, plastic-zone shape and degree of constraint in the joint due to bond thickness, modified from [41]

However, this single parameter (plastic zone diameter) fracture mechanics approach can not predict the constraint effects [43,43]. Capturing constraint effects requires detailed modelling of the mechanics of deformation in both the substrate and the adhesive. Indeed, the mechanisms of cracking of an adhesive layer are very complex, involving

multi-axial plastic deformation and various types of damage phenomena developing at different scales. An important step in this effort has been the introduction of cohesive zone models to describe the response of adhesive layers to mechanical loading and to simulate crack propagation [43-48]. One such model, known as ACZ (Adherend + Cohesive Zone), considers two constituents in the system; the substrate and the adhesive layer with its mechanical response fully represented.

However, modelling the constraint effects in the adhesive joint fracture is not the objective of this work. When comparing bulk and joint adhesive fracture, the plastic zone diameter still remains an effective parameter for defining an optimum bond thickness for which a maximum value of adhesive fracture toughness in the joint can be expected [49].

2.4 Use of nanotechnology in structural adhesives

The chemical industry was leading the way with "nanotechnology" even before the term was invented. Chemicals or molecules are nano-objects. Carbon black, fumed silica and many catalysts are essentially nanoscale products. Advances over the last 10 years in producing nano-structured materials with novel material properties have stimulated research to create multi-functional macroscopic engineering materials by designing structures at the nanometer scale. Motivated by the recent enthusiasm for "nanotechnology", development of nanocomposites is one of the rapidly evolving areas of composites research.

Nano-structured materials in composite research fall into three broad categories:

- metal oxides
- nanoclays
- conductive nanostructures such as carbon nanotubes and carbon nanofibres

They have been found to improve the heat and chemical resistance, flame resistance and general physical properties of composites [50-54]. The first applications in the adhesive field are likely to be those where multiple-functionality is required. Nanomaterials as additives in adhesives will likely first see uses in applications where electrical conductivity, barrier properties and flame resistance are highly valued [55].

2.4.1.1 Mechanics of nanoparticle toughening

It is well known that the presence of rigid (micro-) fillers (spherical or fibrous) may induce several toughening mechanisms in epoxy matrices such as void nucleation [56], crack deflection [57,58], plastic deformation [59], crack pinning [59] and mechanisms such as fibre pull-out [60].

The increase in fracture toughness is not only related to the fibre-like structure of carbon nanotubes. A significant enhancement can also be observed for composites containing spherical nanoparticles. There is clear evidence that the performance is related to the enormous surface area per unit volume of nano-particles in general [61]. Figure 2.12 shows micrographs of carbon nanotubes and silica nanoparticles dispersed in epoxy resins.

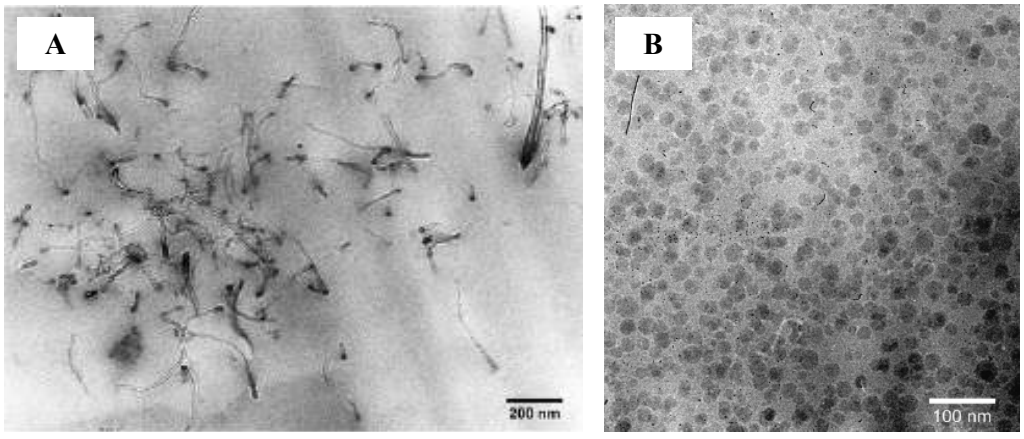

Figure 2.12 – TEM micrographs of epoxy resin containing (A) multi-walled carbon nanotubes [4] and (B) silica nanoparticles [61]

Crack deflection occurs where the crack front tilts and twists when it encounters the particles and hence passes around them. 'Crack pinning' is where rigid particles act as

effective fastening points during fracture and induce plastic deformation of the matrix. As the nanoparticles are so much smaller than the crack-opening displacement, it is unlikely that these in-plane mechanisms are responsible for the toughening effect. These fracture mechanisms assume that the particle diameter is much greater than the plastic zone size, which is not the case with nanoparticles [61]. However, since nanocomposites generally exhibit a partly agglomerated dispersion of the nanofillers, crack deflection and crack pinning at the agglomerates can also be expected to be involved in the resulting toughening effect [4,62].

The void nucleation mechanism involves the debonding of the nanoparticles followed by plastic void growth in the matrix. The voids around particles close-up when the epoxy polymer is heated above its glass transition temperature and is allowed to relax. The debonding process is generally considered to absorb little energy compared to the plastic deformation of the matrix. However, debonding is essential because this reduces the constraint at the crack tip and hence allows the matrix to deform plastically via a void growth mechanism [61].

Figure 2.13 shows evidence of debonding of silica nanoparticles in an epoxy resin and subsequent plastic void growth; it was confirmed that this mechanism is most likely to be responsible for the increased toughness observed with the presence of the nanoparticles [61]. Debonding of carbon nanotubes has been claimed in literature also [4,62] (see Figure 2.14). However, on the evidence provided it is difficult to confirm the existence of voids around the nanotubes. This phenomenon cannot be discounted though and the author believes that the observation of nanoparticle disbonding depends on the matrix material used. In the case of the nanotubes seen in Figure 2.14 and in this work, the matrix materials used do not allow yielding and therefore debonding is unlikely to occur.

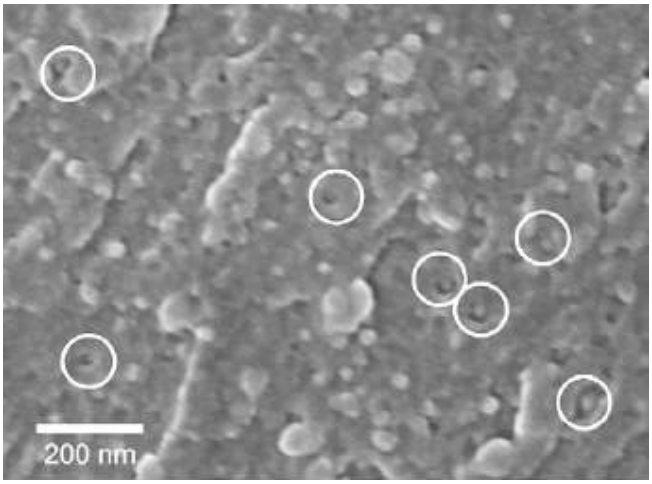

Figure 2.13 – SEM micrograph of the fracture surface of epoxy resin containing 9.6 vol% of nanosilica – Voids with nanoparticles are circled [61]

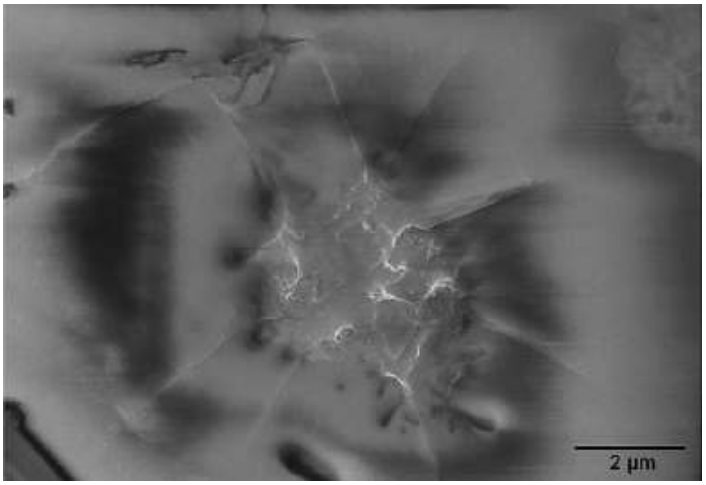

Figure 2.14 – SEM micrograph of the fracture surface of epoxy resin containing functionalised carbon nanotubes. The shear-bands around the agglomerates indicate plastic matrix deformation but there is no clear indication of void nucleation as claimed [62]

2.5 Why use carbon nanotubes in structural adhesives?

Carbon nanotubes (CNTs) have a high potential to improve the mechanical, physical and electrical properties of polymers [50,51,63,64]. They exhibit an exceptionally high aspect ratio in combination with low density, as well as high strength and stiffness,

which make them a strong candidate for the reinforcement of polymeric materials. Since their discovery in 1991 [65] research has shown several effects of carbon nanotubes on the mechanical properties of epoxy resins that could be beneficial and enable the use of state-of-the-art epoxy adhesives on aircraft structures.

Three types of carbon nanotubes shown in Figure 2.15 have been analyzed [62] to date:

- single-walled CNTs (SWCNT)
- double-walled CNTs (DWCNT)
- multi-walled CNTs (MWCNT)

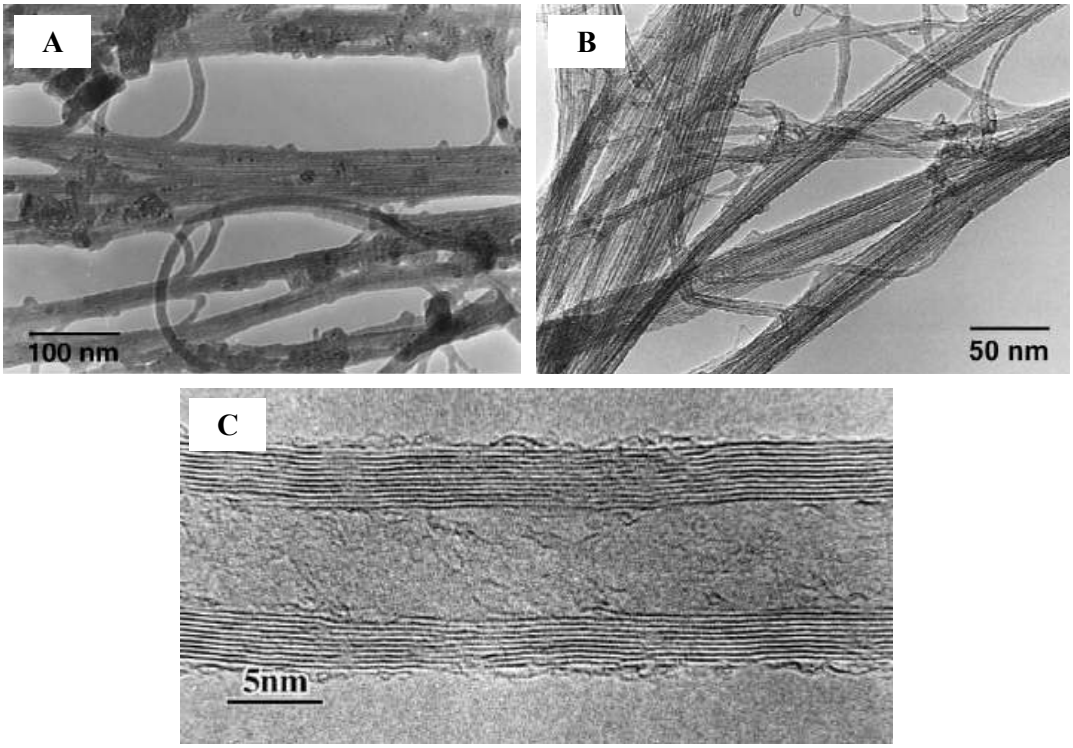

Figure 2.15 – TEM micrographs of (A) single-walled CNTs (SWCNTs) [64], (B) double-walled CNTs (DWCNTs) [64] and (C) multi-walled CNTs (MWCNTs) [66]

The specific surface area (SSA) of carbon nanotubes is dependent on the diameter and the number of sidewalls. The maximum value is achieved with SWCNTs (1300 m^2/g) [62]. Additionally, SWCNTs have the largest aspect ratio of the three types of carbon nanotubes and they have the highest potential to improve the strength of materials. DWCNTs consisting of two concentric layers, exhibit a smaller SSA (600-800 m^2/g)

and lower aspect ratio, but agglomeration is not as pronounced as for SWCNTs. MWCNTs have a much larger diameter and consist of several concentric walls. These nanotubes have a SSA of 200 m^2/g or less and the lowest aspect ratio, but whilst they exhibit a much better dispersibility they provide a smaller interface for stress transfer. Furthermore, the stress transfer between the concentric layers occurs via interlayer shearing transferred by van der Waals forces which are relatively weak. As a conclusion, multi-walled carbon nanotubes are considered to be the least effective in reinforcing materials. However, as they are more readily available, multi-walled carbon nanotubes are selected for the majority of current research. Furthermore, any improvements in mechanical properties achieved will be conservative and may be further enhanced through the adoption of SWCNTs or DWCNTs.

The following section provides an overview of different functionalities of carbon nanotubes, when used as fillers in epoxy resin, which make them an attractive option for use in a structural epoxy adhesive formulation.

2.5.1 CNTs as mechanical reinforcement in epoxy resins

Contrasting findings appear in the literature concerning the mechanical properties obtained with the use of carbon nanotubes in epoxy resins. Promising studies claimed improvements in stiffness (+6%) and especially fracture toughness (+23%) with only 0.3 wt% of MWCNTs [62]. However, other studies observed only marginal improvement or even a decrease in tensile moduli after small additions of nanotubes into an epoxy resin matrix [63,67]. There are two possible explanations for the discrepancy between these two sets of findings; differences in the level of interfacial adhesion with the epoxy resin and / or differences in the level of dispersion of the nanotubes in the matrix. These two issues, explained hereafter, represent the key aspects in reinforcing an epoxy resin with carbon nanotubes.

2.5.1.1 Considerations for manufacturing CNT – polymer composites for mechanical reinforcement

Carbon nanotubes present a high specific surface area which encourages the formation of agglomerates due to intermolecular interactions, such as van der Waals forces. However, they need to be well dispersed in the composite matrix in order to achieve maximum benefit. A further consideration is the weak interfacial adhesion that exists between the nanotubes and the polymer matrix. These two important factors, homogeneous dispersion and interfacial adhesion, represent the key aspects in improving the mechanical properties of an epoxy resin with carbon nanotubes [4]. In contradiction however, for the enhancement of electrical and thermal properties a certain level of agglomeration of the nanotubes and weak interfacial adhesion between the nanotubes and the epoxy resin is required [64]. Interfacial adhesion between carbon nanotubes and epoxy matrix and the influence on the electrical conductivity of the nanocomposite is discussed in Section 2.5.2.1.

Alignment of the carbon nanotubes is a less crucial requirement for mechanical reinforcement [51]. Research has shown the nanocomposite modulus to be a factor of five less for randomly orientated nanotubes than for perfectly aligned. While alignment is necessary to maximise uniaxial strength due to the large uniaxial modulus of carbon nanotubes, it is not always beneficial. Aligned composites have very anisotropic mechanical properties, which may need to be avoided in bulk samples. In macroscopic fibres, however, alignment has no downside and is a good way to maximise reinforcement.

Functionalisation

Controlling the polarity of the carbon nanotubes surface can improve the CNT / matrix interfacial bonding. This is important in order to ensure a shear stress transfer to the reinforcement.

A chemical functionalisation of the particle surface enables the formation of covalent bonds between resin and carbon nanotube. This is also expected to help the dispersion of the filler during manufacturing. The chemical functionalisation process of carbon nanotubes consists of three main steps; oxidation, chemical functionalisation with multifunctional amines and final processing of the nanocomposite (see Figure 2.16) via the use of multifunctional amines [4,68-70]. The oxidation treatment is used to develop carboxylic groups and the opening of the carbon nanotube cap. This first step enables a direct bonding of the tube ends via the carboxylic groups to the matrix. In the second step the carboxylic groups react with multifunctional amines and form either ionic or covalent bonds via an acid / base reaction. With the addition of the epoxy resin in the third step, the free amino functions on the surface of the carbon nanotubes will react with the epoxy molecules forming equivalent bonds. The result is an improved nanotube matrix bonding.

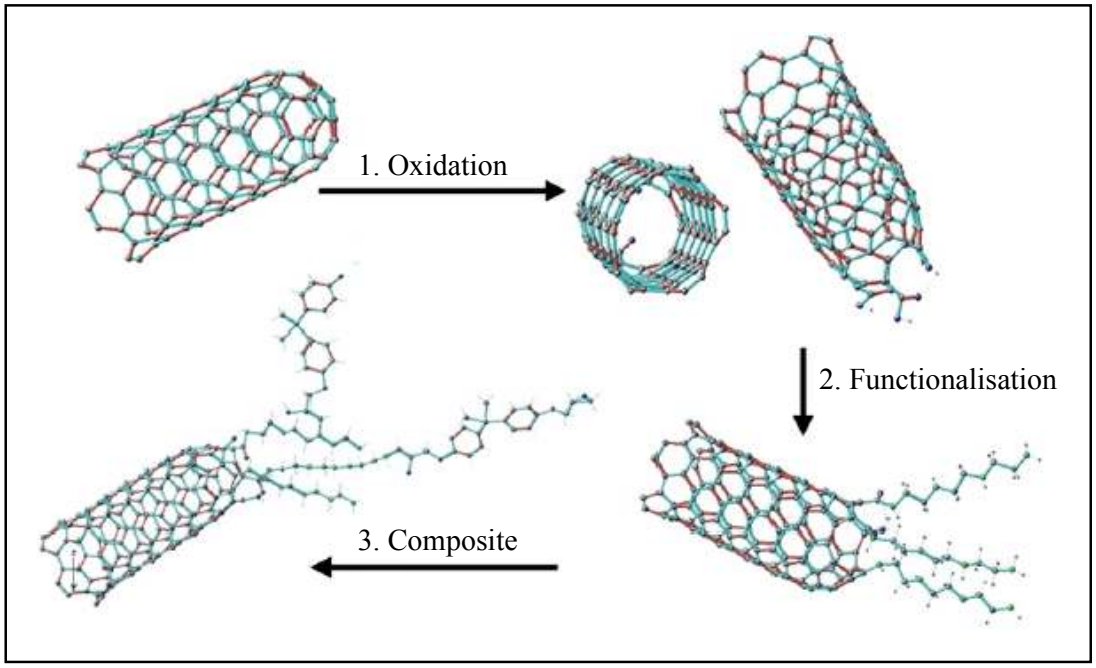

Figure 2.16 – Schematic of the carbon nanotube functionalisation process [4]

Another common method to control the polarity of carbon nanotubes in the matrix is the use of surfactants [71]. The advantage of this procedure is the physical adhesion, which does not reduce the structural quality of carbon nanotubes, whereas a covalent integration of functional groups from chemical functionalisation is always related to

structural changes of graphitic layers. Similar to surfactants, conjugated polymers such as PmPV (poly m-phenylenevinylene-co-2,5-dioctoxy-p-phenylenevinylene), can also physically bond to carbon nanotubes and be used to improve their compatibility with the polymer matrix [72]. However, chemical functionalisation is believed to be more effective in developing carbon nanotubes / polymer composites as a stronger bond between nanofiller and polymer is obtained [4].

Dispersion

Dispersion is probably the main requirement for effective reinforcement with carbon nanotubes [51]. The nanofillers must be uniformly dispersed to the level of isolated nanotubes individually coated with polymer. This is imperative in order to achieve efficient load transfer to the nanotube network. This also results in a more uniform stress distribution and minimises the presence of stress concentration centres.

Different processing methods can be used to fabricate a homogeneously dispersed nanotube reinforced polymer composite [4]:

- sonication
- shear mixing
- calendering

Ultrasonic devices produce a locally high level of energy, but introduce low shear forces. However, the local introduction of the energy may lead to rupture and damage of the nanotubes and the method is only suitable for processing small volumes [73]. Several works have applied the sonication technique to disperse the carbon nanotubes in an appropriate solvent (i.e., acetone, ethanol) [4,74,75]. The suspension was subsequently mixed with the epoxy and the solvent removed by evaporation. However, it has been found that while dispersion was improved, traces of residual solvents had a negative effect on the nanocomposite properties [75].

High shear mixing is a common technique to disperse particles in liquid systems and can be used to disperse nanoparticles as well. Size and shape of the propeller and the

mixing speed control the dispersion result. The MWCNTs can be distributed more easily than DWCNTs and SWCNTs, for which higher shear forces are needed to achieve a fine dispersion. However, all three types of carbon nanotubes have a tendency to re-agglomerate, sometimes even during the mixing process [76-78].

The application of a mini-calender (see Figure 2.17) to disperse carbon nanotubes and nanoparticles in general has recently become a very promising approach in order to reach a good state of dispersion [63]. A major advantage of this method is the efficient manufacturing of larger quantities of nanocomposite.

Figure 2.17 – Mini-calender (three-roll mill) purchased by the Composites Centre at Cranfield University for the dispersion of carbon nanotubes in thermoset matrices

2.5.2 CNTs to assist conductivity and damage monitoring in epoxy resins

The very high conductivity of carbon nanotubes makes them excellent candidates for the production of conductive epoxy adhesives, capable of dissipating electro-static charge build-up [79] and allowing stress-strain monitoring and damage detection techniques to be incorporated into aircraft structures [80]. Another related application

involving much larger currents (up to 200 kA) is lightning strike protection. The key challenge in this application is to either fully dissipate the energy or direct it into an easily repairable failure mode without compromising the structure or the flight performance [18].

For the dissipation of electrostatic charge an electrical conductivity exceeding 10^{-6} S/m is required [18,81]. As previously mentioned in Section 2.1.3, conductive adhesives exist that are filled with high amounts (up to 60 vol%) of powdered silver, nickel or carbon black albeit with a detrimental effect on mechanical properties. The percolation threshold, defined as the filler content to achieve a conductivity of $\sigma \geq 10^{-6}$ S/m, has proved to be lower for fibre-shaped fillers with high aspect ratio like carbon nanotubes than for spherical nanoparticles [64]. The lowest percolation thresholds were observed for CNTs below 0.1 wt% [5,78] whilst 0.75 wt% of carbon black was required to achieve a similar conductivity [82,83]. Furthermore, as introduced in Section 2.5.1 and in contrast to the inclusion of other filler types, carbon nanotubes may also enhance certain mechanical properties of the final nanocomposite.

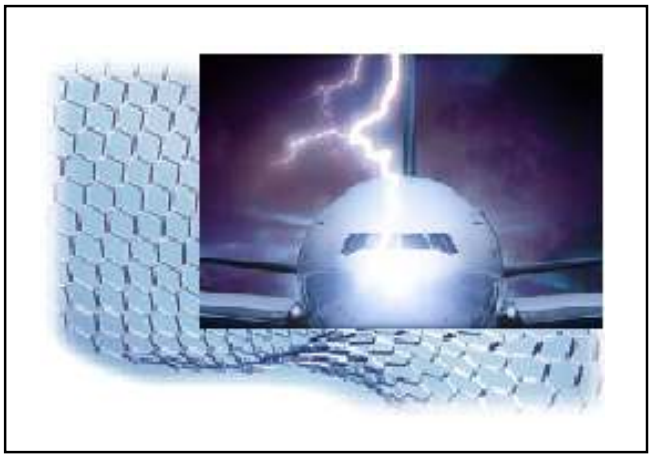

Figure 2.18 – Carbon nanotubes for lightning protection in composite aircraft structures [84]

2.5.2.1 Considerations for manufacturing CNT – polymer composites for conductivity and damage monitoring

The realisation of an electrically conductive polymer through carbon nanotubes use is based on percolated pathways of the conductive nanofillers [5,50,64,78]. The electrical

conductivity achieved can be explained by the established percolation theory [85], with an onset of the conductivity when a critical filler concentration, commonly known as percolation threshold, is reached to form conductive paths. The requirements for the enhancement of the electrical properties by the carbon nanotubes are contradictory to the ones that improve the mechanical properties.

As explained Section 2.5.1.1, homogeneous dispersion of the carbon nanotubes and interfacial adhesion to the matrix are desired in order to improve the mechanical properties. Chemical functionalisation of the nanofillers was mentioned to significantly help with both of these requirements. In contrast, the lowest percolation thresholds were observed for the non-functionalised carbon nanotubes [64]. The reaction of the epoxy resin with the nanotubes' surface-groups created by the chemical functionalisation formed an electrically insulating epoxy layer, which increases the distance between individual nanotubes, reducing the conductivity of the final structure. Moreover, a certain level of agglomeration of the nanotubes is required in order to achieve the conductive network [64].

Furthermore, the mechanical reinforcement by the carbon nanotubes was proved to be more effective for higher specific surface areas which corresponded to the SWCNT type nanotubes. In contrast, MWCNTs appear to have the highest potential for inducing electrical conductivity to an epoxy matrix, due to their relatively low surface area and high aspect ratio [64]. Any kind of treatment, leading to a reduction of the aspect ratio (non-chemical functionalisation, ultrasonication, etc.) decreases the percolation threshold and therefore increases the electrical conductivity.

2.5.3 CTE control

Carbon nanotubes appear to be the ideal candidates to reduce the internal residual stresses caused by thermal expansion. They exhibit an exceptionally high stiffness and strength [86-88] and thermally contract rather than expand like most other filler materials. Indeed, carbon nanotubes have a negative CTE in the tube axis (-12×10^{-6} K^{-1} [1]) as well as in diameter (-1.5×10^{-6} K^{-1} [2]) while epoxy resin CTE is around

54 x10^{-6} K^{-1} [89]. Therefore, although there are no specific published works, carbon nanotubes might be expected to reduce the CTE of epoxy resins by adding much lower loadings than when metallic fillers are used.

2.5.4 Processing control via rheological additives

Rheological additives are usually employed in structural adhesives to control flow properties during manufacture and subsequent cure [90]. The challenge is that the adhesive may need different flow characteristics at different times. Adhesives must flow readily so that they can be evenly applied to a substrate and wet the surface. Yet, there should not be an excess of penetration into porous substrates, nor should the adhesive run or 'bleed' excessively thus leaving a starved joint. Additives to achieve these effects are generally referred to as "thixotropes".

The thixotropic effect is shown in Figure 2.19. The material is first exposed to increasing and then decreasing shear rates. The material remains solid until a critical yield value is reached (yield strength) and then it begins to flow. Because of the decrease in viscosity with time as well as shear rate, the up and down flow curves do not superimpose. Instead, they form a hysteresis loop.

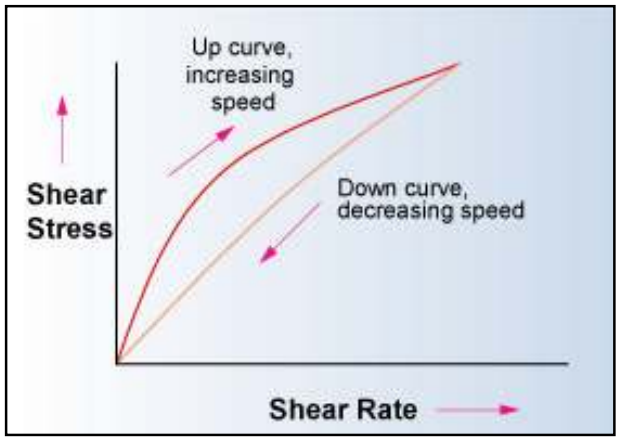

Figure 2.19 – Hysteresis obtained for thixotrope adhesive additives [90]

At one time asbestos fibers were used as the primary thixotrope in the adhesive industry. However, asbestos abruptly disappeared as an additive due to health and

environmental factors. Asbestos fillers also stiffen and harden the resulting product. Although no single material has been found as a direct replacement for asbestos, the need was eventually filled by a number of materials.

Fumed silica, an amorphous silicon dioxide, has long been the dominant thixotrope employed in adhesive formulations. Because of its high surface area to weight ratio, formulations generally require only a little fumed silica (1-5 wt%) to achieve thixotropic properties [90,91].

The high specific surface area of carbon nanotubes (up to 1300 m^2/g [92]), as well as their exceptionally high aspect ratio, make them ideal candidates to control the flow properties of an adhesive [93].

2.5.5 Special consideration: galvanic corrosion

Unlike other kinds of filler, carbon nanotubes in the epoxy adhesive can induce galvanic corrosion in bonded aluminium structures. In a humid environment the contact between carbon-fibre reinforced plastics (CFRP) or carbon nanotube containing epoxy resins and aluminium could lead to corrosion of the aluminium. Figure 2.20 shows aluminium and graphite (carbon fibres, carbon nanotubes…) in the galvanic series.

Research has shown that coating the aluminium surface with a thermoplastic coating like polyetherimide (PEI) gives good isolation [94]. Care should be taken not to damage the aluminium because contact with the carbon can occur again. Another possibility is the placing of a layer of glass fibre or thermoplastic between these two materials. It is common practice in the composite industry to use as little as a 100 μm thick layer of glass fibre to eliminate galvanic corrosion when bonding aluminium to CFRP. However, this technique is inapplicable when the material to be isolated is the adhesive which needs to be in intimate contact with the aluminium.

Recent studies claim that functionalisation of carbon nanotubes and carbon nanofibres by surface coating is an effective technique to overcome the galvanic corrosion

drawback [95]. The surface treatment could at the same time improve electrical and thermal properties of carbon nanotubes.

At present there is a lack of understanding on how carbon nanotubes as fillers in epoxy resins could induce galvanic corrosion when in contact with aluminium. Further studies are needed in order to define this drawback entirely and to find a way to overcome it.

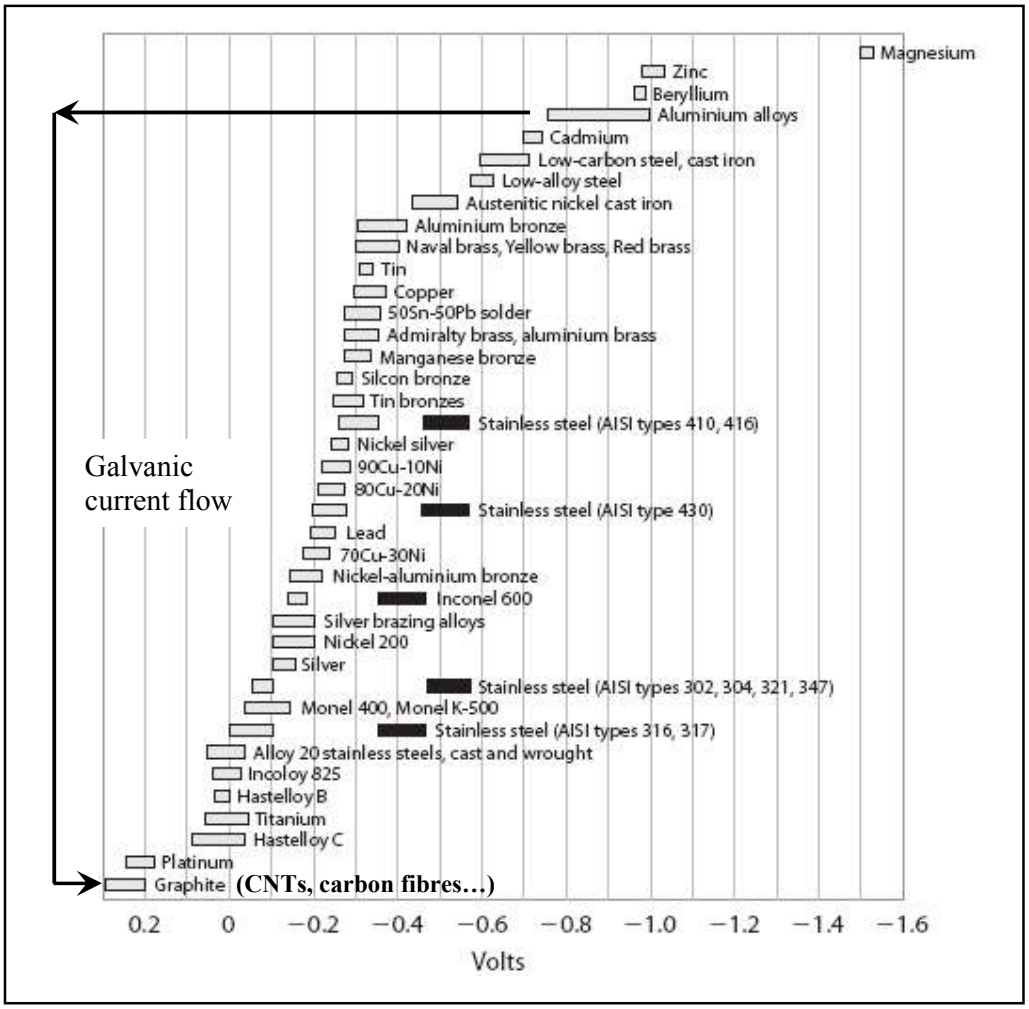

Figure 2.20 – Aluminium and carbon nanotubes in the galvanic series in flowing sea water, modified from [96]

2.6 Cure of ternary thermosetting systems

The phenomena that occur during the curing process of a ternary system of carbon nanotubes, rubber and epoxy are phase separation, gelation, vitrification (devitrification) and degradation [97].

The first phenomenon that occurs during a ternary thermoset cure process is phase separation by the reactive liquid rubber. The epoxy resin and the rubber are initially homogeneous but become heterogeneous due to the curing reaction (see Section 2.2.1). The result is the formation of a two-phase morphology where small rubber domains of a definite size and shape are formed. As the cure reaction progresses, the viscosity of the ternary system increases up to a point where the thermoset no longer behaves as a liquid anymore. Gelation denotes the non-reversible transition from the liquid to the rubbery state. At this point the rubber particles cease growing. Vitrification of the developing polymer network occurs when the glass transition temperature (T_g) of the reacting system reaches the cure temperature due to the increase in molecular weight or crosslink density. This thermo-reversible transformation involves the change of the material from a mobile rubbery state to a frozen glassy state. Due to the decrease of the chain mobility the reaction becomes diffusion–controlled. This eventually results in a complete stop of the reaction, with residual reactive units as a consequence. When the curing temperature is well above the T_g of a fully cured resin, the resin system may undergo degradation.

Inorganic fillers are known to affect the cure kinetics of thermosetting systems. They can change the network structure and affect the kinetics of the epoxy resin acting as inhibitors or accelerators with regard to the reacting system [98]. In particular, addition of carbon nanotubes in thermosetting systems influences both the cure behaviour and the thermo-physical properties of the polymer [99-104]. Acceleration of the reaction has been observed in neat epoxy resins [101,102,104] while the final glass transition temperature has been found to increase or decrease depending on the chemistry of the systems involved, the type of interaction between resin and nanofiller and the quality of dispersion of CNTs in the matrix [100,105]. In contrast, deceleration of the reaction has been observed in toughened thermosetting matrices [106] where the presence of

nanotubes reduces the final crosslinking density, leading to a composite with lower final glass transition temperature.

Review of the studies cited above shows that few efforts have been made to address the influence of carbon nanotubes on the cure of a thermoset matrix. Furthermore, there is an interest gap in literature in regard to the effects of incorporating reactive liquid rubber to the CNT / epoxy systems. This work contributes to the gap in literature by studying the cure kinetics of the ternary system of carbon nanotubes, rubber and epoxy which represents the novel adhesive formulation.

2.6.1 Cure kinetics modelling of thermosetting systems

There are two main approaches to modelling the reaction of thermosetting systems [97], mechanistic and phenomenological. Both analyses result in mathematical expressions for the reaction rate ($d\alpha/dt$) in the following general form:

$$\frac{d\alpha}{dt} = f(\alpha, T) \quad \text{..... (2.4)}$$

Where:

α is the fractional conversion or degree of cure

T is the temperature

t is the time

Mechanistic kinetic models assume certain paths for the reaction which involve a number of steps [97,107-109]. The initial reactants transform to a final product through these steps. These models have certain advantages. They offer a more rigorous description of the chemical process, compared to the phenomenological models. They can also be used to study the effect of different initial concentrations of the reactants on the curing reaction. On the other hand, the nature of the polymerisation reaction makes it difficult to find the correct, or more influential, reaction paths. Furthermore, the complexity of the reaction means that the fitting of mechanistic models to experimental data can become very time consuming.

The phenomenological approach uses kinetic equations that describe the reaction in a broader manner [110-112]. The equations are formed after some experimental data have been gathered and analysed. According to the experimental results, an assessment of whether the reaction is of n^{th} order or has autocatalytic behaviour is performed. Based on such general observations, model equations are fitted to the experimental data. Phenomenological models have a limited envelope of application compared to mechanistic models and no straightforward physical meaning in chemistry terms. Nevertheless, their simplicity, compared to the mechanistic models, makes them attractive for describing complex commercial systems, especially when prior knowledge of the chemical composition of such systems is not available.

A non-parametric procedure for modelling of the chemical cure kinetics has been introduced [113]. In this alternative modelling approach no analytical equation is developed for the modelling of experimental data obtained by differential scanning calorimetry (DSC). Direct interpolation is used instead for the prediction of conversion from reaction rate and temperature data. The method is purely numerical and provides no information on the chemistry of the system. The quality of experimental data is more critical compared to the other two approaches since no fitting is performed, which means no averaging of errors. On the other hand, it gives predictions of similar quality and it is much easier to implement compared to both the mechanistic and phenomenological approaches.

Summary

A review of published research has shown a number of potential advantages and disadvantages of the incorporation of carbon nanotubes into structural epoxy adhesives. Overall, their use as fillers is very promising for the mechanical reinforcement of these types of adhesive. Additionally, their electrical properties which would make the adhesive conductive are particularly attractive for the aerospace industry where good electrical bonding of a joint is needed to assist in controlling and dissipating the build-up of electrostatic charge.

Chapter 3

Materials

This chapter details all of the raw materials used to formulate the different adhesive compositions and those selected for the manufacture of test specimens and structures used in the characterisation of the bonded joint mechanical properties.

Users should be aware of the safety guidelines which accompany all of these materials and ensure that the correct safety equipment is used when handling them. This is to minimise personal risk and prevent contamination of the materials themselves. As carbon nanotubes are a component of many of the systems and in the absence of generally recognised relevant safety protocols, all reasonable caution was used when handling the materials.

3.1 Raw materials

The raw materials used in this work for the formulation of the different adhesive compositions are described in the following sections.

3.1.1 Epoxy resin – hardener system

Araldite® MY750 [114], a liquid diglycidyl ether of bisphenol-A (DGEBA) epoxy resin, was obtained from Huntsman Advanced Materials. This resin has a dynamic viscosity of 12-16 Pa·s at 25°C and an epoxide equivalent weight (EEW) of 182 g/eq. The amine curing agent used was 3,3'- diamino diphenyl sulphone (3,3'- DDS) [115], a solid aromatic diamine supplied by Hexcel Composites Ltd. The amine hydrogen equivalent weight (AHEW) of this curing agent is 62 g/eq. It is relatively insoluble in the epoxy resin at room temperature but melts and becomes soluble at the cure conditions adopted in this work. The stoichiometric mixing ratio of this resin and this hardener is 1 / 0.34. Because of the low reactivity of this system, a catalyst was added to the formulation. Boron trifluoride-monoethylamine (BF_3-MEA), a complex, produced by Chemos GmbH, which acts as cationic initiator for epoxy resins was added at a concentration of 1 wt% [42,116]. The chemical structures of these three materials are shown in Figure 3.1.

3.1.2 Toughener

Three carboxyl-terminated butadiene-acrylonitrile (CTBN) rubber versions were used in this work; a reactive liquid CTBN rubber and two epoxy-CTBN adducts in different states, one liquid and one solid. Figure 3.2 shows the chemical structures of the reactive liquid rubber and the epoxy-CTBN adduct.

The epoxy-CTBN adducts were made by functionalising the end groups of CTBN to epoxy groups in an excess of DGEBA epoxy. The reaction typically employs 8-10 equivalents of epoxy per equivalent of CTBN along with a catalyst and is carried out at high temperatures (150-160°C) [29,42]. Under these conditions, the CTBN and catalyst

react to produce a carboxylate salt whose subsequent reaction with an epoxy group is quite rapid. The pre-reacted product contains substantial epoxide activity and can be further diluted with the same or a different epoxy resin to obtain the required final rubber concentration. The catalysts suitable for this reaction, preferably tris-dimethylamino phenol or piperidine [29], are designed to promote specifically the carboxyl-epoxy reaction in reasonably short times.

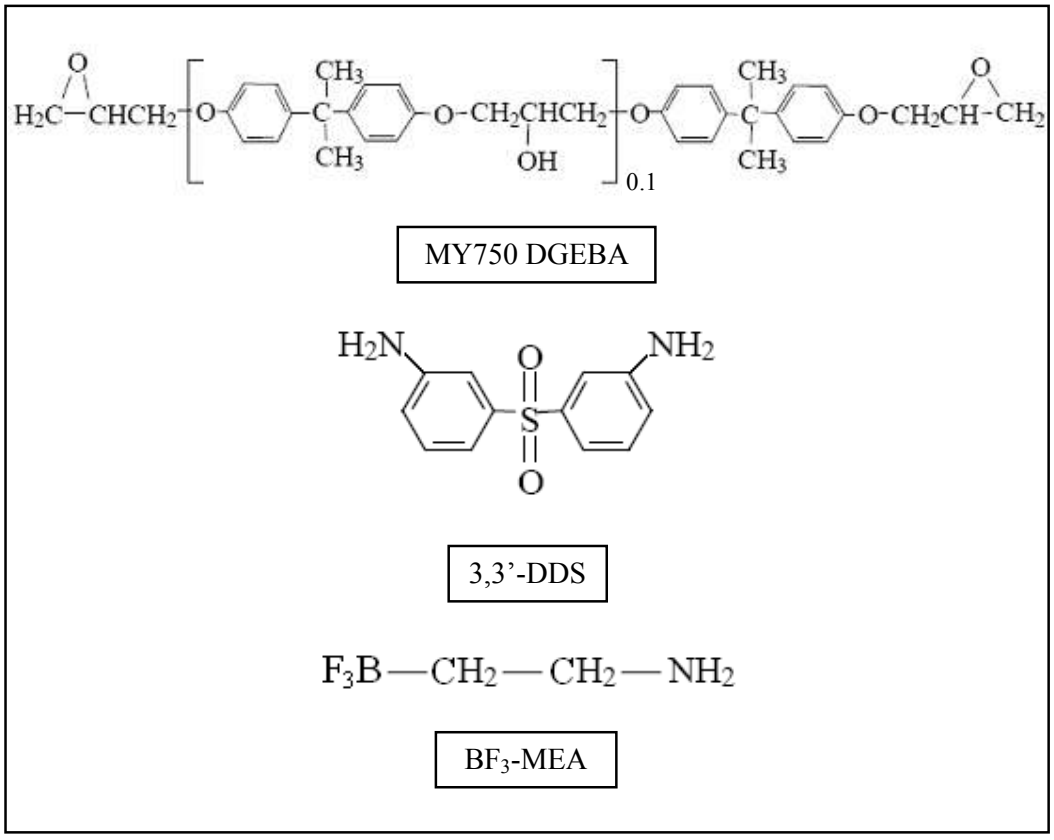

Figure 3.1 – Chemical structures of the epoxy resin MY750 [117], hardener and catalyst

Hycar® 1300×8 [118] was the reactive liquid rubber used. This material has an acrylonitrile content of 18%, viscosity of 135 Pa·s and molecular weight of 3550 g/mol. HyPox™ RK84 [119] was the solid adduct supplied as pellets. The elastomer content of this material is 32%. It has an EEW of 1200-1800 g/eq. Hypox™ RA840 [120] was the adduct in liquid form. The elastomer content of this material is 40%. It has a dynamic viscosity of 150-230 Pa·s at 25°C and an EEW of 325-360 g/eq. All these three materials were produced by Emerald Performance Materials.

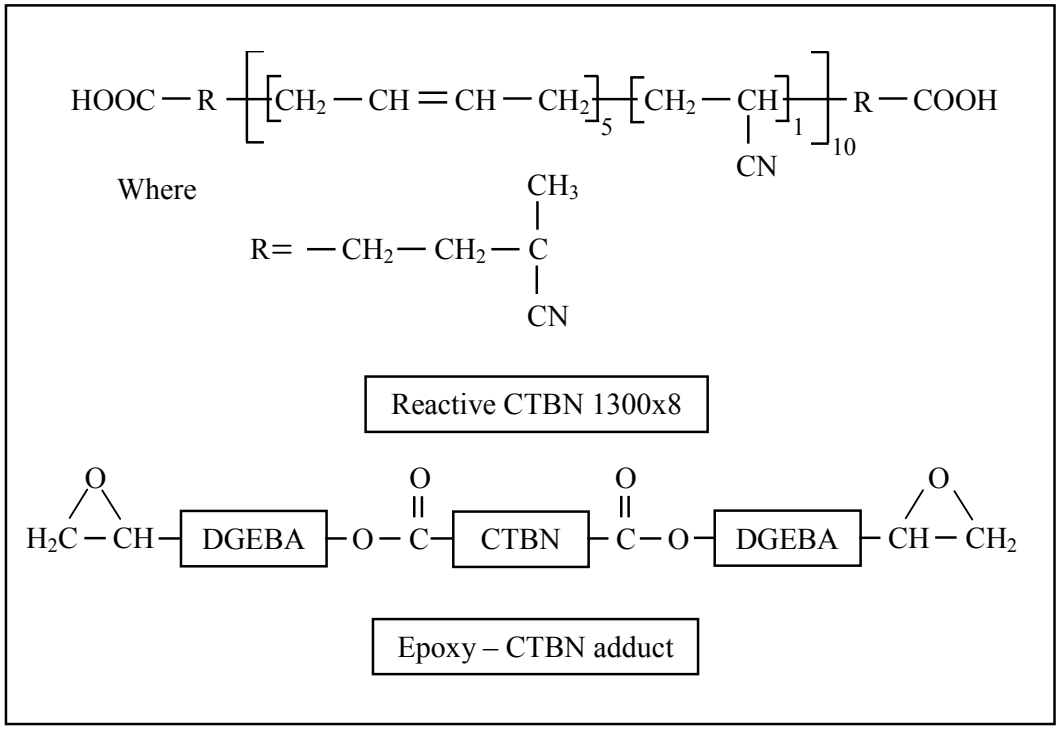

Figure 3.2 – Chemical structures of the toughener materials used in this work; reactive CTBN 1300x8 [121] and chemical bonds between molecules in the CTBN-epoxy adduct

3.1.3 Carbon nanotubes

Two types of carbon nanotubes were used in this work; MB1215-00 [122], a carbon nanotube-epoxy masterbatch supplied by Hyperion Catalysis and NC-7000 [123], a powder of neat multi-walled carbon nanotubes (MWCNTs) supplied by Nanocyl. The composition of the MB1215-00 masterbatch is 79.4% Epon® 828 resin, 17.3% Epon® 1009F resin and 3.06% MWCNTs, having an EEW of 701 g/eq. The MWCNTs in the NC-7000 have 90% carbon purity and are produced by a chemical vapour deposition (CVD) process. Figure 3.3 shows scanning electron micrographs of these carbon nanotubes as received, showing a highly-entangled structure. The properties as provided by the manufacturer are detailed in Table 3-1.

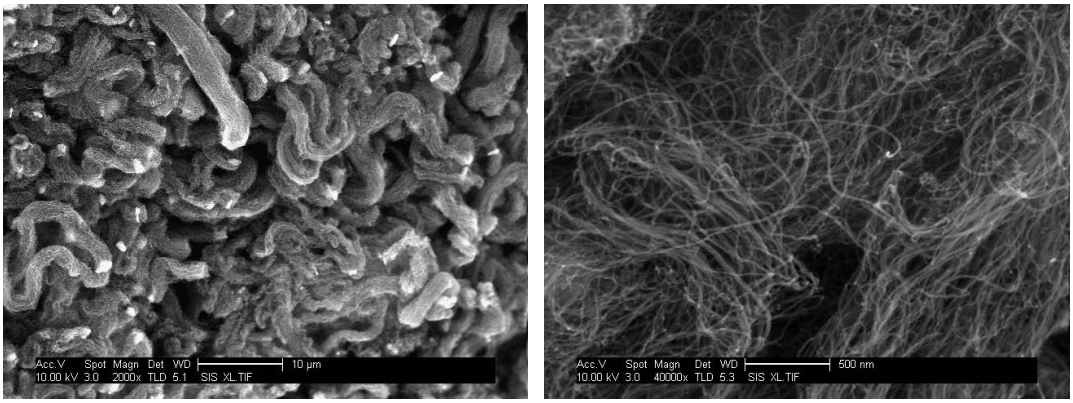

Figure 3.3 – SEM images of the NC-7000 multi-walled carbon nanotubes as supplied

Average diameter	9.5 nm
Average length	1.5 µm
Carbon purity	90%
Metal oxide (impurity)	10%
Surface area	250-300 m^2/g

Table 3-1 – Properties for NC-7000 multi-walled carbon nanotubes [123]

3.1.4 Carbon nanofibres

The carbon nanofibres used in this work are PR-24-XT-LHT-OX [124] were manufactured by Pyrograf Products, Inc. and supplied by BAE Systems. Figure 3.4 shows SEM images of the nanofibres as received. This powder-like material is produced by CVD and heat-treating at 1500ºC. This heat treatment process converts any carbon deposited on the surface of the fiber to a short range ordered structure. As a result, the inherent conductivity of the fibre is increased. The nanofibre properties as provided by the manufacturer are detailed in Table 3-2.

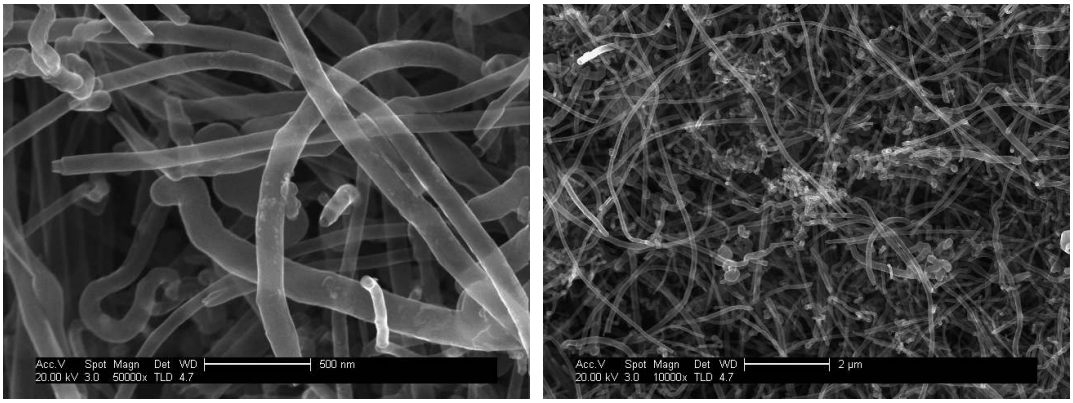

Figure 3.4 – SEM images of the PR-24-XT-LHT-OX carbon nanofibres, as supplied

Fibre diameter (average)	150 nm
Fibre length	20-100 µm
Surface area	43 m^2/g
Bulk density	0.016-0.048 g/cm^3
Iron	<14000 ppm

Table 3-2 – Properties for PR-24-XT-LHT-OX carbon nanofibres [124]

3.2 Veils

Two types of veils were used to reinforce the adhesive films manufactured; a woven architecture polyester veil (F0826) and honeycomb architecture nylon veil (A1050). The manufacturer of both these materials is Heathcoat Fabrics Ltd. Figure 3.5, Figure 3.6 and Figure 3.7 show images of these two veils.

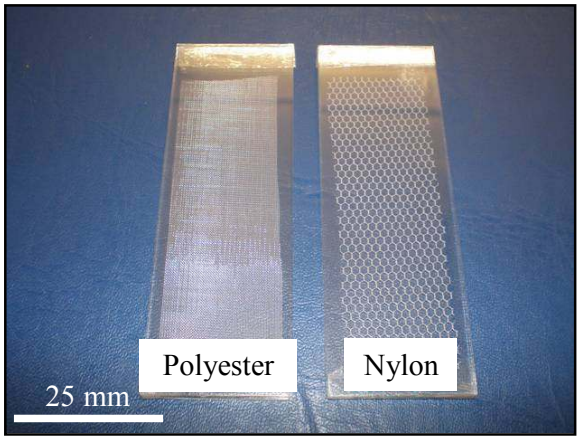

Figure 3.5 – Polyester (F0826) and nylon (A1050) reinforcing veils used in the manufacture of supported adhesive films

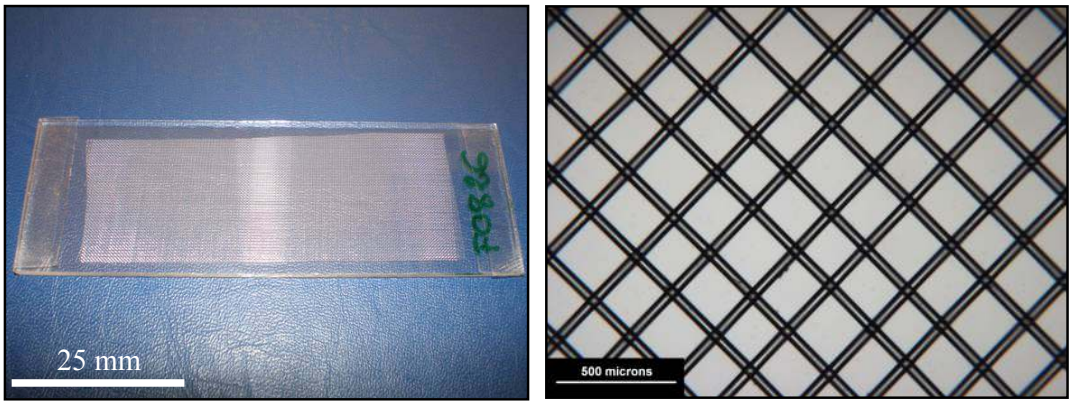

Figure 3.6 – Polyester veil (F0826) with magnification of the woven architecture

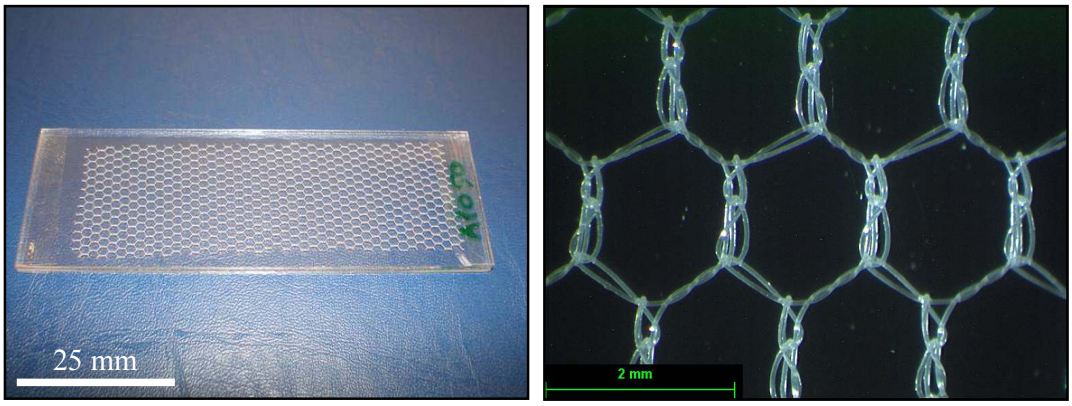

Figure 3.7 – Nylon veil (A1050) with magnification of the honeycomb architecture

3.3 Commercial adhesives

The commercial film adhesives used as references for the performance of the adhesive under development were FM® 94K and FM® 1515-3M, both supplied by Cytec Engineered Materials Ltd. This section also includes a two part adhesive paste used for attaching end tabs to the test specimens.

3.3.1 FM® 94K modified epoxy film

FM® 94K [125] is a 120ºC cure modified epoxy film adhesive designed for bonding metallic and composite structures. This adhesive film presents a nominal thickness of 0.25 mm and contains a knitted polyester veil and provides structural performance in the temperature range of -55ºC to 104ºC. The manufacturer's recommended cure cycle is summarised in Table 3-3.

Heat-up rate	1.7 to 2.8°C/min
Cure temperature	120°C
Cure pressure	0.28 MPa
Cure time	90 minutes

Table 3-3 – FM® 94K cure cycle

3.3.2 FM® 1515-3M film adhesive

FM® 1515-3M [126] is a modified epoxy film adhesive which includes a random architecture nylon veil and presents a nominal thickness of 0.5 mm. It can be cured at 120ºC or 177ºC and provides a service temperature range between -54ºC and 160ºC. The manufacturer's recommended cure cycle is given in Table 3-4.

Heat-up rate	0.5 to 3°C/min
Cure temperature	177°C (can be cured at 120°C)
Cure pressure	Full vacuum: 88 kPa Clave pressure: 310 kPa
Cure time	120 minutes
Post-cure required	No

Table 3-4 – FM® 1515-3M cure cycle

3.3.3 Araldite® 420 A/B

All tabbing of test specimens was carried out using Araldite® 420. This epoxy adhesive, supplied by Huntsman [127], is a two-component paste adhesive suitable for aerospace materials and applications. The two components are mixed (4 parts hardener per 10 parts epoxy by weight), applied to the prepared bonding surfaces and oven cured at 70°C for 2 hours. The shear strength of this adhesive at ambient temperature as stated by the manufacturer is 37 MPa. Removal of end tabs from tested specimens is possible by heating the adhesive to 150°C. At this temperature the adhesive degrades and the bonded parts can be separated with a firm tap.

3.4 Substrates

3.4.1 Glass-fibre reinforced plastic (GFRP)

HexPly® UD E-glass / 913 [128] epoxy system, supplied by Hexcel Composites Ltd., was selected to manufacture bonded specimens. This material was stored in the freezer in a sealed bag whilst not in use to prevent degradation and premature cure. Prior to use this material was allowed to fully defrost before removal from the sealed bag to prevent the pick up of moisture. Properties for cured 913 epoxy resin are detailed in Table 3-5 and the manufacturer's recommended cure cycle is given in Table 3-6.

Tensile strength	65.5 MPa
Tensile modulus	3.4 GPa
Glass transition temperature (T_g)	131°C
Cured density	1.23 g/cm^3

Table 3-5 – Cured properties for neat 913 epoxy resin [129]

Heat-up rate	2 to 8°C/min
Cure temperature	125°C
Cure pressure	700 kN/m^2 (7 bar)
Cure time	1 hour
Post-cure required	No

Table 3-6 – 913 pre-preg cure cycle

Hexcel 913 uncured epoxy, when heated, is very prone to hazardous exotherms and must be treated with extreme caution. In the worst case it can cause a severe fire risk, to a lesser extent it can lead to darkening of the matrix colour which in this case was undesirable as it would reduce visibility of the adhesive failure. To avoid this the slowest heat-up rate was used and the recommended cure cycle was modified to include two dwell periods, one at 60°C for 1 hour and the second at 100°C for 1 hour.

3.4.2 Aluminium alloy

The aluminium alloy used as substrate in this work is an aluminium-zinc alloy 7085 T 7651 supplied by Alcoa Inc. This designation stands for a solution treated, over-aged heat treated manufacture to improve its corrosion and fatigue resistance. Properties for this specific alloy are detailed in Table 3-7.

Tensile strength	510 MPa
Yield strength	476 MPa
Tensile modulus	71.7 GPa
Flexural modulus	69 GPa
Density	2.7 g/cm^3

Table 3-7 – Properties for aluminium 7085-T7651 [130]

The surface preparation of this aluminium alloy was carried out at Airbus Germany. The process used included vapour degreasing followed by an alkaline clean and completed with an immersion in sodium dichromate-sulphuric solution at 68ºC for 15 minutes and finally rinsed with water. After this process the surface is highly active not only towards the adhesive but also to atmospheric contamination. Indeed, after this pretreatment the surface requires to be bonded within a few hours. To meet this requirement and retain manufacturing flexibility it is a common practice to apply a primer compatible with the adhesive to the surface soon after pretreatment. Airbus Germany applied and cured the primer BR® 127 [131] to improve corrosion resistance at the same time. The primed surface can then be left, often for several months, before application of the adhesive.

Summary

The epoxy resin, toughener and carbon nanofillers used to formulate the adhesive compositions have been introduced together with their most relevant properties for this purpose. Two different veils selected to reinforce the adhesives in the film form have also been presented. All the commercial materials and products obtained for this work have been detailed with manufacturer's information.

Chapter 4

Manufacturing: constraints, design and methodology

This chapter presents the design process of the novel adhesive composition. The process has considered the constraints on the formulation imposed by the processability and final performance of the adhesive. Moreover, the chapter includes the formulation and manufacture of different adhesive variants created from separating the constituents of the novel composition. Additionally, the preparation of films and cast samples from these formulations is included. The chapter concludes with the manufacture of all the bonded specimens and structures used for mechanical testing.

4.1 Designing the formulation

This section contains details of all the preliminary work which was carried out in order to produce a working adhesive. The development of the formulation was carried out in conjunction with tests by trying different variants and different concentrations of two of the constituents, carbon nanotubes and CTBN rubber. The author's discernment during the process was based on both the processability of the adhesive film and the expected performance either from literature review or from targeted tests. The complex development process is presented as a whole in a flow chart (see Figure 4.1). The chart refers to sections in the text in which a detailed explanation is included.

4.1.1 Glass transition temperature requirement

As mentioned in Chapter 1, the formulation of the adhesive has constraints imposed by the project in which this work is involved. Aerospace grade structural adhesives are currently cured at temperatures in excess of 120ºC and one of the major considerations is their ability to perform across a wide temperature range or 'thermal cycle'. In addition, the adhesive requires a glass transition temperature, T_g, of over 120ºC with the 120ºC cure.

The T_g signifies a transition of the polymer from a glassy to a rubbery state. As the temperature of a polymer is raised above its T_g, the effective distance between molecular segments is increased. Flexibility, toughness and susceptibility to solvent penetration also increase at temperatures above the T_g, whilst cohesive strength and elastic modulus decrease. Figure 4.2 illustrates general trends of a range of adhesive properties related to temperature or molecular mobility.

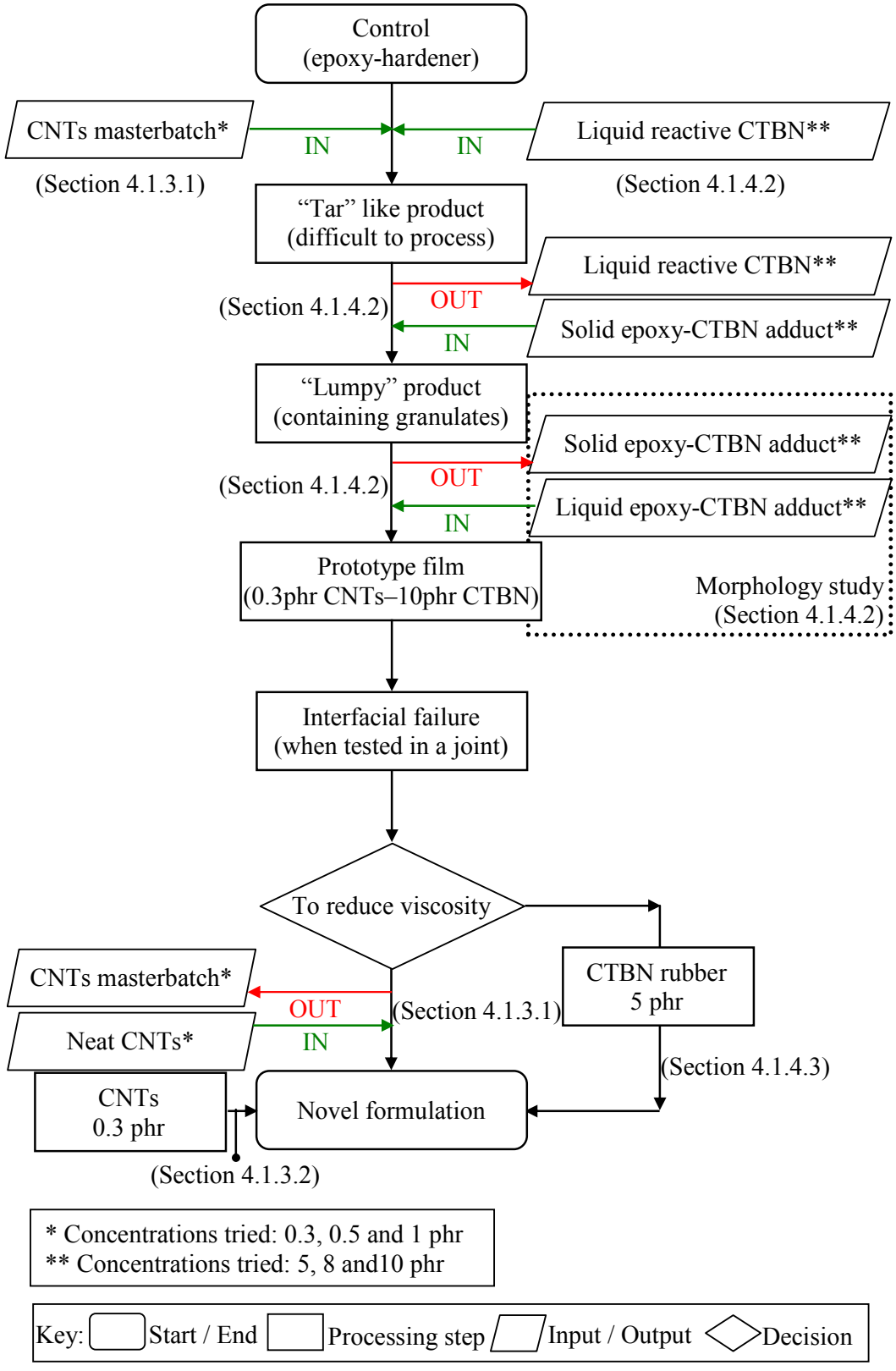

Figure 4.1 – Overview of the development process for the novel adhesive formulation

There are several options available for modifying the T_g of an adhesive system. These options are primarily through polymer selection and formulating with additives, such as plasticiser which increases the ductility of the polymer. In the present work it was decided that additives would not be used in order to keep the adhesive formulation as simple as possible. One of the reasons for selecting the main constituents for the adhesive was to meet the T_g requirement of 120ºC for the 120ºC cure.

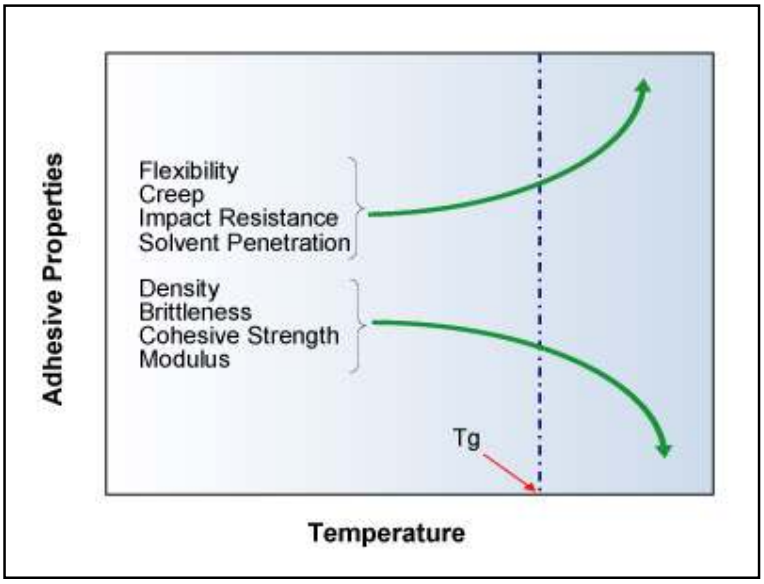

Figure 4.2 – General trends of adhesive properties related to temperature or molecular mobility [132]

4.1.2 Selection of the "control" epoxy – hardener system

In selecting the adhesive constituents there were constraints which came from the requirement of the adhesive formulation to be processed in film form. The main advantages of film adhesives are that they are a single component requiring no need for metering or mixing and that they can be cut to size and applied uniformly to a substrate. The components are mixed and processed to a stage where the resulting adhesive product is in a solid but uncrosslinked state. Once the film is in place between the substrates, the joint is heated under pressure so that the adhesive becomes slightly fluid,

flows into the micro-roughness on the substrate and wets the substrate. With additional time at the curing temperature, the adhesive completely crosslinks to a fully cured state.

Solid epoxy adhesives generally rely on high molecular weight epoxy resin, such as DGEBA for the solid appearance of the uncured adhesive. In the same context, DGEBA is generally formulated with a curing agent such as 3,3'-diamino diphenyl sulphone (3,3'-DDS) [116] which reacts with the epoxy only on heating. It is relatively insoluble in the epoxy resin at room temperature. However, it melts and becomes soluble at its "activation" temperature. It also provides high temperature properties and chemical resistance. Moreover, the DGEBA / 3,3'-DDS system can be cured at temperatures ranging from 115-150ºC and meets the T_g requirement of 140ºC for the 120ºC cure [115,133]. Because of the low reactivity of this system, a catalyst, such as BF_3-MEA, is employed at 1 wt% concentration.

4.1.3 Carbon nanotubes as fillers

Carbon nanotubes had been selected as fillers to be incorporated into the adhesive formulation. The concentration of carbon nanotubes is more relevant to initial aims than the concentration of rubber which will be added to the formulation later (see Section 4.1.4). Both constituents increase the viscosity of the system. Good dispersions of carbon nanotubes are found to greatly increase the viscosity of the mixture, especially at filler weight concentrations above 0.1 wt% [79]. Therefore the concentration of nanotubes was decided first, followed by the concentration of rubber based on the 'left-over' viscosity of the mix which still permitted film processing.

4.1.3.1 Selection of carbon nanotube forms

Two types of multi-walled carbon nanotubes were investigated; MB1215-00, a carbon nanotube-epoxy masterbatch and NC-7000, a powder of neat carbon nanotubes.

The masterbatch is a combination of two DGEBA epoxy resins, Epon® 828 and Epon® 1009F with the carbon nanotubes pre-dispersed in the mix. The concentration of

nanotubes is stated as 3.06 wt%. The two epoxy resins have different molecular weights and forms. Epon® 828 is a liquid resin with dynamic viscosity of 11-15 Pa·s at 25ºC and Epon® 1009F is a solid resin having a melt viscosity >50 Pa·s at 150ºC [134]. The masterbatch is very viscous, bordering on a solid state at room temperature. Figure 4.3 shows the consistency, a thick 'tar-like' material unable to be poured. The advantages for studying this masterbatch were the compatibility with the DGEBA epoxy resin of this work and that the carbon nanotubes were already dispersed. Dilution and dispersion of the masterbatch with the remaining constituents in the formulation is relatively straightforward using high-shear mixing.

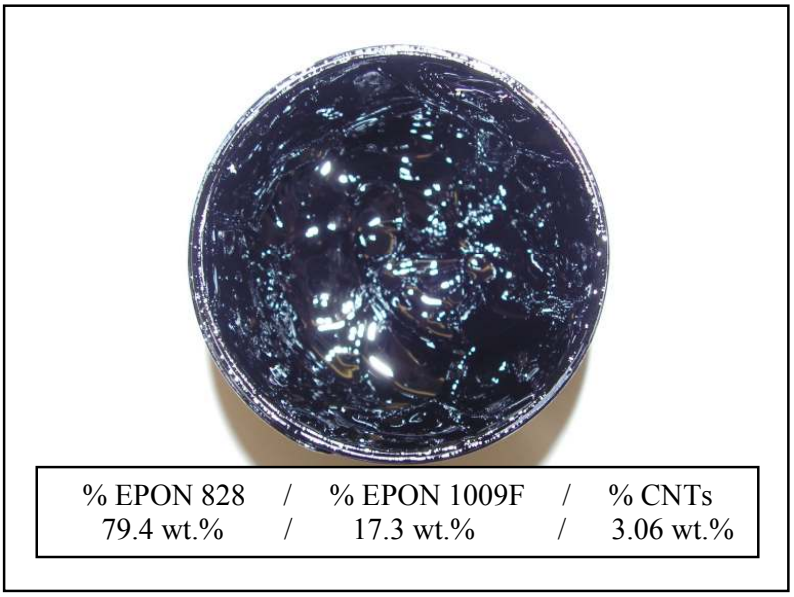

Figure 4.3 – MB1215-00 multi-walled carbon nanotubes-epoxy masterbatch at room temperature

Trials with this carbon nanotube-epoxy masterbatch gave the author the first prototype adhesive. The final viscosity was very high making it extremely difficult to process. Moreover, the dilution of the masterbatch with high-shear mixing alone gave a very poor dispersion of the nanotubes in the final product.

When using neat carbon nanotubes these needed to be dispersed into the resin using ultrasonication in addition to high-shear mixing. The final product showed a lower viscosity and therefore better processability as well as improved nanotube dispersion in relation to the masterbatch.

From this study, the neat NC-7000 multi-walled carbon nanotubes were selected to be included in the adhesive formulation.

4.1.3.2 Selection of carbon nanotube concentration

Various multi-walled carbon nanotube concentrations were tried; 0.3, 0.5 and 1 wt%. These early trials with a prototype adhesive film gave the author an insight into its mode of failure. It was noticed that the high viscosity of the adhesive did not allow full wetting of the substrate surface resulting in an undesirable interfacial failure. In order to tackle this problem a decision was taken to limit the concentration of carbon nanotubes in order to achieve the lowest possible adhesive viscosity. Therefore, the multi-walled carbon nanotubes concentration was fixed at the minimum value considered, 0.3 wt%.

At this concentration level of 0.3 wt% the electrical percolation threshold may still be expected [5,64], as well as enhancement in mechanical properties, namely stiffness, fracture toughness and interlaminar shear strength [19,62,135].

4.1.4 Toughener

Carboxyl-terminated butadiene-acrylonitrile (CTBN) was selected as the toughening agent for the adhesive formulation. The following sections detail the choice of the CTBN product used and its final concentration in the novel adhesive formulation.

4.1.4.1 Selection of toughener form

Three CTBN rubber materials were investigated; a reactive liquid rubber and two epoxy-CTBN adducts in different states, one liquid and one solid. Hycar® 1300x8 was the reactive liquid rubber used. HyPox™ RK84 was the solid adduct supplied as pellets which needed to be ground to a fine powder before use. Hypox™ RA840 was the adduct in liquid form.

The reactive liquid CTBN rubber was tried but produced highly sticky films which were difficult to process and handle and was therefore subsequently ruled out.

The solid epoxy-CTBN adduct was considered to provide a more controlled 'tackiness' [136]. However, the author encountered difficulty in grinding the pellets satisfactorily. A double roll mill was used for breaking down the pellets which were previously immersed in liquid nitrogen to prevent them from melting during the grinding process. The grain size obtained was too big (like coarse sand, between 0.5-1 mm) and resulted in films with high heterogeneity (see Figure 4.4). At this point, the author still needed to check if the cooling process could have changed the morphology of the material by cavitation of the rubber (see also Section 2.2.2.2).

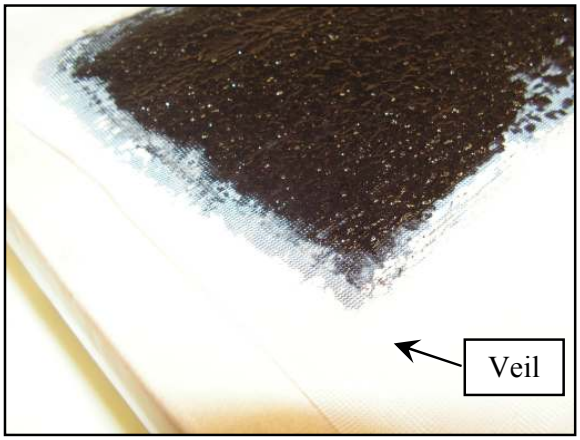

Figure 4.4 – "Lumpy" adhesive film obtained by using ground epoxy-CTBN adduct

Figure 4.5, images A-B, show SEM micrographs of the cryo-fracture surfaces for a formulation containing 5 wt% of the solid adduct. Qualitative investigation of these micrographs reveals the rubber material is not dispersed with the epoxy resin and there is no indication of phase-separated rubber particles either. Figure 4.5, images C-D show the formulation containing 10 wt% of the liquid rubber. This formulation displayed a two-phase morphology with a rigid epoxy continuous phase and a dispersed rubbery phase of isolated spherical particles. The elastomer material was phase separated from the hard epoxy matrix during the early stage of cure. These specimens, solid and liquid, were prepared by mixing the adduct with 3,3'-DDS / BF_3-MEA, the hardener-catalyst mixture, before being cast into rectangular specimens. The curing cycle was 6 hours at 120ºC for both formulations.

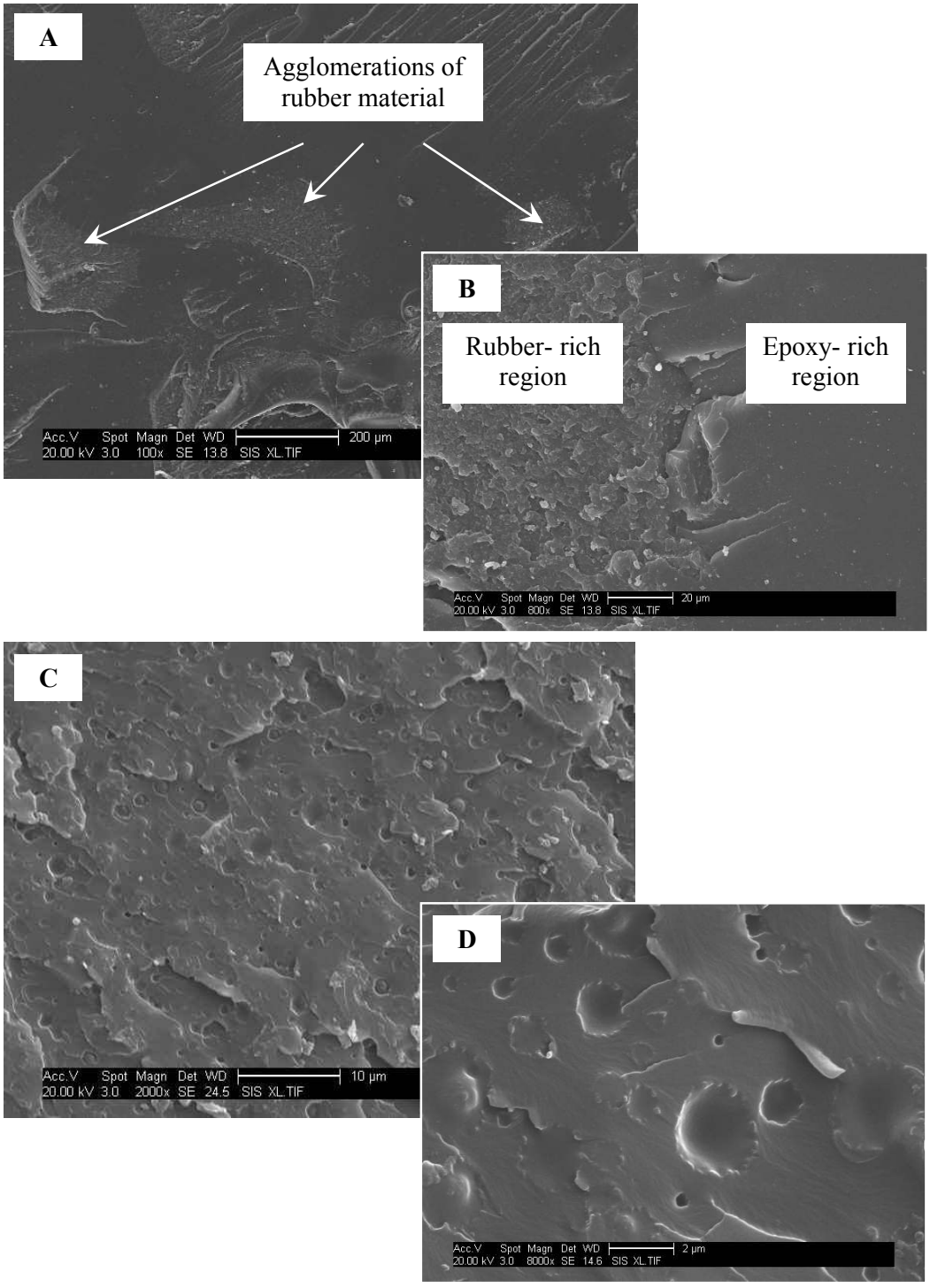

Figure 4.5 – SEM micrographs of fracture surfaces for epoxy-rubber adduct formulations containing solid CTBN at 5 wt% (A & B) and liquid CTBN at 10 wt% (C & D)

Additionally, the liquid epoxy-CTBN adduct gave the author easy-to-process films which were less tacky than the ones obtained with reactive liquid rubber. From the

observations described above, the liquid epoxy-CTBN adduct, HyPox™ RA840 was selected to be used for toughening the novel adhesive.

4.1.4.2 Selection of toughener concentration

Once the toughener type was selected, its concentration was determined by the desired filming characteristics of the final adhesive paste. One of the disadvantages of using CTBN as toughener is its high viscosity. Commercial toughened adhesives employ elastomer concentrations of between 5-15 wt% [137]. For the present study CTBN concentrations of 5, 8 and 10 wt% were tried. The three variant compositions created for comparison are listed in Table 4-1.

The pastes for these formulations were made as described later in Section 4.2.3. These were processed as unsupported films (without veil). The filming process was as described in Section 4.2.5.2.

Sample	CTBN (wt%)	MWCNTs (wt%)
R1	5	0.3
R2	8	0.3
R3	10	0.3

Table 4-1 – Variants compositions created for selecting the rubber concentration in the novel adhesive

Filming is a manufacturing process that strongly relies on the adhesive paste viscosity. If the paste is very liquid it is difficult to film, the mixture does not hold together and full coverage of the surface is not possible (discontinuity). One aid to ensure surface coverage is the use of a veil to create a supported film. On the other hand, if the paste is very viscous the challenge is being able to spread it homogeneously. Supported films (with veil) were also made using two veil types, woven polyester F0826 and honeycomb nylon A1050, to experience the behaviour of the pastes on these materials as well. The use of veils can assist therefore in the selection of toughener concentration.

After filming the different adhesive pastes, supported and unsupported, the experience gained helped the author settle on a concentration of 5 wt% of CTBN rubber. This decision was made to minimise the viscosity of the formulation in order to help wetting the substrate surfaces, as previously mentioned in Section 4.1.3.2.

4.1.5 Novel adhesive formulation finalised

Following the design studies, the novel adhesive formulation was fixed. It contains 5 wt% of CTBN rubber and 0.3 wt% of MWCNTs (Figure 4.6). The CTBN rubber was in the form of a liquid epoxy-CTBN adduct (HyPox™ RA840) and the carbon nanotubes in the form of a neat powder (NC-7000).

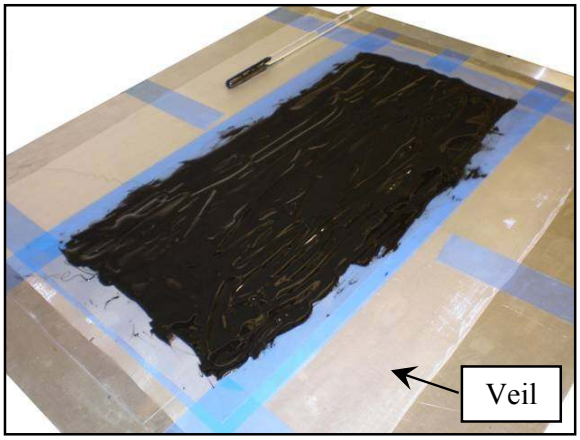

Figure 4.6 – Supported novel adhesive film containing 5 wt% of CTBN rubber and 0.3 wt% of MWCNTs

4.2 Processing

Alongside the finalised novel adhesive, three variants were created with the aim of separating the effects on mechanical performance of the constituents in the formulation. All these formulations are detailed in Table 4-2. A shorthand nomenclature is used; C is the abbreviation for the control formulation, CR for the control with rubber formulation, CN for the control with carbon nanotubes and finally, CRN denominates the novel adhesive (the control formulation containing rubber and carbon nanotubes).

Sample	CTBN (wt%)	MWCNTs (wt%)
C	0	0
CR	5	0
CN	0	0.3
CRN	5	0.3

Table 4-2 – Adhesive compositions formulated for the present work

4.2.1 Dispersion of carbon nanotubes into epoxy resin

A study was carried out to find the most suitable method to disperse the carbon nanotubes into the formulation. In this study a carbon nanotube-epoxy mixture of 110 g containing 0.48 wt% of carbon nanotubes was used. This nanotube concentration is needed to obtain a 0.3 wt% in the final formulation after adding the remaining constituents. The carbon nanotubes were first dispersed in the base epoxy using a Dispermat CN10-F2 high shear rotational mixer (see Figure 4.7) at 3000 rpm for one hour so that the carbon nanotubes were fully wetted out in the epoxy resin. During the stirring the temperature of the mixture was kept at 100ºC in order to maintain a low viscosity. To avoid the formation of air bubbles while mixing, this equipment was operated with the mixture under vacuum.

After the initial dispersion, the mixture was placed in a closed system (Figure 4.8) and ultrasonicated using a sonicator horn (see Figure 4.9). The mix was placed in a three-neck, round-bottom flask heated by an electric mantle and stirred continuously. The temperature of the mix was monitored by a thermocouple connected to the data acquisition system. The mix was sampled on-line using a peristaltic pump and directed to a flow-through cell to measure the electrical resistivity of the liquid.

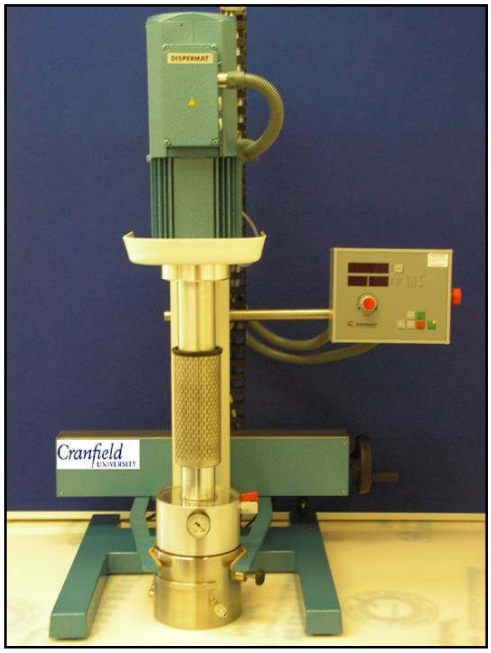

Figure 4.7 – Dispermat CN10-F2 high shear rotational mixer

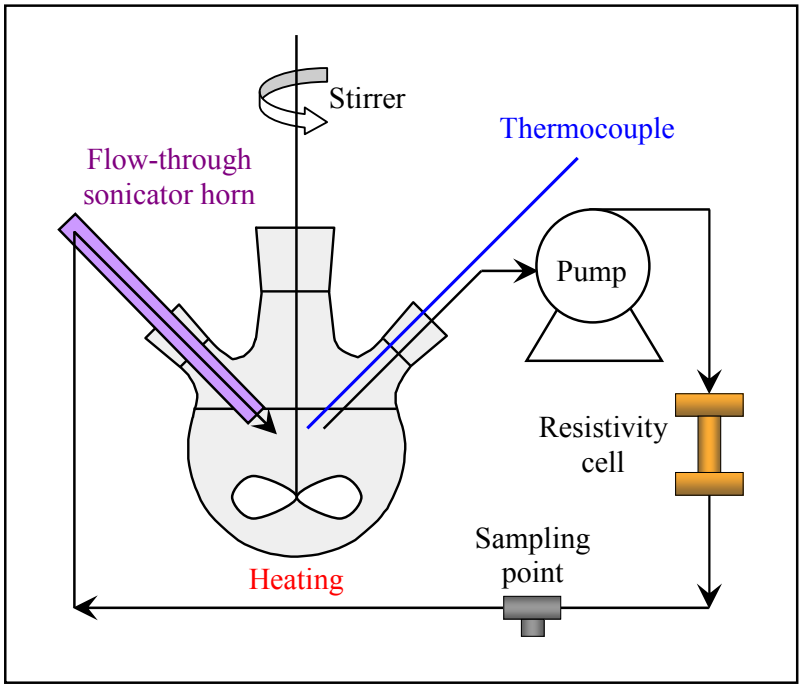

Figure 4.8 – Closed system used for studying the carbon nanotubes sonication process [93]

Figure 4.9 – Branson S-450D ultrasonic cell disruptor / homogenizers [138]

Such on-line electrical conductivity measurements have been shown by other authors to provide a way of monitoring qualitatively the dispersion of the CNTs [93]. In Figure 4.10, the top graph shows the energy applied to the system while the bottom graph shows the evolution of the mix resistivity during the sonication process.

A significant decrease of resistivity, which is equivalent to an increase in conductivity, is an indication of an improved state of dispersion. The stabilization of the resistivity towards the right hand side of the graph indicates that the dispersion of carbon nanotubes has been completed. This stabilisation was chosen as the "end of dispersion" limit and corresponds to 1.2 kJ/g of applied energy (133 kJ was applied to the total batch of 110 g). In the same way, it was possible to define the "mid-dispersion" with 0.5 kJ/g of energy applied. Therefore, 1.2 kJ/g of energy is needed in order to obtain a good dispersion of carbon nanotubes in the novel adhesive formulation. The study of dispersion in the following section aims to provide visual verification of the dispersion quality.

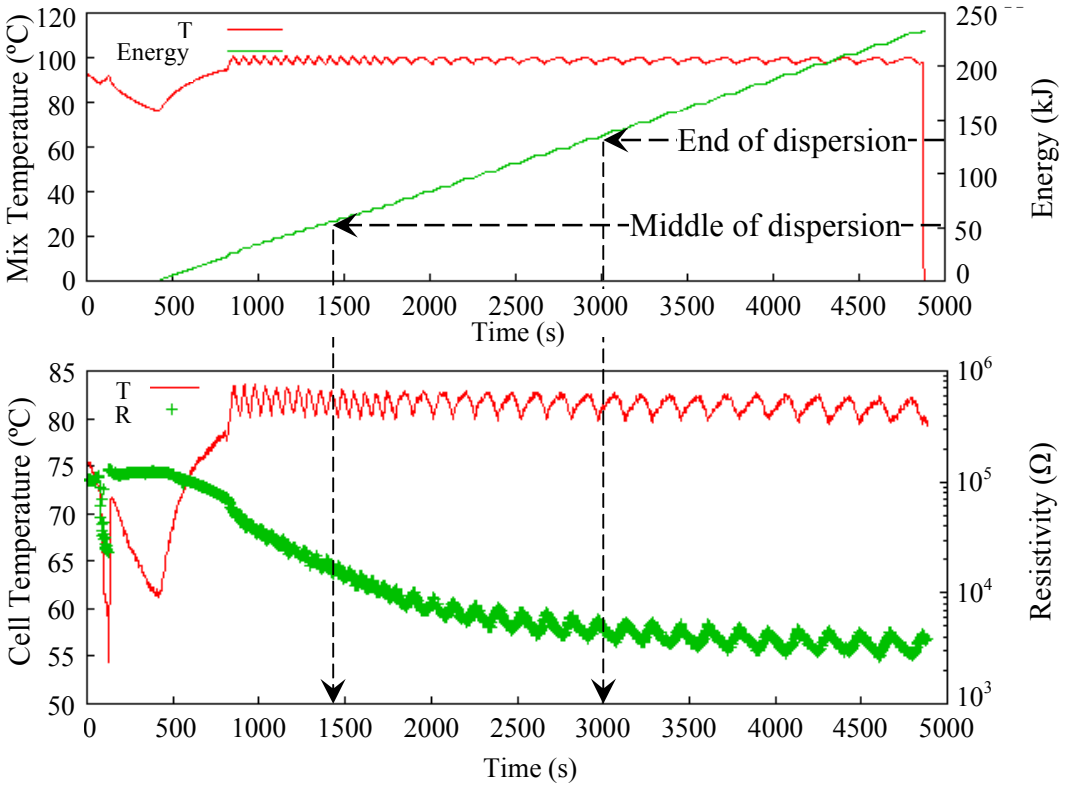

Figure 4.10 – Recordings from the sonication process showing (A) energy applied to the system and temperature of the mix and (B) evolution of resistivity and temperature of the resistivity cell

4.2.1.1 Study of dispersion: Optical microscopy and SEM

The effectiveness of the sonication process to disperse the nanotubes was also verified by transmission light microscopy. Carbon nanotube-epoxy samples (without hardener) taken during the sonication process were examined with this microscopy technique. A small drop of each sample was placed between two glass microscope slides. The microscope transmits visible light through the drop through multiple lenses to allow a magnified view of the sample. The contrasted image obtained shows the nanotubes as dark spots.

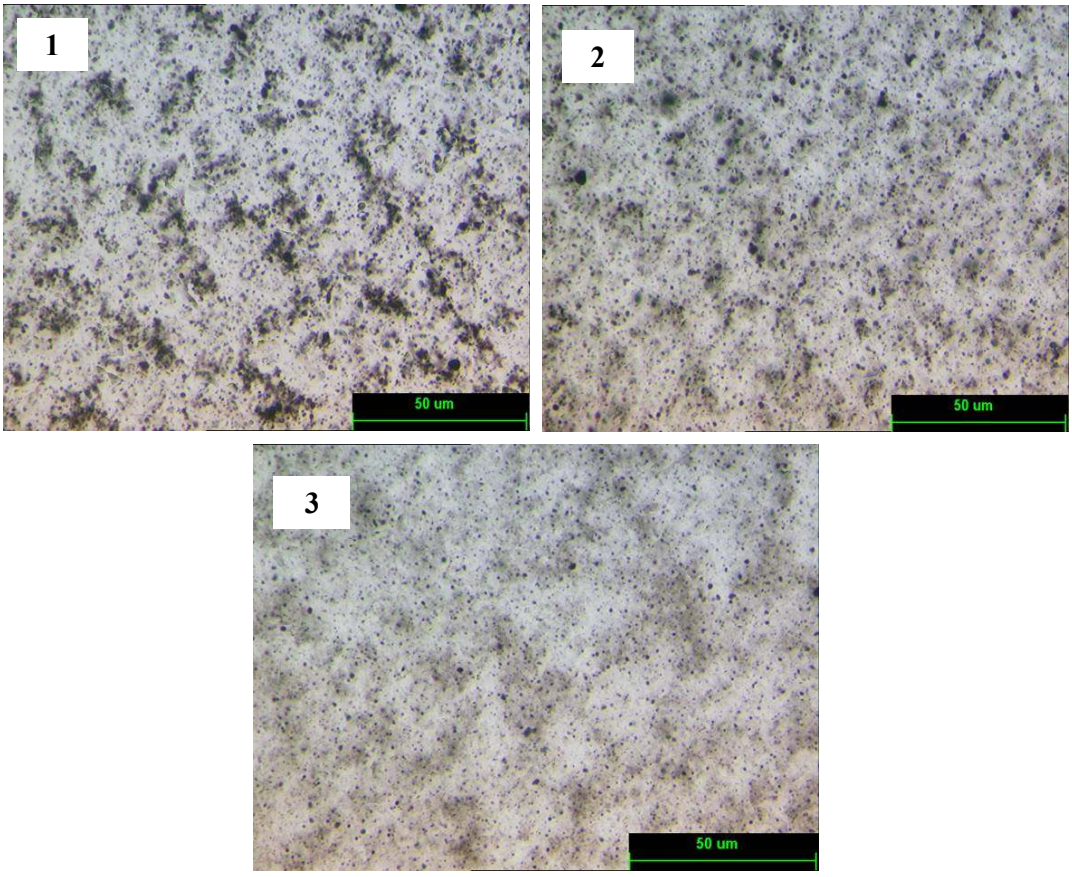

Figure 4.11 – Optical images of the carbon nanotubes-epoxy mixture subjected to sonication showing (1) before sonication, (2) middle of the sonication process and (3) end of the sonication process

Figure 4.11, images 1-3, show the results obtained from examining the carbon nanotubes-epoxy samples. The resolution of these images is 0.5 μm. Image 1 shows that the high shear mixing process before sonication was sufficient to disperse the nanofillers uniformly in the epoxy resin but large agglomerates still remain. The dispersion improves at the middle of the sonication process (Image 2). At the end of the sonication process the sample showed an improved level of dispersion (Image 3), indicated by the reduced optical density of the agglomerates rather than their extent.

Furthermore, Figure 4.12, shows SEM micrographs of two samples prepared from the carbon nanotubes-epoxy mixture, one with no sonication (1) and the other one from the end of the sonication process (3). The final composition for these samples is the novel adhesive composition; 0.3 wt% of MWCNTs and 5 wt% of CTBN rubber. In the images

the bright dots are the ends of carbon nanotubes. Qualitative investigation of these micrographs again reveals big agglomerates for the sample before sonication. These agglomerates are broken down with the use of the sonication process.

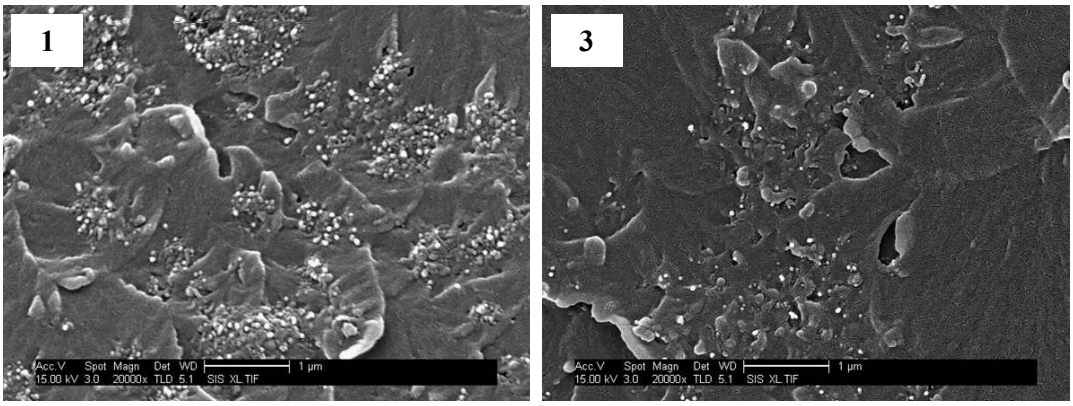

Figure 4.12 – SEM micrographs of fracture surfaces containing 0.3wt% of carbon nanotubes and 5wt% of CTBN rubber showing (1) non-sonicated sample and (3) fully sonicated sample

Scanning electron microscopy also proves to be a successful technique for studying the nanofiller dispersion within the epoxy resin. The conclusion from this study is that sonication helps to disperse the carbon nanotubes into the epoxy resin by breaking down further the agglomerates which remain after shear mixing alone.

For all further work the dispersion process, for a final concentration of 5 wt% of CTBN rubber and 0.3 wt% of MWCNTs, is defined by high shear mixing for 1 hour at 3000 rpm and 100ºC, followed by a sonication process at 100ºC applying a specific energy of 1.2 kJ/g in the sonication process.

4.2.2 Degassing of resins: preparation for final mixing

Before mixing the adhesive constituents, the base resin, the sonicated CNT-epoxy mixture and the epoxy-CTBN adduct need to be degassed thoroughly. In particular the last two are high viscosity systems and are therefore particularly difficult to degas.

Normally, a degassing process is carried out at the highest temperature the material can work to in order to lower the viscosity of the system as much as possible. This provides

the least resistance to the exiting gas bubbles under vacuum. The author's experience found that with this method a complete state of degassing could not be reached for the adhesive mixture. In this case, when full vacuum was applied, bubbles would form rapidly and rise to the surface of the mixture in a chaotic fashion. The disturbance caused resulted in the mixture bubbling over the sides of the container. A further observation was that the material did not reach a fully degassed state.

This was obviously undesirable and therefore a more controlled process was developed. For the vacuum-oven equipment available it was not possible to control the level of vacuum applied, instead the method of control was the management of the mixture temperature. It was found that subjecting the mixture to small increments of temperature, up to the maximum temperature that the material could work to, whilst under full vacuum, resulted in the production of smaller bubbles. The production of these smaller bubbles occurred at a steady, controlled rate and the bubbles would break at the surface causing no further disturbance to the mixture. This process would continue until the mixture was fully degassed.

A possible explanation for the greater success of the latter approach to degassing, accounting for bubble nucleation energy and mixture surface or 'die' temperature, is offered by [139] which is in line with the author's practical findings. The specifics of the approach followed are now described in greater detail.

The mixture was placed in a container in a vacuum oven. A starting temperature of 30ºC was attained and then vacuum applied. At this stage the viscosity of the mixture is still high so the average bubble sizes and bubble volume fraction are small. As bubbles rose and subsequently exited the mixture at the surface the vacuum level indicator would start to indicate a decrease. When this occurred, the oven temperature was increased slightly (+10°C). The small temperature increase further reduced the viscosity of the mixture and the nucleation of new bubbles occurred (see Figure 4.13). This technique was repeated until the maximum temperature of 70ºC. The result was that the degassing process lasted longer but at a steadier, controlled rate leaving a fully degassed mixture.

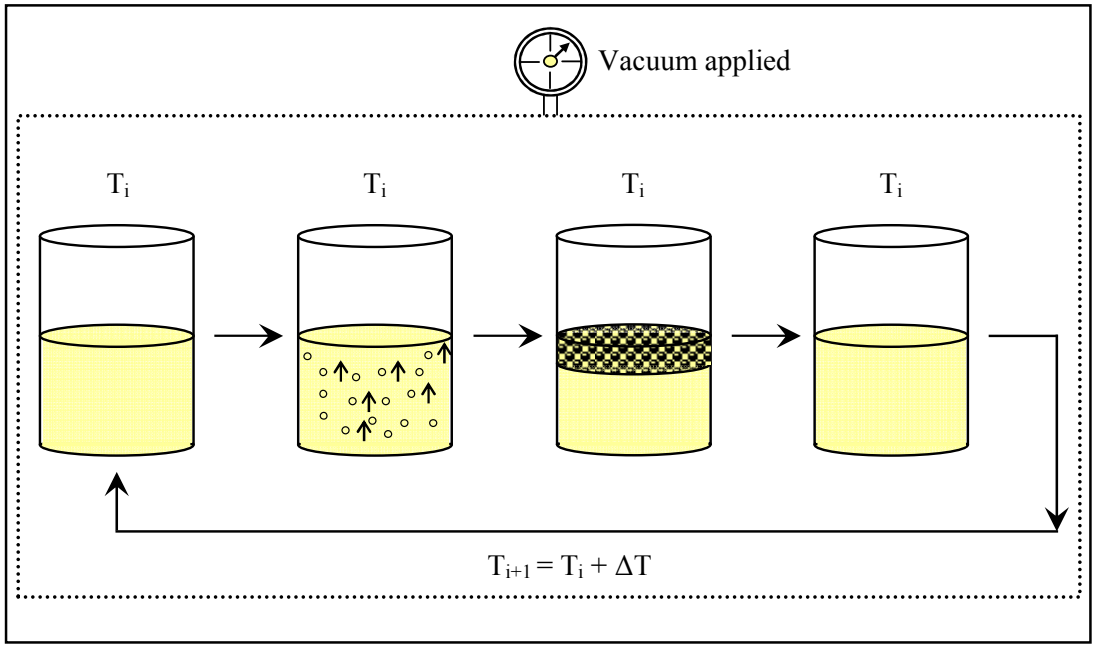

Figure 4.13 – Degassing technique developed for highly viscous systems

4.2.3 Mixing of the constituents

The different adhesive formulations created in the present work were processed as follows:

- The C formulation was processed by stirring the hardener-catalyst mixture into the epoxy resin for 30 minutes at 3000 rpm.

- The CR formulation was processed by stirring the rubber-epoxy adduct into the epoxy resin for 30 minutes at 3000 rpm. The hardener-catalyst mixture was then added and stirred under the same conditions.

- The CN formulation was processed by dispersing the carbon nanotubes into the epoxy as explained in Section 4.2.1. This was followed by stirring the hardener-catalyst mixture into the carbon nanotube-epoxy suspension for 30 minutes at 3000 rpm.

- The novel adhesive formulation, CRN, was processed by dispersing the carbon nanotubes into the epoxy as explained in Section 4.2.1. The suspension obtained was mixed with the epoxy-CTBN adduct for 30 minutes at 3000 rpm. The mixture of hardener and catalyst was added afterwards and stirred for another 30 minutes at 3000 rpm.

All the stirring processes were carried out in the high-shear mixer keeping the mixtures under vacuum at 80ºC. No significant cure reaction occurred while stirring the hardener-catalyst mixture into each of the formulations (see Section 6.1).

The various formulations obtained after mixing are hereafter referred to as "pastes" which were ready for casting or filming.

4.2.4 Casting

Flat plaques between 3 and 6 mm thickness were cast from all the formulations included in Table 4-2, using a metal-glass mould after thorough degassing (see Figure 4.14). The glass plate was first covered with Tygaflor PTFE coated glass cloth, which has good heat and chemical resistance along with excellent non stick properties, to ensure release of the resin plaques. The metal mould was covered and securely fixed to the glass plate using heat resistant tape.

The quality of bulk specimens is influenced by the presence of air bubbles. In a specimen under stress, small bubbles will give rise to regions of stress concentration at which failure can initiate prematurely. To eliminate air bubbles produced during pouring, the cure was carried out in an air oven under partial vacuum. The curing cycle was 6 hours at 120ºC for all the formulations. Figure 4.15 shows the bulk adhesive plaques in the mould after the curing process.

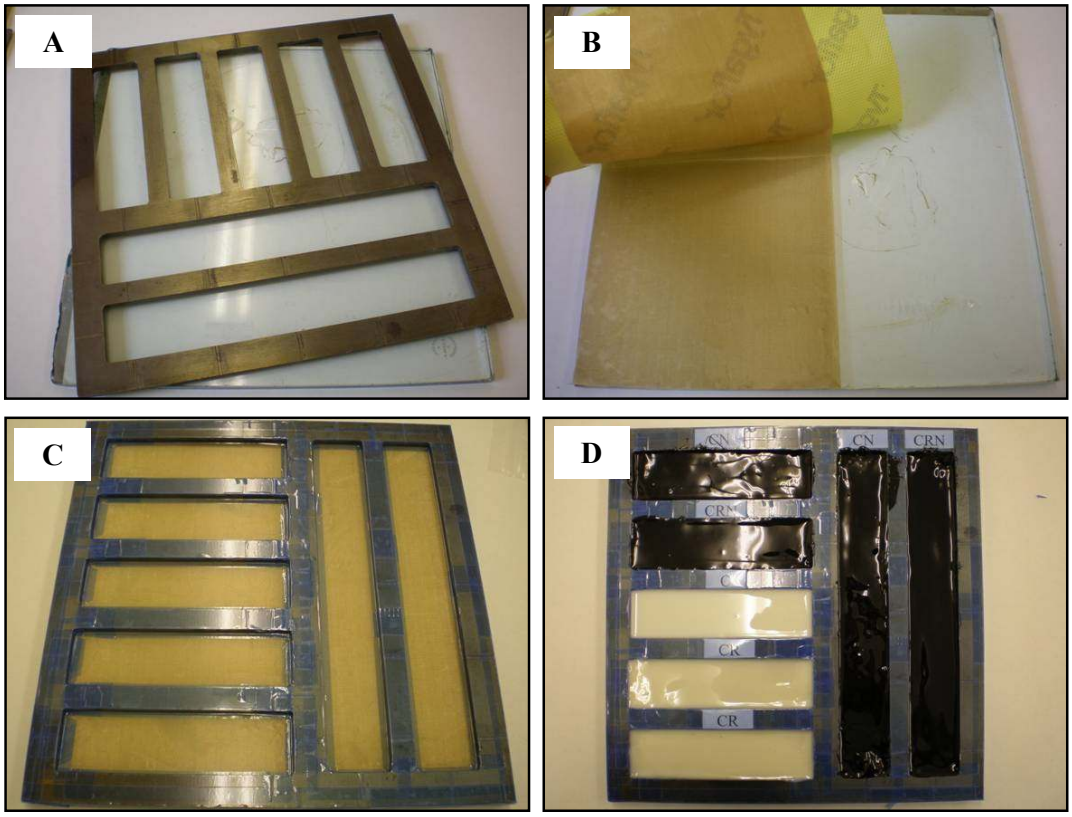

Figure 4.14 – Casting of specimens showing (A) glass plate and steel mould, (B) covering the glass plate with coated glass cloth, (C) glass plate and steel mould assembled and secured using heat resistant tape and (D) poured adhesive pastes

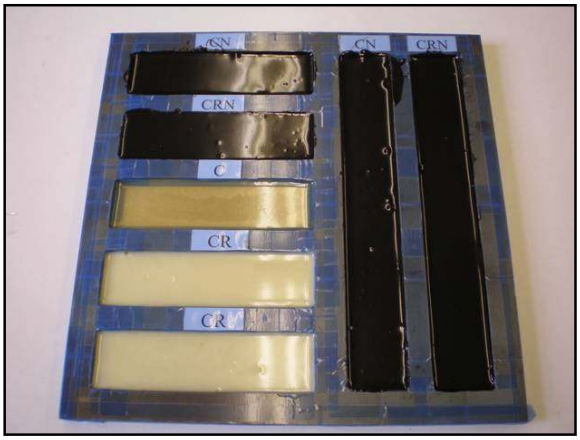

Figure 4.15 – Casting mould after the curing process

4.2.5 Filming

Unsupported films were produced from all the formulations included in Table 4-2. Supported films were also produced from the CRN novel formulation using two different veils, polyester and nylon. Another supported film was also processed from the CR formulation using the polyester veil.

4.2.5.1 Importance of the veil

The main purpose of the veil is to provide a means by which the bond line thickness can be controlled [116]. The author was privileged to have technical discussions with a leading adhesive film manufacturer. From these discussions, the author learned that both the fibre type and architecture used in the veil are important in the final performance of an adhesive joint. A crucial parameter is the dimension of the 'open holes' in the veil structure. Figure 4.16 shows the differences on dimension and structure of 'open holes' for the veils in this work.

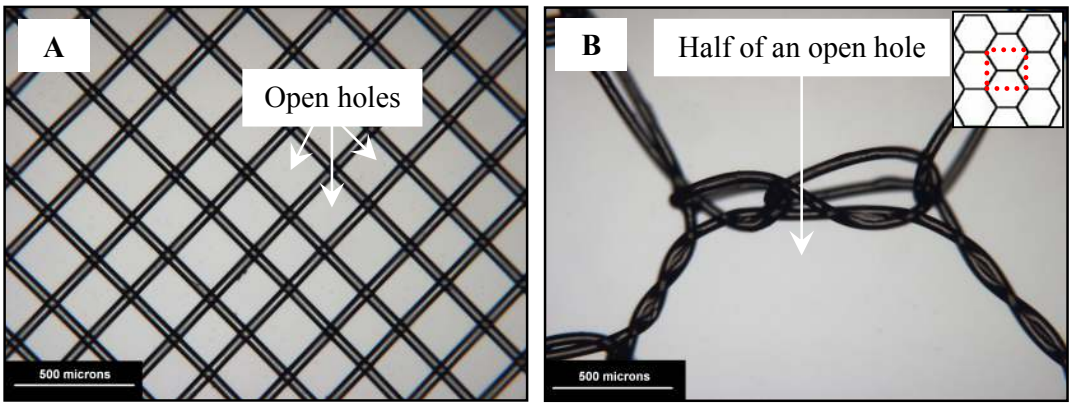

Figure 4.16 – Veil architectures showing the open hole dimensions for polyester veil (A) and nylon veil (B)

The selection of the most suitable veil comes from experience in using various combinations of resins and veils. However, two technical considerations when selecting a veil for adhesive films are as follows:

- Nylon, unlike polyester, retains water which has a detrimental effect on the durability of an adhesive joint.
- A random fibre architecture is ideal for promoting stable crack propagation.

The author selected two commonly used, commercially available veils to study in this work; polyester F0826 (woven architecture) and nylon A1050 (honeycomb architecture). Unfortunately, a random architecture veil was not available at the time.

4.2.5.2 Filming process

The films were processed using a specially designed lab-scale 'filming-line' (see Figure 4.17). This unit consists of a Clifton digital hotplate, an aluminium carrier plate covered with silicone coated release paper and a doctor blade.

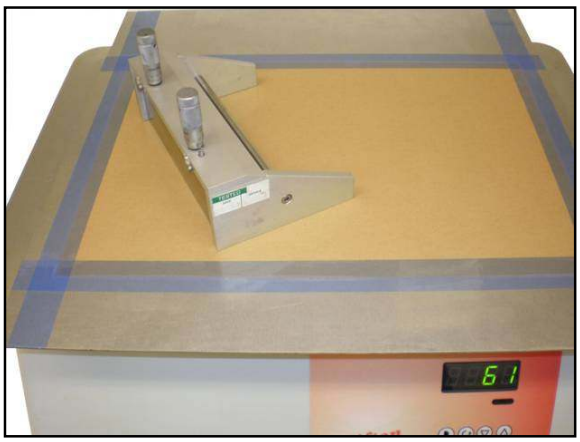

Figure 4.17 – Lab-scale 'filming-line'

The unsupported films were manufactured by spreading the adhesive paste with the doctor blade over the coated carrier plate. Similarly, the supported films were manufactured by spreading the adhesive paste with the doctor blade over the veil which was securely fastened to the carrier plate using temperature resistant tape. An example of filming showing a supported CR film is given in Figure 4.18.

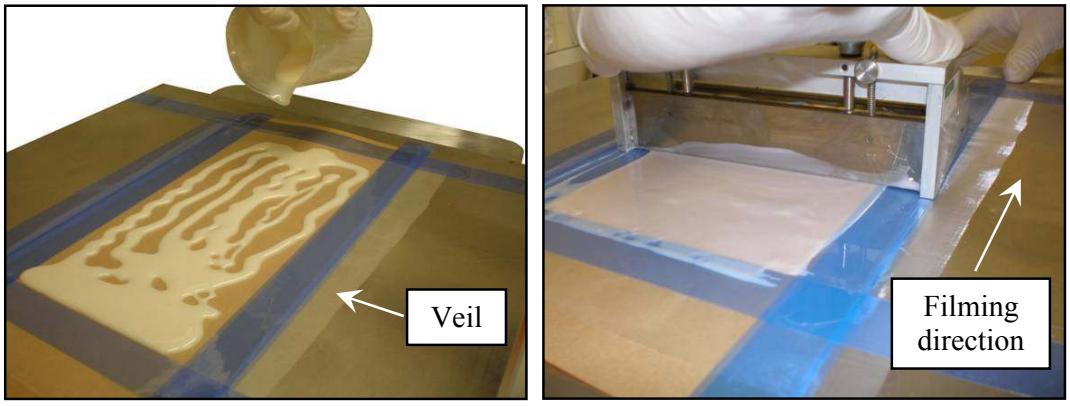

Figure 4.18 – Filming process

The temperature of the hot plate was set for the different formulations depending on the viscosity of the pastes. The temperature used for each formulation was determined by the author's experience. These temperatures are detailed in Table 4-3.

Sample	Filming temperature (ºC)
C	30
CR	50
CN	55
CRN	60

Table 4-3 – Filming temperatures for the different adhesive formulations

After spreading, each film produced was placed in the freezer for 30 minutes in order to prevent further uncontrolled spreading. Following this, each film was returned to the hot plate and pressed to ensure as uniform a thickness across the film as possible. Pressing was achieved by covering the film with silicone release paper and placing several metal weights on top as shown in Figure 4.19. The film was heated to the filming temperature for 10 minutes so that the small decrease in viscosity allowed the material to be pressed uniformly. The final thickness for all the films was fixed as close as possible to 500 μm.

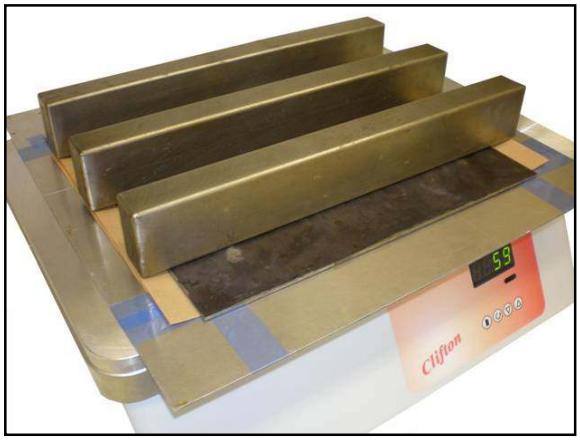

Figure 4.19 – Shaping the adhesive films

Each filming step was fine-tuned over time as the author's experience and skill level developed. The most challenging aspect of the whole process came in trying to prevent discontinuity during spreading of the unsupported films and veil wrinkling in the supported films.

4.2.5.3 Films obtained

Figure 4.20, images A-D show the unsupported adhesive films produced. Figure 4.21, images A-B show the CRN supported film versions using the two different veils, nylon and polyester.

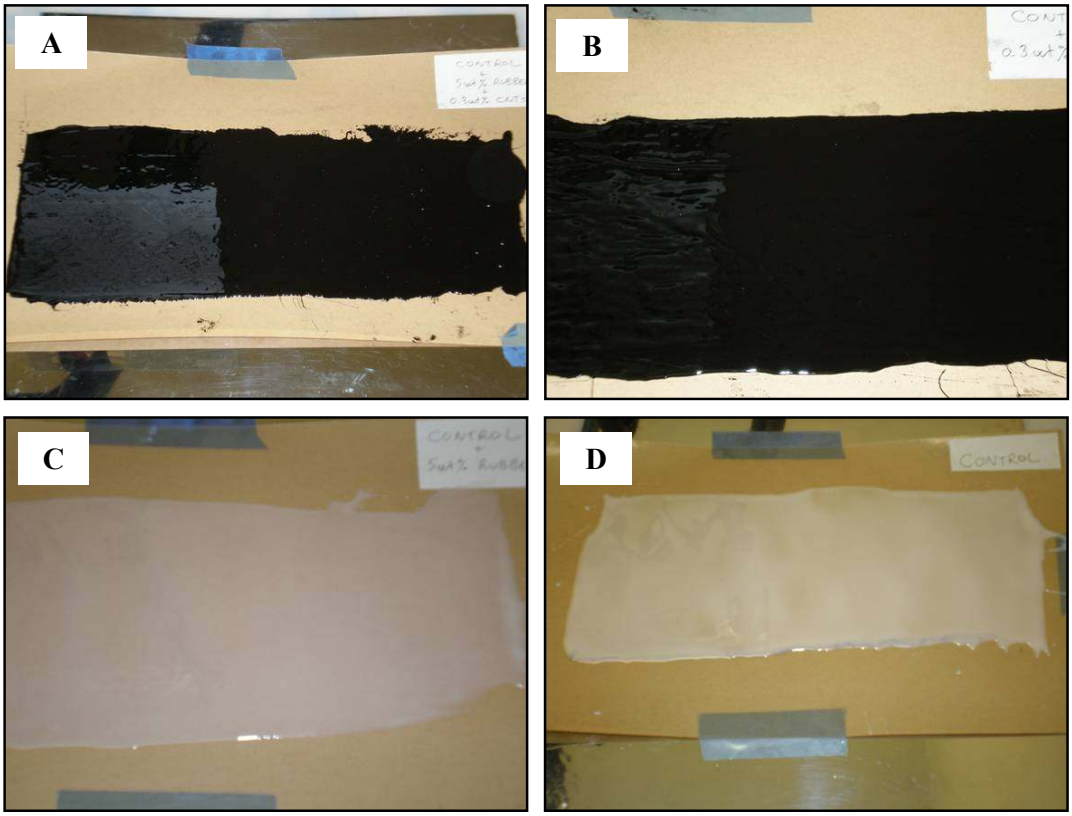

Figure 4.20 – Unsupported adhesive films showing (A) CRN; (B) CN; (C) CR and (D) C

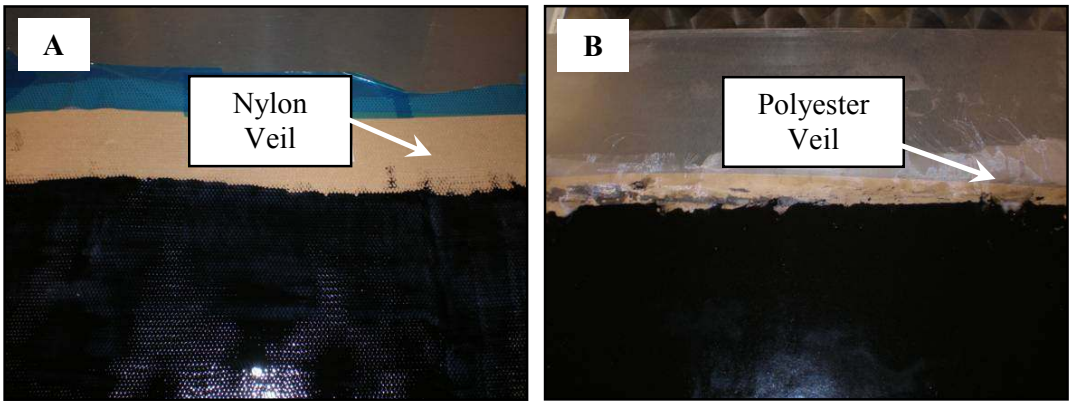

Figure 4.21 – Supported CRN films showing (A) nylon veil version and (B) polyester veil version

Figure 4.22 shows the polyester veil supported version of the CR formulation.

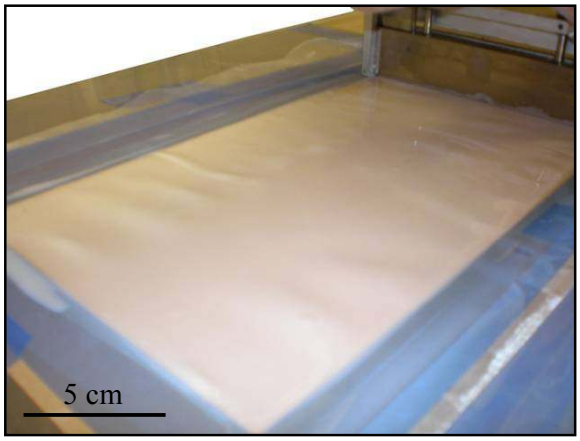

Figure 4.22 – Polyester veil supported CR film

4.2.5.4 Improving adhesion through the use of a surface primer

A CR formulation 'primer' was used in this work to help the wetting process. This primer was used in conjunction with the CRN formulation which was too viscous to achieve good wetting on its own. A thin layer of the CR formulation was applied with a razor blade onto the substrate surface before laying on the CRN adhesive film. This CR formulation was chosen for the primer as it was compatible with the CRN formulated film. Figure 4.23 shows GFRP substrate surfaces prepared for bonding following the application of the primer.

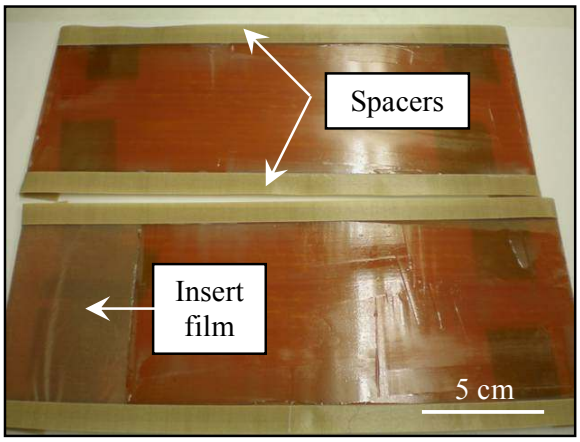

Figure 4.23 – Priming the GFRP substrate surfaces before bonding

4.2.6 Alternative processing routes considered

4.2.6.1 Spraying CNTs onto adhesive surface

A weak substrate boundary layer can provide a 'weak-link' leading to reduced bond strength or premature failure. Figure 4.24 shows the five regions in to which every adhesive joint can be divided [9]. When the surface region becomes the weakest link, it may result in catastrophically low failure strength and an inconsistency in failure values. Thus, it is imperative that these surface characteristics be controlled in some manner.

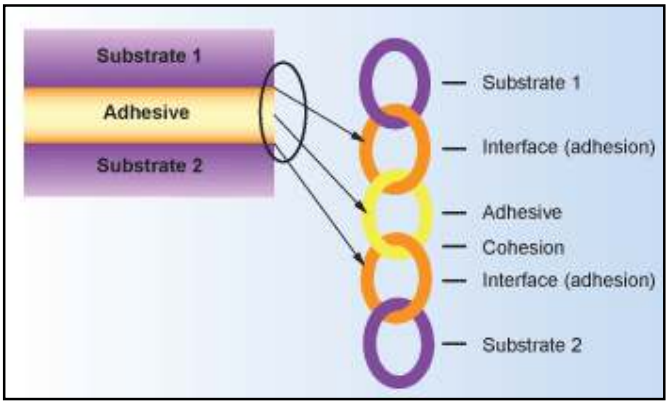

Figure 4.24 – Adhesive joint structure divided into five regions [9]

From the author's own work and experience in manufacturing the carbon nanotube loaded adhesive, an alternative method of incorporating the carbon nanotubes in the joint became apparent. This alternative was the spraying of the carbon nanotubes onto the contact surfaces of the adhesive film prior to bonding. The major advantage of this approach would be the targeted application of the nanotubes to the area where reinforcement is most needed; at the adhesive-substrate interface.

The idea considered dispersion of the nanotubes in a solvent prior to being applied to the adhesive using a spray gun (see Figure 4.25). Solvents suitable for this application would need to maintain the carbon nanotubes dispersion. Ethanol and methyl ethyl ketone (MEK) have been reported to suspend carbon nanotubes well [140,141]. The drawbacks however, are the safety concerns in evaporating these solvents and the

possibility of small amounts entering and remaining in the adhesive after the evaporation process.

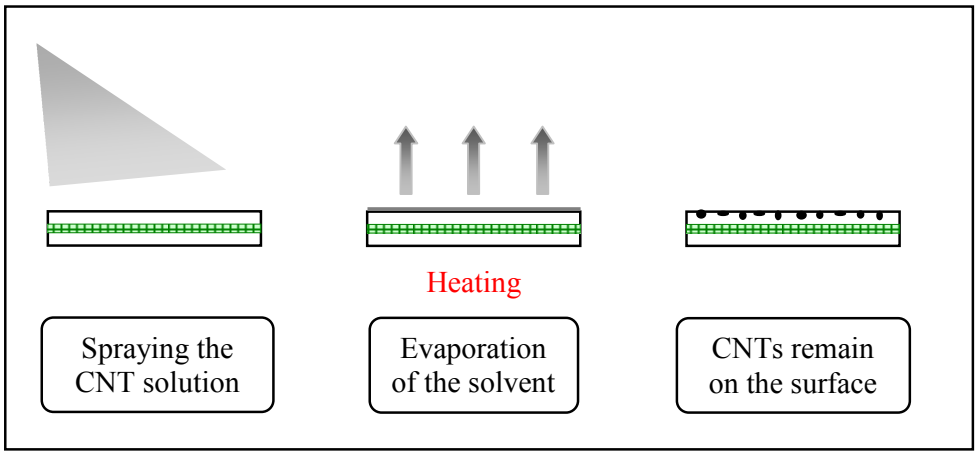

Figure 4.25 – Proposed idea of spraying carbon nanotubes directly onto adhesive surface

One of the benefits of this technique would be to remove the need of dispersing the carbon nanotubes into the epoxy resin thus avoiding the difficulties of processing this complex and highly viscous mixture. The lower viscosity of the adhesive formulation without nanotubes would increase the concentration of rubber which can be incorporated, whilst maintaining the processability of the paste, thus enhancing the toughness of the adhesive. A greater benefit would be the instant compatibility with commercially available adhesive systems.

This proposed application remained as an idea for future studies but was not implemented in the present work.

4.2.6.2 Targeting nanofillers at the adhesive-substrate interface

The interface role in the performance of the adhesive joint was investigated in a small pilot study. An unsupported film was produced, formulated from 1 wt% of carbon nanofibres (CNF) dispersed in the control system. The idea was to implement this additional film directly at the adhesive-substrate interfaces. These unsupported films, hereafter called CF, were placed either side of the main CR adhesive film containing a polyester veil in the joint. Figure 4.26 shows the bonding sequence of this structure.

Carbon nanofibres were chosen as they are larger than carbon nanotubes and therefore the presence of any 'fibre bridging' will be easier to detect [142]. This form of toughening occurs where debonding of the nano particles has taken place but not all have fractured and some continue to bridge the faces of the crack wake [143]. As the crack opens under the action of the applied stress, some of the stress will be transferred to the fibres which will deform elastically. The resulting effect is an increase resistance to crack growth.

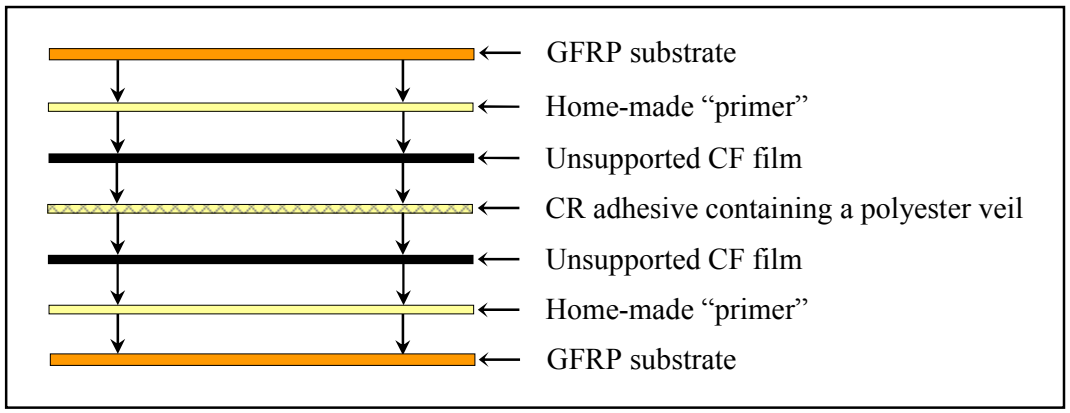

Figure 4.26 – Bonding sequence of the structure with CF films at the interfaces

The manufacture specifics of this film were as follows. The carbon nanofibres were dispersed into the DGEBA epoxy resin using the Dispermat CN10-F2 high shear rotational mixer (see Figure 4.7) at 60˚C and 2400 rpm for 30 minutes [144]. The hardener-catalyst mixture was added afterwards and stirred for 30 minutes at 3000 rpm and 80ºC. Stirring was carried out under vacuum. The film was processed using a filming temperature of 55ºC. The result is shown in Figure 4.27. The manufacture of the bonded structure, as shown in Figure 4.26 and the mechanical data obtained can be found in Section 4.3.2 and Chapter 7 respectively.

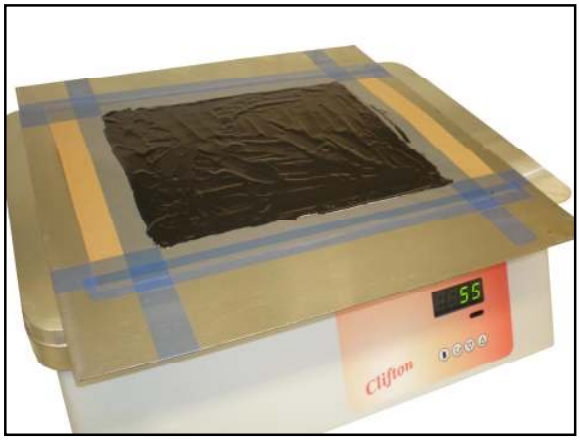

Figure 4.27 – Unsupported CF film

4.3 Specimen preparation

This section reports the preparation of cast specimens from the adhesives formulated and the manufacture of all bonded test specimens and structures used in this work.

4.3.1 Cast specimens

Various test specimens were machined from the cured plaques prepared as described in Section 4.2.4. The reader should be aware that all specimens were obtained from plaques which were cured simultaneously under identical processing conditions. The cutting was done using a Buehler Isomet precision saw with a water-cooled diamond blade. Afterwards, they were polished on a Buehler Metaserv Motopol 12 polishing wheel using polishing papers up to P1200 silicon carbide grade. The equipment used is shown in Figure 4.28.

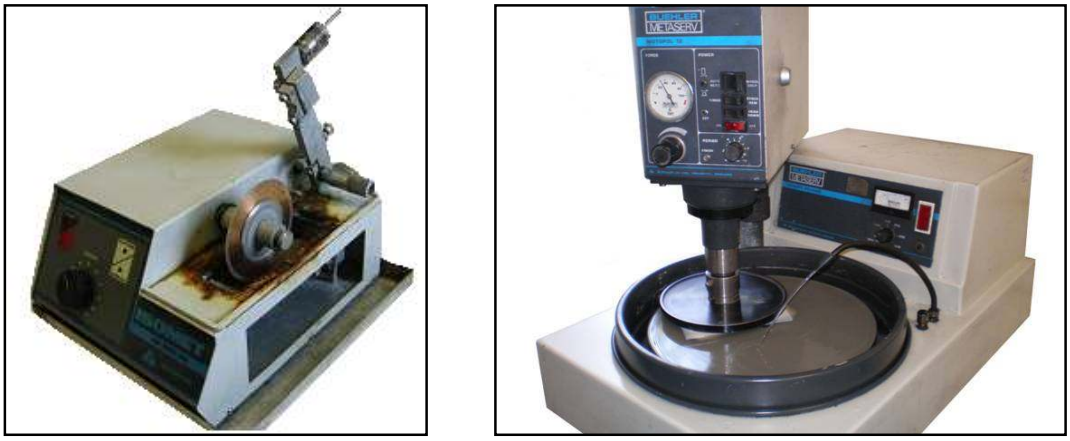

Figure 4.28 – Buehler precision saw (left) and Buehler Metaser Motopol 12 polisher (right)

4.3.1.1 Dynamic mechanical thermal analysis (DMTA) specimens

DMTA specimens were prepared for measuring the glass transition temperature, $T_{g\infty}$, of the different adhesive formulations. The specimen dimensions are suitable for DMTA testing under compressive loading conditions. As such, the preparation was critical as the obtaining of good results is heavily dependent on ensuring that the ends of the samples are perfectly parallel. Specimens were manufactured for the C, CR, CN and CRN formulations, the dimensions of which are shown in Figure 4.29.

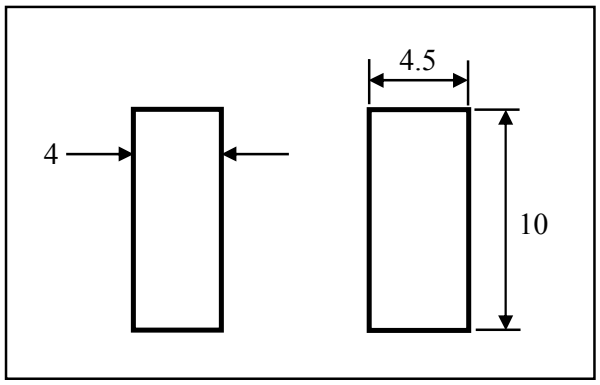

Figure 4.29 – DMTA specimen dimensions (mm)

4.3.1.2 Thermal mechanical analysis (TMA) specimens

Specimens were prepared for measuring the coefficient of thermal expansion (CTE) of the different adhesive formulations by TMA. Precise preparation was again critical in order to achieve accurate results. The dimensions for TMA specimens are given in Figure 4.30.

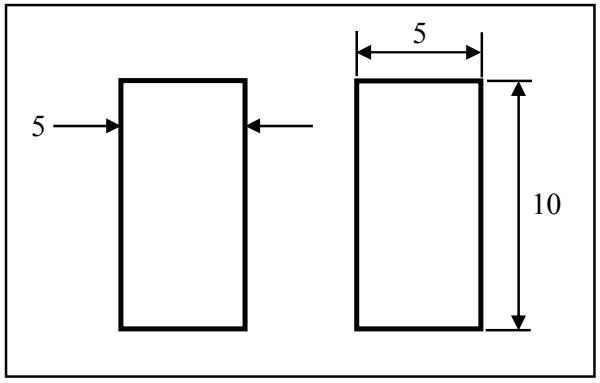

Figure 4.30 – TMA specimen dimensions (mm)

4.3.1.3 Fracture specimens: 3 point bending

Single edge-notched bending (SENB) specimens were prepared in accordance with test standard ISO 13586:2000 [145]; the dimensions are given in Figure 4.31.

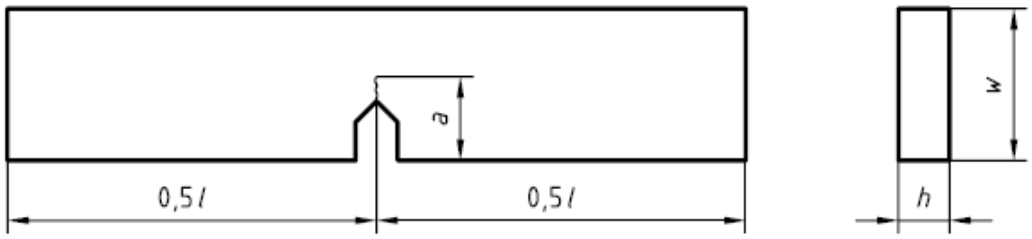

Where:

w	width	
l	overall length	$(l > 4.2w)$
h	thickness	$(w/4 < h < w/2)$
a	crack length	$(0.45w \leq a \leq 0.55w)$

Figure 4.31 – SENB test specimen diagram

For the C and the CR formulations the dimensions were as follow: h = 4 mm, w = 15 mm and l = 80 mm. For the CN and CRN formulations the values used were: h = 3 mm, w = 12 mm and l = 60 mm.

Prior to testing, a natural pre-crack was introduced by tapping a razor blade into the specimen at the base of the machined notch (see Figure 4.32). The constraint on the required pre-crack depth is to be between 45% and 55% of the specimen width. Different techniques exist for creating this natural pre-crack [146]. For each crack, a new razor blade was used in order maintain the quality of manufacture and ensure consistent results.

The test is valid only if the specimens' dimensions are in accordance with the linear elastic fracture mechanics (LEFM) guidelines which are stated as follows:

$$h, a, \left(w - a\right) > 2.5\left(\frac{K_{IC}}{\sigma_{yt}}\right)^2 \quad \text{..... (4.1)}$$

Where:

K_{IC} critical stress intensity factor

σ_{yt} uniaxial tensile yield stress

This criterion ensures that h is sufficient to achieve plane strain and fracture initiation conditions and (w-a) has to be sufficient so as to avoid excessive plasticity in the ligament.

In order to select the final specimen dimensions initial estimates of the values for K_{IC} and σ_{yt} were introduced into Equation 4.1. Figure 4.33, images A-B, shows the finished specimens prepared for testing.

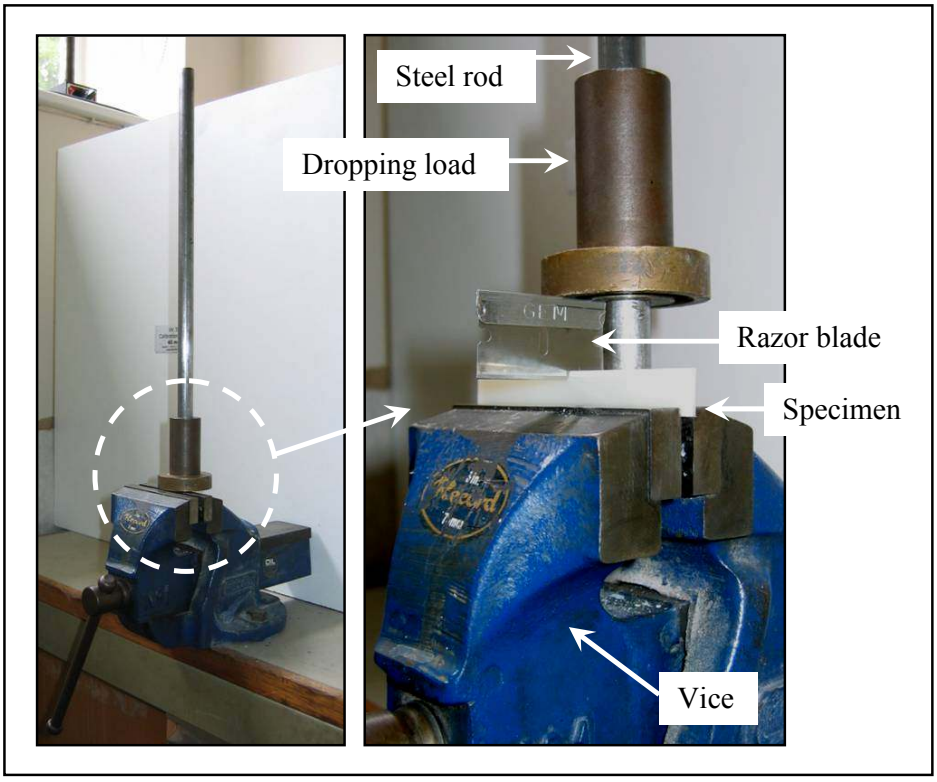

Figure 4.32 – Tapping system used to generate the natural pre-crack on the SENB specimen

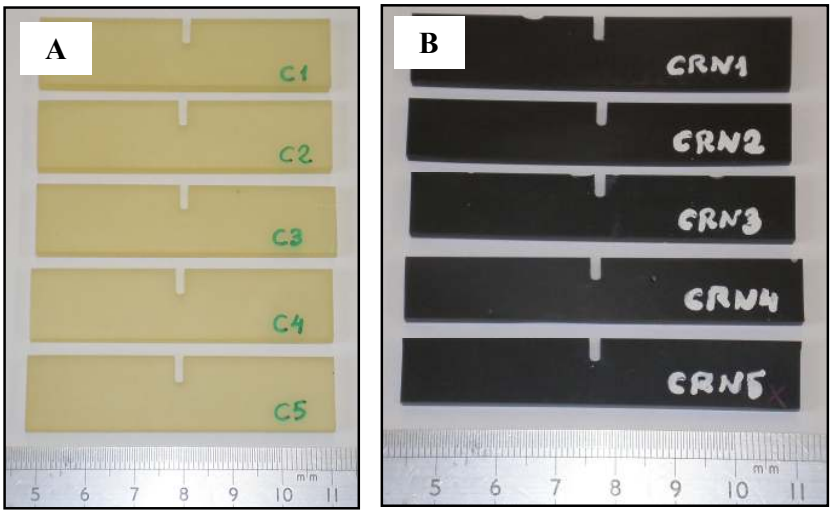

Figure 4.33 – SENB specimens from the C formulation (A) and the CRN formulation (B)

4.3.1.4 Flexural specimens

Rectangular flexural specimens were prepared for measuring the flexural modulus of the different adhesive formulations in accordance with Figure 4.34.

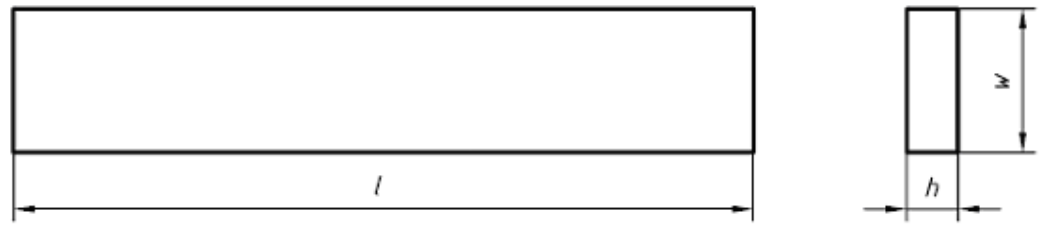

Where:

w	width
l	overall length $l > 20h$
h	thickness

Figure 4.34 – Flexural test specimen diagram

For the C and the CR formulations the dimensions were as follows: h = 3 mm, w = 15 mm and l = 80 mm. For the CN and CRN formulations the values used were: h = 2 mm, w = 12 mm and l = 60 mm. These dimensions are as given by the test standard, ISO 178:2001 [147].

All surfaces and edges were free from scratches, sink marks and flash. Figure 4.35 shows flexural specimens prepared from the C and CRN formulations.

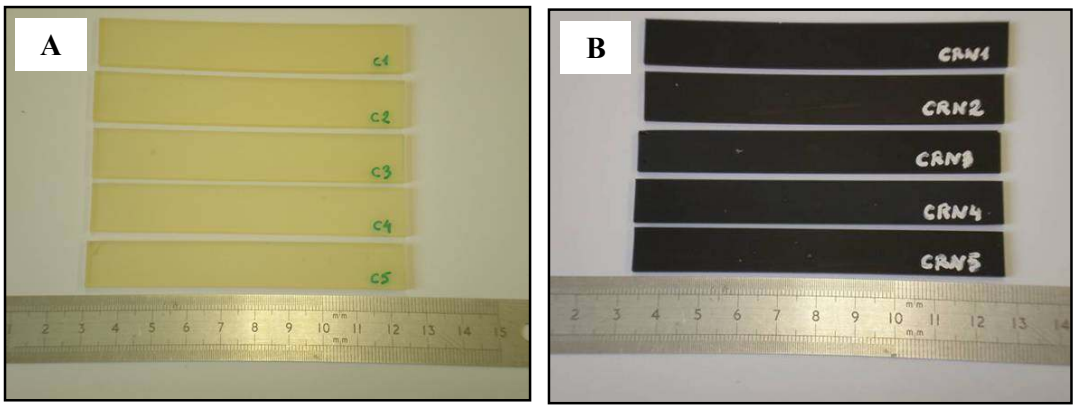

Figure 4.35 – Flexural specimens, showing the C formulation (A) and the CRN formulation (B)

4.3.1.5 Compression specimens

Compression specimens were prepared for determining the uniaxial compressive yield strength (σ_{yc}) of the different adhesive formulations. The specimen dimensions are taken from test standard ISO 604:2003 [148] and are shown in Figure 4.36. Great care was taken in machining to ensure smooth, flat, parallel surfaces and sharp, clean edges, perpendicular to the longest axis of the specimen.

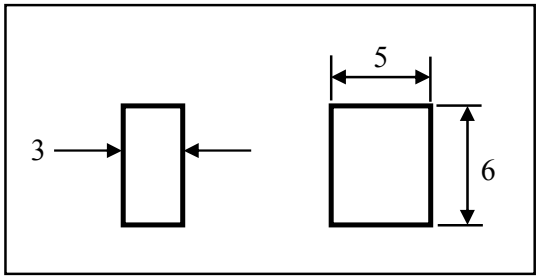

Figure 4.36 – Compression specimen dimensions (mm)

4.3.1.6 Electrical conductivity specimens

Rectangular specimens were manufactured for measuring DC electrical resistivity according to test standard ASTM D4496:2004 [149] and AC electrical resistivity. The largest faces were painted with silver paint to provide good contact (see Figure 4.37).

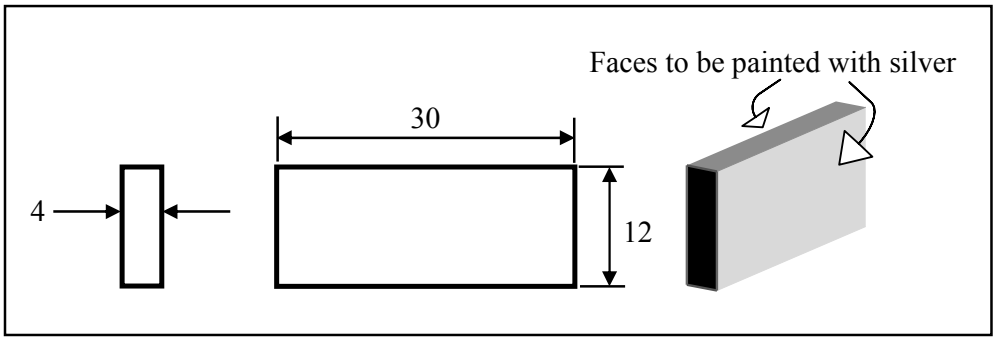

Figure 4.37 – DC and AC conductivity measurement specimen dimensions (mm)

Figure 4.38 shows some of the specimens prepared from four different adhesive formulations.

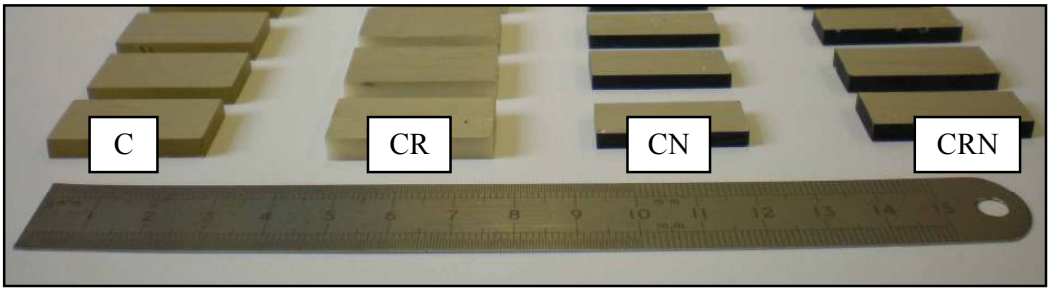

Figure 4.38 – DC and AC conductivity specimens for the different adhesive formulations

4.3.2 Adhesively bonded specimens

Several tests were performed requiring specimens manufactured by bonding adhesive films to substrates. Two substrate materials were used; aluminium alloy and glass-fibre reinforced plastic (GFRP) composite. The aluminium alloy was supplied by Alcoa after being surface treated by Airbus Germany (see Section 3.4.2). GFRP panels were manufactured by the author as described in the following section.

4.3.2.1 Manufacture of GFRP plates

Six plates measuring 250x300 mm were made from UD E-glass / 913 epoxy pre-preg. Four plates were manufactured to 2 mm nominal thickness and the remaining two plates to 3 mm nominal thickness. The corresponding numbers of plies needed to achieve these thicknesses are given in Table 4-4.

Thickness	Plies required	Stacking sequence
2 mm	15	0_{15}
3 mm	23	0_{23}

Table 4-4 – Lay-up details for GFRP plates

The UD lay-up was automatically symmetric and balanced and ensures the plates would not warp during cure. The stacking sequences are given in Table 4-4. Debulking was carried out on a heated vacuum table (15 minutes at 35ºC) after every 5 plies were laid down and finally once the stack was complete (25 minutes at 35ºC). A nylon peel ply

was added as the last layer in the lay-up of every panel before curing. Before any adhesives were bonded this peel ply was removed (see Figure 4.39).

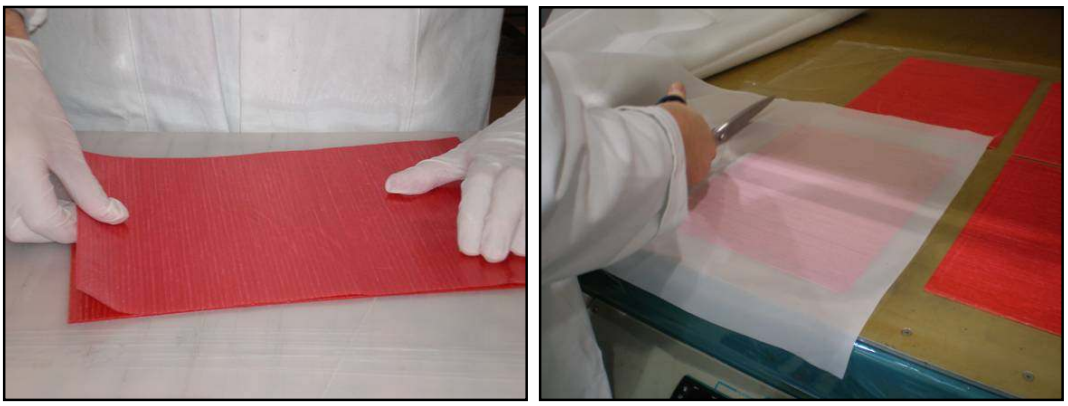

Figure 4.39 – Lay-up and peel ply placement on the bonding side of the plates

The plates were cured in an autoclave according to the manufacturer's recommended cure cycle for the material, detailed in Chapter 3. Figure 4.40 shows the autoclave preparation prior to curing the plates.

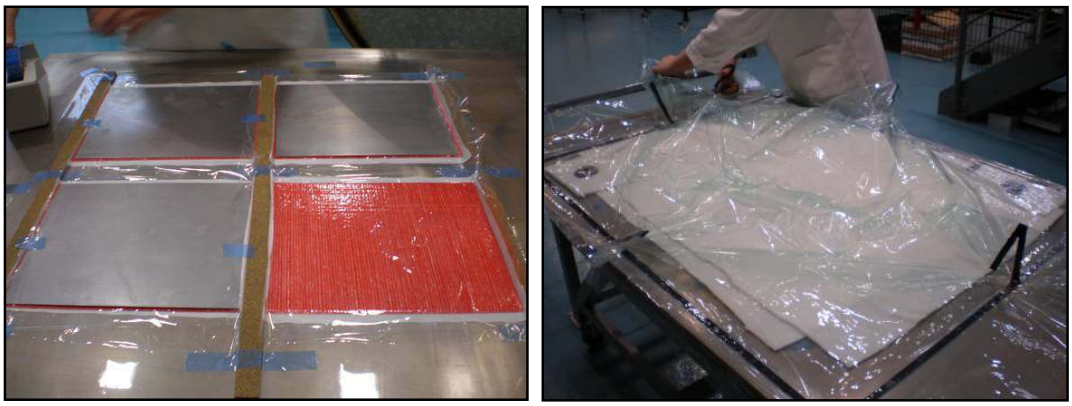

Figure 4.40 – Preparing the autoclave for curing the plates

Figure 4.41 shows the two surfaces from one of the cured plates. Image A shows the shiny base surface cured with no peel ply. Image B shows the peel ply being removed from the surface on which the adhesive would eventually be applied. The matt finish obtained with use of a peel ply is noticeable.

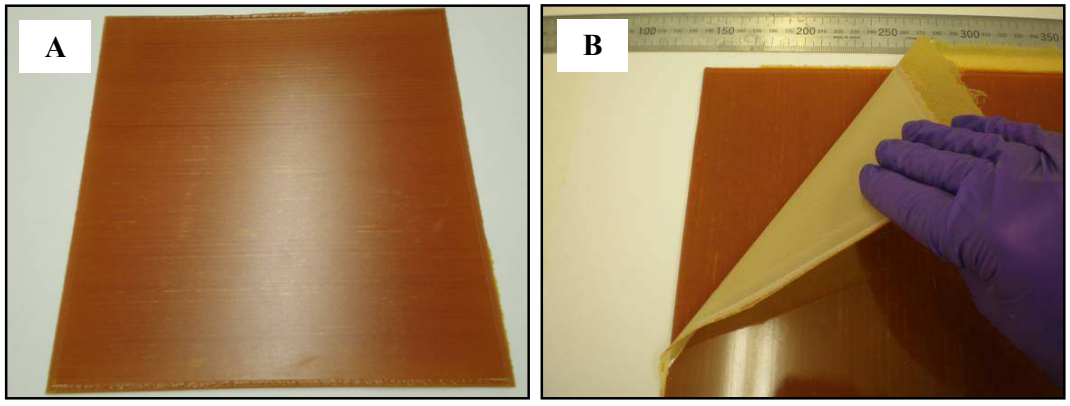

Figure 4.41 – Cured GFRP plates showing (A) a shiny surface and (B) a matt surface obtained when using a peel ply

SEM was used to examine the GFRP surface after removal of the peel ply. The micrographs in Figure 4.42 shows the features created in the surface; negatives from the nylon fibre texture in the peel ply.

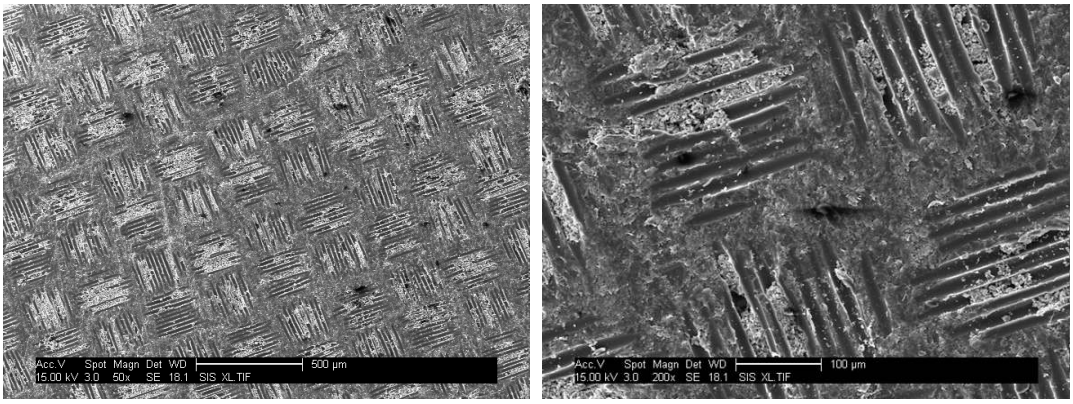

Figure 4.42 – SEM micrographs showing the resulting composite surface after the removal of the peel ply

4.3.2.2 Preparation of bonding surfaces

The strength of an adhesive joint is significantly increased when loose deposits such as rust, scales and organic contaminants are removed from the surface so that the adhesive can fully wet the substrate. Composite adherends are even more dependent than metals on surface preparation. Most of these materials have complex formulations and their surfaces are often contaminated with mould release agents or additives that can migrate to the surface during processing. These contaminants must be removed before bonding.

GFRP Substrates

The peel ply applied to the surfaces before curing the GFRP panels was used to create a consistent and controlled roughness on the surfaces to be bonded. This roughness is intended to give improved adhesion by increasing the effective surface area to be bonded. The adhesive can also flow deeper into the surface. After removal of the peel ply, the surfaces were gently abraded with P1200 silicon carbide polishing paper. Following this, dust and debris were removed by cleaning with methyl ethyl ketone [150] and the plates were dried in the oven at 80ºC for two hours.

Aluminium alloy Substrates

The surface preparation of the aluminium alloy provided by Alcoa was carried out at Airbus Germany. The process was described in Section 3.4.2. Prior to bonding in this work, the prepared surfaces were cleaned with acetone also.

4.3.2.3 DCB test coupons

Double cantilever beam (DCB) test coupons were manufactured by bonding adhesive films to both GFRP and aluminium alloy substrates.

These coupons incorporate a crack starter film from which crack growth is initiated during the test. As such the test results obtained are dependent on the quality of manufacture of this coupon detail. There are a number of considerations, specific to adhesively bonded coupons, manufactured using a single layer of adhesive film, as for this work, which need to be explained.

In the case of coupons manufactured using a single supported adhesive film it is not possible to produce a perfectly symmetric coupon geometry in the region of the crack starter film. When constructing such test coupons, the starter film will always be either above or below the veil in the adhesive layer. This will produce a crack propagation bias through the corresponding region of the adhesive layer unless the propagating crack

finds a path which passes through the veil. This detail is regularly omitted in literature [151,152].

The obvious way to achieve symmetry in this case and meet the test standard requirement for the crack starter film to be positioned along the centre plane of the test coupon, would be to use two films of supported adhesive and place the crack starter film in between. However, this is not representative of the way in which adhesives are used in industrial application as it somewhat negates the use of the veil as a bond line thickness control measure. In addition, propagation of the crack is artificially encouraged to occur cohesively as the propagation path is constrained between the two veils. Whilst interfacial failure is undesirable it cannot be forcibly omitted form the test. Furthermore, manufacturing trials showed that the independent movement of the two adhesive layers during cure has the effect of distorting the starter film at the edge from which crack propagation is initiated during the test. A clean, sharp edge is required in order to obtain accurate, reproducible results.

Whilst ensuring that the manufacture of the test coupons does not artificially encourage cohesive failure, consideration must also be given to ensure that an interfacial failure is not overly encouraged. Considering the single adhesive layer test coupon again, if the starter film is simply placed on the surface of the adhesive film then, as Figure 4.43 shows, the initiation of crack propagation is heavily biased to occur at the adhesive-substrate interface.

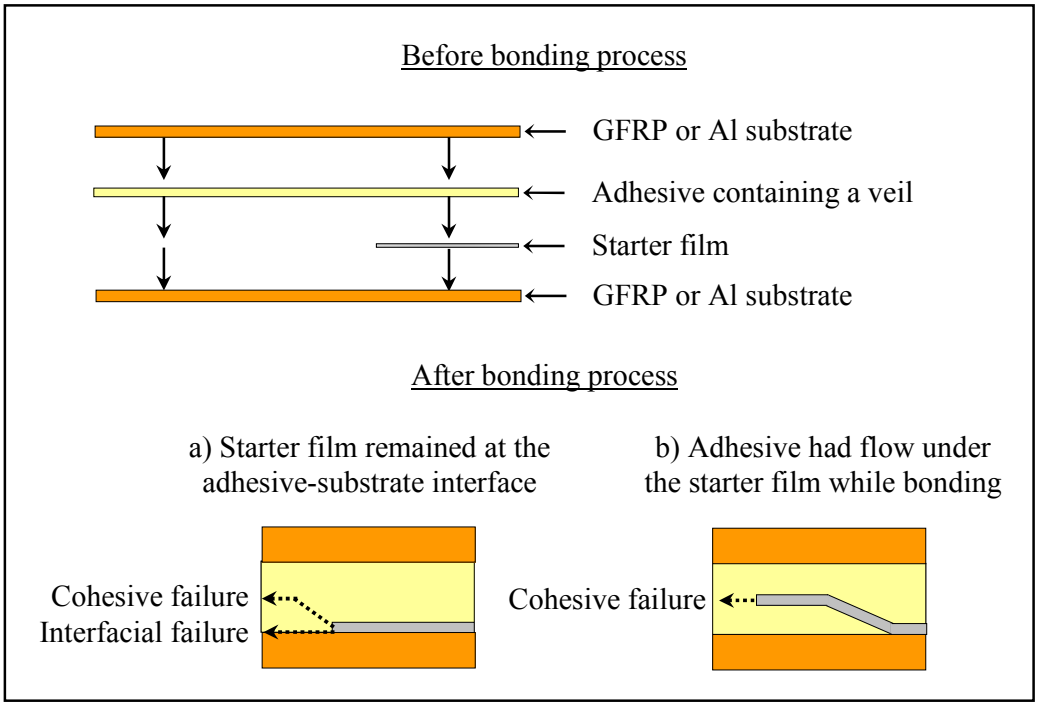

Figure 4.43 – Position of crack starter film in a single adhesive film bonded delamination test coupon

A disbond occurring in a region of poor surface preparation is far more common in the industrial environment than a crack existing in the adhesive layer. The flow of the adhesive during cure tends to fill any voids and/or defects which may exist in the adhesive layer prior to bonding. There is an argument therefore, in contradiction of the test standard that leaving the starter film at the adhesive-substrate interface is an acceptable practice. It is the author's opinion that this does produce a bias towards interfacial failure and should be avoided. For the DCB (and ELS) testing of these adhesives this is undesirable as it does not encourage the production of test data which are relevant to the adhesive itself, rather the interfacial properties of the chosen coupon materials.

However, the failed test coupons were examined following each delamination test and showed that during cure, the adhesive had flowed a short distance (approximately 4mm) under the substrate side of crack starter film. This was the case for all of the adhesive film types manufactured and tested. The coupon geometry, in the crack starter film region, prior to testing would therefore have seen the crack tip still on one side of the

veil but completely embedded in adhesive. This was perhaps a fortunate occurrence brought about through the decision to not use any flow control agents in the formulations created. The author would encourage further consideration and study regarding the placement of the crack starter film in delamination coupons containing single adhesive layers. Flow properties will obviously be different between adhesive products and the actual test geometry in the locality of the crack starter film is likely to display some variation therefore.

GFRP substrate

The GFRP panels were divided into manageable plates measuring 72x240 mm for bonding. To manufacture DCB specimens, two of these plates were placed together with the film adhesive laid between them. A thin, 13 μm insert film was also laid at one end (see Figure 4.44).

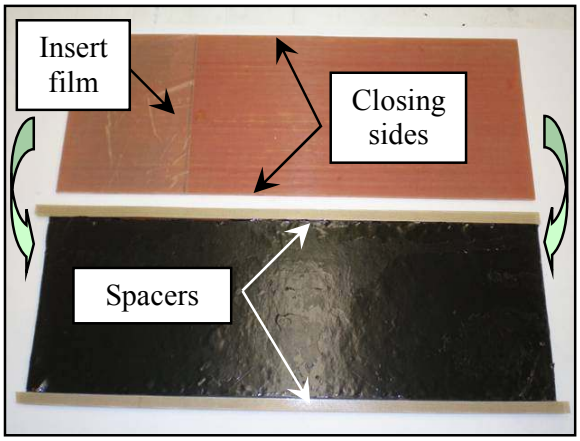

Figure 4.44 – Manufacturing the bonded panels

Spacers 0.25 mm thick were used along the long edges to control the final adhesive thickness and were particularly important as these formulations did not contain flow control agents. The long edges of the stack were sealed with heat resistant tape as a further flow control measure by limiting the adhesive bleed, which was considerable, to one direction. The stack was placed on a heated vacuum table where the adhesive was cured. The curing cycle was 360 minutes at 120ºC with 69 kPa of applied pressure.

Figure 4.45 shows the panel layout for the final bonded plate from which DCB specimens were cut.

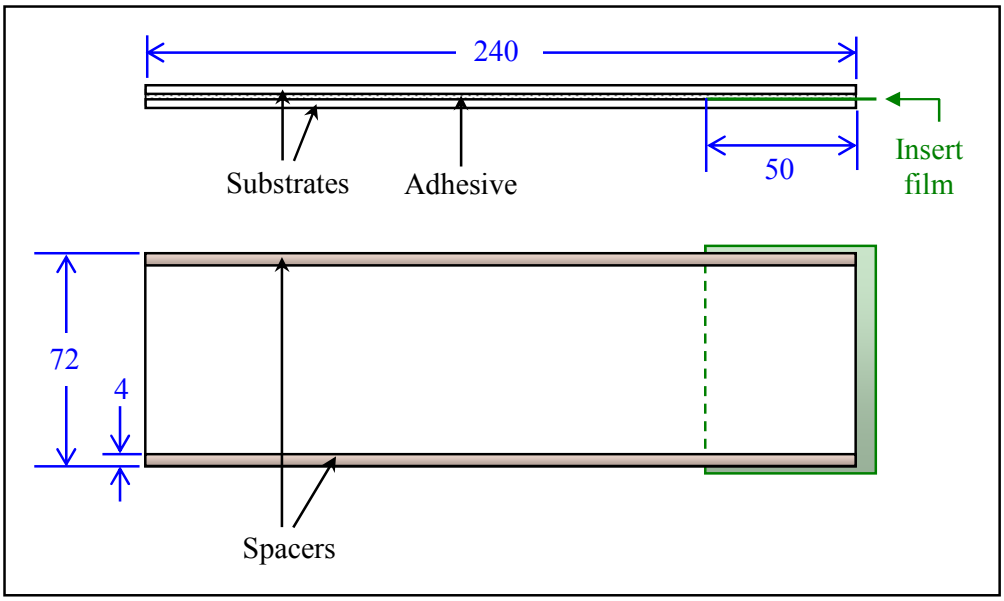

Figure 4.45 – Panel layout for bonded GFRP testing coupons (dimensions in mm)

Table 4-5 lists the bonded panels manufactured in this way for testing. The prefix 'U' in the panel ID column refers to the adhesive film used being unsupported; 'P' is used where a polyester veil is present in the adhesive film and 'N' where a nylon veil is present. The curing cycle was believed to be well in excess of the time required to achieve complete cure at this temperature for all the bonded panels.

Plate ID	Adhesive film	Veil type
GFRP-U-C	Control	-
GFRP-U-CR	Control + Rubber	-
GFRP-U-CN	Control + MWCNTs	-
GFRP-U-CRN	Control + Rubber + MWCNTs	-
GFRP-N-CRN	Control + Rubber + MWCNTs	Nylon
GFRP-P-CRN	Control + Rubber + MWCNTs	Polyester

Plate ID	Adhesive film	Veil type
GFRP-P-CR	Control + Rubber	Polyester
GFRP-U-CF / P-CR	Control + CNFs at interfaces & P-CR	Polyester
GFRP-FM94	Commercial adhesive FM® 94K	Polyester
GFRP-FM15	Commercial adhesive FM® 1515-3M	Nylon

Table 4-5 – GFRP bonded panels manufactured

Three specimens were obtained from each plate. End tabs, specifically required for the DCB test, were bonded to the top and bottom surfaces of each coupon with Araldite® 420 adhesive (see Section 3.3.3) at the insert film end. Figure 4.46 shows the geometry of the DCB coupons.

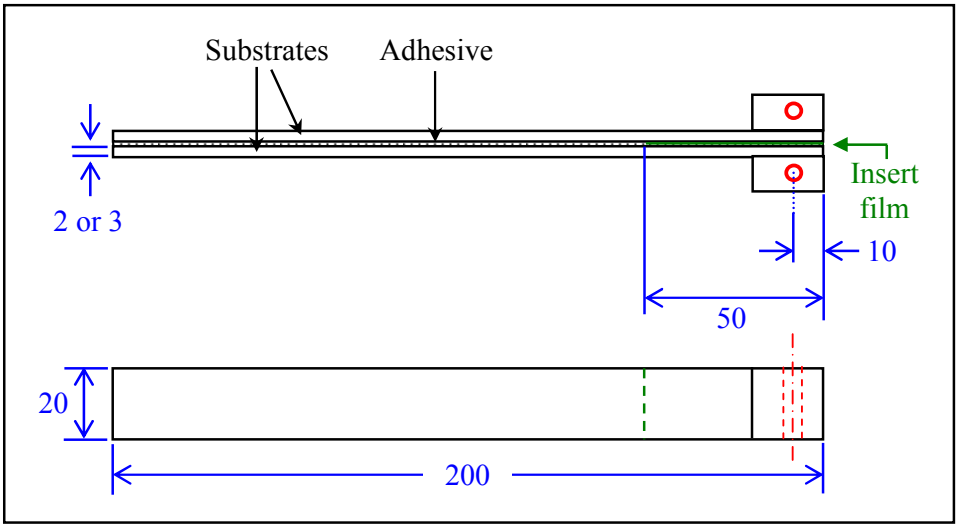

Figure 4.46 – DCB test coupon geometry for GFRP substrates (dimensions in mm)

Aluminium alloy substrate

Aluminium alloy substrate plates were stacked as for the GFRP type described in the previous section. The full list of stacks produced is given in Table 4-6.

Plate ID	Adhesive film	Veil type
Al-P-CRN	Control + Rubber + MWCNTs	Polyester
Al-FM94	Commercial adhesive FM® 94K	Polyester
Al-FM15	Commercial adhesive FM® 1515-3M	Nylon

Table 4-6 – Al bonded panels

Figure 4.47 shows the layout of the aluminium alloy plates, identical for the three adhesive films used, from which coupons for DCB were cut.

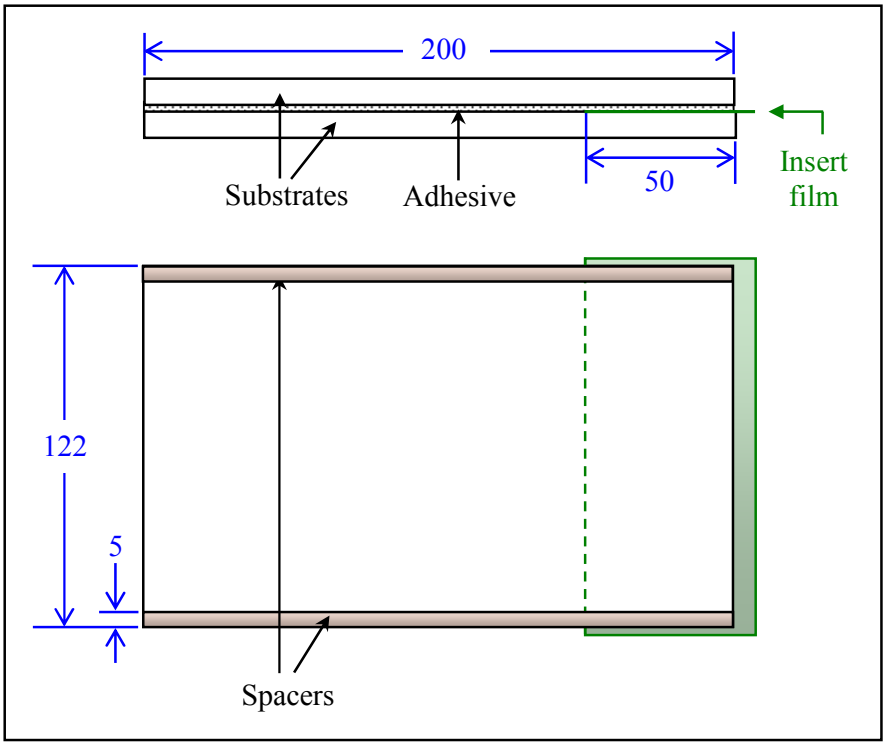

Figure 4.47 – Panel layout for bonded aluminium alloy testing coupons (dimensions in mm)

Five specimens were obtained from each bonded plate. Loading holes were drilled through the arms of the substrates which replaced the need for bonding end tabs as for the GFRP DCB specimens. Figure 4.48 shows the final geometry of the aluminium alloy DCB specimens.

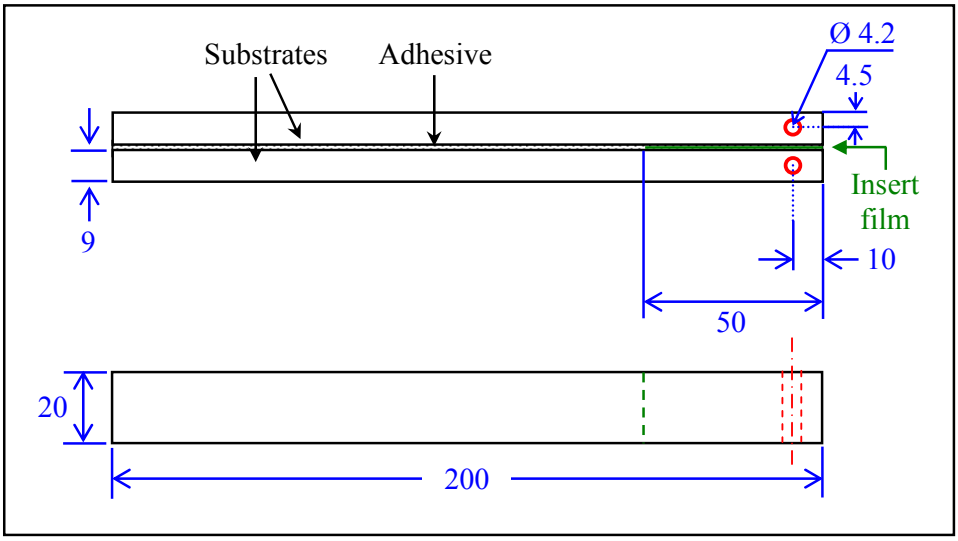

Figure 4.48 – DCB test coupon geometry for aluminium alloy substrates (dimensions in mm)

4.3.2.4 ELS coupons

End loaded split (ELS) test coupons were manufactured from adhesive bonded structures made with GFRP substrates.

The same GFRP test specimens used for DCB testing were used for ELS testing afterwards. In order to do so, the tabs were removed from the specimen and the insert film end was machined to adjust the cracked length to the initial value required for the ELS test. An end tab was re-bonded to the bottom surface of each coupon with Araldite® 420 adhesive (see Section 3.3.3) at the insert film end. Figure 4.49 shows the geometry of the ELS test coupon.

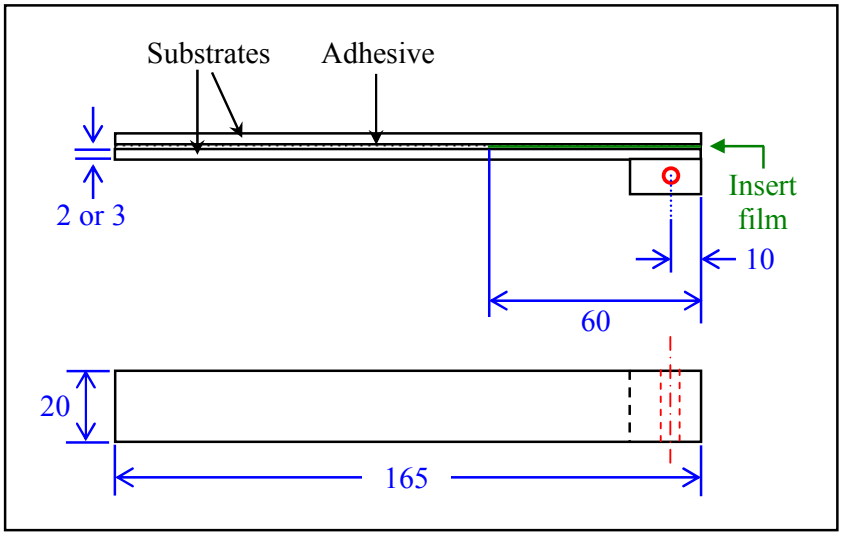

Figure 4.49 – ELS test coupon geometry for GFRP substrates (dimensions in mm)

4.3.2.5 Bonded Crack Retarder (BCR) structure

A specialist structure for measuring the effects on fatigue crack propagation was prepared by bonding two unidirectional GFRP straps to one side of 7085 T 7651 aluminium alloy sample. This structure was part of an in house project which provided a background to the present PhD study as previously introduced in Section 2.1.4. The design of the structure and testing conditions were imposed by the project. This work provided a potential application by which the mechanical performance of novel adhesive formulation could be compared against an identical structure fabricated using the commercial adhesive FM® 94K (see Chapter 7 for the mechanical performance). The aluminium alloy sample is detailed as supplied in Figure 4.50.

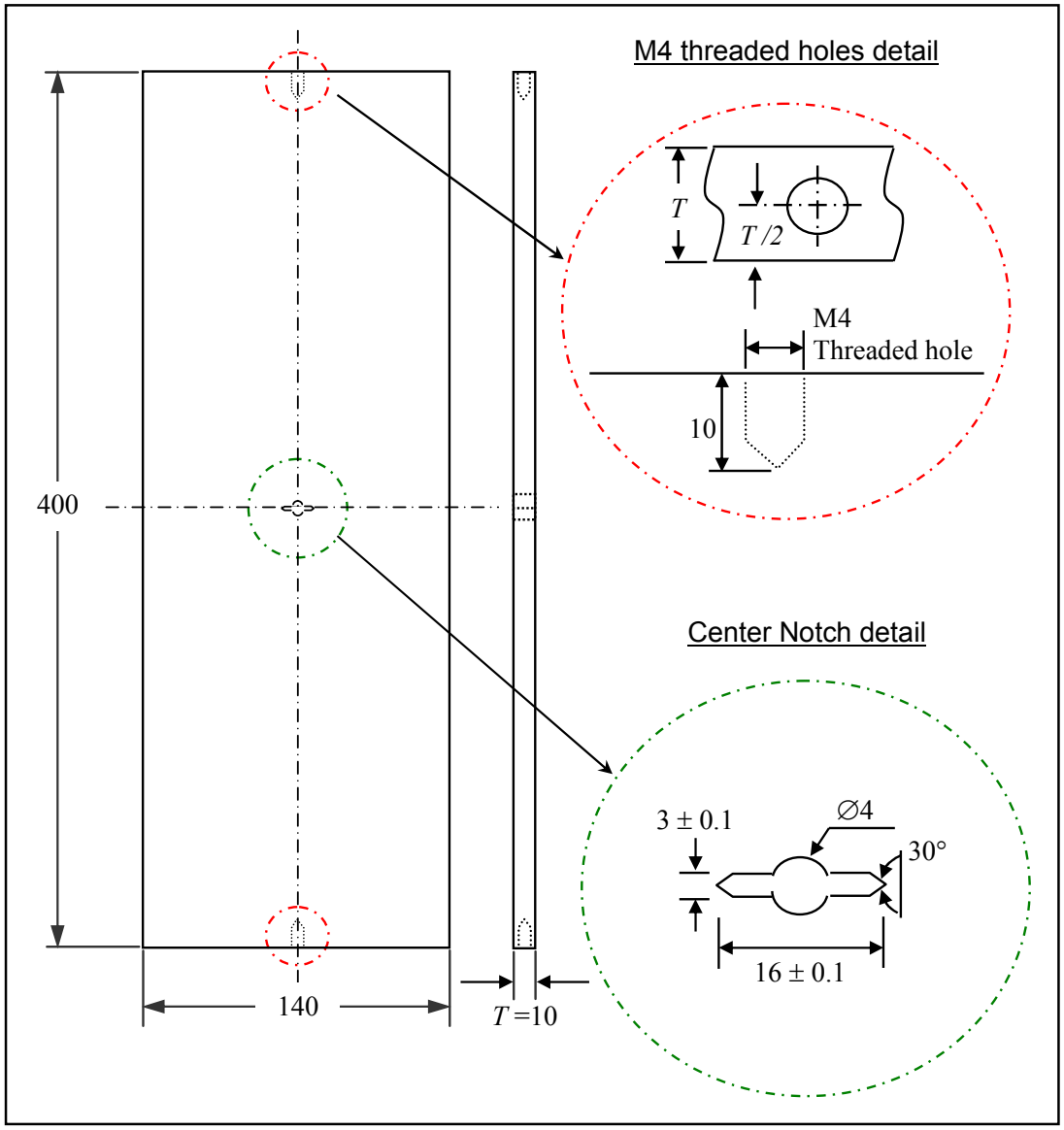

Figure 4.50 – Aluminium alloy plate 'as received' for the Bonded Crack Retarders study

The aluminium alloy sample was first covered by heat resistant tape in order to avoid the adhesive flowing through into the precisely machined crack during cure. A thin layer of the home-made CR primer was applied to the bonding areas on the aluminium alloy sample and the GFRP straps using a razor blade (see Figure 4.51).

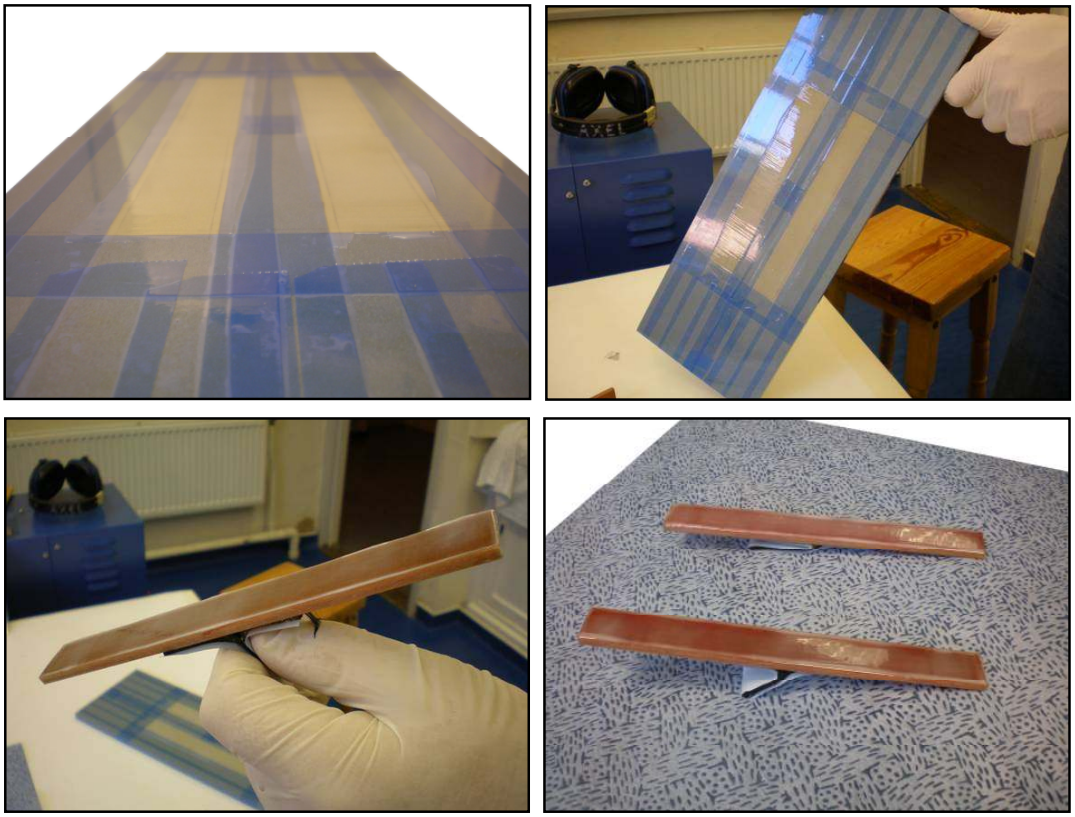

Figure 4.51 – Priming the BCR structure substrates before bonding

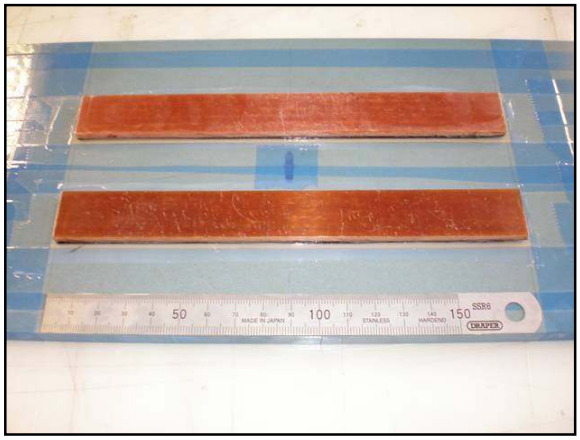

Figure 4.52 – BCR structure before bonding

The CRN adhesive film was cut in two sections exactly with the same dimensions as the straps. The cutting was helped by positioning each strap on top of the film, applying pressure and cutting around the perimeter of the strap. The adhesive was applied to the

GFRPs and then carefully positioned onto the bonding area on the aluminium alloy sample (see Figure 4.52).

Figure 4.53 shows an exploded view of the bonded stack.

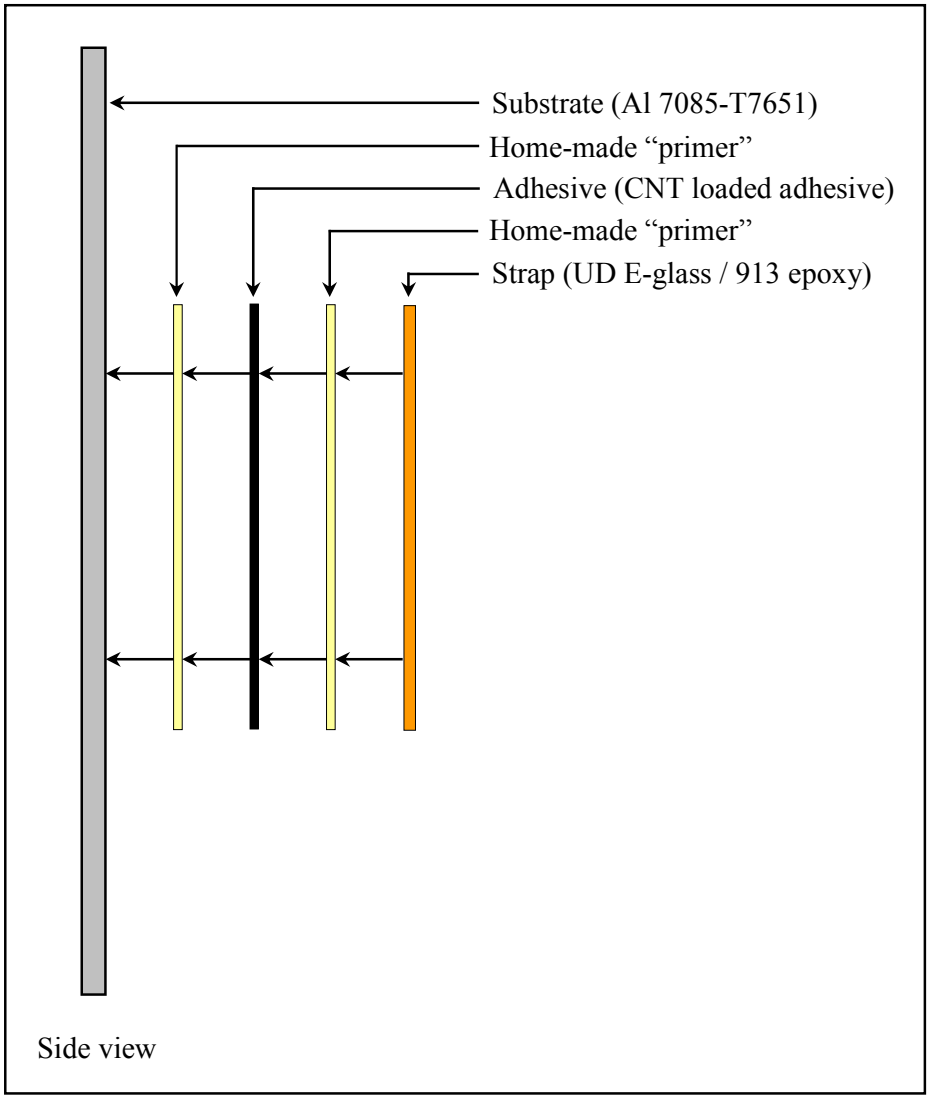

Figure 4.53 – Bonding sequence of the BCR structure

The stack was loaded onto a heated vacuum table where the adhesive was cured. Care was taken to ensure that the straps did not slip under the applied curing pressure. The curing cycle was 360 min at 120ºC with 69 kPa of applied pressure. Figure 4.54 shows the panel after the bonding of the straps. The final, dimensioned structure is illustrated in Figure 4.55.

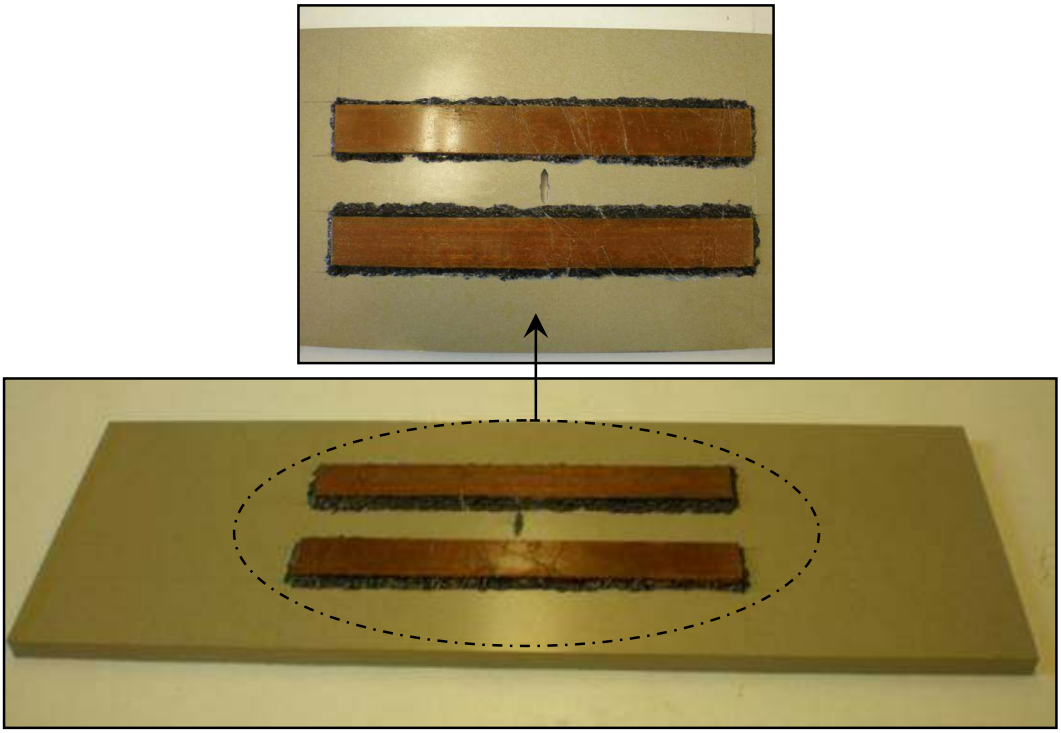

Figure 4.54 – BCR structure after bonding

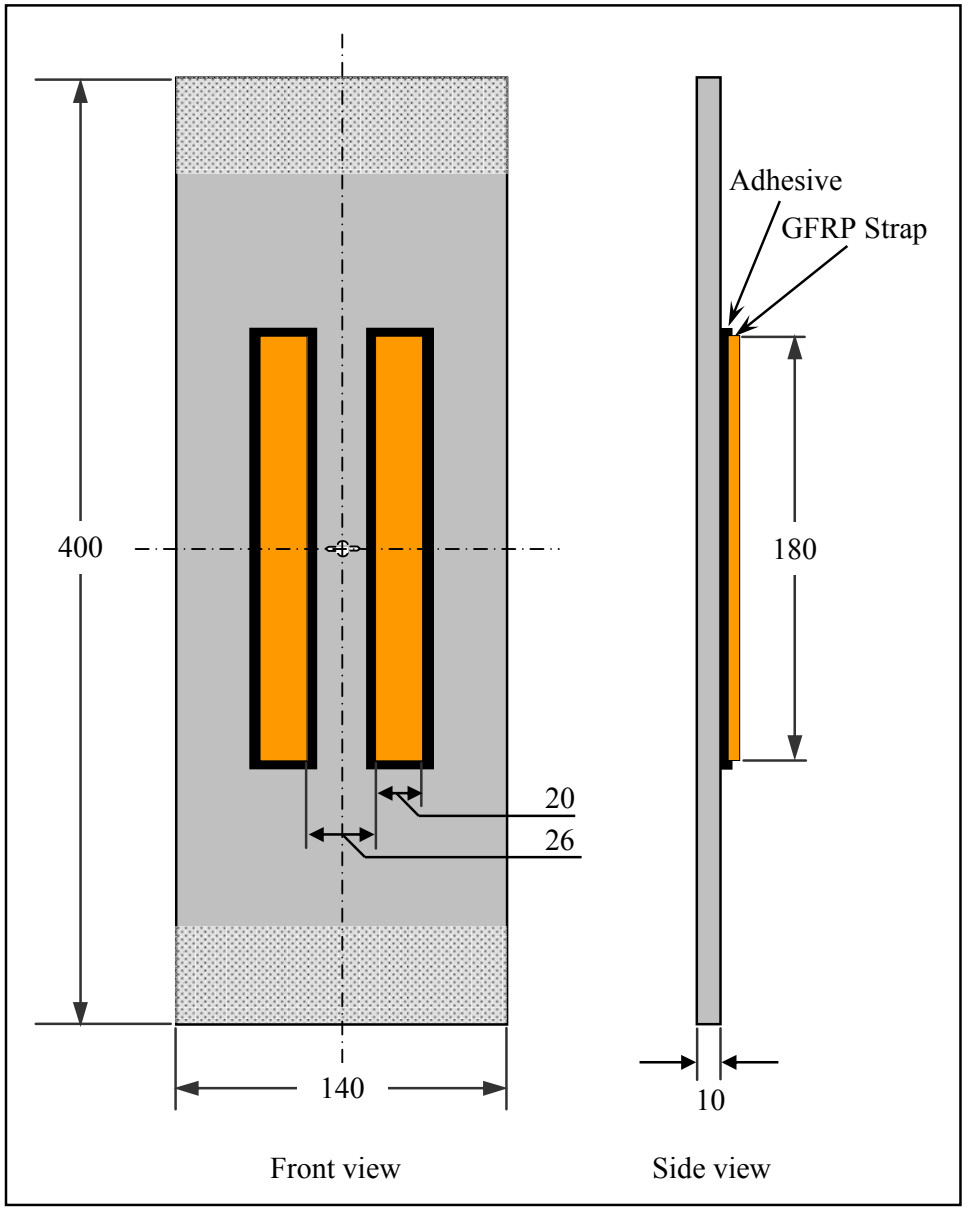

Figure 4.55 – BCR structure (dimensions in mm)

Summary

A novel adhesive formulation has been designed considering its desired performance as well as its processability in film form. Different adhesive variants have been created by separating the individual constituents in order to analyze and better understand their

contribution to the full formulation. This chapter has presented the manufacture of cast specimens and bonded specimens made from film versions of the adhesives. All of these specimens are to be used to characterise the novel adhesive formulation in the following chapters.

Chapter 5

Test methods

This chapter details the test methodologies for all experimental work undertaken in this study.

Some of the test methods described in this section follow published international test standards directly and the specifications for these are detailed. For those test methodologies which are non-standard the reader should be aware that protocols for similar, standardised tests were consulted in developing the methods used.

5.1 Resin characterisation: cure study

Differential scanning calorimetry (DSC) was the technique used in this work to study the cure reactions. DSC measures the concentration of the reacting species indirectly by measuring the exothermic heat produced by the reaction [153]. A typical DSC cell is shown in Figure 5.1.

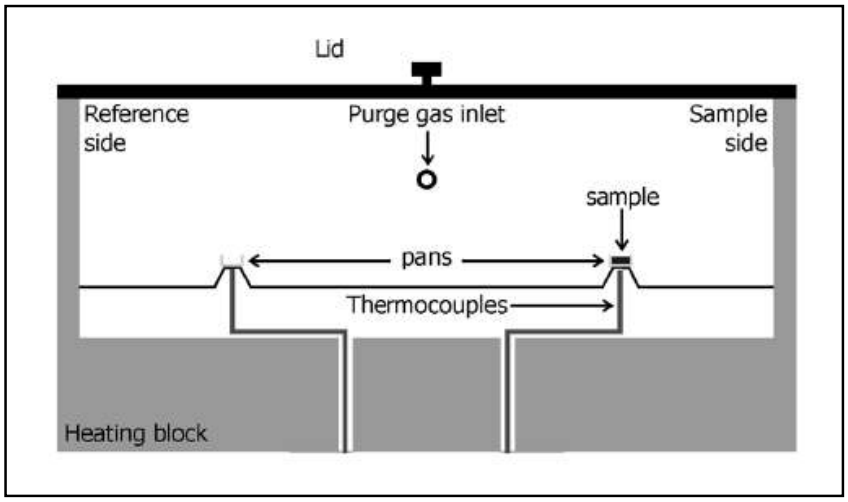

Figure 5.1 – Schematic of a typical DSC cell [154]

Dynamic and isothermal cure experiments were carried out in this study from uncured CR and CRN blends. All the sample weights range from 5 to 6 mg, in order to ensure that thermal gradients within samples were negligible. In the isothermal runs, a 20°C/min heating ramp was used in order to get to the dwell temperature. Since the resin will start to cure before its temperature reaches the dwell temperature, by increasing the temperature in a controlled manner, the cure of the resin prior to the isothermal segment can be monitored and quantified [155]. The non-isothermal conditions were heating ramps at constant rates. The heat flow was recorded as a function of time (isothermal experiments) and temperature (non-isothermal experiments). All experiments were repeated from 2 to 4 times, depending on the reproducibility of the curves. Integration of heat flow curves was carried out using a horizontal baseline for both dynamic and isothermal data. The presented results are averages of the repeated runs.

5.1.1 Determination of T_g by MDSC

Cured samples were used to measure the glass transition temperature in modulated differential scanning calorimetry (MDSC) [156] experiments. The MDSC has the capability of discerning heat capacity changes from irreversible thermal events such as curing [157,158]. It is therefore ideal for identifying the T_g that corresponds to the current state of the material. From a MDSC heating scan, the T_g is identified at the devitrification point (step increase) on the specific heat capacity vs. temperature curve (see Figure 5.2).

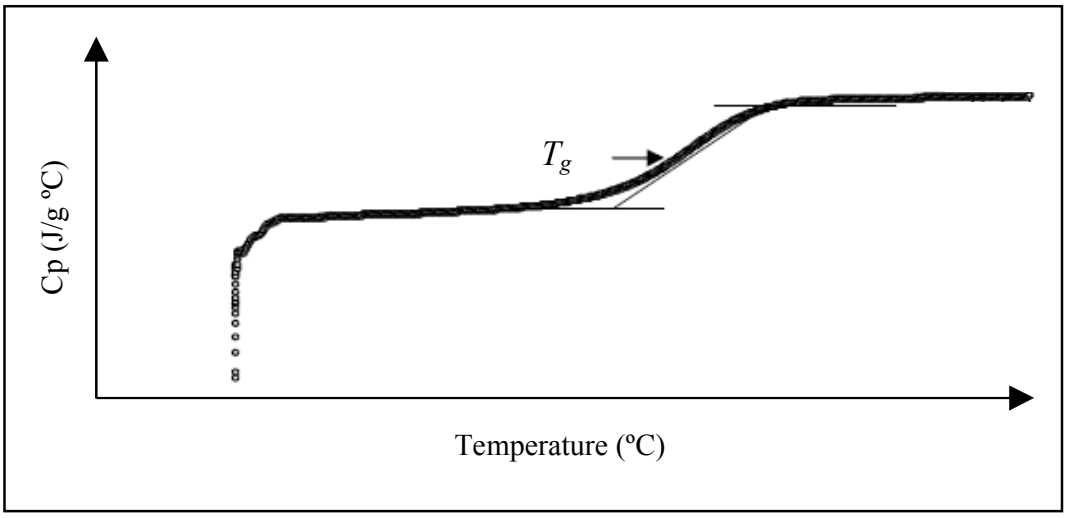

Figure 5.2 – Determination of the T_g from the MDSC trace of heat capacity vs. temperature

Samples weights range from 5 to 6 mg were cured at 120ºC isothermal conditions up to 360 minutes (not final degree of cure). At this point the experiments were stopped and the samples were rapidly cooled. Then MDSC was applied to the cured sample for the evaluation of the T_g values. Initially the sample was left to equilibrate in the cell at 25ºC. Afterwards an underlying heating rate of 1ºC/min was imposed accompanied by a temperature modulation of 1ºC with a period of 60 seconds. The experiments were repeated at least three times each so that a good reproducibility of the results could be achieved.

5.2 Resin characterisation: cast specimens

5.2.1 Post-cure analysis by DMTA

Cast samples were tested using an Eplexor dynamic mechanical thermal analyzer (DMTA) under compression as shown in Figure 5.3. The purpose of this test was to evidence any increase in crosslink densities in the blends, such as a post-cure, as well as to determine the glass transition temperatures of the resins in the fully cured state ($T_{g\infty}$).

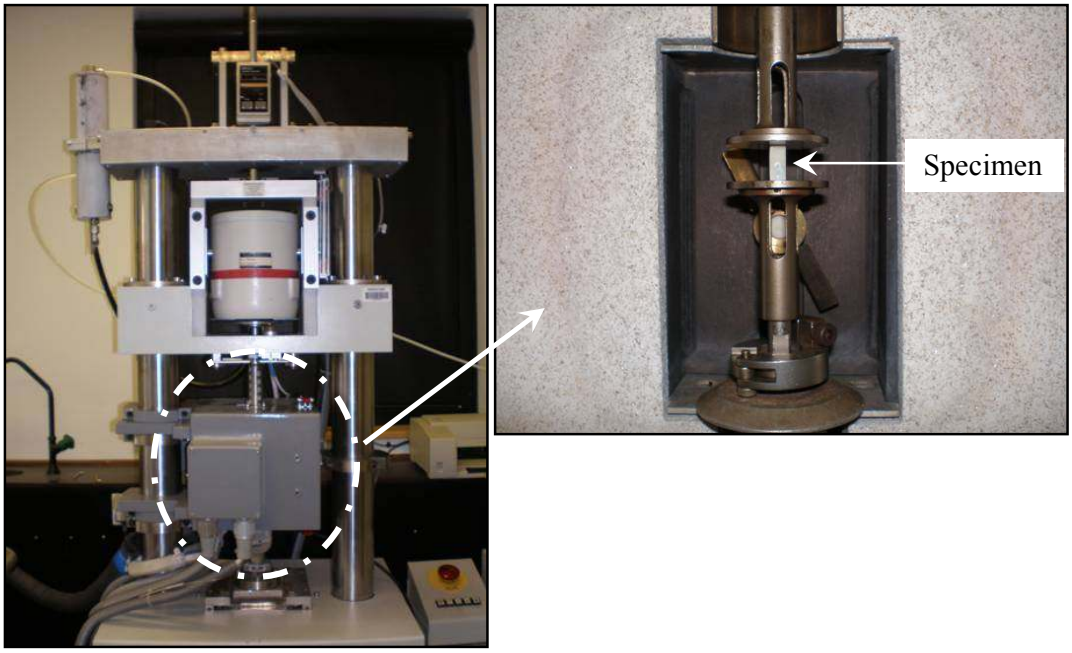

Figure 5.3 – DMTA (Gabo Qualimeter GmbH, Germany) with close-up of the incorporated measurement system

DMTA is a measurement of the dynamic moduli (in phase and out of phase) in an oscillatory mechanical deformation experiment during a programmed temperature scan at controlled frequency. The peak of the tan δ (see Equation 5.1) is a discriminatory measure of the T_g, although this is the centre of the relaxation [159,160]. In the MDSC (modulated differential scanning calorimetry) experiments the T_g is reported as the onset temperature of the relaxation. In such a case the MDSC T_g will be lower than that for DMTA by an amount that varies with the specific polymer [161,162].

$$\tan\delta = \frac{energy\,lost}{energy\,stored}\,per\,cycle \quad \text{..... (5.1)}$$

The test also eliminates any residual reactivity in the specimens which could hinder the T_g measurement. Cooling and reheating cycles are useful as any shift in the peak and decrease of the peak height shows that initially the material was not fully cured and has enhanced crosslinking. The T_g obtained from the second DMTA cycle is representative of the fully cured state of the material ($T_{g\infty}$) whilst in the MDSC (modulated differential scanning calorimetry) experiments the T_g is reported as the current state of the material.

The measurements for the adhesives formulations were carried out at a heating rate of 2K/min in the temperature range from 100 to 200ºC. The measurement frequency used was 10 Hz. Cooling and reheating cycles were used in order to remove residual reactivity in the polymer, and values of the $T_{g\infty}$ were obtained from repeat cycles as the maximum point on the tan δ curve (see Figure 5.4).

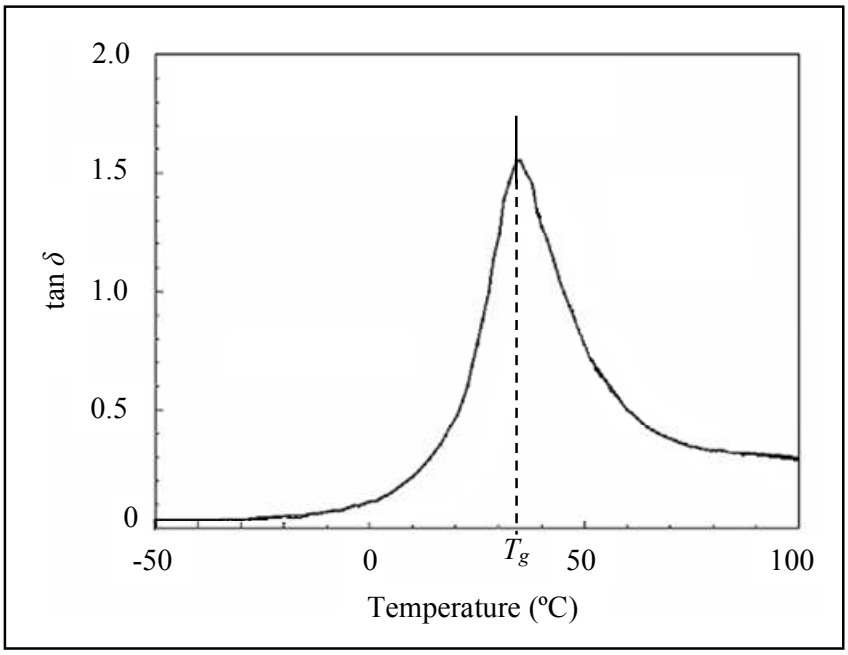

Figure 5.4 – Determination of the T_g from the tan δ vs. temperature curve (schematic)

5.2.2 Determination of CTE by TMA

The coefficient of thermal expansion (CTE) of the cast adhesive samples was measured using a thermal mechanical analyser (TMA) which measures dimensional changes in the sample length caused by the temperature variations (see Figure 5.5).

Good temperature control can be achieved in the -50 to +135ºC temperature range using a mechanical cooling accessory (low heat sink) and the TMA furnace (variable heat sink) [163,164]. The TMA has an accuracy of 1 μm. The sample length (measured automatically by the machine before each test) has an accuracy of 0.01 μm. The stand on which the samples are placed and the measurement probe are made of quartz with a known CTE around zero [163].

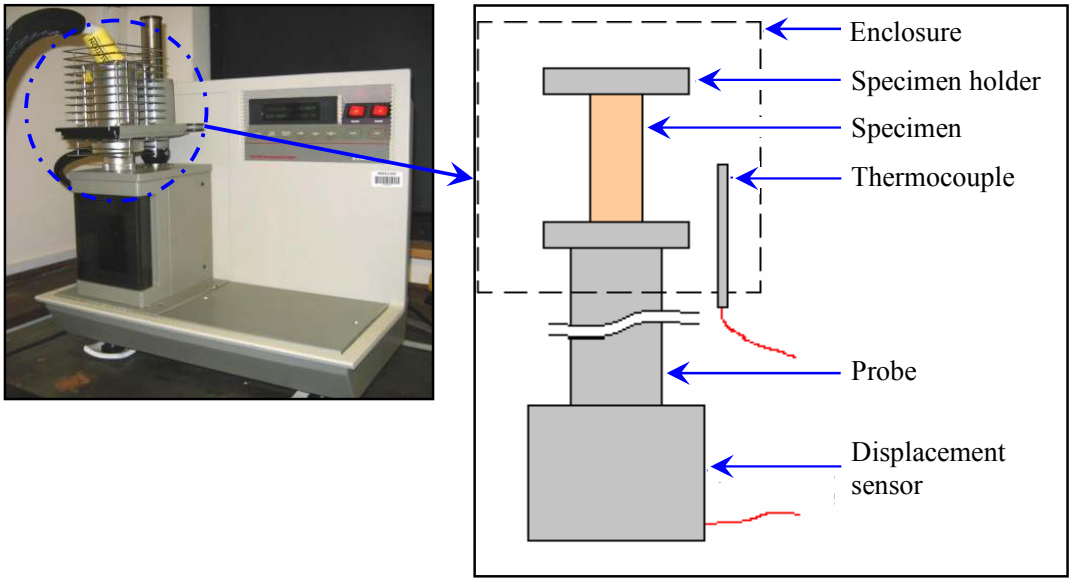

Figure 5.5 – TMA (TA Instruments 2940) with details of the enclosed measurement system

Thermo-mechanical tests were performed according to the principles stated in test standard ISO 11359-2:1999 [165]. After placing the specimen in the cell the linear dimension of the sample was monitored between -50ºC and 100ºC at a heating rate of 1K/min. Initial cooling and reheating cycles were used in order to remove residual stresses in the polymer, the thermal expansion coefficients were obtained from repeat cycles.

From typical TMA plots of temperature vs. specimen length (see Figure 5.6) the mean coefficient of linear thermal expansion (α) in reciprocal Kelvin (K^{-1}), between two temperatures T_1 and T_2, can be obtained from the following equation:

$$\alpha = \frac{\Delta l}{\Delta T} \times \frac{1}{l_0} \quad \text{..... (5.2)}$$

Where:

l_0 is the length of the specimen, in μm, at room temperature

Δl is the difference in length, in μm

$\Delta T = (T_2 - T_1)$ is the temperature difference, in K

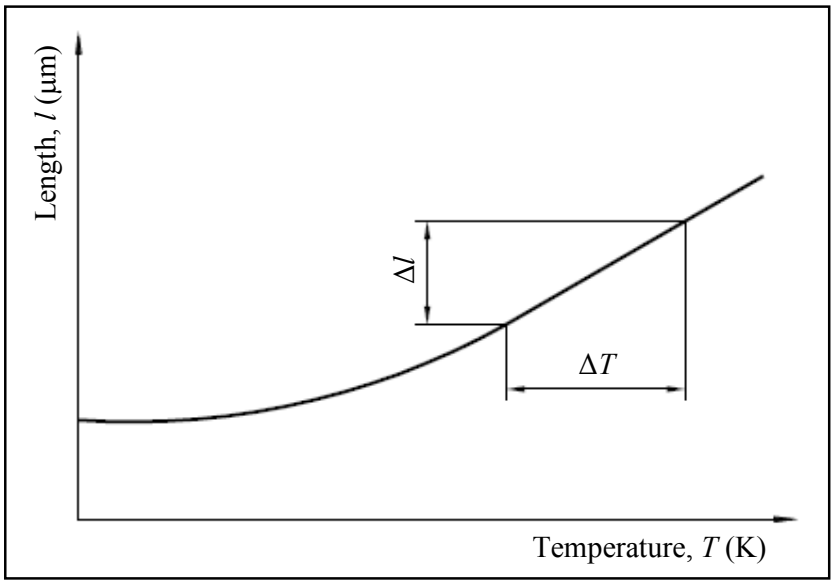

Figure 5.6 – Determination of the mean coefficient of linear thermal expansion *α*

5.2.3 Fracture testing: determination of K_{IC} and G_{IC}

The purpose of carrying out fracture tests on single edge-notched bending (SENB) specimens was to determine the fracture toughness (K_{IC}) and fracture energy (G_{IC}) of the adhesive formulations created in the present work. The test procedure followed here was ISO 13586:2000 [145] which uses the linear elastic fracture mechanics (LEFM) approach.

A displacement controlled Instron 5500R universal testing machine equipped with a 5 kN load cell was used to load the specimens at a speed of 10 mm/min. The specimens were placed on support rollers, set at a span of four times greater than the specimen width, equidistant from a central loading roller. Figure 5.7 shows the configuration for the fracture test.

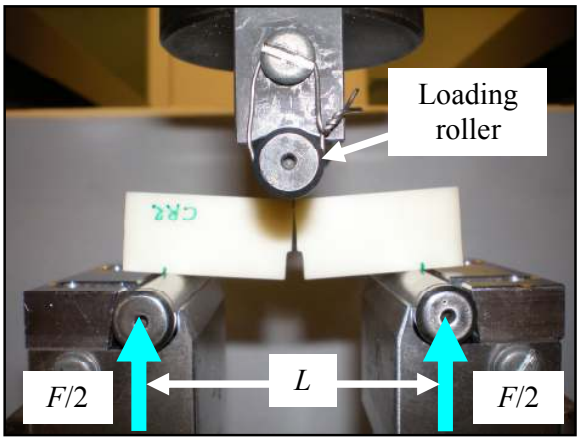

Figure 5.7 – Three point loading arrangement at the end of fracture testing

The vertical distance between the loading and support rollers was reduced until fracture of the specimen occurred. A plot of force vs. displacement is obtained from the test. Displacement was recorded from the test machine crosshead (accurate to ±0.5%). Force was measured directly from the load-cell. The maximum loading, F_{max} was noted for each formulation tested.

After testing all the specimens of one adhesive formulation an 'indentation correction' for the material was measured to correct the analysis. This correction factor accounts for the indentation of the rollers in the specimen during the test. A broken half specimen was placed in the test jig using a zero span width. The test was carried out at the same loading rate, 10 mm/min, but was stopped at a predetermined load, 50% greater than the highest load achieved for the adhesive formulation under the fracture test. In an ideal case, the plot of force vs. displacement would produce a linear response with the indentation correction being the compliance (the displacement-force gradient). However, the additional compliance of the test machine and non-ideal behaviour of the

specimen typically result in a curve similar to as shown in Figure 5.8. The slope of the response corresponding to F_{max} was used for the indentation correction.

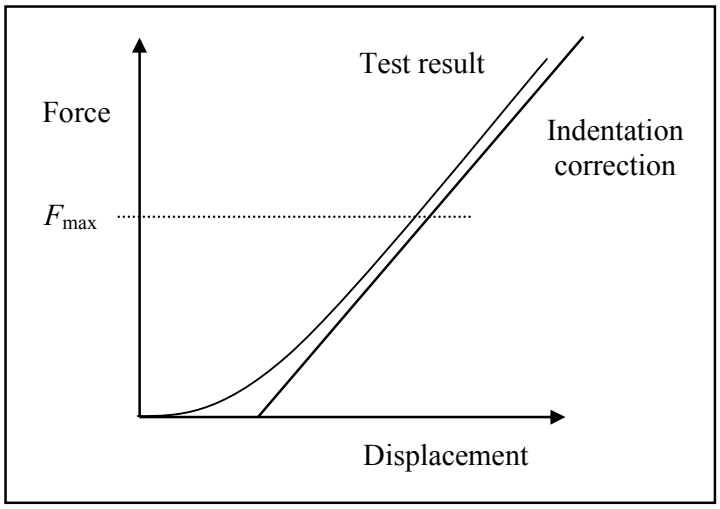

Figure 5.8 – Calculation of indentation correction

The notch depth or crack length (a) can only be measured accurately after fracture of the specimen, using a travelling microscope. The portion of the notch produced with the razor is usually quite apparent, displaying a smooth, glassy surface in comparison to the rougher machine notched area. The fracture surface contains additional features which distinguish it from the razor notched area (see Figure 5.9).

The next step was to calculate the applied force at the initiation of crack growth (F_Q) which is dependent on the fracture behaviour of the material. Brittle fracture of the specimens occurred and the force vs. displacement curves were linear, with an abrupt drop in the force at the instant of crack growth initiation. Therefore, F_Q was identified with the maximum force (see Figure 5.10). The deformation factor, C_Q, is the reciprocal of the force vs. displacement slope.

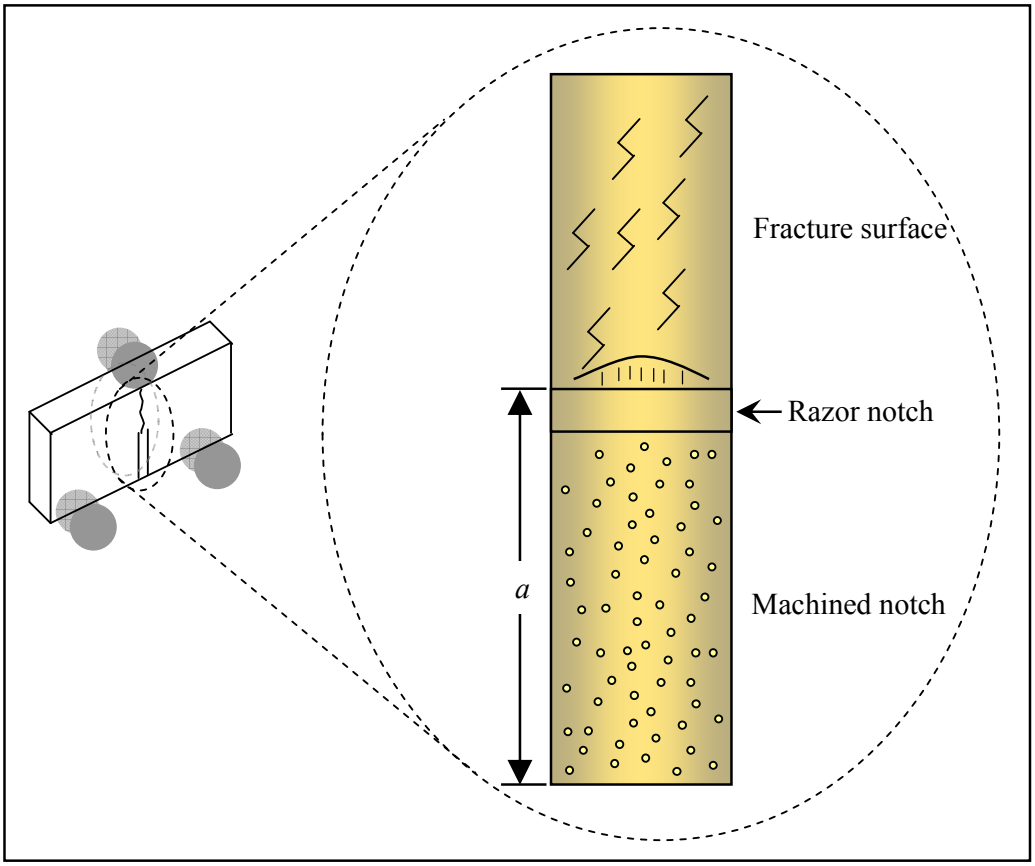

Figure 5.9 – Use of travelling microscope to determine notch depth

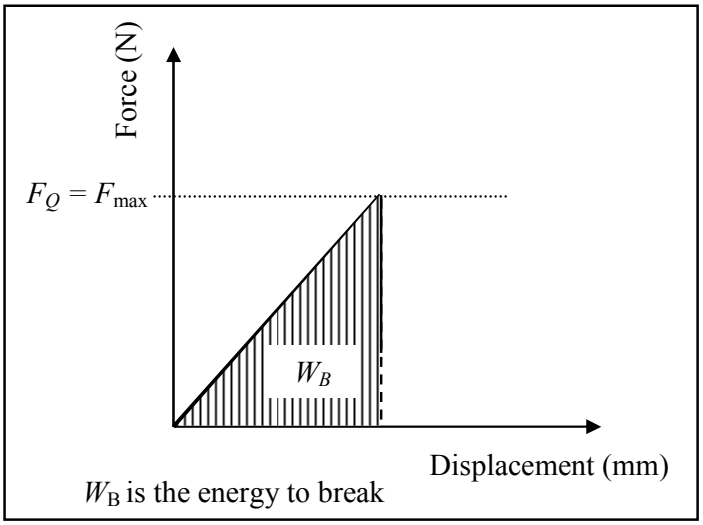

Figure 5.10 – Force vs. displacement curve for a notched test specimen

The analysis of the test data includes the following correction factors which are detailed fully in Appendix A, both depending on the crack length, a and the specimen width, w:

- Energy calibration factor ($\phi(a/w)$)
- Geometry calibration factor (f(a/w))

To calculate the critical energy release rate (G_{IC}) from the energy up to the initiation of crack growth the following equation is used:

$$G_{IC} = \frac{W_B}{hw\phi} \quad \text{..... (5.3)}$$

Where:

W_B is the energy to break, in J

h is the specimen thickness, in m

w is the specimen width, in m

To calculate the critical stress intensity factor K_{IC} from the force F_Q at crack growth initiation and the original crack length a:

$$K_{IC} = f\frac{F_Q}{h\sqrt{w}} \quad \text{..... (5.4)}$$

Where:

F_Q is the force at crack growth initiation, in N

5.2.4 Flexure testing: determination of E_f

Cast specimens for the four adhesive formulations in the present work were subjected to the three point bend (3PB) test in order to obtain the flexural modulus (E_f) according to test standard ISO 178:2003 [147].

A displacement controlled Instron 5500R universal testing machine equipped with a 5 kN load cell was used to load the three point bend specimens at a speed of 1 mm/min. The span to thickness ratio (L / h) was set at 16 for all the formulations. The mid-span

deflection was recorded from the test machine crosshead displacement (accurate to ±0.5%). Figure 5.11 shows the configuration for the 3 point bend test.

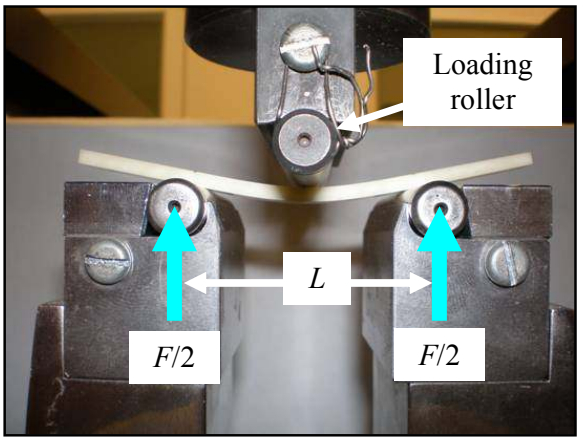

Figure 5.11 – Three point loading arrangement at the end of flexure testing

From the test, a plot of force vs. deflection is obtained. The linear gradient of this plot ($\Delta F/\Delta s$) expressed in N/mm, taken between 5 and 25% flexural strain, is used to obtain the material flexural modulus.

$$E_f = \frac{L^3}{4wh^3}\left(\frac{\Delta F}{\Delta s}\right) \quad \text{..... (5.5)}$$

Where:

E_f	is the flexural modulus of elasticity, in MPa
L	is the span, in mm
w	is the specimen width, in mm
h	is the specimen thickness, in mm
s	is the displacement, in mm

The specimens were not tested until failure, only until sufficient data points were recorded to capture the 25% flexural strain value.

5.2.5 Compressive test: determination of σ_{yc}

The uniaxial compression test was used to determine the yield stress under compression, (σ_{yc}) of the adhesive formulations according to test standard ISO 604:2003 [148].

The compression test fixture used was a 10 kN rated Instron compression cage. This test jig is self aligning in that it is loaded in tension, compressing the specimens between two parallel plate faces as shown in Figure 5.12. No lubricating agent was used on the specimen surfaces.

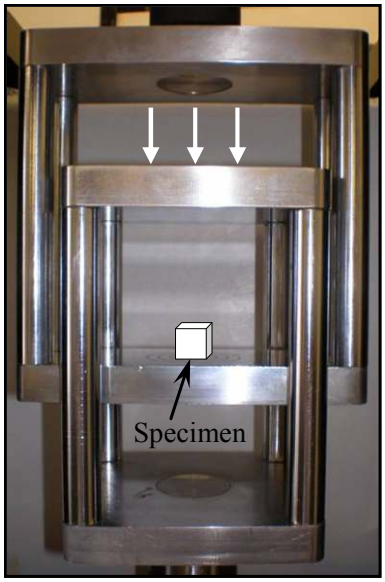

Figure 5.12 – Compression arrangement by using the compression cage

The test was carried out with the compression cage mounted on an Instron 5500R displacement controlled test machine equipped with a 5 kN load cell. The test specimens were compressed along the major axis at constant speed of 0.6 mm/min until yielding was observed. For all tests the force and sliding displacement were recorded from the load cell and the test machine crosshead (accurate to ±0.5%) respectively.

The compressive stress (σ_c) was calculated with the following equation:

$$\sigma_c = \frac{F}{A} \quad \text{..... (5.6)}$$

Where:

F is the force, in N

A is the initial cross-sectional area of the specimen, in mm^2

The compressive strains, ε_c, were obtained using the following equation:

$$\varepsilon_c = \frac{\Delta L_0}{L_0} \quad \text{..... (5.7)}$$

Where:

ε_c is the compressive strain

L_0 is the gauge length of the test specimen, in mm

ΔL_0 is the decrease in the specimen length between the gauge marks, in mm

Figure 5.13 shows the typical stress vs. strain curve obtained from compressive test. The following are the parameters included in the interpretation of the curve:

σ_{yc} is the first stress at which an increase in strain occurs without an increase in stress, in MPa

ε_{yc} is the strain corresponding to the compressive stress at yield, in %

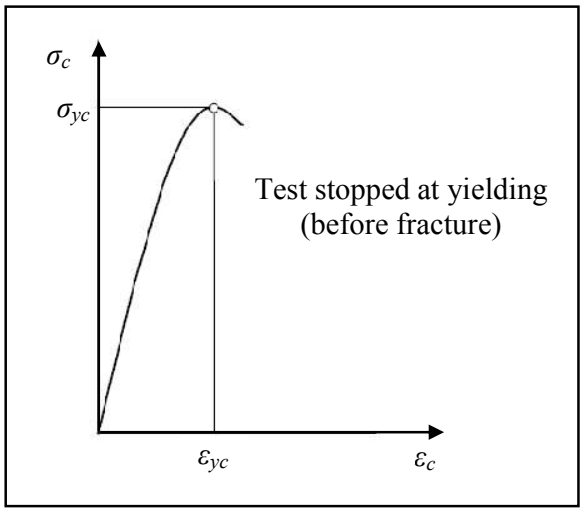

Figure 5.13 – Typical stress vs. strain curves for compression

The σ_{yc} values of the adhesive formulations were taken from the stress vs. strain curves, as shown in Figure 5.13.

5.2.6 Electrical conductivity measurement

DC electrical resistivity was obtained from cast samples according to the principles stated in ASTM standard D-4496:2004 [149]. Figure 5.14 shows the in-house setup used to perform the measurements.

The specimen is placed between the copper blocks in contact with its silver coated surfaces. Electrodes are connected to the copper blocks and Kapton layers are used to isolate the blocks from the rest of the apparatus. Kapton is a polyimide film developed by DuPont and is widely used as an insulator material [166]. Direct current (DC) voltage is applied across the electrodes and resistance measurements are taken.

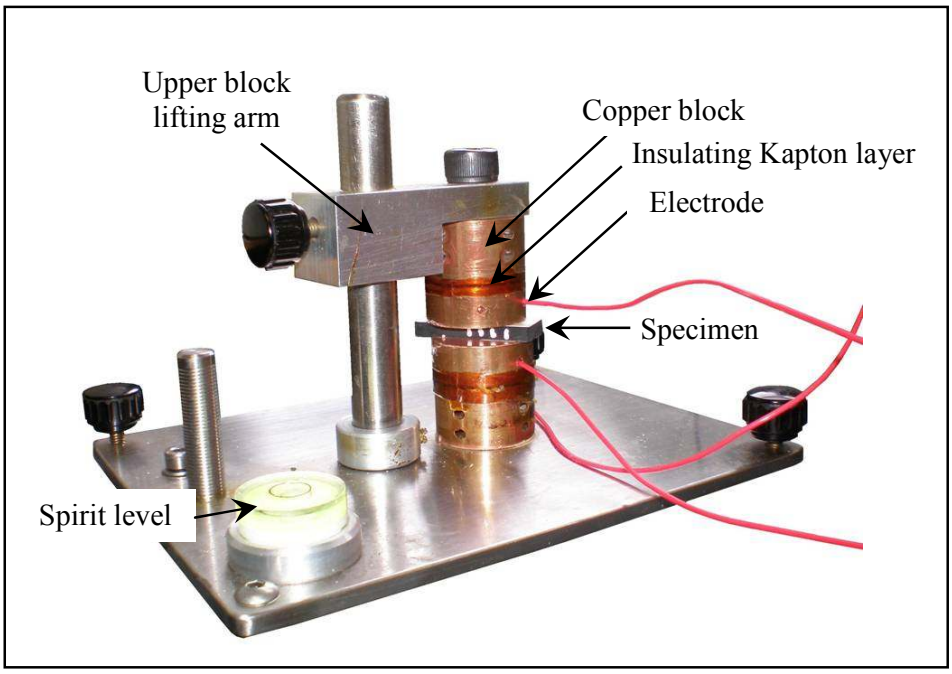

Figure 5.14 – In-house setup for DC conductivity measurements

The resistance measurements for the adhesive formulations C and CR were performed using a Keithley 6517A electrometer [167] with a measuring range of 1 MΩ to 210 TΩ. The resistance of the formulations containing carbon nanotubes, CN and CRN, were obtained using a combination of a Keithley 6220 DC precision current source and a Keithley 2182A nano-voltmeter [168] appropriate for a lower resistance range (10 nΩ to 1 GΩ).

The data acquisition was carried out for 1 minute of voltage application. The electrical conductivity of the material (σ) was calculated from the following equation:

$$\sigma = \frac{l}{AR} \quad \text{..... (5.8)}$$

Where:

R is the measured resistance, in Ω·m

l is the sample length, in m

A is the sample cross-sectional area, in m^2

The AC electrical response of the materials was investigated using a Solartron SI 1260 frequency response analyser [169]. Twenty seven frequencies in the 1 Hz to 3.16 MHz range were swept on a logarithmic scale using an excitation voltage of 1 V. The conductivity was calculated as follows:

$$\sigma(f) = \frac{h}{\left|Z^*(f)\right| A} \quad \text{..... (5.9)}$$

Where:

f is the frequency, in Hz

h is the sample thickness, in m

A is the sample cross-sectional area, in m^2

$Z^*(f)$ is the complex impedance, in Ω

5.3 Adhesive characterization: bonded specimens

5.3.1 Flexure testing

The UD E-glass / 913 epoxy pre-preg material used as a substrate for bonded specimens was subjected to a three point bend test, as previously described in Section 5.2.4, in order to obtain the flexural modulus which was required to be used in the DCB and ELS

test analyses described in this section. The test procedure followed here was ISO 14125:1998 [170], specifically for fibre-reinforced plastic composites.

A displacement controlled Instron 5500R universal testing machine equipped with a 5 kN load cell was used to load the 3 point bend specimens at a speed of 2 mm/min. The specimens were placed on support rollers set at a span of 80 mm equidistant from a central loading roller. The testing procedure and analysis of results are similar to those explained in Section 5.2.4.

5.3.2 Mode I: Double cantilever beam (DCB) tests

DCB tests were performed on adhesively bonded specimens manufactured using both GFRP and aluminium alloy substrates, as detailed in Chapter 4. The tests were carried out in order to measure the mode I adhesive fracture energy, G_{IC}, by using the standard BS 7991:2001 [171].

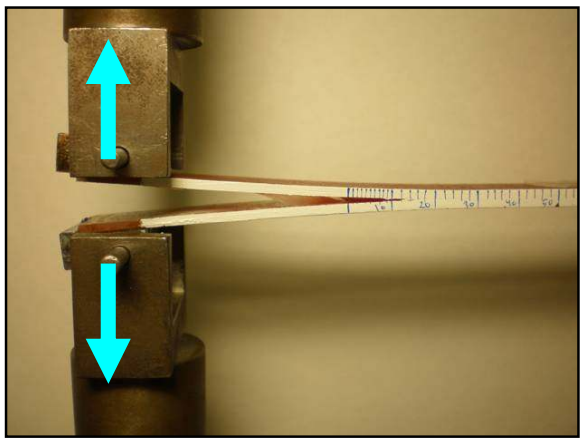

Figure 5.15 – DCB test arrangement

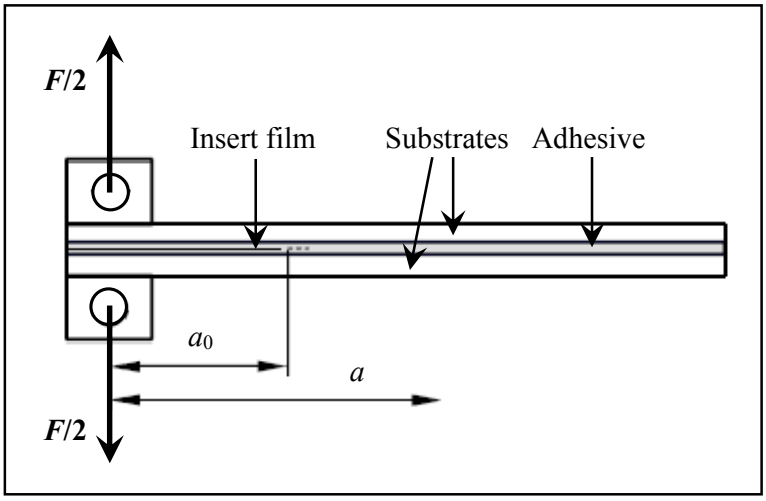

Figure 5.16 – GFRP DCB specimen arrangement with bonded loading blocks

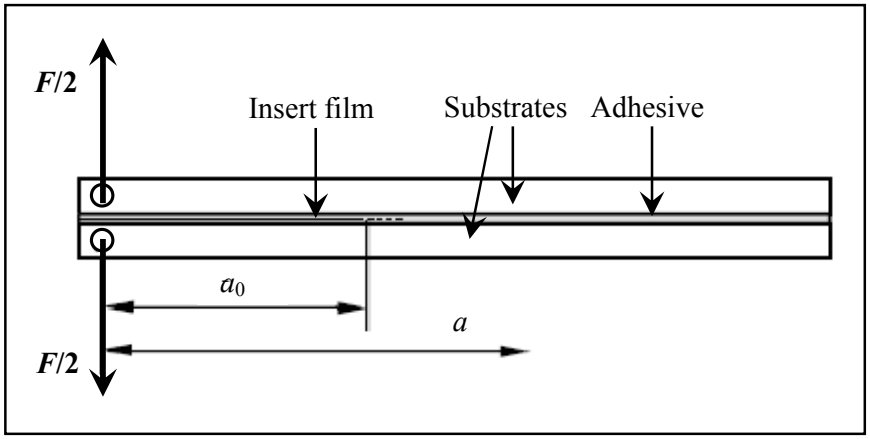

Figure 5.17 – Aluminium alloy DCB specimen with loading holes drilled through the loading arms

Before testing, the specimens were coated on one side with white correction fluid onto which millimetre increments were drawn. This was done to allow the crack tip position to be monitored.

The specimen is then loaded in the testing machine. The GFRP specimen was loaded via two pin-loaded load blocks bonded to the specimen as shown in Figure 5.16. The aluminium alloy specimen was loaded via two pin-loaded load holes drilled through the specimen as shown in Figure 5.17. The testing machine used was a Zwick Z010 screw driven, displacement controlled test machine equipped with a 2 kN load cell.

The specimens were manufactured to include a thin, 13 μm PTFE insert film to simulate an existing crack in the material. Every specimen was tested first to advance this manufactured crack tip a few millimetres further into the material. This pre-cracking step is important to ensure that initiation data gathered upon loading in the real test is generated from within the material itself and not from, or a function of, the insert film. The position of the crack tip at this point is designated a_0 [172]. This pre-cracking test was performed at a speed of 0.4 mm/min. Afterwards the machine was unloaded and the real test performed at the same testing speed, 0.4 mm/min.

The position of the crack tip was relatively easy to monitor. As the specimen deformed, the position of the crack tip, the load and the loading point deflection were recorded at regular intervals, usually about every 2 mm. The data acquisition system was triggered to plot markers on the load vs. deflection response curve when the crack tip passed the increments drawn on the specimen. An example material response curve is shown in Figure 5.18. The crack tip positions are noted and related to the corresponding markers on the response curve upon completion of the test.

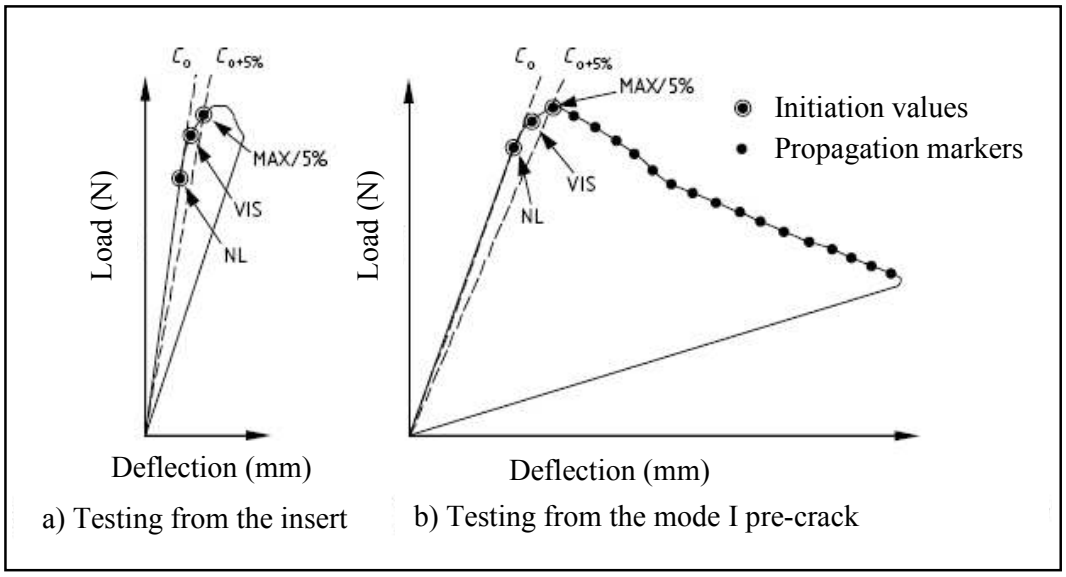

Figure 5.18 – Typical DCB test load vs. deflection curves testing from the insert and from the mode I pre-crack

Data reduction of the load, deflection (measured from the test machine crosshead displacement to ±2 μm accuracy) and crack length data allows a mode I material

resistance curve (or R-curve) to be drawn. A mode I R-curve is a measure of the adhesive's apparent mode I fracture energy (G_{IC}) plotted against crack length (a). Three different analyses exist for calculating G_{IC}, a sign of the development of the DCB test for adhesives in the recent past [173-175].

The corrected beam theory (CBT) [151] was the analysis selected for the present work. This analysis includes certain correction factors which are detailed fully in Appendix B and account for the following:

- Crack length correction (Δ) – extends beam theory approach to apply for a specimen that is not perfectly built-in
- Large deflection correction (F) – extends beam theory approach to apply for large specimen deflections
- Load block correction (N) – takes account of the local stiffening effect of the load block on the specimen

The CBT method is expressed as follows:

$$G_{IC} = \frac{3P\delta}{2b\left(a+\left|\Delta\right|\right)}\frac{F}{N} \quad if\ load-blocks \qquad (5.10)$$

$$G_{IC} = \frac{3P\delta}{2b\left(a+\left|\Delta\right|\right)}F \quad if\ drilled\ holes \qquad (5.11)$$

Where:

δ	is the measured deflection, in mm
a	is the crack length, in mm
P	is the load corresponding to each delamination length, in N
b	is the specimen width, in mm

5.3.3 Mode II: End loaded split (ELS) test

ELS tests were performed on bonded specimens manufactured from GFRP pre-preg system detailed in Chapter 4 in order to measure the mode II adhesive fracture energy, G_{IIC}. A Zwick Z010 screw driven, displacement controlled test machine equipped with

a 2 kN load cell was used to perform mode II testing. The rig used is shown in Figure 5.19.

To date, no standard test has been agreed on for mode II testing of fibre-reinforced composites. The ESIS TC4 protocol [176] describes the ELS test method followed here.

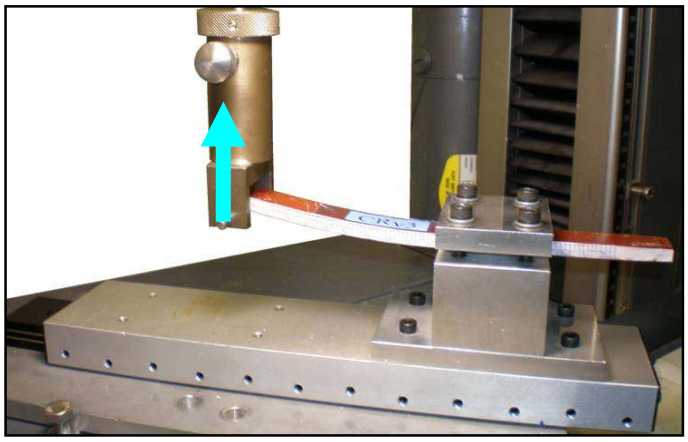

Figure 5.19 – ELS test arrangement

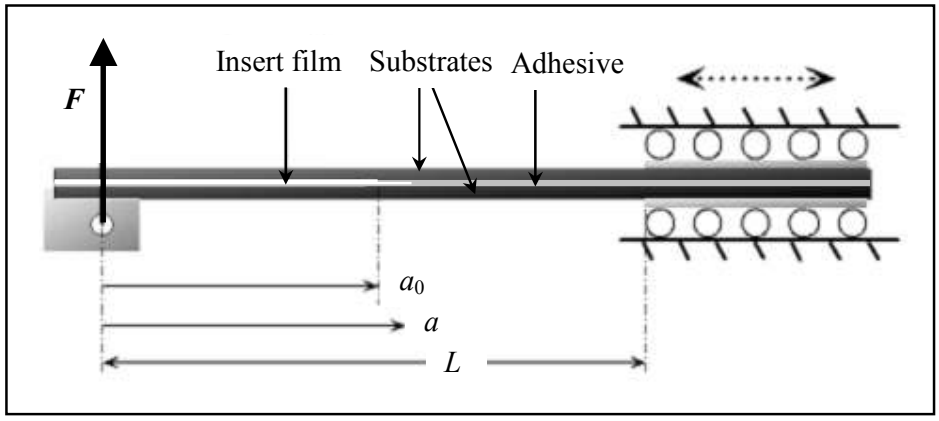

Figure 5.20 – ELS test arrangement diagram

Before testing, the specimens were coated on one side with white correction fluid onto which millimetre increments were drawn. This was done to allow the crack tip position to be monitored. The specimens were manufactured to include a thin, 13 μm PTFE insert film to simulate an existing crack in the material. Every specimen was tested first in mode I to advance this manufactured crack tip a few millimetres further into the material. This pre-cracking step is important to ensure that initiation data gathered upon

loading in the real test is generated from within the material itself and not from, or a function of, the insert film. The position of the crack tip at this point is designated a_0 [172,177].

Prior to testing a calibration procedure was performed. This procedure allows the sliding displacement of the ELS fixture to be accounted for in the analysis. The specimen is clamped, with the insert film at the clamp end (opposite to as shown in Figure 5.19), at 10 mm intervals between span lengths of 110 mm and 50 mm. For each of these seven span lengths the specimen is loaded to 250 N and the deflection measured.

The specimen is then clamped at one end as shown in Figure 5.20 so that only horizontal motion is permitted. The opposite end of the specimen is loaded via a pin-loaded load block bonded to the specimen. The test was performed at a speed of 0.4 mm/min.

The position of the crack tip was particularly difficult to monitor. As in the case of mode I measurements, as the specimen deformed, the position of the crack tip, the load and the loading point deflection were recorded at regular intervals, usually about every 2 mm. The data acquisition system was triggered to plot markers on the load vs. deflection response curve when the crack tip passed the increments drawn on the specimen. An example material response curve is shown in Figure 5.21. The crack tip positions are noted and related to the corresponding markers on the response curve upon completion of the test.

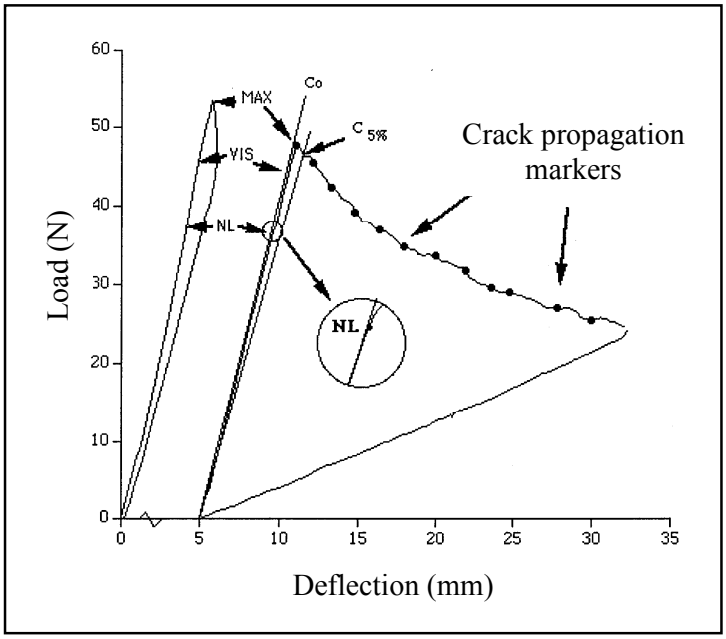

Figure 5.21 – A typical ELS test load vs. deflection curve with crack propagation markers

Data reduction of the load, deflection (measured from the test machine crosshead displacement to ±2 μm accuracy) and crack length data allows a mode II material resistance curve (or R-curve) to be drawn. This mode II R-curve plots the adhesive's apparent mode II fracture energy (G_{IIC}) against crack length (a). Four different analyses exist for calculating G_{IIC} [152,178-180].

The corrected beam theory with effective crack length (CBTE) [152] was the analysis selected for the present work. This analysis includes certain correction factors which are detailed fully in Appendix C and account for the following:

- Delamination length correction (Δ_{II}) – takes account of crack tip rotation
- Large deflection correction (F) – extends beam theory approach to apply for large specimen deflections
- Load block correction (N) – takes account of the local stiffening effect of the load block on the specimen
- Clamping correction (Δ_{clamp}) – updates the specimen span length (L) to take account of the clamping fixture movement

The CBTE method is expressed as follows:

$$G_{IIC} = \frac{9P^2 a_c^2}{4E_f b^2 \left(h/2\right)^3} F \quad \text{..... (5.12)}$$

Where:

E_f is the material flexural modulus, in MPa

a_c is the calculated crack length, in mm

P is the load for each calculated crack length, in N

h is the specimen thickness, in mm

5.3.4 Fatigue delamination test

A fatigue test was performed on the bonded crack retarder structure, detailed in Chapter 4, in order to examine the effects of the GFRP straps plus CRN adhesive on the fatigue life of the structure. The test procedure followed here for measurement of fatigue crack growth rates was ASTM E 647-2000 [181].

Prior to testing, the two bonded GFRP straps were ultrasonically scanned for defects within the strap / adhesive interface. The regions of the straps still attached to the aluminium alloy plate would be scanned again after completion of the test for comparison in order to identify the fatigue propagated delamination. The scanning equipment used was an Olympus OmniScan® MX (see Figure 5.22).

Figure 5.22 – Olympus OmniScan® MX with the phased array (PA) module

Two pairs of probes were attached to the specimen to allow the measurement of the crack growth by an automatic electro-potential drop method as shown in Figure 5.24 [182,183]. One pair of probes was attached to the aluminium alloy plate either side of the machined notch, one on the front of the plate and the other on the rear (see Figure 5.23). The rear of the plate was scribed every 1 mm in the region of the pre-crack and every 5 mm thereafter. This was done to allow the crack tip position to be monitored visually. The second pair of probes was connected to the top edge of the aluminium alloy substrate.

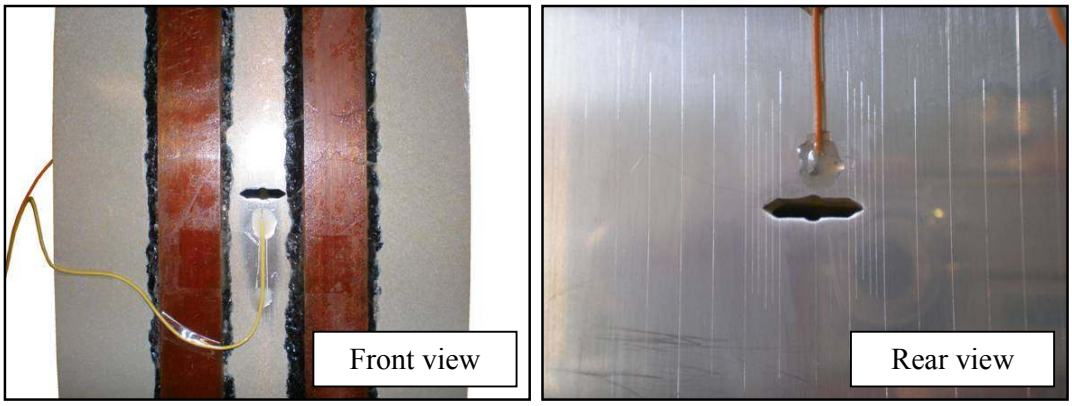

Figure 5.23 – Probes attached to the crack horizontal centreline

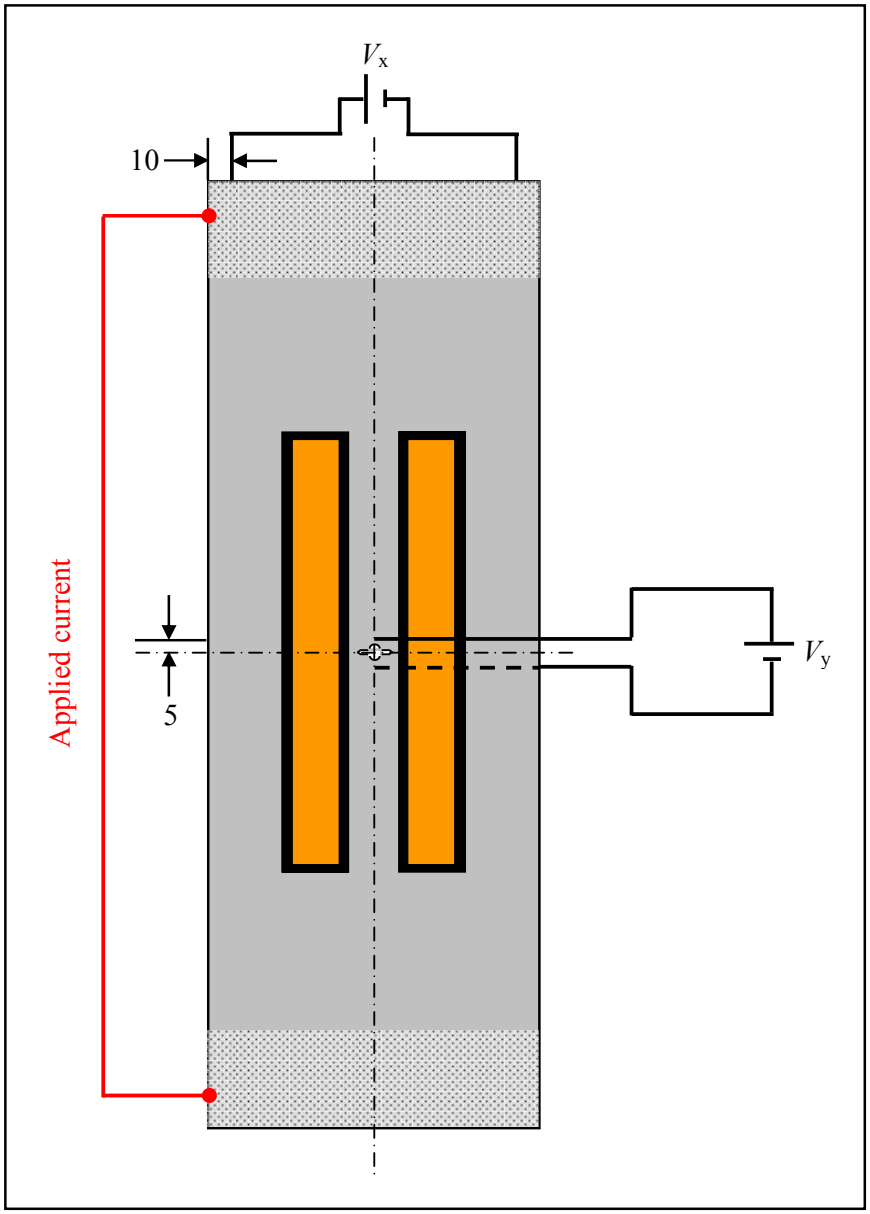

Figure 5.24 – Schematic representation of the experimental setup (Electrical potential technique)

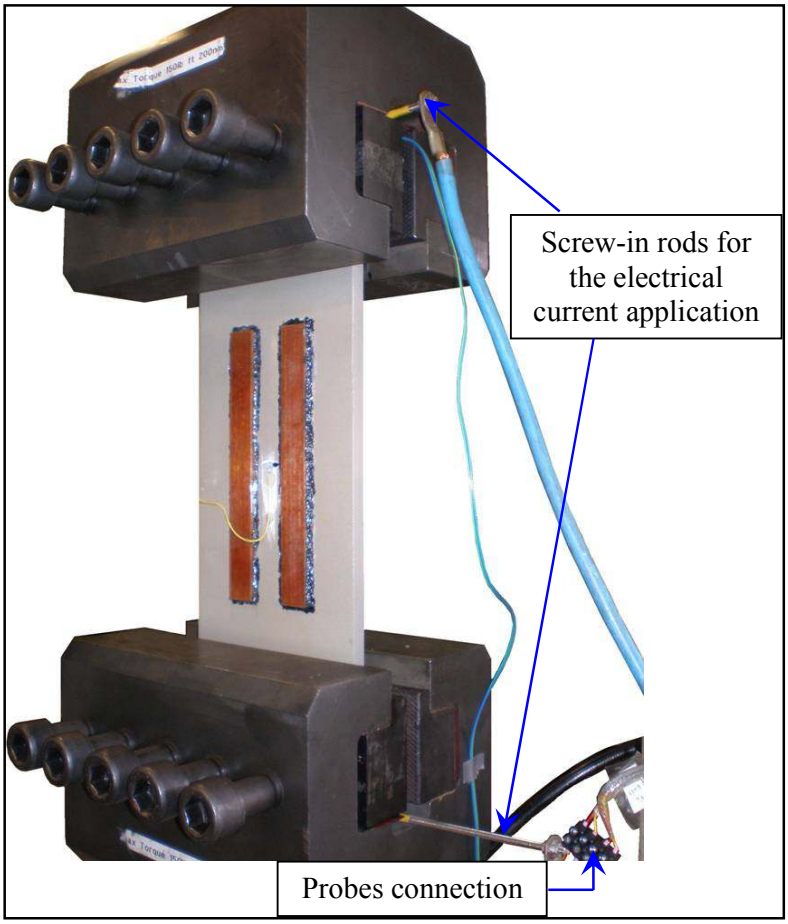

Figure 5.25 – Fatigue test arrangement

The specimen is then clamped as shown in Figure 5.25 in a computer controlled Instron 8500 servo-hydraulic test machine with a capacity of 250 kN.

A pair of steel threaded rods was screwed inside two holes deliberately drilled in the upper and bottom sides of the specimen (see Chapter 4). These rods were used for the application of the electrical current required for the electrical drop potential procedure. The specimen was then clamped in the grips of the test machine, at so as to keep the length / width ratio equal 1.95.

Prior to testing the specimen was pre-cracked by fatigue loading the structure until a crack ($\alpha_{pre\text{-}cracking}$) of 2.5 mm length was observed beyond the tip of the machined central notch (see Figure 5.26).

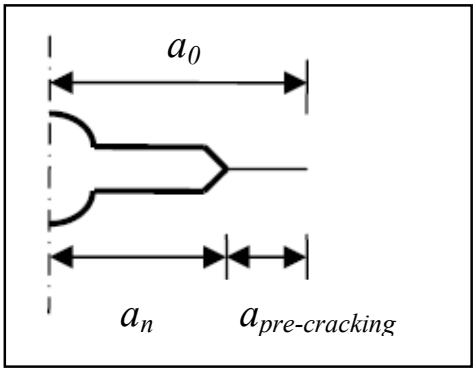

Figure 5.26 – Pre-cracking length for the fatigue test

Further crack growth was measured using the electrical potential drop technique. In this technique a constant direct current (DC) was applied at the top and bottom of the specimen. As the crack grows the electrical potential drops as a consequence of the modification of the electrical field at the crack plane. This change in potential was measured by the two probes attached at the crack region and by the two probes attached to the top edge of the specimen (see Figure 5.24) and are related to crack size through an analytical calibration relationship. The equipment used to apply the current and measure the voltage is shown in Figure 5.27.

Figure 5.27 – Xantrex XPD Programmable DC Power Supply and Keithley 2000 Multimeter

The fatigue test was carried out at constant amplitude cyclic loading of 37.8 kN, with a loading stress ratio (R) of 0.1 and a frequency of 10 Hz. The maximum applied load was 84 kN and the corresponding mean applied load (set point) 46.2 kN. Therefore, the resulting maximum remote applied stress for the specimen cross section was 60 MPa.

The data collected and stored for each test were as follows:

- The total number of fatigue cycles (N)
- The measured voltage values of the potential field distributed through the specimen
- The crack length corresponding to these voltage values, as measured using the electro-potential drop method

The crack length measurements were then converted into crack growth rate and fatigue life [23-25,182,183]. Fatigue life is considered here as the point at which ultimate failure of the structure occurs.

Summary

All the test methodologies used in this work have been presented. The first part of the chapter has detailed the experiments used to characterise the cast adhesive formulations. The second part detailed the tests which have been carried out on bonded specimens. The final part of the chapter has introduced the fatigue testing performed and its background as developed through the Bonded Crack Retarders project.

Chapter 6

Characterisation of ternary resin blends

This chapter focuses on the description of the microstructures of the cured adhesive blends and their thermo-mechanical, mechanical and electrical properties in the solid state. The analysis of the different blends will clarify the contribution of each constituent to the novel adhesive formulation. The chemical cure kinetics of the adhesive blends is also analysed.

6.1 Cure study of the resin blends

6.1.1 Effect of carbon nanotube addition on CRN cure

Dynamic and isothermal cure experiments on the CR and the CRN formulations were carried out to study the effect of the addition of the carbon nanotubes. The dynamic cure experiments were conducted at a heating rate of 2.5ºC/min from 25ºC up to 300ºC where the material was fully cured. Figure 6.1 shows the dynamic curves obtained for these two formulations.

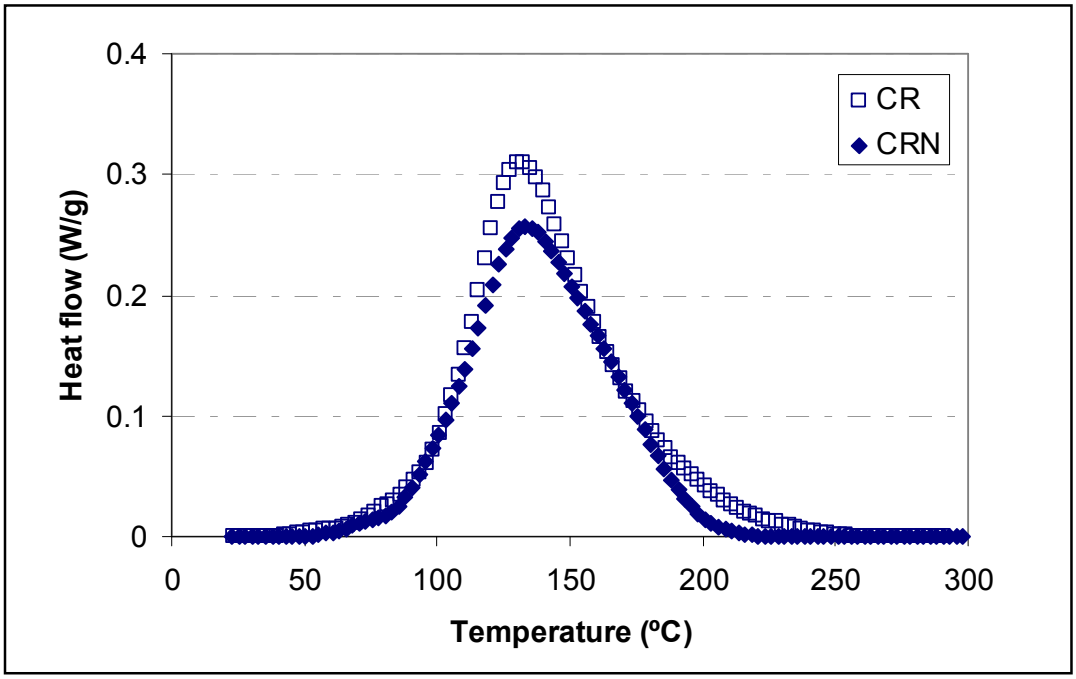

Figure 6.1 – Heat flow vs. temperature for the dynamic cure of the CR and the CRN formulations

The total enthalpy of the curing reaction (measured by integrating the area under the heat flow vs. temperature curve) was 449 J/g and 380 J/g for the CR and the CRN formulations respectively. These values indicate lower crosslinking density of the thermoset system containing carbon nanotubes than the control. A single exothermic peak occurred in both dynamic cure experiments. The peak shifts 3ºC to the right when the carbon nanotubes are incorporated in the formulation. This trend is in agreement with reported trends of similar epoxy resins containing carbon nanotubes [106].

The isothermal cure experiments were conducted at 120ºC. This temperature was selected as it was the cure temperature for all the resin blends in this work (see Section 4.2.4). The experimental procedures consisted of three segments; a heating rate of 20ºC/min from 25ºC up to 120ºC, a dwell period of around one minute to equilibrate the samples at temperature and finally an isothermal period of around 110 minutes to complete the cure of the samples under these conditions. Figure 6.2 shows a comparison of the isothermal curves obtained for the two formulations, CR and CRN. Time zero is taken at the moment when the samples reached 120ºC. In these isothermal conditions the peak of the reaction occurs slightly later in the CR formulation than in the carbon nanotubes containing formulation, CRN.

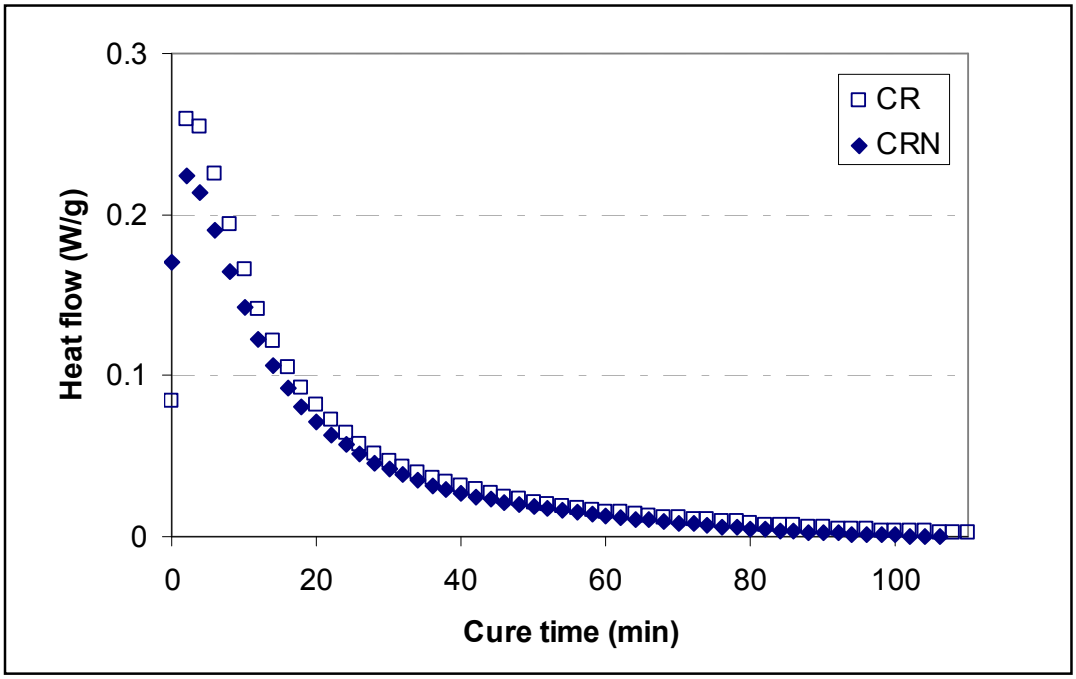

Figure 6.2 – Heat flow vs. cure time for the CR and CRN formulations at 120ºC

Figure 6.3 shows the degree of cure, attained for the CR and the CRN formulations during the isothermal cure at 120ºC. Final conversions after 100 minutes of isothermal cure were 0.73 and 0.75 for the CR and the CRN respectively which suggest that the presence of carbon nanotubes, at this 120ºC isothermal cure temperature, has no significant effect on the maximum degree of cure.

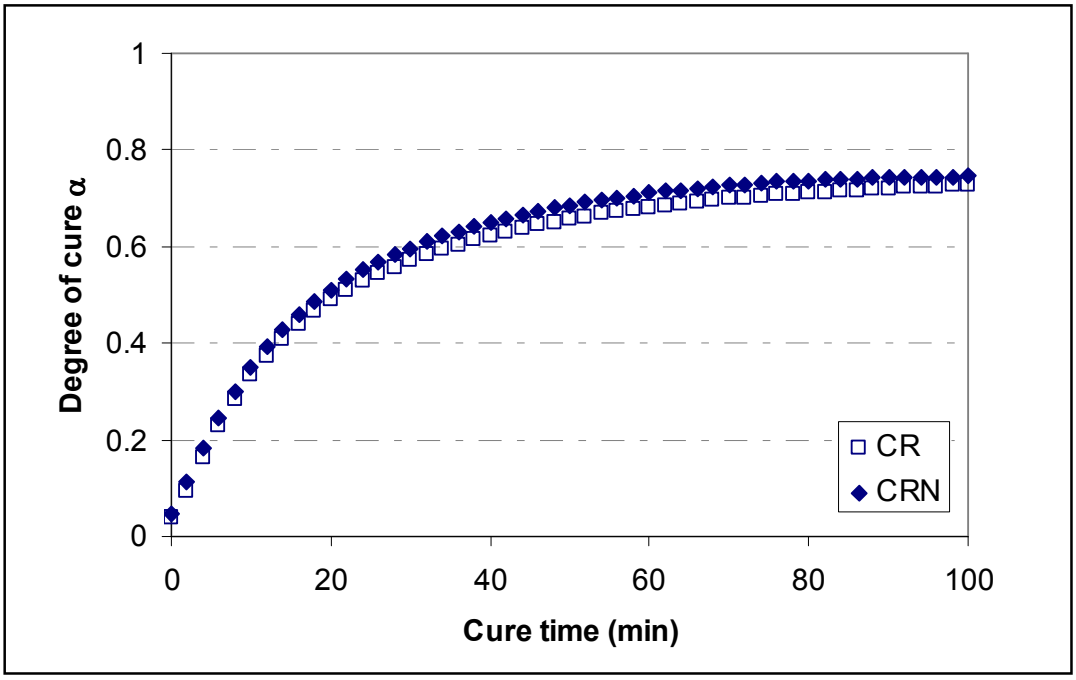

Figure 6.3 – Degree of cure vs. cure time for the CR and CRN formulations at 120ºC

Overall, the presence of the carbon nanotubes decreases the crosslink density of the thermoset system under dynamic conditions. This can be explained by possible consumption of reactive groups by the carbon nanotubes, which then does not allow complete crosslinking to occur. In isothermal cures below 120ºC, no significant effect of the presence of the carbon nanotubes on the maximum degree of cure obtained is detected. In these cases the reactants are probably not consumed fully, thus allowing the carbon nanotube filled system to reach similar final degree of cure levels as the system without the nanofillers.

6.1.2 Modelling the cure of the CRN formulation

The study of the cure kinetics is of great importance in polymer products for the analysis and design of processing operations. Dynamic and isothermal cure experiments on the novel CRN adhesive formulation were carried out in order to model its cure mechanism.

The experimental data, when combined, reveal thermal history effects which become evident on the superposition of the dynamic and isothermal data, on a reaction rate vs. degree of cure diagram [184]. A unique value of the reaction rate may exist for every point in the temperature and conversion space, so that the curing mechanism may be independent of the thermal history. The validity of this assumption can be tested using the superposition of isothermal and dynamic cure reaction rate data [113] illustrated in Figure 6.4.

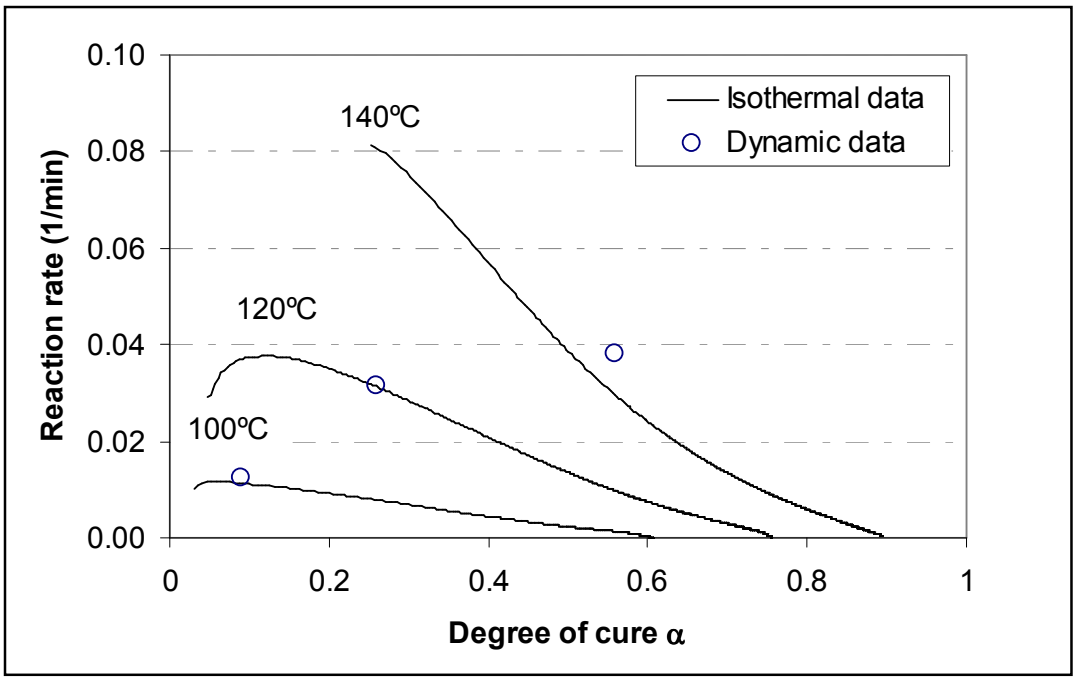

Figure 6.4 – Superposition of dynamic and isothermal DSC reaction rate vs. conversion for the CRN formulation

It can be observed that the superposition holds with a satisfactory accuracy at lower temperatures. The comparison between the isothermal and dynamic data is qualified by the relative error, which is an indication of the validity of superposition. This relative error was calculated using Equation 6.1 and a value of 14% was obtained. Overall errors induced due to differences between dynamic and isothermal data are in the range of 10-15%. Consequently, conventional cure kinetics modelling can be considered approximately valid for the CRN formulation of this study.

$$RE_{Superposition} = \frac{1}{n}\sum \frac{\left[\left(d\alpha/dt\right)_{iso} - \left(d\alpha/dt\right)_{dyn}\right]}{\left(d\alpha/dt\right)_{iso}} \quad \text{..... (6.1)}$$

Where:

n	is the number of experimental points
$(d\alpha/dt)_{iso}$	is the isothermal reaction rate
$(d\alpha/dt)_{dyn}$	is the dynamic reaction rate

The validity of the superposition between the isothermal and the dynamic cure data allows for the construction of a cure kinetics model. The proposed model used to fit the kinetic data is the autocatalytic Kamal-Sourour model [185] with an exponential term for diffusion limitations which follows the relation:

$$\frac{d\alpha}{dt} = \left(k_1 + k_2\alpha^m\right)\left(1-\alpha\right)^n D\left(\alpha\right) \quad \text{..... (6.2)}$$

The rate constants k_1 and k_2 have an Arrhenius dependence on temperature (T):

$$k_1 = A_1 \exp\left(-E_1 / RT\right) \quad \text{..... (6.3)}$$

$$k_2 = A_2 \exp\left(-E_2 / RT\right) \quad \text{..... (6.4)}$$

Where:

α	is the degree of cure
t	is the time, in min
T	is the temperature, in K
E_1 and E_2	are the activation energies, in J mol^{-1}
R	is the universal gas constant, in J mol^{-1} K^{-1}
A_1 and A_2	are the pre-exponential factors, in min^{-1}
m and n	are cure kinetics model exponents

Diffusion limitations to the curing reaction are incorporated in the model via factor $D(\alpha)$ as follows [186]:

$$D(\alpha) = \frac{1}{1 + e^{C[\alpha - (\alpha_{cT} T - \alpha_{c0})]}} \quad \text{..... (6.5)}$$

The parameter C controls the breadth of transition from a chemically to diffusion controlled reaction and parameters α_{cT} and α_{c0} define the dependence of the degree of cure at which the transition from chemical to diffusion control occurs on curing temperature.

Estimation of the ten parameters in the cure kinetics model described by Equations 6.2, 6.3, 6.4 and 6.5 was carried using a binary genetic algorithm (GA) described in [154,187]. Both isothermal and dynamic data were fed into the GA routine. The parameters were estimated with an average relative error of 5%. This small error, calculated using Equation 6.6, indicates that a very accurate fit was achieved.

$$RE_{Cure\ Kinetics} = \frac{1}{n} \sum \frac{\left[\left(d\alpha / dt \right)_{\exp} - \left(d\alpha / dt \right)_{est} \right]}{\left(d\alpha / dt \right)_{\exp}} \quad \text{..... (6.6)}$$

Where:

n	is the number of experimental points
$(d\alpha/dt)_{\exp}$	is the experimental (isothermal and dynamic) reaction rate
$(d\alpha/dt)_{est}$	is the estimated reaction rate calculated using the model

The parameters which define the model to give an accurate fit to the experimental data are summarised in Table 6-1.

ΔH (J/g)	380
A_1 (min^{-1})	6.12 x10^{6}
E_1 (kJ mol^{-1})	61.5
A_2 (min^{-1})	1.67 x10^{6}
E_2 (kJ mol^{-1})	58.8
m	1.74
n	1.57
C	29.3
α_{cT} (K^{-1})	7.58 x10^{-3}
α_{c0}	2.42 x10^{-1}

Table 6-1 – Estimated parameters for the CRN cure kinetic model

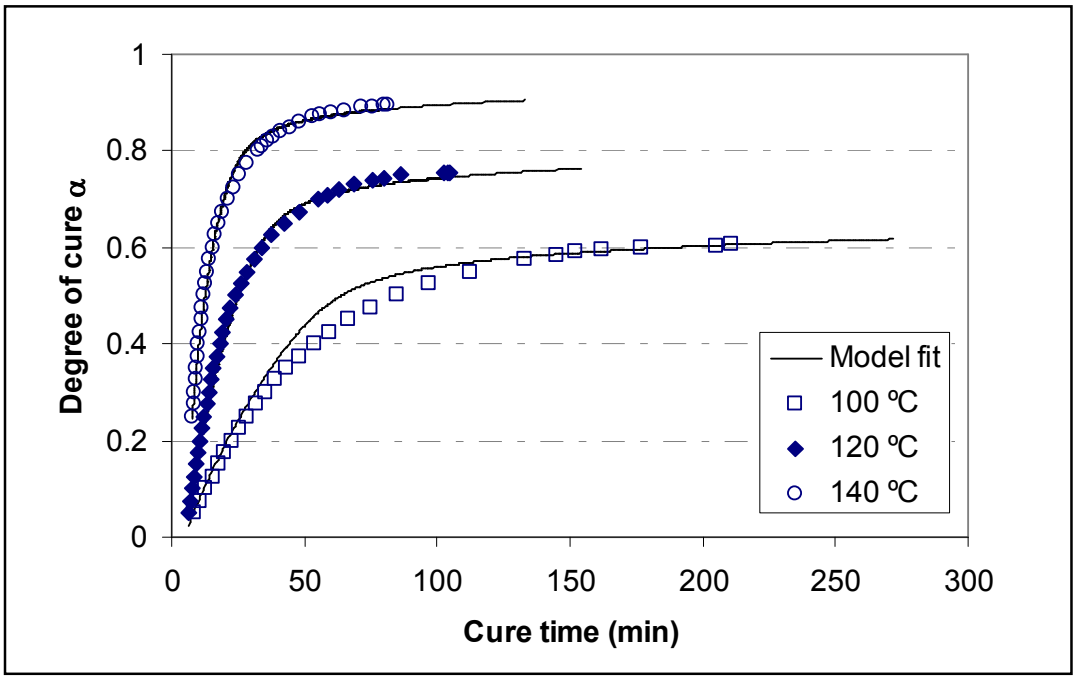

Figure 6.5 – Cure kinetics model fit – Evolution of degree of cure with time for the CRN isothermal experiments

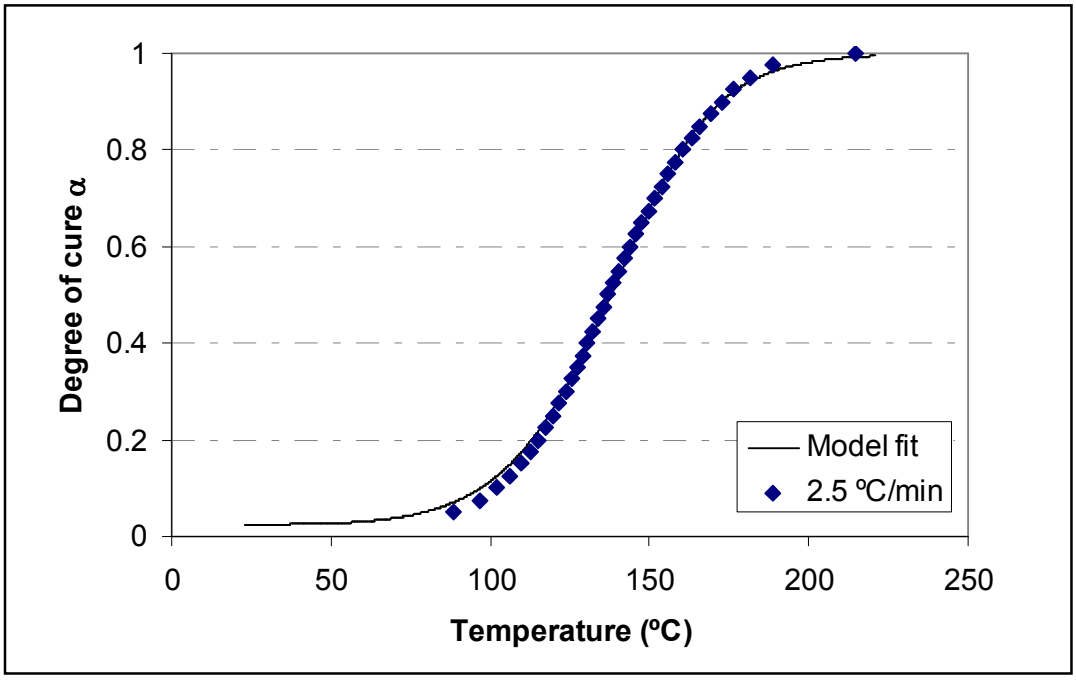

Figure 6.6 – Cure kinetics model fit – Evolution of degree of cure with temperature for a 2.5ºC/min CRN dynamic experiment

The quality of the fit under isothermal and dynamic heating conditions is illustrated in Figure 6.5 and Figure 6.6 respectively. The model gives a good fit to the measured data in both the chemically controlled (early stages) and the diffusion controlled (latter stages) regions of the reaction.

6.2 Thermo-mechanical properties

The four different adhesive variants of this work were tested to obtain two thermo-mechanical properties; the glass transition temperature, T_g and the coefficient of thermal expansion, CTE.

6.2.1 Glass transition temperature, T_g

Table 6-2 reports the T_g values for the 120ºC cured (73%-75% conversion) specimens determined by modulated differential scanning calorimetry (MDSC) as explained in Section 5.1.1.

Formulation	T_g (ºC)
C	133 (± 1)
CR	134 (± 1)
CN	133 (± 1)
CRN	134 (± 1)

Table 6-2 – Glass transition temperatures of the 76% cured specimens determined by MDSC

As previously shown in Section 6.1, below 120ºC cure there are no significant effects of the presence of the carbon nanotubes on the final degree levels achieved by the blends, even after 6 hours. This is reflected in the similar T_g values obtained. The reactants are probably not consumed fully, thus allowing the carbon nanotube filled systems to reach similar crosslink densities as the systems without the nanofillers.

The T_g values of the formulations containing rubber are slightly higher than those of the formulation without rubber. This is consistent with the fact that there is some rubber dissolved in the epoxy that has not phase separated. The T_g values are expected to be directly related to the amount of rubber dissolved in the epoxy phase. The CTBN rubber of this work showed a T_g of –50ºC. By applying the Fox equation [188] (Equation 6.7) to the glass transition data, the weight fraction of rubber that has not phase separated and is dissolved in the epoxy was estimated to be 2 wt% from the total rubber content of 5 wt%.

$$\frac{1}{T_g^{eff}} = \frac{w_{epoxy}}{T_g^{epoxy}} + \frac{1 - w_{epoxy}}{T_g^{CTBN\ rubber}} \quad \text{..... (6.7)}$$

Where:

T_g^{eff} is the glass transition temperature of the mixture

T_g^{epoxy} is the glass transition temperature of the epoxy

$T_g^{CTBN\ rubber}$ is glass transition temperature of the CTBN rubber

w_{epoxy} is the weight fraction of epoxy in the continuous phase

6.2.2 Post-cure analysis and $T_{g\infty}$

The 120ºC cured (73%-75% conversion) specimens prepared as detailed in Section 4.3.1.1 were post-cured in an oven at 200ºC for 80 minutes. DMTA analyses were performed on the post-cured specimens as specified in Section 5.2.1. The glass transition temperatures representative of the fully cured state of the materials ($T_{g\infty}$) are taken as the temperature corresponding to the maximum recorded value of tan δ (see Figure 6.7).

Table 6-3 reports the glass transition temperatures representative of the fully cured state of the materials ($T_{g\infty}$) and determined after post-curing the specimens in the oven. The values are taken as the temperature corresponding to the maximum value of tan δ from an average of three specimens.

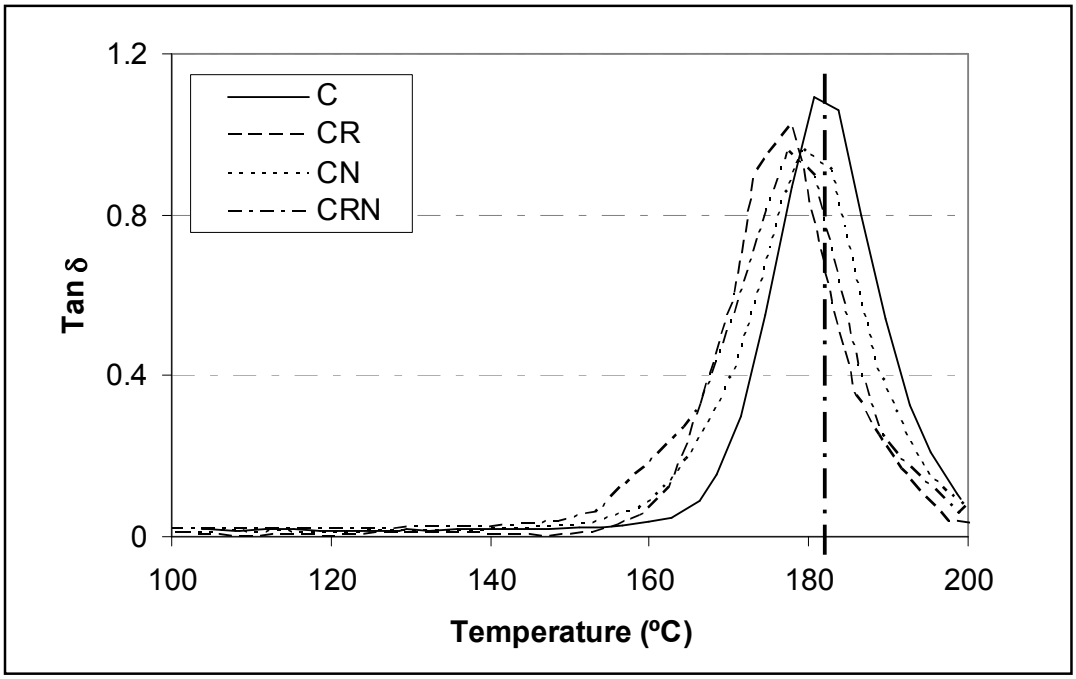

Figure 6.7 – DMTA traces from measurements made on the C, the CR, the CN and the CRN post-cured formulations

Formulation	$T_{g\infty}$ (ºC)	
	DMTA analysis	MDSC analysis
C	181 (± 1)	163 (± 1)
CR	177 (± 1)	158 (± 1)
CN	179 (± 1)	165 (± 1)
CRN	178 (± 1)	162 (± 1)

Table 6-3 – Glass transition temperatures of the fully cured specimens ($T_{g\infty}$) determined by DMTA and by MDSC

The $T_{g\infty}$ representative of the fully cured state of the materials were also measured in modulated differential scanning calorimetry (MDSC). As explained in Section 5.1.1, MDSC was applied to samples weight range from 5 to 6 mg from the post-cured specimens. The $T_{g\infty}$ values obtained are listed in Table 6-3. The difference between the 'apparent' $T_{g\infty}$ values determined by the two different measurements types has been observed previously when comparing these techniques [61].

The DMTA and MDSC measurements show a difference between samples with and without rubber, with lower values for those compositions which contain the rubber. Reduction of the $T_{g\infty}$ with the inclusion of CTBN rubber has been reported previously [189,190].

There is difference of over 40ºC between the $T_{g\infty}$ values and the values of the 120ºC cured (73%-75% conversion) specimens. This suggests that the durability of the blends should be considered. Namely, since they are capable of undergoing high levels of post-cure, that might be detrimental in terms of their hot-wet properties.

6.2.3 Coefficient of thermal expansion, CTE

The coefficients of thermal expansion were measured from 73%-75% cured specimens prepared as detailed in Section 4.3.1.2 and using a thermal mechanical analyzer (TMA), as explained in Section 5.2.2. Cooling and reheating cycles were used in order to remove residual stresses in the polymer and the thermal expansion coefficients were obtained from the second cycles. These cooling and reheating cycles could not eliminate the residual reactivity of the specimens as the maximum temperature in the cycle was below the 120ºC cure, 100ºC. The CTE is obtained from the slope of the extension versus temperature curves, in the temperature range of interest (see Figure 6.8). The CTE values at room temperature were determined from an average of three specimens and are shown in Table 6-4.

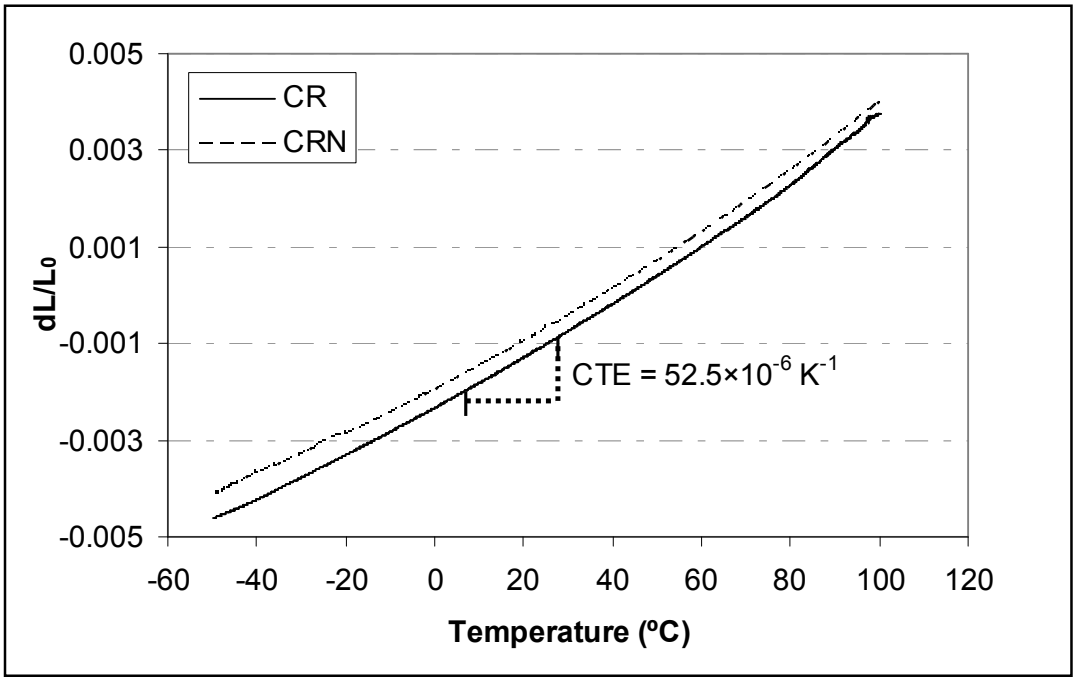

Figure 6.8 – Thermo-mechanical curves obtained for cured samples of the CR and the novel formulation, CRN

Formulation	CTE (10^{-6} K^{-1})
C	51.93 (± 0.03)
CR	52.11 (± 0.39)
CN	51.84 (± 1.01)
CRN	51.62 (± 0.77)

Table 6-4 – Coefficients of thermal expansion of the formulations determined by TMA

The differences in the values for the specimens tested here cannot be considered significant, but may indicate the potential for a higher concentration of nanotubes to reduce the CTE of an epoxy matrix. A possible increase in the T_g of the blends for more highly crosslinked specimens is expected to result in slightly lower values of CTE.

6.3 Mechanical properties

A series of mechanical tests, fracture, flexure and compression, were performed in order to characterise the room temperature behaviour of the different adhesive formulations.

6.3.1 Fracture toughness, K_{IC} and fracture energy, G_{IC}

The fracture toughness, K_{IC} and fracture energy, G_{IC}, were determined from the 120ºC cured (73%-75% conversion) notched specimens prepared as detailed in Section 4.3.1.3 and tested in the three-point bending configuration as explained in Section 5.2.3. The full set of experimental data and analysis are included in Appendix A. Figure 6.9 shows optical micrographs of the fracture surfaces of the various formulations. The initial transparency of the control formulation, C, indicates a high degree of miscibility between the epoxy resin and the hardener. All the fracture surfaces were free of air bubbles and exhibited a brittle fracture appearance with characteristic 'river-markings'.

Table 6-5 reports the values of fracture toughness and fracture energy obtained for all the various adhesive formulations.

Formulation	No. of specimens	K_{IC} (MPa m$^{0.5}$)	G_{IC} (J/m^2)
C	3	0.8 (± 0.1)	144 (± 26)
CR	5	1.1 (± 0.1)	317 (± 36)
CN	5	0.9 (± 0.1)	177 (± 15)
CRN	4	1.3 (± 0.1)	551 (± 21)

Table 6-5 – Fracture toughness, K_{IC} and fracture energy, G_{IC}, of the various formulations

In view of the results, there is a noticeable increase in the stress intensity factor upon the addition of rubber to the control formulation. The addition of carbon nanotubes alone shows no significant effect. However, the inclusion of nanotubes and rubber in the formulation provides a further increase in K_{IC}, 25% more than for when rubber alone is added. The same trend is obtained for the fracture energy. The inclusion of nanotubes and rubber results a further 163% increase in G_{IC} than when rubber was used alone. Possible reasons for the synergy on toughness found for the combination of rubber toughening and the addition of carbon nanotubes are discussed later in Section 6.5.

Any increase in crosslink densities in the blends, such as would be achieved with a post-cure, is expected to slightly decrease the G_{IC} values as the more highly reticulated material will present reduced ductility [190].

Previous research has shown that when carbon nanoparticles are incorporated into a resin system two main effects may be expected [191,192]:

- Extra consumption of the amine hardener, which would result in a reduction of the thermoset reactivity and consequently a reduction of T_g;
- Creation of chain mobility limitations which would result in an increase of the T_g

Depending on each material formulation one of the phenomenon will prevail over the other and as a consequence a reduction or an increase in the final T_g value will be observed. However, the variations in the final T_g that have been reported are less than

10% [100,106,193] and therefore are not expected to induce major changes upon mechanical properties such as fracture toughness.

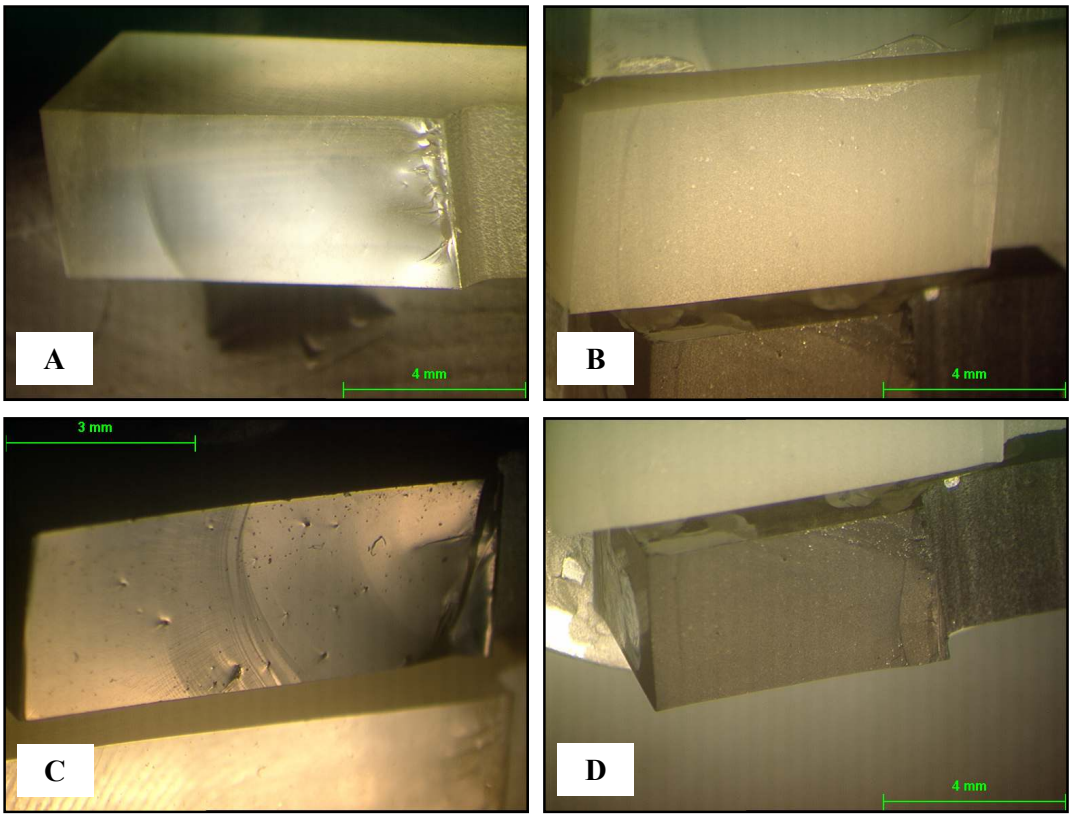

Figure 6.9 – Optical micrographs of the fracture surfaces of the formulations (A) C, (B) CR, (C) CN and (D) CRN

6.3.2 Flexural modulus, E_f

Flexural tests were performed using the three-point bending configuration as detailed in Section 5.2.4 on the 73%-75% cured flat specimens prepared as explained in Section 4.3.1.4. The flexural modulus, E_f, was taken as the ratio of the stress difference between 5 and 25% flexural strain, as shown in Figure 6.10, from an average of five specimens.

Table 6-6 reports the flexural modulus values obtained from an average of six specimens for all the various formulations.

Formulation	E_f (GPa)
C	3.4 (± 0.1)
CR	2.9 (± 0.1)
CN	3.2 (± 0.1)
CRN	2.7 (± 0.2)

Table 6-6 – Flexural modulus of the formulations

In view of the values, the addition of the relatively low modulus, rubber–rich particles to the base formulation results in a reduction in the flexural modulus of 15%. This is as expected in rubber toughened epoxies [31,32,35], whereas no stiffening effect of nanotubes has been found [63,194].

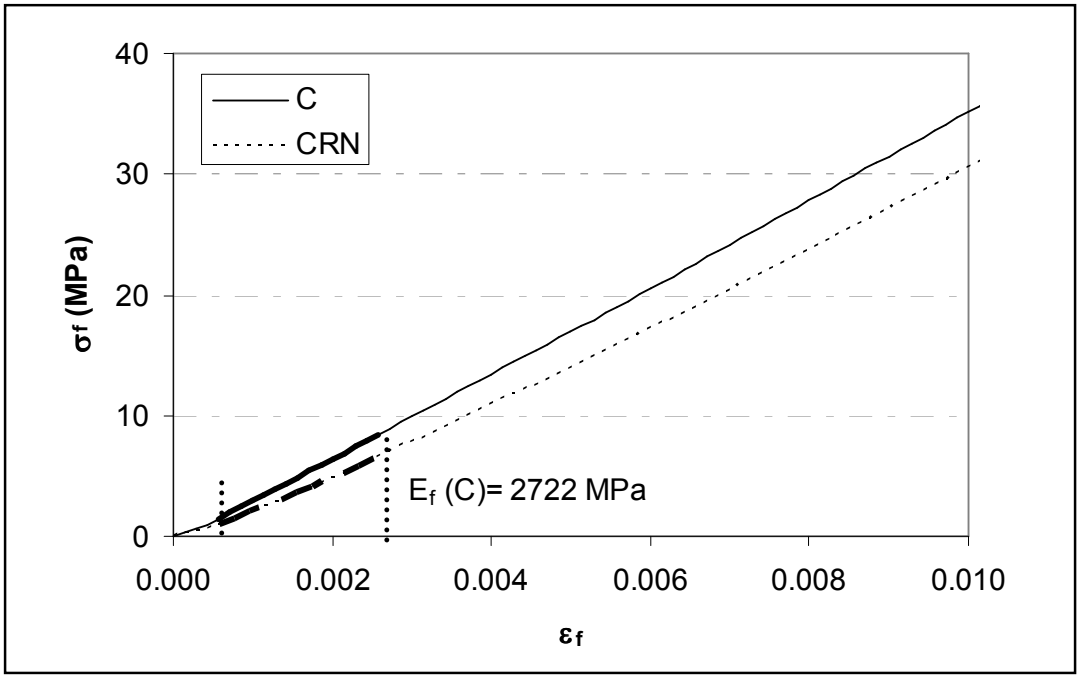

Figure 6.10 – Flexural stress vs. flexural strain for the C and the CRN formulations

6.3.3 Compression yield stress, σ_{yc}

Compression tests were performed on the 73%-75% cured specimens prepared as detailed in Section 4.3.1.5. These specimens were tested in a compression test fixture as

detailed in Section 5.2.5. No global buckling was observed and the stress vs. strain curves showed a clear yield point, taken as the maximum engineering stress, as shown in Figure 6.11.

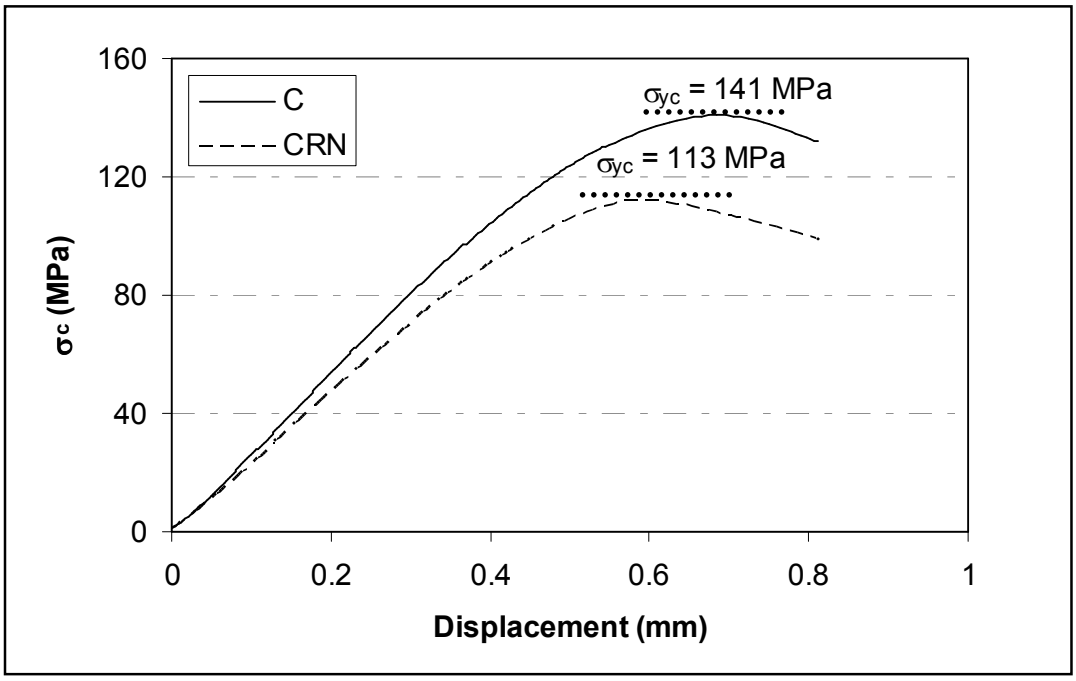

Figure 6.11 – Compression curves for the C and the CRN formulations

Table 6-7 presents the compression yield stress values obtained.

Formulation	σ_{yc}(MPa)
C	141 (± 1)
CR	114 (± 2)
CN	141 (± 1)
CRN	113 (± 2)

Table 6-7 – Compression yield stress of the formulations

In view of the values it can be concluded that the compressive yield strength is reduced by the addition of rubber. This was expected as the rubber inclusions are softer in

comparison to the epoxy. On the other hand, inclusion of carbon nanotubes shows no effect.

Any increase in crosslink densities in the blends, such as a post-cure, is expected to raise the compressive yield stress values as the more highly reticulated material will present reduced ductility [190].

6.4 Electrical conductivity

DC electrical resistivity was measured as detailed in Section 5.2.6 from cured specimens prepared as explained in Section 4.3.1.6. The electrical conductivity of the material (σ) was calculated using the Equation 5.8 from the measured resistance, the sample length and cross-sectional area. Table 6-8 shows the electrical conductivity obtained from an average of five specimens for the various formulations.

Formulation	σ (S/m)
C	$<10^{-9}$
CR	3.2×10^{-9} ($\pm$ 1.1×10^{-9})
CN	1.6×10^{-3} ($\pm$ 2.3×10^{-4})
CRN	3.6×10^{-3} ($\pm$ 3.2×10^{-4})

Table 6-8 – DC electrical conductivity of the formulations

AC electrical conductivity is illustrated as a function of frequency in Figure 6.12. The formulations without carbon nanotubes, C and CR, followed a pure capacitive behaviour with the characteristic slope of unity in the conductivity vs. frequency log-log plots. In contrast, the carbon nanotube containing formulations, CN and CRN, showed a frequency independent conductivity, characteristic of ohmic behaviour. This behaviour, which is typically observed in nanotube-epoxy composites with nanotubes forming a conductive network [5], is maintained up to a knee frequency over which a transition to a dielectric response occurs. The AC spectra can be used for the validation of the DC

properties using the plateau conductivity observed at low frequencies for CN and CRN. The values obtained are identical to the DC measurements reported in Table 6-8.

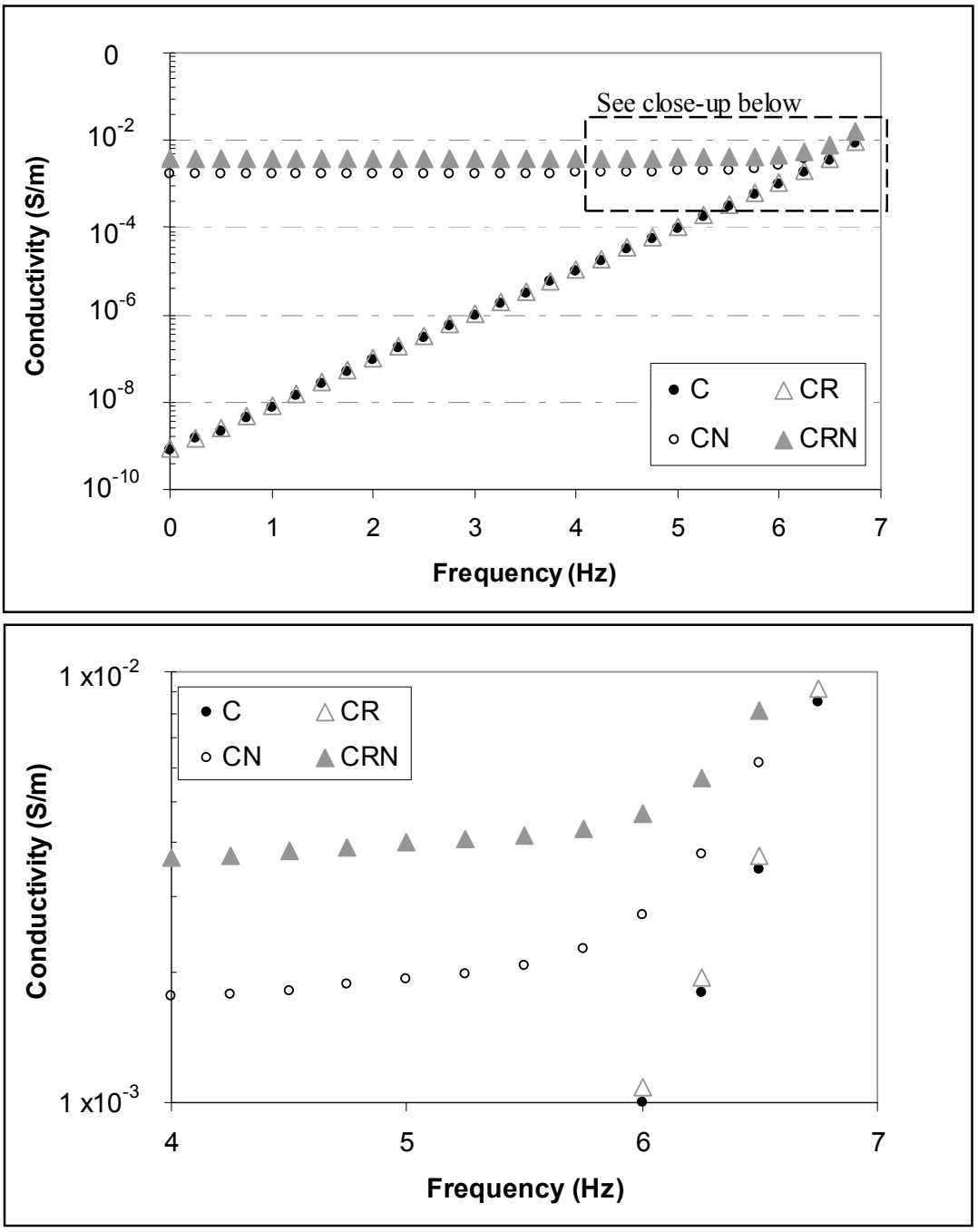

Figure 6.12 – AC conductivity spectra for all the formulations, C, CR, CN and CRN. The close-up graph at the bottom shows detail of the response of CN and CRN at the higher frequencies

The addition of the carbon nanotubes was found to increase the conductivity of the adhesive formulations. The combination of rubber and carbon nanotubes showed slightly higher conductivity than the addition of carbon nanotubes alone. This result may indicate the preference of the carbon nanotubes to remain in the epoxy-rich regions of the ternary blend. As a consequence the nanotubes are concentrated in a smaller volume, resulting in the formation of a more densely connected and therefore more conductive network. The selective location of the carbon nanotubes in the ternary blend can be observed later in Section 6.5.

Increasing the crosslink density of the CN and CRN formulations by curing at a higher temperature may lead to an increase in their conductivity values. Research has shown that high temperatures during the curing process promote further agglomeration of the initial nanotube clusters and led to finer and more homogeneously dispersed nanotube aggregates [5]. This curing temperature dependence of the cluster formation can be explained by considering the curing behaviour of the epoxy. The higher the curing temperature, the lower the initial viscosity and, therefore, early particle movement in the dispersion would be enhanced at higher temperatures. In case of increasing the crosslink density of the 120ºC cure specimens with a post-curing process, effects on the conductivity values are not expected as the conductive network was already formed at the 73-75% degree of cure.

6.5 Structure-property relationships

Scanning electron microscopy (SEM) was used to examine room temperature fracture surfaces of the samples which give information about fracture mechanisms and the influence of particle modification on the fracture behaviour. Cryo-fracture surfaces were also examined as they generally offer cleaner fracture surfaces, although in the samples of this work the difference in appearance was minimal. The cryo-fracture samples containing rubber were etched in toluene for 2.5 hours at ambient temperature in order to extract the dispersed rubber phase [195].

Figure 6.13 shows SEM micrographs of the cryo-fracture surfaces of the formulations containing nanotubes; CN and CRN. In these images the bright dots are the ends of carbon nanotubes. Qualitative investigation of these micrographs reveals the carbon nanotubes homogeneously dispersed and the absence of large agglomerates. The presence of the nanoparticles reflects itself in a significantly increased roughness of the fracture surface surrounding the CNTs, as previously noted by other authors [62].

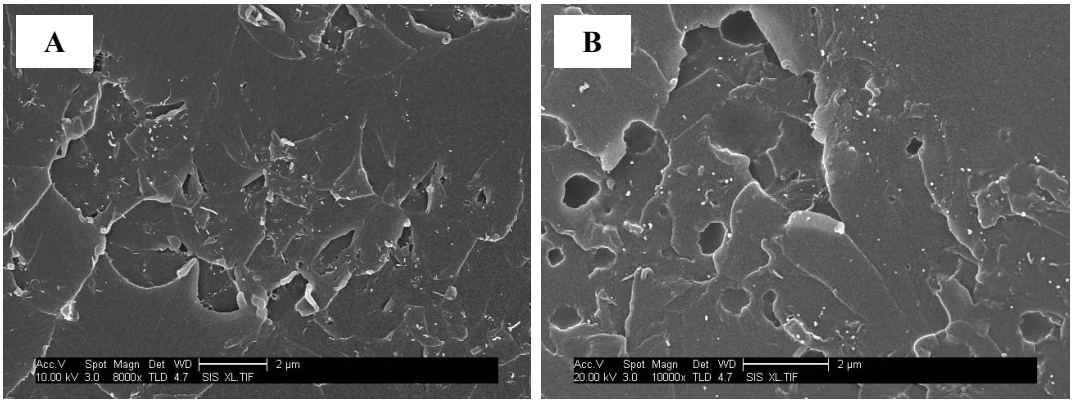

Figure 6.13 – SEM micrographs of cryo-fracture surfaces (A) CN and (B) etched CRN

All the formulations containing rubber displayed a two-phase morphology with an epoxy rigid continuous phase and a dispersed rubbery phase of isolated spherical particles. On these cryo-fracture micrographs only the imprints of the (etched out) rubber particles are visible.

In terms of the fracture energy of the formulations, as explained in Section 6.3.1, the CTBN rubber increases the fracture energy of the epoxy. The fracture mechanisms observed for the CR formulation (Figure 6.14 A-B) are rubber particle cavitation and subsequent shear yielding in the matrix.

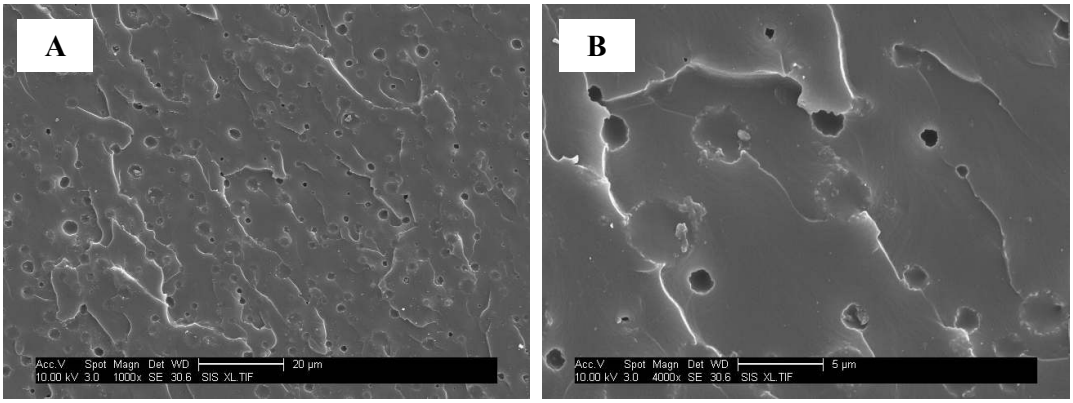

Figure 6.14 – SEM micrographs of three-point bending room temperature fracture surfaces of CR at two magnifications

The incorporation of carbon nanotubes alone for the CN formulation has only a slight toughening effect on the epoxy. Examination of relevant fracture surfaces failed to show up any clear toughening mechanism attributable to the filler.

Figure 6.15 indicates the distribution and sizes of the precipitated rubber particles for the CR and CRN formulations respectively. The mean size of the rubber particles was significantly larger in the CR formulation than in the CRN sample. This decrease in size with the addition of the carbon nanotubes is thought to be associated with the increase in viscosity of the system caused by the dispersed nanotubes, which may inhibit the growth of the rubbery domains in the pre-gel phase. The possibility of particle nucleation being enhanced by the nanotubes also cannot be discounted [195,196].

A synergistic effect in toughness was found when rubber and carbon nanotubes are combined in the CRN formulation. Previous research on effects of the particle size and size distribution has suggested that toughening is not enhanced by large particles (>1 μm) but may be dependent on the concentration of smaller particles [31,32,34]. Therefore, the reduction of the mean rubber particle size observed with the inclusion of the nanotubes (Figure 6.15 C-D) may be the cause for the increase in toughness in this formulation.

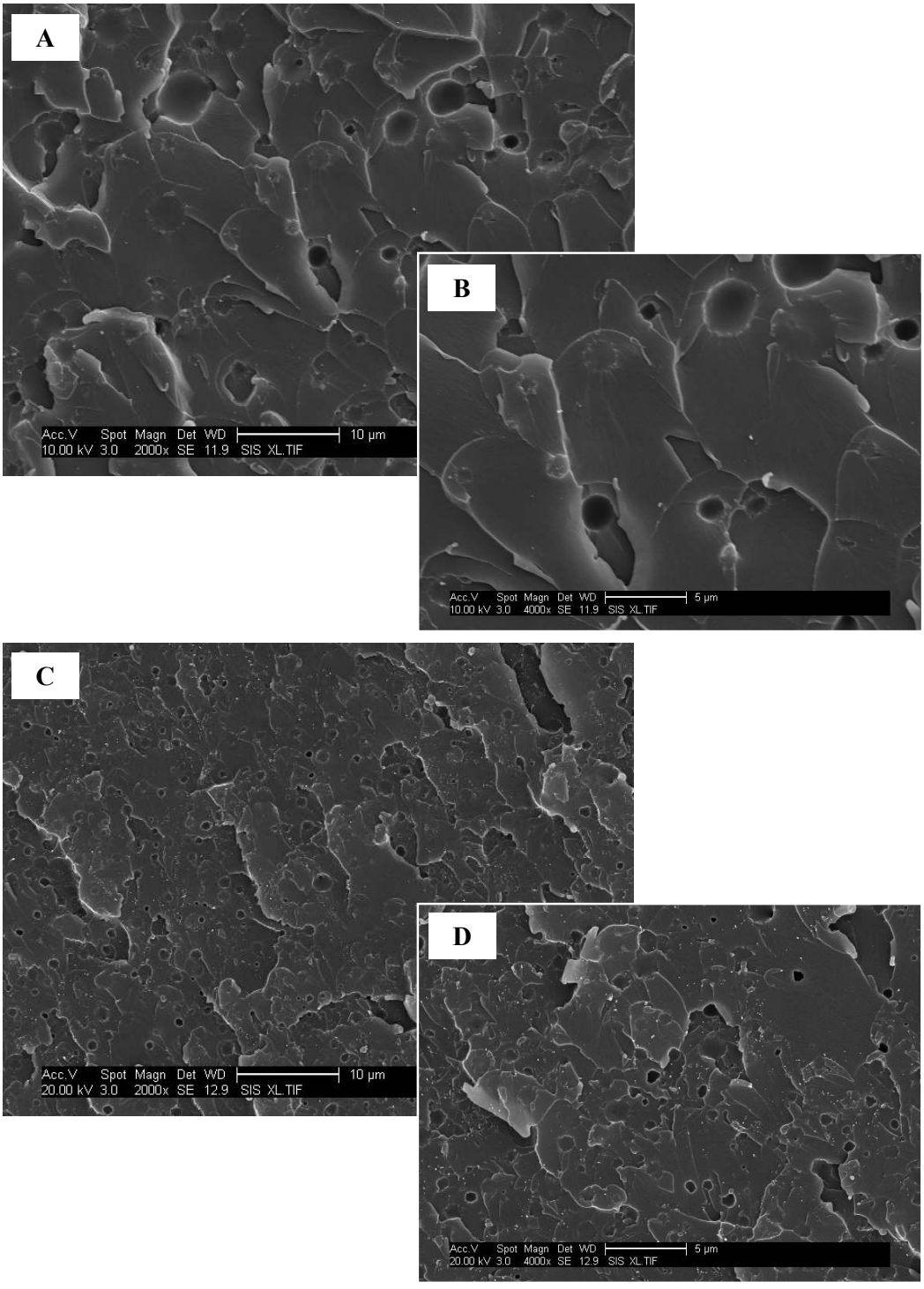

Figure 6.15 – SEM micrographs of etched cryo-fracture surfaces at two magnifications (A) and (B) CR; (C) and (D) CRN

This synergistic effect on toughening for the CRN formulation is seen more clearly in the data shown in Figure 6.16. The height of the columns represents the mean values and the error bars represent the scatter. In this particular system, the increase in fracture energy is accompanied by an increase in the electrical conductivity, giving the solid CRN samples an attractive overall balance of properties.

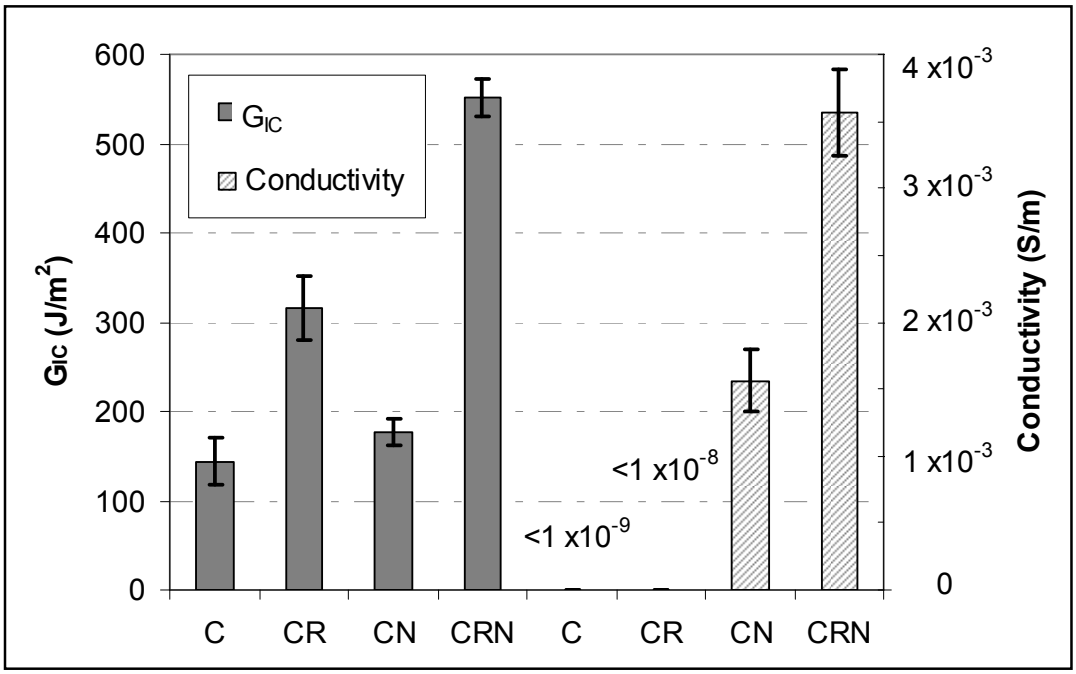

Figure 6.16 – Fracture energy, G_{IC} and electrical conductivity of the formulations employed

The most noticeable effect found in this work is the reduction of the mean rubber particle size in the rubber toughened epoxy samples also containing carbon nanotubes. In other ternary systems studied in the context of adhesives preparation, the incorporation of silica nanoparticles did not result in any change in the rubber particle size distribution [197,198]. However, it should be noted that the silica nanoparticles also have little effect upon the chemoviscosity of the system, unlike the carbon nanotubes used in this study.

Summary

Characterisation of the novel CRN ternary resin blend of this work has been illustrated by the contribution of each constituent in its thermo-mechanical, mechanical and electrical properties in the solid state. Scanning electron microscopy has contributed successfully to relate the change in properties with the modifications in the morphology of the formulations.

Chapter 7

Characterisation of adhesives in bonded specimens

This chapter details the results obtained from testing the novel adhesive in structural joints. Mode I and mode II delamination testing and analysis, undertaken to determine the adhesive fracture energies in both modes, are described. These tests were performed on two different substrate materials, GFRP (composite) and aluminium alloy (metal). The performance of the novel adhesive film is compared against commercially available adhesive films. Attention is also given to the comparison between the bulk sample toughness values obtained in Chapter 6 and those achieved from DCB testing of bonded specimens containing the various adhesive formulations.

Finally, a specialist fatigue test was performed to show the behaviour of the novel adhesive film in an application where damage tolerance is required. Again, the performance of the novel adhesive is presented in comparison with a commercially available adhesive.

7.1 Flexural modulus of substrates

Flexural modulus values for the substrate materials used in this work were required for the mode I and mode II analysis (see Section 5.3.2 and Section 5.3.3). Table 7-1 shows the values for the UD E-glass / 913 epoxy composite and for the metal (aluminium-zinc alloy 7085 T 7651). The GFRP value was measured using the 3 Point Bend (3PB) test as detailed in Section 5.3.1. The flexural modulus for the aluminium alloy was taken from literature [23,130] (see Section 3.4.2).

Material	Flexural Modulus (GPa)
UD GF / 913	36.9 (± 0.7)
Aluminium alloy	69.0

Table 7-1 – Flexural modulus of substrate materials

7.2 Mode I adhesive fracture energy

DCB test coupons were manufactured to the specification described in Section 4.3.2.3 and prepared for testing as described in Section 5.3.2. The majority of these joints were made with GFRP substrates. A small number of tests were carried out with aluminium alloy substrates. For each type of adhesive joint, three specimens were tested and analyzed. Optical microscopy was used to determine the bondline thickness at three positions along the length of the specimen and the average value was used for the analysis. All data analysis has been carried out using Microsoft Excel© spreadsheets. These spreadsheets automatically performed all the data reduction and plotted the linear regression analyses and the R-curves [199]. The non-linear (NL) initiation value defined by the test standard [171] is used for comparison of results as this is the most conservative of the three existing methods for obtaining the initiation values [151].

7.2.1 Unsupported films: contribution of each constituent in the adhesive joint

Figure 7.1 shows the mode I R-curves obtained for the unsupported adhesive films, U-C, U-CR, U-CN and U-CRN adhered to GFRP substrates and showing both initiation and propagation values.

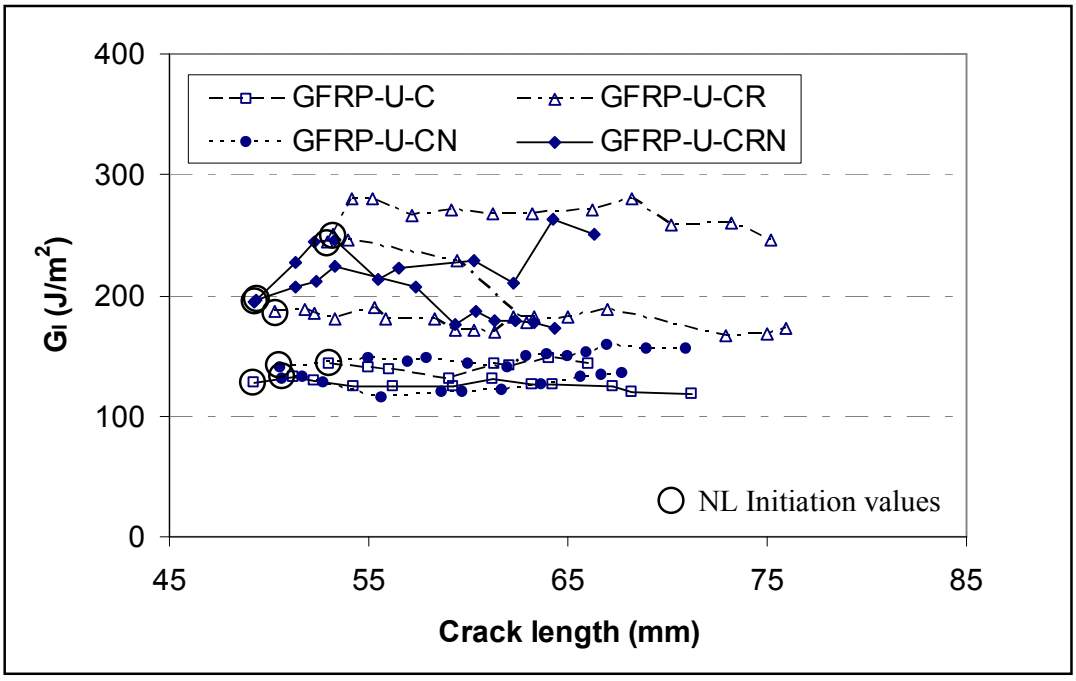

Figure 7.1 – Mode I R-curves for the unsupported adhesive films

Table 7-2 shows the bondline thicknesses, the initiation G_{IC} values, the mean propagation G_{IC} values and modes of failure obtained from testing three DCB joints of each unsupported film. Where three test curves are not shown in Figure 7.1, the results considered suspect have been removed and were therefore not included in the calculation of the values in Table 7-2.

The U-C and U-CN formulations produced flat R-curves as is expected for stable crack growth. However, for the U-CR and U-CRN formulations there are apparent changes in the values of G_{IC} with increasing crack length which are not desirable results. Mixed mode of failure was observed for the U-CR and U-CN formulations and interfacial failure for the U-CRN. These failure mode observations could explain the

corresponding R-curves being non-flat and the large scatter in the mean propagation G_{IC} values. Comparison of these unsupported films was therefore made based on initiation values.

Plate ID	**Bond thickness (μm)**	**Initiation G_{IC} (J/m^2) (NL)**	**Mean propagation G_{IC} (J/m^2)**	**Failure mode**
GFRP-U-C	35	124 (± 19)	133 (± 8)	C
GFRP-U-CR	200	227 (± 29)	209 (± 25)	M
GFRP-U-CN	210	135 (± 5)	138 (± 25)	M
GFRP-U-CRN	170	196 (± 1)	213 (± 21)	I

Key: C – Cohesive failure I – Interfacial failure M – Mixed failure

Table 7-2 – Comparison of mode I testing of unsupported adhesive films

Looking at the G_{IC} initiation values, a measurable increase in the adhesive fracture energy upon the addition of rubber to the control formulation is obtained. The addition of carbon nanotubes alone and along with rubber shows no significant effect. This finding differs from the fracture toughness results from testing the bulk adhesives (Section 6.3.1) where the inclusion of nanotubes and rubber provided a further increase in toughness. The interfacial failure observed for this formulation may be the cause of this discrepancy.

As previously introduced in Section 2.3, the adhesive bond thickness has an influence on the mode I fracture of adhesive joints. A detailed discussion of this is given in Section 7.2.7.

The following sections will continue with the presentation of the mode I adhesive fracture energy experiments. After finding interfacial and mixed modes of failure for three of the formulations in the unsupported films, the author implemented the idea of

improving adhesion through the use of a surface primer, as detailed in Section 4.2.5.4, in an attempt to achieve cohesive failure. The motivation for obtaining cohesive failure was to ensure that the experimental data obtained was representative of the adhesive itself rather than the interface between the adhesive and the substrate. All the results presented from this point forward were obtained with the use of the primer with the exception of the tests using the commercially available adhesives.

7.2.2 Selecting the veil for the novel adhesive film

Figure 7.2 shows the mode I R-curves obtained for the novel adhesive incorporating the two veil types, polyester or nylon and bonded to GFRP substrates. These curves show mode I crack initiation and propagation values. Three specimens were tested and have been analyzed for each adhesive system.

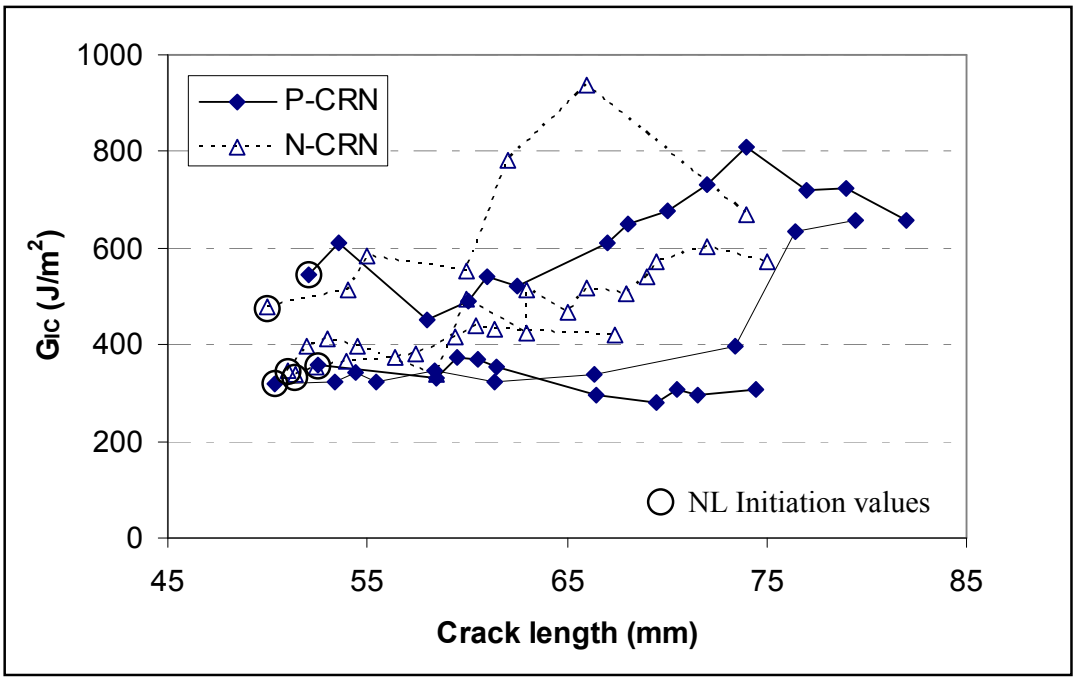

Figure 7.2 – Mode I R-curves for CRN supported films with polyester (GFRP-P-CRN) and nylon veil (GFRP-N-CRN)

The R-curves obtained from these experiments are non-flat, showing an increasing and unstable trend of G_{IC} with increasing crack length. These trends are the reflection of the load vs. displacement traces illustrated in Figure 7.3. The cracks propagated

intermittently in a stick-slip manner exhibiting load values appropriate to both crack initiation and crack arrest. The bridging effects introduced by the veils in these adhesive film versions are claimed to be responsible for this stick-slip behaviour [200]. In this case, the Annex B of the standard BS 7991:2001 was followed to obtain the Mode I R-curves.

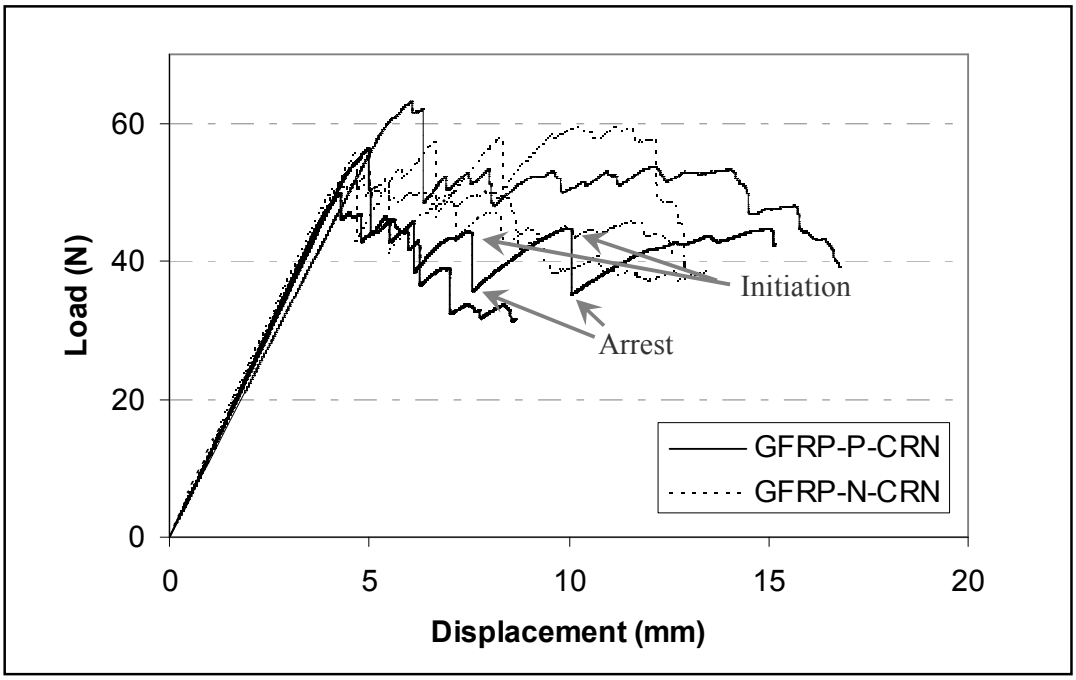

Figure 7.3 – Mode I load vs. displacement curves for CRN supported films with polyester (GFRP-P-CRN) and nylon veil (GFRP-N-CRN)

Table 7-3 shows the G_{IC} initiation and propagation values, adhesive bond thicknesses and modes of failure obtained from testing the supported CRN films. From the curves and the values obtained, no conclusions can be drawn as to the contribution of either veil to the mode I adhesive fracture energy due to the large scatter. Figure 7.4 shows the fracture surfaces resulting from testing the different film versions. Qualitative investigation of these images reveals that the nylon veil caused an interfacial failure whilst the polyester veil produced a cohesive failure mode. From this observation, the polyester veil was selected to be used for further studies as the veil in the novel adhesive film.

Plate ID	Bond thickness (μm)	Initiation G_{IC} (J/m^2) (NL)	Mean propagation G_{IC} (J/m^2)	Failure mode
GFRP-P-CRN	150	407 (± 99)	455 (± 129)*	C
GFRP-N-CRN	320	388 (± 64)	518 (± 115)*	M

* Taken from points on the load vs. displacement curve corresponding to crack arrest

Key: C – Cohesive failure I – Interfacial failure M – Mixed failure

Table 7-3 – Comparison of mode I testing of supported CRN adhesive films

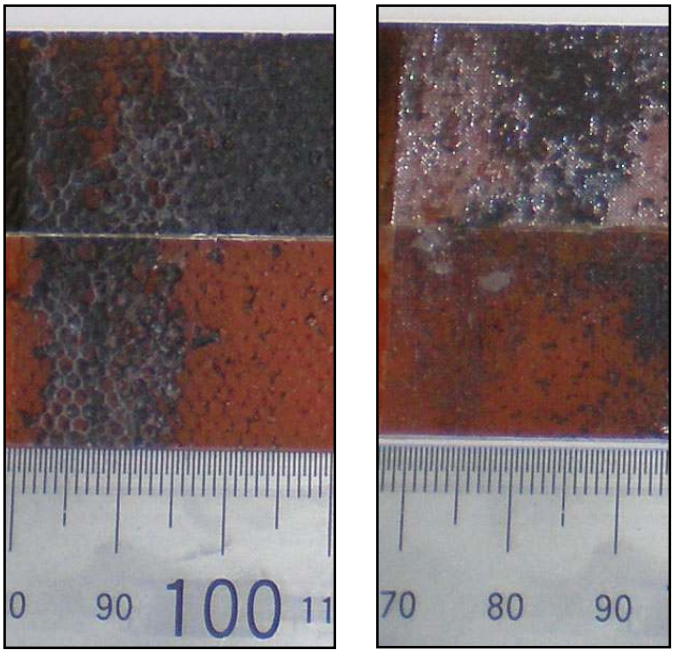

Figure 7.4 – Fracture surfaces of the CRN formulation with nylon veil, GFRP-N-CRN (left) and polyester veil, GFRP-P-CRN (right)

7.2.3 CNTs contribution to the novel adhesive film

Figure 7.5 shows a comparison of mode I R-curves for the CRN and CR supported films containing the polyester veil, both adhered to GFRP substrates. Three specimens of each system were tested; one suspect CR test result has been omitted. The idea of this

study was to derive the contribution of the carbon nanotubes in the overall joint performance. Table 7-4 lists the G_{IC} values obtained from these experiments.

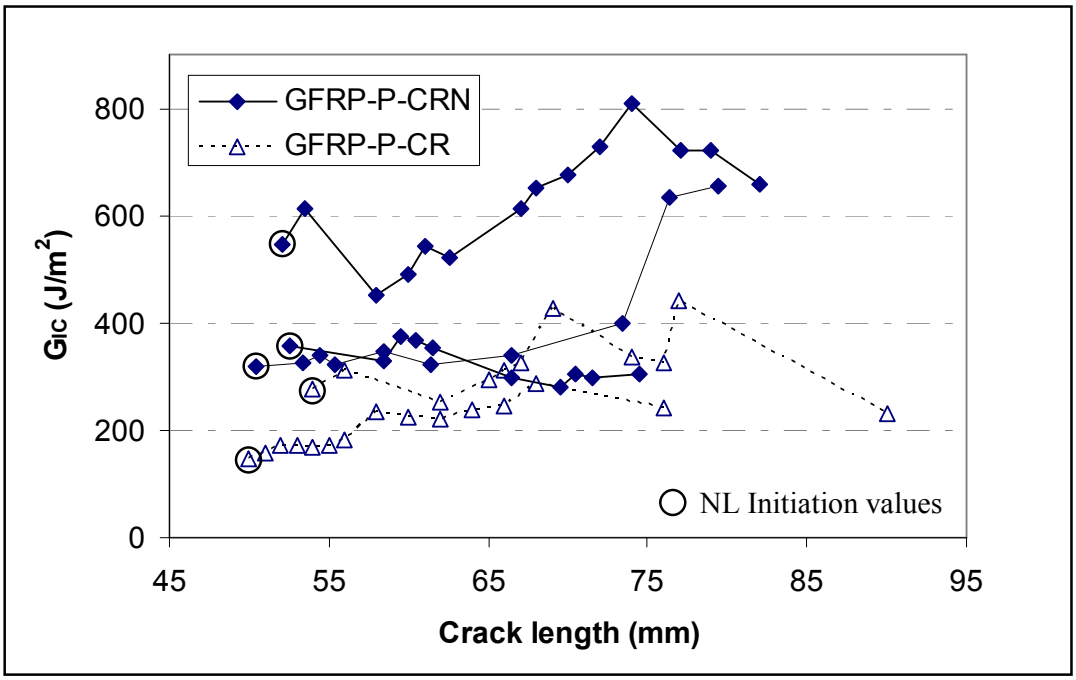

Figure 7.5 – Mode I R-curves for the CRN and the CR formulations with polyester veil

Plate ID	Bond thickness (μm)	Initiation G_{IC} (J/m^2) (NL)	Mean propagation G_{IC} (J/m^2)	Failure mode
GFRP-P-CRN	150	407 (± 99)	455 (± 129)*	C
GFRP-P-CR	130	212 (± 65)	267 (± 59)*	C

* Taken from points on the load vs. displacement curve corresponding to crack arrest

Key: C – Cohesive failure I – Interfacial failure M – Mixed failure

Table 7-4 – Comparison of mode I testing of the CRN and the CR formulations with polyester veil

The mode of failure was observed to be cohesive for both P-CRN and P-CR films. From the investigation of these curves along with the values of G_{IC}, a toughening effect might be attributed to the inclusion of carbon nanotubes. However, a poor wetting of the veil

by the CR formulation was noticed, as shown in Figure 7.6. This weaker adhesion between the veil and the adhesive paste, in relation to that observed for the CRN formulation (Figure 7.4), would have offered less resistance to crack propagation. The poor wetting of the veil is therefore thought to be the main reason for the lower G_{IC} values obtained for the CR formulation.

Figure 7.6 – Fracture surfaces of the CR formulation with polyester veil, GFRP-P-CR

7.2.4 Targeting nanofillers at the adhesive-substrate interface

As explained in Section 4.2.6.2, a specialised adhesive system was created in order to study the effect of reinforcing the adhesive-substrate interfaces. This study was implemented by placing two unsupported films containing carbon nanofibres either side of the main polyester veil supported CR adhesive film in the DCB joint. This adhesive system is designated U-CF / P-CR and was bonded to GFRP substrates. As for the previous studies, three specimens of this system were tested and compared against the results obtained for GFRP-P-CR. Figure 7.7 shows the mode I R-curves obtained whilst

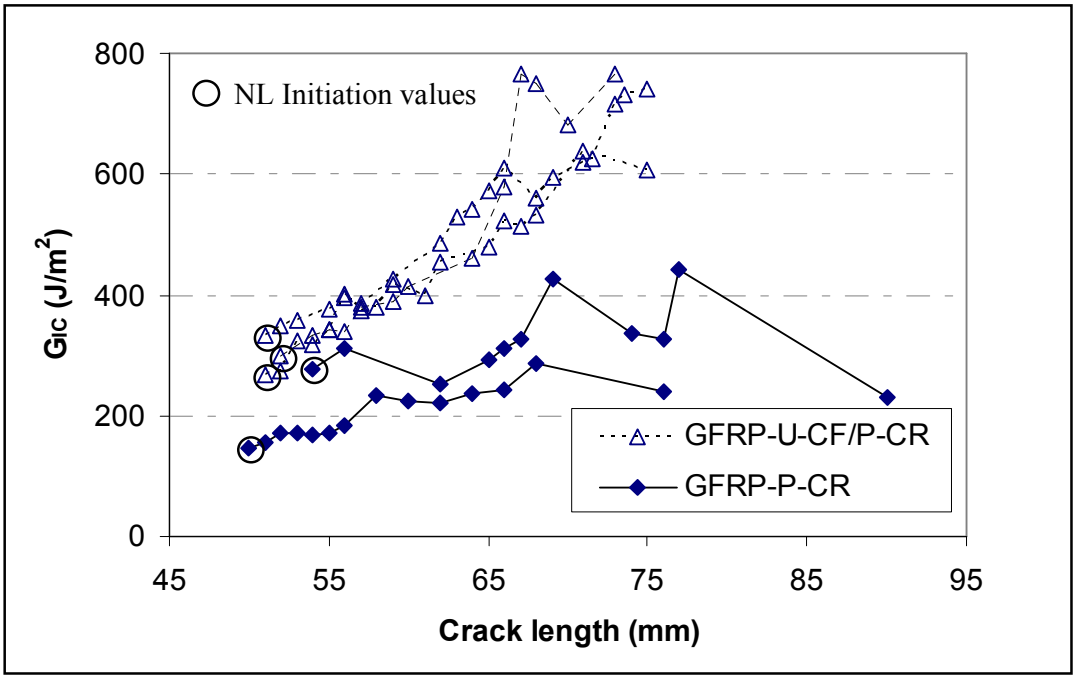

Figure 7.7 – Mode I R-curves for GFRP-P-CR and GFRP-U-CF / P-CR

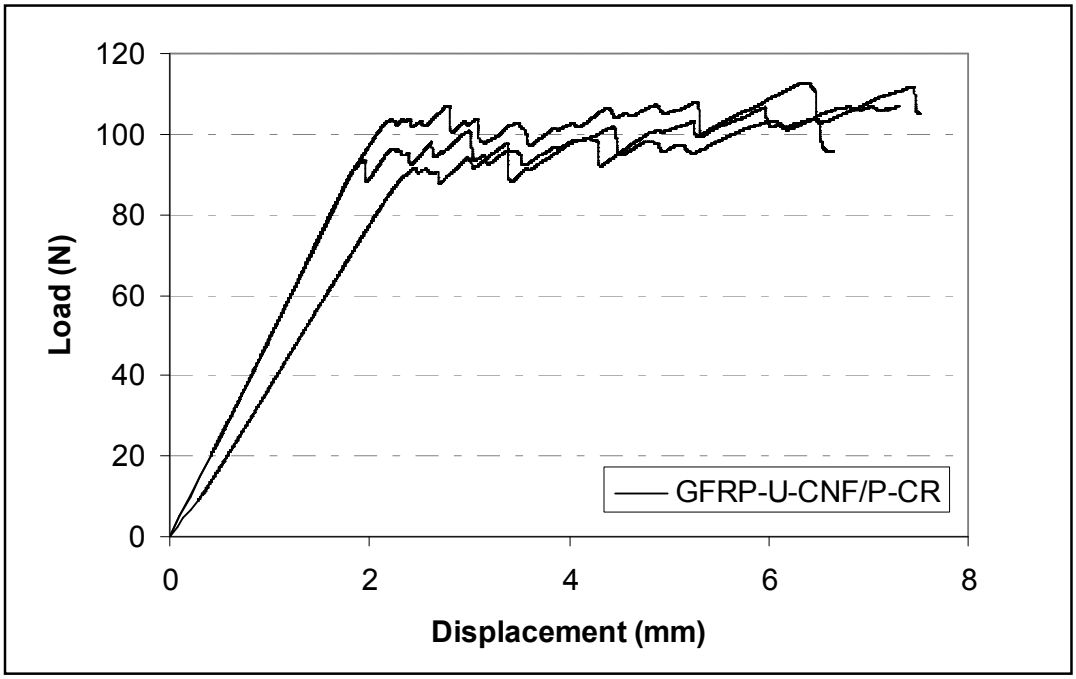

Figure 7.8 – Mode I load vs. displacement curves for GFRP-U-CF / P-CR adhesive system

Figure 7.8 presents the load vs. displacement traces for the U-CF / P-C adhesive system. Visual inspection of the fracture surfaces confirmed cohesive failure for both of these systems.

Plate ID	**Bond thickness (μm)**	**Initiation G_{IC} (J/m^2) (NL)**	**Mean propagation G_{IC} (J/m^2)**	**Failure mode**
GFRP-P-CR	130	212 (± 65)	267 (± 59)*	C
GFRP-U-CF / P-CR	140	277 (± 16)	-	C

* Taken from points on the load vs. displacement curve corresponding to crack arrest

Key: C – Cohesive failure I – Interfacial failure M – Mixed failure

Table 7-5 – Comparison of mode I testing of the P-CRN and the U-CF / P-CR adhesive systems

From looking at the curves the reader will notice steeply rising R-curves in the case of the GFRP-U-CF / P-CR where carbon nanofibres were placed at the adhesive-substrate interface. A gradual increase in fracture toughness is obtained with increasing crack length. This effect is also reflected in the load vs. displacement traces which exhibit rising stick-slip behaviour. From Table 7-5, the initiation G_{IC} values are similar for both adhesive systems, as expected, when the crack starts from the middle of the joint. However, due to the rising trend of the GFRP-U-CF / P-CR system a mean propagation G_{IC} cannot be computed, but the toughening effect of the nanofibres at the interfaces is apparent. A similar effect on mode I fracture toughness curves has been observed through the use of 'z-pinning' [201,202], a through-the-thickness reinforcement technique for composite laminates. In the case of z-pins, the rising toughness trend is attributed to a 'crack bridging' mechanism as they 'pull-out' of the composite. It is therefore likely that the nanofibres are bridging the mode I crack in these tests in a similar manner to pull-out with z-pins and fibre bridging in other fibrous-composite laminates [142,143].

Figure 7.9 shows an SEM micrograph of the fracture surface after testing the GFRP-U-CF / P-CR system. This micrograph shows nanofibre pull-out and nanofibre bridging.

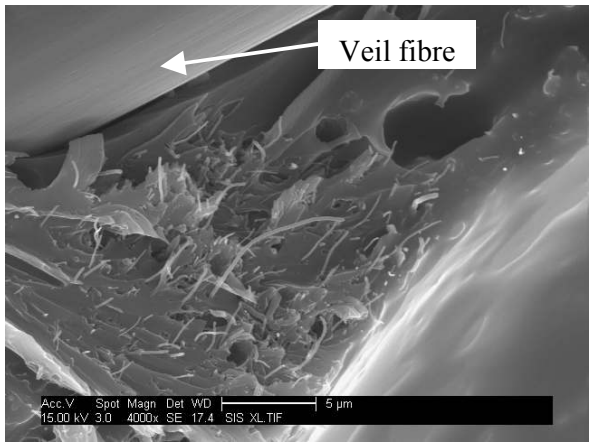

Figure 7.9 – 'Fibre bridging' in the GFRP-U-CF / P-CR joint

However, as the carbon nanofibres are much smaller than the crack opening displacement it is unlikely that the nanofibre bridging detected had an effect on toughness. Z-pins, however, can work much further behind the crack tip as their length is equal to the total joint thickness.

7.2.5 Novel adhesive film against commercially available adhesive films

Figure 7.10 shows the mode I fracture performance of the novel adhesive film, P-CRN, against two commercially available adhesive films FM® 94K and FM® 1515-3M. Three specimens of each adhesive bonded to GFRP were tested. The mode I load vs. displacement curves for the commercially available adhesive films are shown in Figure 7.11. Table 7-6 shows the adhesive bond thicknesses, the initiation and mean propagation G_{IC} values and the mode of failure for each adhesive film.

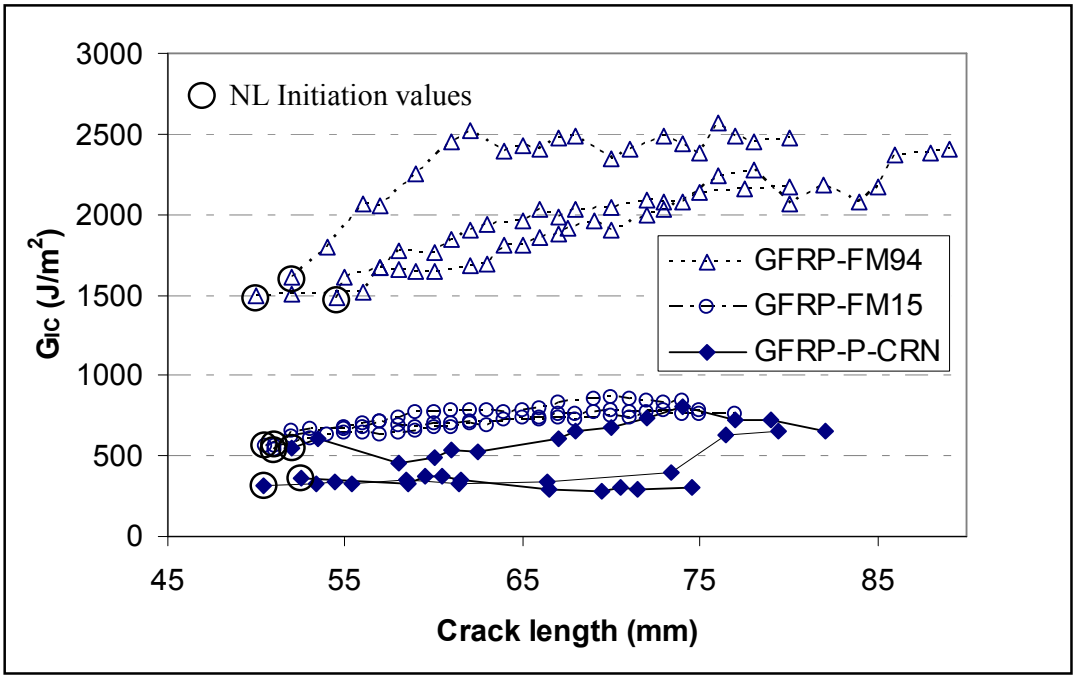

Figure 7.10 – Mode I R-curves for GFRP-P-CRN and the commercially available adhesive films, GFRP-FM94 and GFRP-FM15

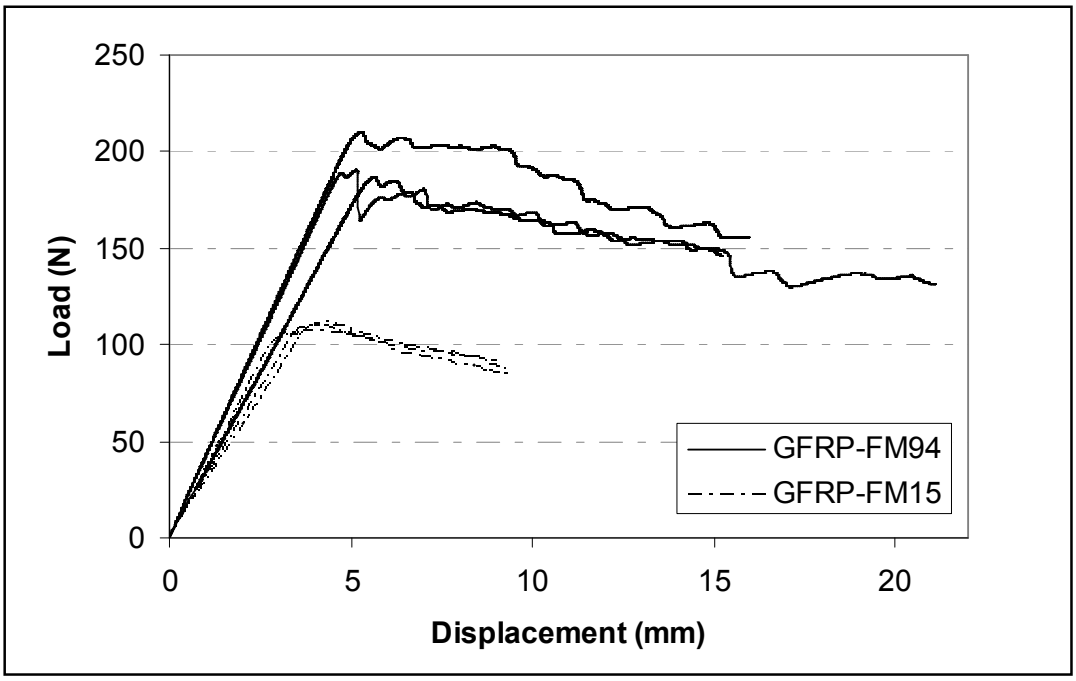

Figure 7.11 – Mode I load vs. displacement curves for GFRP-P-CRN and the commercially available adhesive films, GFRP-FM94 and GFRP-FM15

From these mode I R-curves it can be seen that the FM® 1515-3M adhesive shows a remarkably steady crack propagation. In particular, this commercial adhesive contains a veil with random fibre architecture and, as mentioned previously in Section 4.2.5.1, is known to promote stable crack propagation. A larger scatter is seen in the propagation results of the FM® 94K adhesive film. The honeycomb architecture of its polyester veil performed a 'crack bridging' mechanism through the mode I crack propagation which resulted in rising R-curves. For this adhesive, regions of both cohesive and interfacial failure (mixed failure mode) were observed on the fractured surfaces. The mode of failure for the novel adhesive film (see Figure 7.4) and for FM® 1515-3M (Figure 7.12) was cohesive.

Plate ID	**Bond thickness (μm)**	**Initiation G_{IC} (J/m^2) (NL)**	**Mean propagation G_{IC} (J/m^2)**	**Failure mode**
GFRP-P-CRN	150	407 (± 99)	455 (± 129)*	C
GFRP-FM15	200	554 (± 16)	732 (± 31)	C
GFRP-FM94	220	1527 (± 56)	2080 (± 215)*	M

* Taken from points on the load vs. displacement curve corresponding to crack arrest

Key: C – Cohesive failure I – Interfacial failure M – Mixed failure

Table 7-6 – Comparison of mode I testing for GFRP-P-CRN and the commercially available adhesive films, GFRP-FM94 and GFRP-FM15

The novel adhesive film shows a mode I adhesive fracture energy (~500 J/m^2) closer to the FM® 1515-3M adhesive film (~700 J/m^2) , both of which are far below the values measured for the FM® 94K adhesive film (~2000 J/m^2).

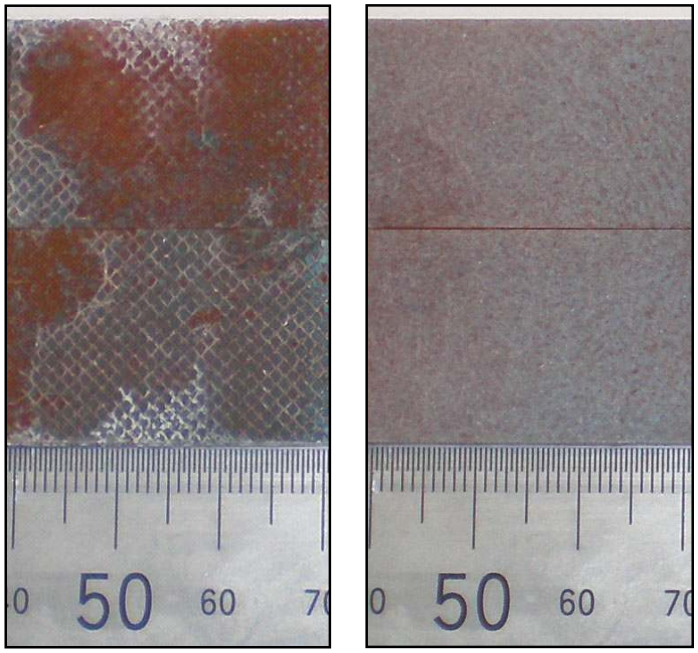

Figure 7.12 – Fracture surfaces images of the mixed mode failed GFRP-FM94 (left) and the cohesive mode failed GFRP-FM15 (right)

7.2.6 Adhesion: GFRP vs. Aluminium alloy

Several DCB tests were carried out for the novel adhesive film and for the commercial adhesive films using aluminium alloy substrates (see Section 4.3.2.3) in order to assess the influence of the substrate material on the fracture performance. These results are compared against those measured previously for the GFRP joints.

Figure 7.13 shows a comparison of mode I propagation R-curves for the novel adhesive film P-CRN bonded to GFRP and aluminium alloy. From these curves it can be concluded that bonding with the aluminium alloy substrate produces a more stable propagation of the crack compared to the GFRP composite substrate. In view of the fracture surfaces illustrated in Figure 7.14, the reason for steadier crack propagation is associated to a more cohesive mode of failure for the Al-P-CRN system.

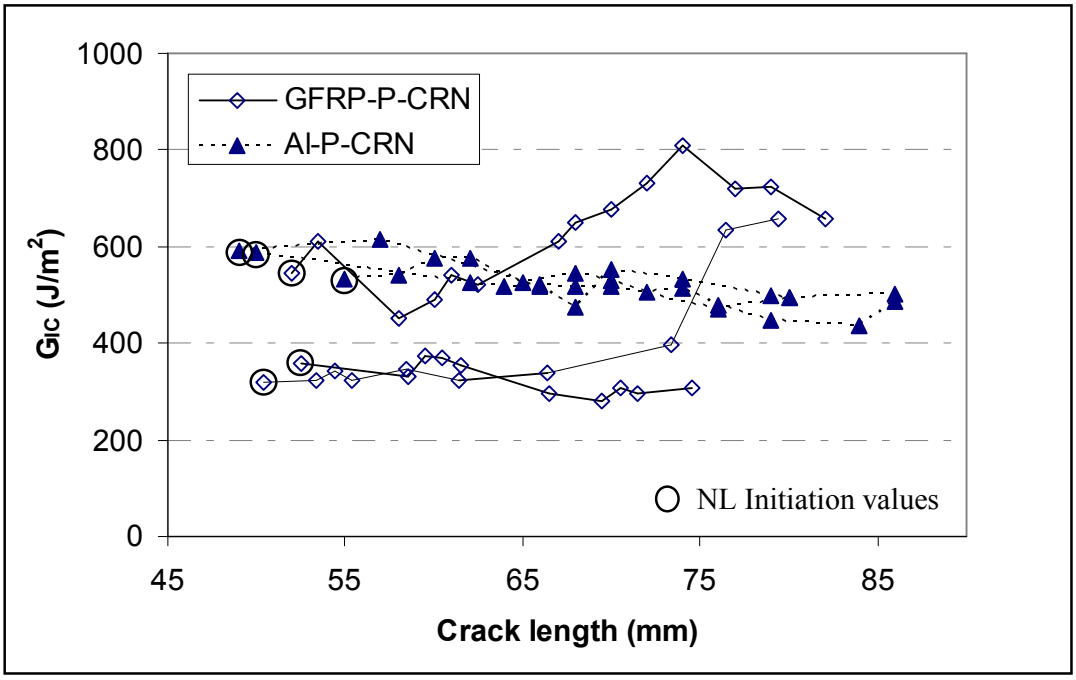

Figure 7.13 – Mode I R-curves for the P-CRN to GFRP & the P-CRN to Al

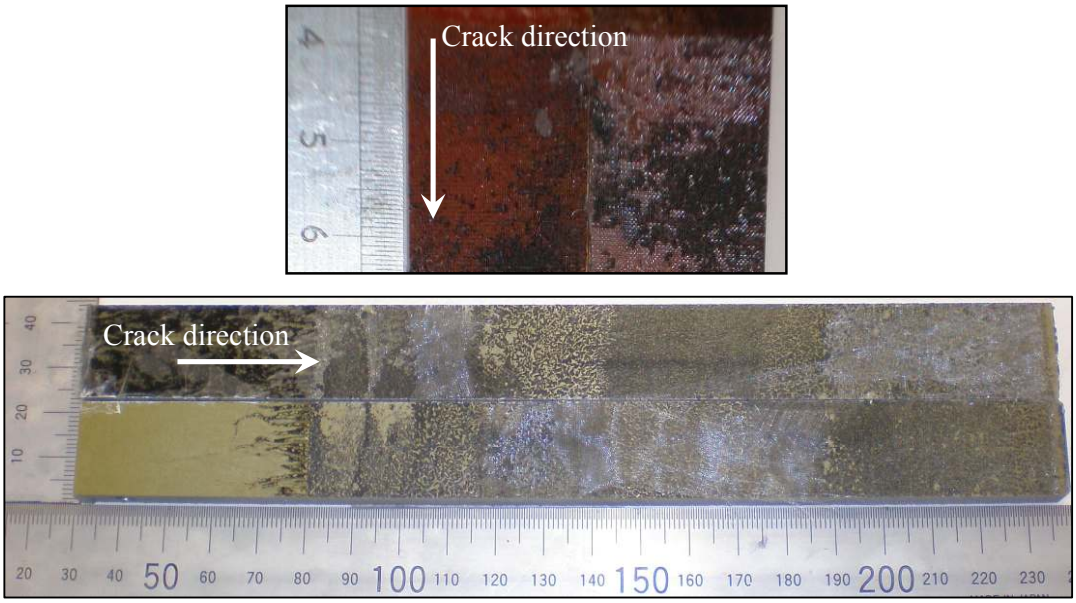

Figure 7.14 – Fracture surface images of GFRP-P-CRN (top) and Al-P-CRN (bottom)

Figure 7.15 shows a plot of the mode I adhesive fracture energy for the novel adhesive film and the commercially available films with aluminium alloy as substrate material.

The data for the commercial adhesives, already analysed in the form of R-curves, were provided by Dr. D. D. R. Cartié during the Bonded Crack Retarders project.

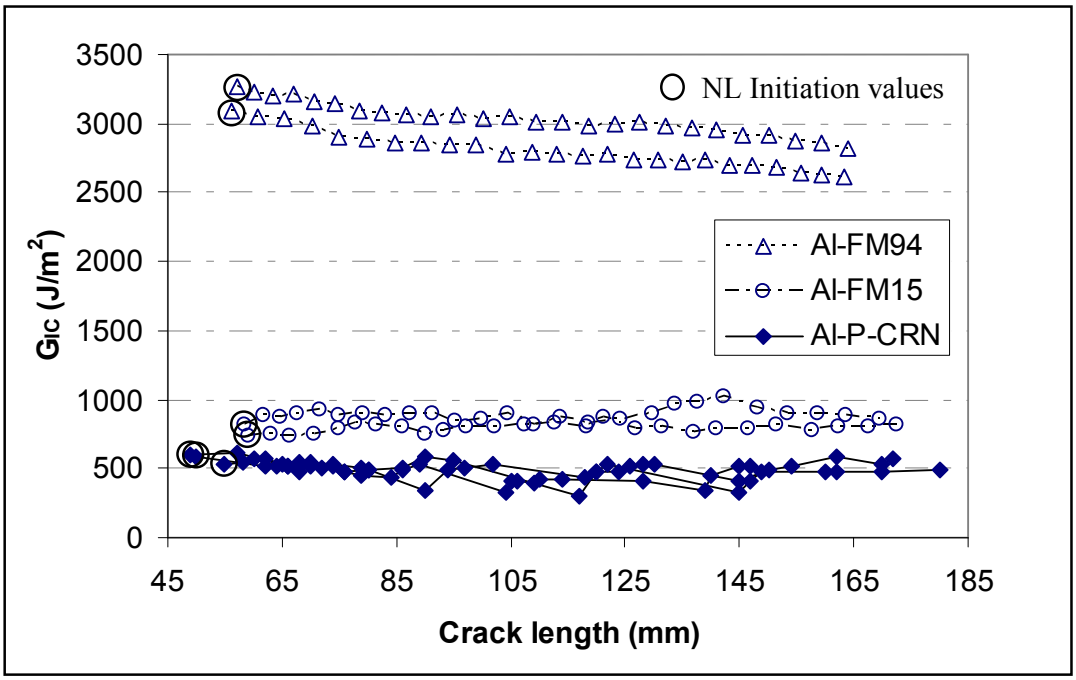

Figure 7.15 – Mode I R-curves for the Al-P-CRN and the commercially available adhesive films, Al-FM 94 and Al-FM15

Again there is an indication of steadier crack propagation when using aluminium alloy rather than GFRP (see Figure 7.10 for reference) and an associated increased cohesive failure tendency. A striking feature of this graph is the apparent decrease in the values of G_{IC} with crack length for the FM® 94K adhesive film. Since G_{IC} is a material property, such apparent dependence with the crack length is unacceptable. The same effect has been reported in literature when testing structural adhesive pastes in DCB joints [151,203]. Lately the test standard [171] has incorporated an empirical system compliance which has proved successful in correcting the significant displacement errors that may be introduced when the very stiff DCB specimens were tested [151]. A further improved calculation of the system compliance has been introduced by the use of an analytical model with the incorporation of adhesive's parameters such as Young's modulus, shear modulus and Poisson's ratio [203]. Presumably, the data for the FM® 94K adhesive film bonding the stiff thick aluminium alloy substrates needs to be corrected for the effect of system compliance. The author could not perform the

correction as the raw testing data needed for this task were not available. However, a general comparison can still be made between the three adhesive films.

Plate ID	Bond thickness (μm)	Initiation G_{IC} (J/m^2) (NL)	Mean propagation G_{IC} (J/m^2)	Failure mode
GFRP-P-CRN	150	407 (± 99)	455 (± 129)*	C
GFRP-FM15	200	554 (± 16)	732 (± 31)	C
GFRP-FM94	220	1527 (± 56)	2080 (± 215)*	M
Al-P-CRN	170	570 (± 34)	487 (± 22)*	C
Al-FM15	200	778 (± 60)	845 (± 71)	C
Al-FM94	220	3180 (± 122)	2911 (± 164)*	C

* Taken from points on the load vs. displacement curve corresponding to crack arrest

Key: C – Cohesive failure I – Interfacial failure M – Mixed failure

Table 7-7 – Comparison of mode I adhesive fracture energy with GFRP and with aluminium alloy substrates

Table 7-7 reports the test results from testing DCB joints of the three adhesive films bonded to both GFRP and aluminium alloy substrates. The G_{IC} values recorded are higher for the aluminium alloy substrate tests compared to those obtained for the GFRP substrate, especially for the commercially available adhesives. Literature has also shown different mode I adhesive fracture energies obtained from different substrate materials [151,204,205], which is in agreement with the results obtained in this work. Further studies have related the substrate dependence to the cured adhesive in the different joints possessing different glass transition temperatures [206]. The existence of pre-bond moisture in composite substrates and variations in heat-up rate during cure were both shown to affect the T_g of the cured adhesive [151]. Additional possibilities within this work for higher G_{IC} values for the aluminium alloy substrates are attributed to the better cohesive mode of failure which are discussed in Chapter 9.

7.2.7 Comparison between resin and joint fracture with reference to plastic-zone models

As introduced in Chapter 2, the more complex behaviour of the adhesively bonded joints compared to cast adhesive samples is caused by the constraints imposed upon the adhesive layer when it is sandwiched between the substrates [41]. Analysis of the plastic zone in the cast samples can assist in predicting the adhesive joint fracture performance.

The plastic-deformation zone diameters for the adhesive formulations have been calculated from fracture mechanics analysis using the resin (bulk) properties G_{IC}, E_f and σ_{yc} as detailed in Chapter 6. The plastic zone diameters obtained for the two conditions, plane-stress and plane-strain, were calculated from equations 2.1 and 2.2 respectively. The Poisson's ratio, v, for all the formulations was taken to be 0.35 [173]. The values obtained are listed in Table 7-8.

Formulation	Plane-stress Plastic zone diameter (μm)	Plane-strain Plastic zone diameter (μm)
C	14	5
CR	40	15
CN	16	6
CRN	65	25

Table 7-8 – Plastic-deformation zone diameters for the different adhesive formulations

The field near the crack tip varies from plane-stress in a very thin specimen, or in the edge regions of a thick specimen, to plane-strain in the central regions of a thick specimen [41]. The increased constraints introduced under the influence of plane-strain conditions elevate the tensile stress necessary for yielding and therefore the plastic zone is smaller. This is confirmed by these results, the plastic zone diameters calculated for the plane-strain condition are consistently smaller than those for the plane-stress

condition. The joints in this work were tested under plane-strain conditions. Therefore, further analysis will use for comparison the plastic zone calculated for plane-strain.

Bulk formu-lation	**Plastic zone diameter (μm)**	**G_{IC} BULK (J/m^2)**	**Equivalent adhesive film ID**	**Bond thickness (μm)**	**G_{IC} JOINT (NL) (J/m^2)**	**Failure mode**
C	5	144 (± 26)	U-C	35	124 (± 19)	C
CR	15	317 (± 36)	U-CR	200	227 (± 29)	M
CN	6	177 (± 15)	U-CN	210	135 (± 5)	M
CRN	25	551 (± 21)	U-CRN	170	196 (± 1)	I

Key: C – Cohesive failure I – Interfacial failure M – Mixed failure

Table 7-9 – Comparison of bulk and joint adhesive fracture test results

Table 7-9 compares the cast adhesive (G_{IC} BULK) and adhesive joint (G_{IC} JOINT) fracture toughness values obtained from mode I tests. The joint fracture results are obtained from GFRP substrates bonded with unsupported films, as detailed in Section 7.2.1.

From the values in Table 7-9 it can be seen that the bond thickness is far larger than the plastic zone diameter for all the formulations tested.

Comparison with the qualitative scenarios set out in Figure 2.11, these large bond thicknesses mean that in all cases the joint is under-constrained (negligible constraint assumed) and thus the G_{IC} JOINT values will be below the possible maximum. In addition the G_{IC} JOINT values should be similar to the values obtained for G_{IC} BULK. This is consistent in the G_{IC} values obtained for the C formulation where the bond thickness is twice the plastic zone diameter. For the CR, CN and CRN formulations the bond thickness ranges from 2.5 to 14 times the corresponding plastic zone diameter and the G_{IC} values become incomparable. The largest discrepancy between the G_{IC} values

occurs for the CRN formulation where interfacial failure was observed which has undoubtedly produced a result which is not representative of the adhesive itself.

Little else can be concluded from these values other than stress the importance for a tight control over the bond thickness through the continued use of veils and an improved 'filming line' manufacturing method.

Table 7-10 details toughness values for the CRN formulation. An additional result is included of a CRN joint containing a polyester veil.

Bulk formu-lation	**Plastic zone diameter (μm)**	**G_{IC} BULK (J/m^2)**	**Equivalent adhesive film ID**	**Bond thickness (μm)**	**G_{IC} JOINT (NL) (J/m^2)**	**Failure mode**
CRN	65	551 (± 21)	U-CRN	170	196 (± 1)	I
			P-CRN	150	407 (± 99)	C

Key: C – Cohesive failure I – Interfacial failure M – Mixed failure

Table 7-10 – Comparison of bulk and joint adhesive fracture for the unsupported and supported CRN adhesive films

One question remains as to why the plastic zone diameter is so dissimilar to the bond thickness. The reason is that the formulations in this work have not been developed to optimise the plastic zone diameter. Future work should concentrate on matching the plastic zone diameter to the veil thickness, which strongly controls the final bond thickness, to achieve the maximum possible G_{IC}. Plastic zone diameter for commercial adhesives is sensitive information. In addition, these products are supplied containing veils making the manufacture of bulk samples impossible. The author would expect for these products, which have undergone many years of development, that the plastic zone diameter would be around 200 μm, far closer to the final bond thickness than has been achieved here.

7.3 Mode II adhesive fracture energy

End loaded split (ELS) tests were performed to obtain the mode II adhesive fracture energy of the adhesive films in this work. Only GFRP substrates were used for these tests. The test coupons were manufactured to the specification detailed in Section 4.3.2.4 and tested as described in Section 5.3.3. Two different thicknesses of GFRP substrates were used thus giving different thicknesses for the final joint coupons. Calibration checks were performed on the test apparatus using a single specimen of each thickness type. For each type of adhesive joint three specimens were tested and analysed. The bondline thickness was measured at three positions along the specimen length using optical microscopy and the average value recorded. The load, displacement and visually determined crack length data were entered into a Microsoft Excel© spreadsheet for data analysis [207]. These spreadsheets automatically performed all the data reduction and plotted the linear regression analyses and the R-curves.

From ELS adhesive test experiments, the lower values of G_{IIC} have always been given by the non-linear initiation points and then a pronounced rising R-curve was always observed, reaching a more or less stable, plateau, region of approximately constant G_{IIC} after some 10 mm of crack propagation [152]. There has been some evidence that G_{IC} is equivalent to a mode II crack initiation value [152]. The elevations in the values of G_{IIC} would appear to originate from the development of the characteristic damage mechanism involving the initiation and propagation of inclined micro-cracks as the ones shown in Figure 7.16 [152,208,209]. Comparison of the propagation results in this work is done with the definition of a 'mean plateau' value of G_{IIC} as the arithmetic mean of the G_{IIC} values recorded over the part of the R-curve with approximately constant values of G_{IIC}.

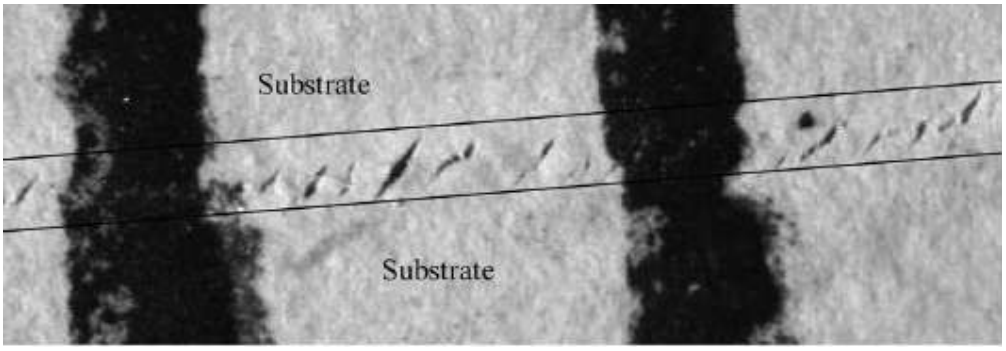

Figure 7.16 – Photographs of micro-cracking in the adhesive layer from ELS testing of an epoxy adhesive film - The vertical black lines are drawn 1mm apart [152]

ELS tests were carried out on the unsupported films U-C, U-CR, U-CN and U-CRN in order to evaluate the mode II fracture energy contribution from each constituent in the formulation. Unfortunately, the crack propagation was unstable for each film. Under these circumstances it was not possible to obtain reasonable values for the mode II adhesive fracture energy. The manufacture of these specimens did not include the use of the surface primer resulting in weak interfacial adhesion and interfacial failure. The results presented later in this section, excluding the commercially available adhesives, were obtained from specimens manufactured with the use of the surface primer, as detailed in Section 4.2.5.4, in an attempt to achieve cohesive failure.

ELS tests on adhesive joints manufactured with aluminium alloy were considered. An initial batch of joints was manufactured and a brief series of trial tests were carried out. The testing could not be completed as the maximum permissible load for the test setup was reached and a crack propagation state could not be reached.

7.3.1 CNTs contribution to the novel adhesive film

Figure 7.17 shows the mode II propagation R-curves for the CRN and the CR films with polyester veil, GFRP-P-CRN and GFRP-P-CR respectively. These R-curves exhibit a strong rising behaviour. At a certain crack length the R-curves level off to a plateau region of approximately constant G_{IIC}. For the P-CRN film, levelling off was observed but not the plateau of a steady propagation. In this case the adhesive failed interfacially

just before reaching the steady state. However, for the P-CR film a steady mode II propagation state was reached with a cohesive mode of failure.

In view of the mode II R-curves, the fracture toughness is higher for the P-CRN film. A contribution to the increase in toughness may be related to the addition of carbon nanotubes in the adhesive formulation. However, the major contribution to toughness is here attributed to a better wetting of the veil by the CRN formulation compared to the CR formulation. This poor wetting by the CR formulation was also highlighted as being responsible for the lower G_{IC} values presented in Section 7.2.3 (see Figure 7.4 and Figure 7.6). The polyester veil architecture, when strongly adhered to the adhesive paste, may 'scrunch-up' in the wake of the crack, under mode II loading, thus applying further resistance to propagation. This is believed to be the main cause for the mode II toughness increase of the P-CRN adhesive film.

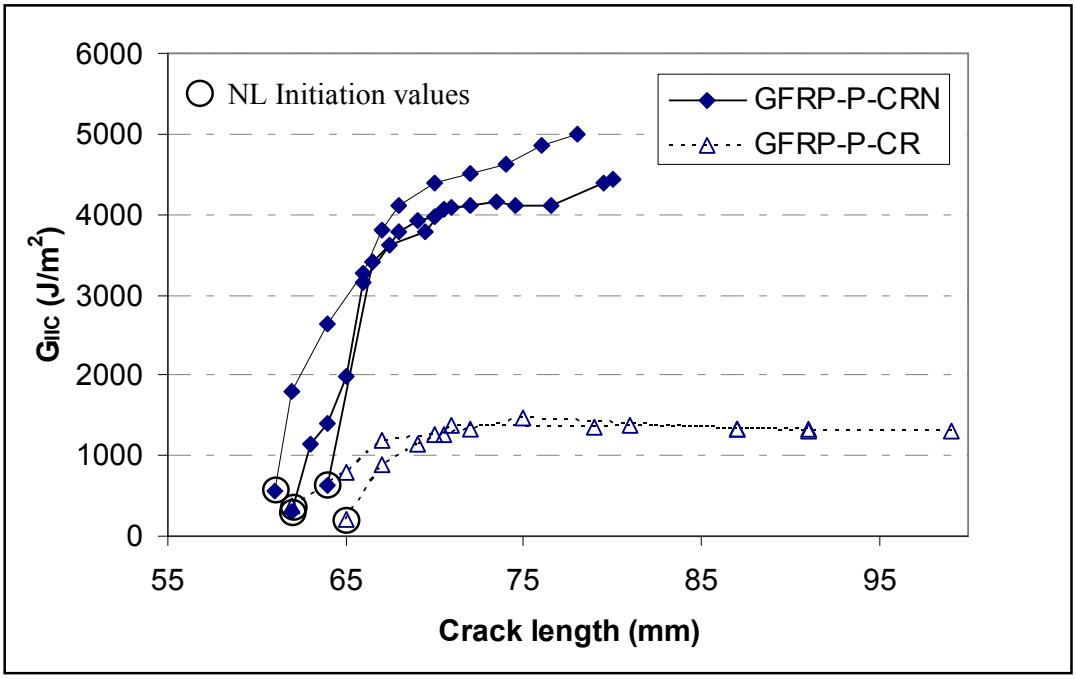

Figure 7.17 – Mode II R-curves for the CRN and the CR formulations with polyester veil

Furthermore, Table 7-11 presents the NL initiation G_{IIC} and the mean plateau G_{IIC} values for the GFRP-P-CR and the GFRP-P-CRN joints. The initiation values are in good agreement with the G_{IC} values listed in Table 7-4.

Plate ID	Bond thickness (μm)	Initiation G_{IIC} (J/m^2) (NL)	Mean propagation G_{IIC} (Plateau) (J/m^2)	Failure mode
GFRP-P-CRN	150	503 (± 167)	4215 (± 230)	M
GFRP-P-CR	130	288 (± 122)	1147 (± 13)	C

Key: C – Cohesive failure I – Interfacial failure M – Mixed failure

Table 7-11 – Comparison of mode II testing of the GFRP-P-CRN and the GFRP-P-CR systems

7.3.2 Targeting nanofillers at the adhesive-substrate interface

Figure 7.18 shows the mode II R-curves for the GFRP-P-CR and the GFRP-U-CF / P-CR joints. As explained in Section 7.2.4 and Section 4.2.6.2 the U-CF / P-CR adhesive system joint consists of two unsupported films containing carbon nanofibres either side of the main polyester veil supported CR adhesive film.

For the GFRP-U-CF / P-CR system, levelling off to a steady propagation state was only observed in one of three specimens tested. Only this specimen failed cohesively whilst the other two specimens failed interfacially, just before reaching the steady state. In view of the mode II R-curves, the fracture toughness is higher for the GFRP-U-CF / P-CR system. The carbon nanofibres at the interfaces of this system may have contributed to the increase in toughness compared to the CR adhesive film. However, the major contribution to toughness is also here attributed to a better wetting of the veil by the U-CF / P-CR adhesive system compared to the CR one, as can be appreciated from Figure 7.19.

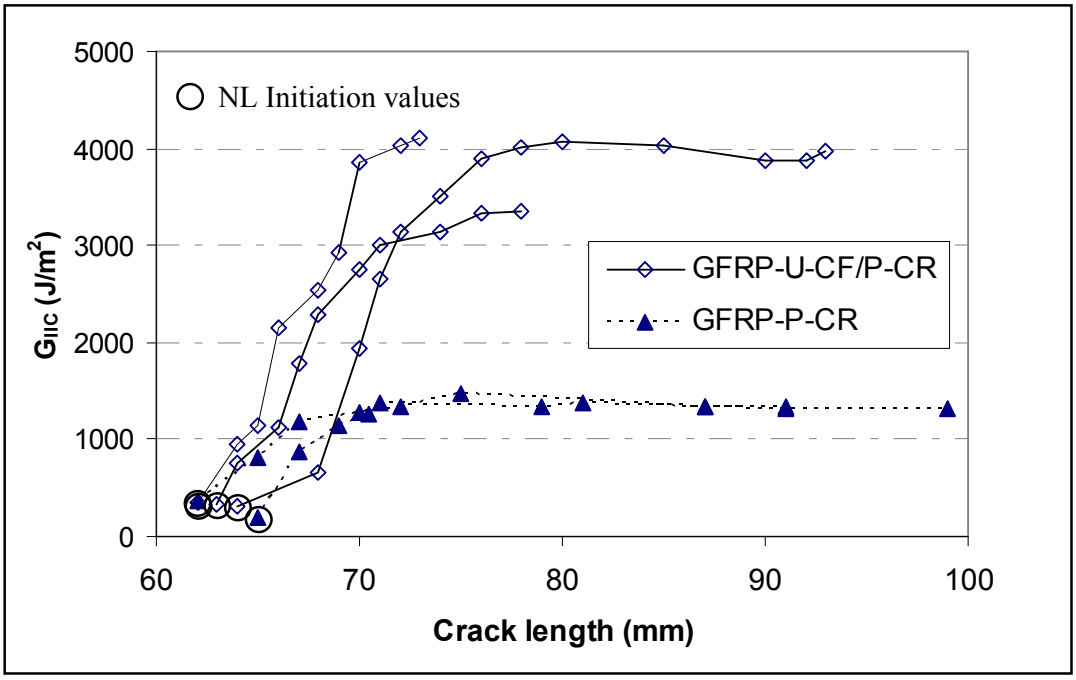

Figure 7.18 – Mode II R-curves for the GFRP-P-CR and the GFRP-U-CF / P-CR joints

Table 7-12 lists the NL initiation G_{IIC} and the mean plateau G_{IIC} values for these two adhesive systems. The initiation values are in good agreement with the G_{IC} values reported in Table 7-5.

Plate ID	Bond thickness (μm)	Initiation G_{IIC} (J/m^2) (NL)	Mean propagation G_{IIC} (Plateau) (J/m^2)	Failure mode
GFRP-P-CR	130	288 (± 122)	1147 (± 13)	C
GFRP-U-CF / P-CR	140	330 (± 10)	3769 (± 364)	M

Key: C – Cohesive failure I – Interfacial failure M – Mixed failure

Table 7-12 – Comparison of mode II testing of the P-CRN and the U-CF / P-CR adhesive systems

Figure 7.19 – Fracture surface images of GFRP-U-CF / P-CR system

7.3.3 Novel adhesive film compared against commercially available adhesive films

Figure 7.20 shows the mode II R-curves for the novel adhesive film, P-CRN and the commercially available adhesive films FM® 94K and FM® 1515-3M, all of them adhered to GFRP substrates.

As well as for P-CRN, the FM® 94K adhesive film showed a strong rising behaviour. At a certain crack length the R-curves level off to a more stable region of G_{IIC}. For the FM® 1515-3M film, levelling off to a steady propagation state is more pronounced. The reason behind this effect is attributed to its random fibre architecture veil which promoted more stable crack propagation. In this case the veil could have not developed the 'scrunching-up' effect previously related to the polyester veil architectures and therefore offered less resistance to the propagation of the crack.

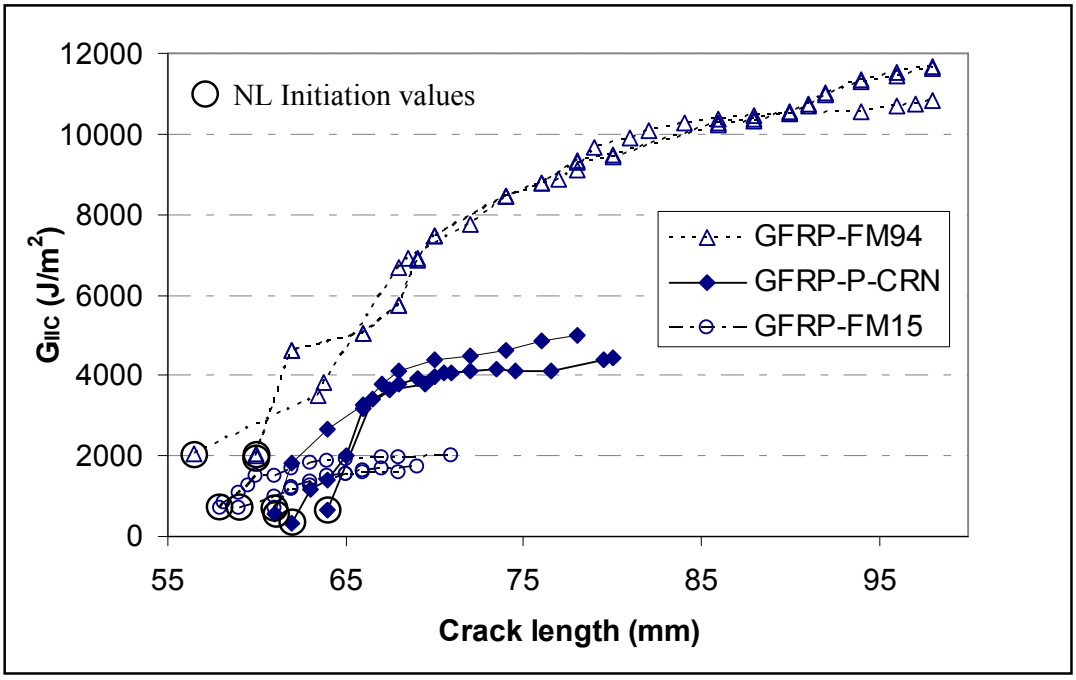

Figure 7.20 – Mode II R-curves for the GFRP-P-CRN and the commercially available adhesive films

Plate ID	Bond thickness (μm)	Initiation G_{IIC} (J/m^2) (NL)	Mean propagation G_{IIC} (Plateau) (J/m^2)	Failure mode
GFRP-P-CRN	150	503 (± 167)	4215 (± 230)	M
GFRP-FM15	200	704 (± 9)	1718 (± 195)	M
GFRP-FM94	220	2036 (± 13)	10828 (± 148)	M

Key: C – Cohesive failure I – Interfacial failure M – Mixed failure

Table 7-13 – Comparison of mode II testing for the GFRP-P-CRN and the commercially available adhesive films

Table 7-13 reports the G_{IIC} values for the novel adhesive film, P-CRN and the commercially available adhesives, FM® 94K and FM® 1515-3M. As expected, the initiation values are in good agreement with the G_{IC} values previously reported in Table

7-6. Under mode II loading conditions the novel adhesive film proved to be tougher than the FM® 1515-3M commercial adhesive film mainly due to the different veil architecture.

7.4 Fatigue crack propagation

A specialist structure for measuring the effects on fatigue crack propagation was prepared by bonding two unidirectional GFRP straps to one side of an aluminium alloy sample, as detailed in Section 4.3.2.5. This bonded crack retarder (BCR) structure was tested as described in Section 5.3.4 in order to obtain its crack growth rate.

The results obtained from the fatigue test are compared here against two similar structures which were manufactured, tested and analysed within the project in which this work was involved. The first one was the aluminium alloy plate without straps. The second one was the aluminium alloy plate with the identical unidirectional GFRP straps bonded together with the FM® 94K commercial adhesive film. Crack length vs. number of cycles curves obtained from testing these structures are presented in Figure 7.21.

There is a significant increase in the fatigue life for the two GFRP reinforced structures over the un-strapped aluminium alloy structure. As mentioned in Chapter 5, fatigue life is considered here as the point at which ultimate failure of the structure occurs. This increase in fatigue life is largest for the straps bonded with the novel adhesive film created in this work. The novel adhesive film provided a 30% increase in the structure life compared to the commercial adhesive.

For the straps bonded with FM® 94K adhesive the fatigue retardation, which is indicated by a change in the curvature of the recorded trace, started when the crack front encountered the edge of the strap. However, for the novel adhesive film structure, the retardation appeared when the crack front was approximately at the strap centreline.

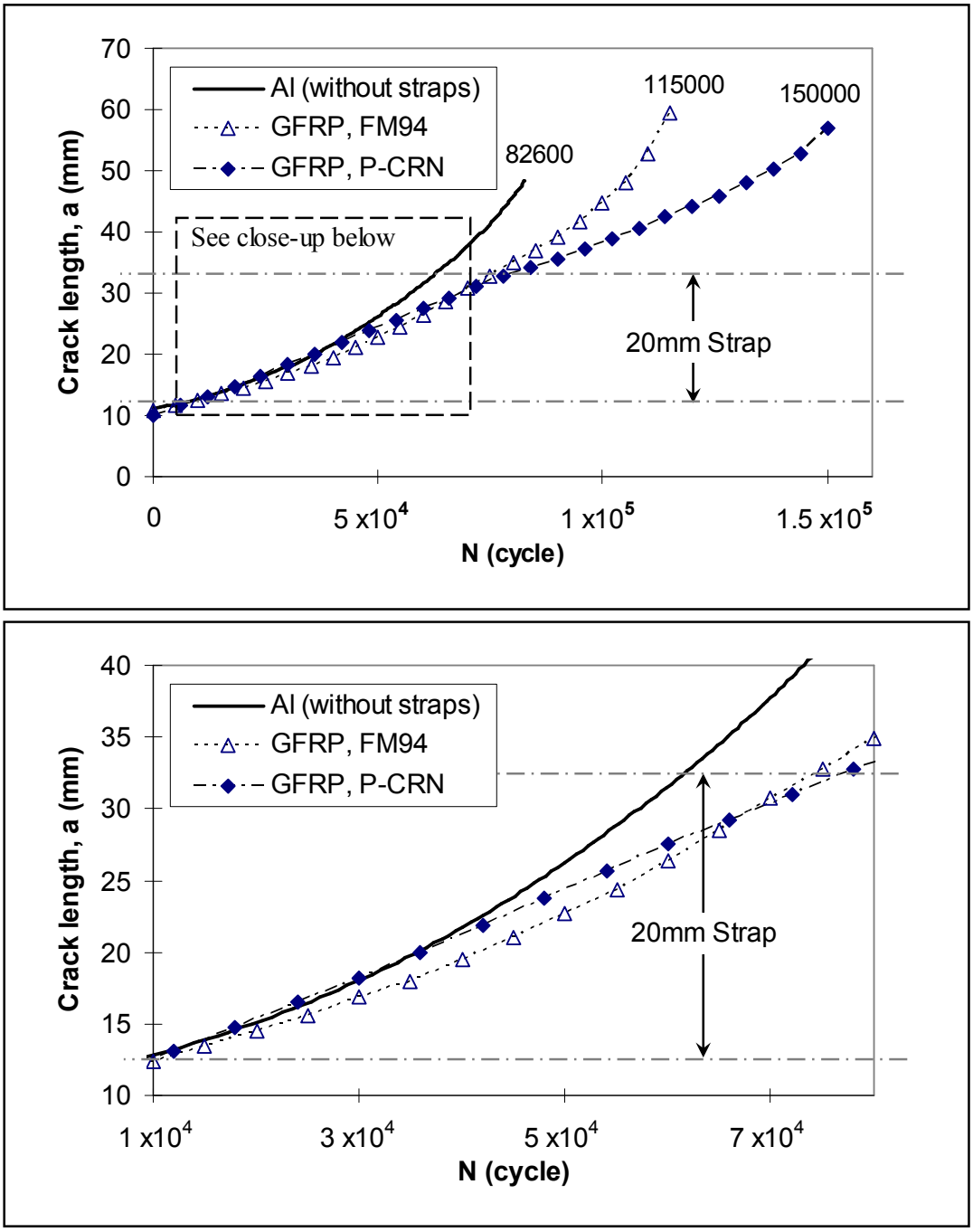

Figure 7.21 – Crack length vs. number of cycles and close-up for the Al without straps, the Al with straps bonded with FM® 94K and the Al with straps bonded with the novel adhesive film

The same effect is reflected in the crack growth rate curves plotted in Figure 7.22. The fatigue crack growth rates for the reinforced aluminium alloy plates were significantly lower than those for the un-strapped aluminium alloy plate. For the FM® 94K bonded plate the crack growth rate gradually decreased as the crack grew under the straps, the rate being two times lower at the end of the reinforcements than for the un-strapped plate. However, for the straps bonded with the novel adhesive film there was an abrupt decrease in the crack growth rate, occurring when the crack was passing through the middle of the straps. For this structure the crack growth rate was three times lower than for the un-strapped structure. In order to explain this unusual effect, whereby the retardation occurs midway through the strap, inspection of the fracture surfaces was carried out.

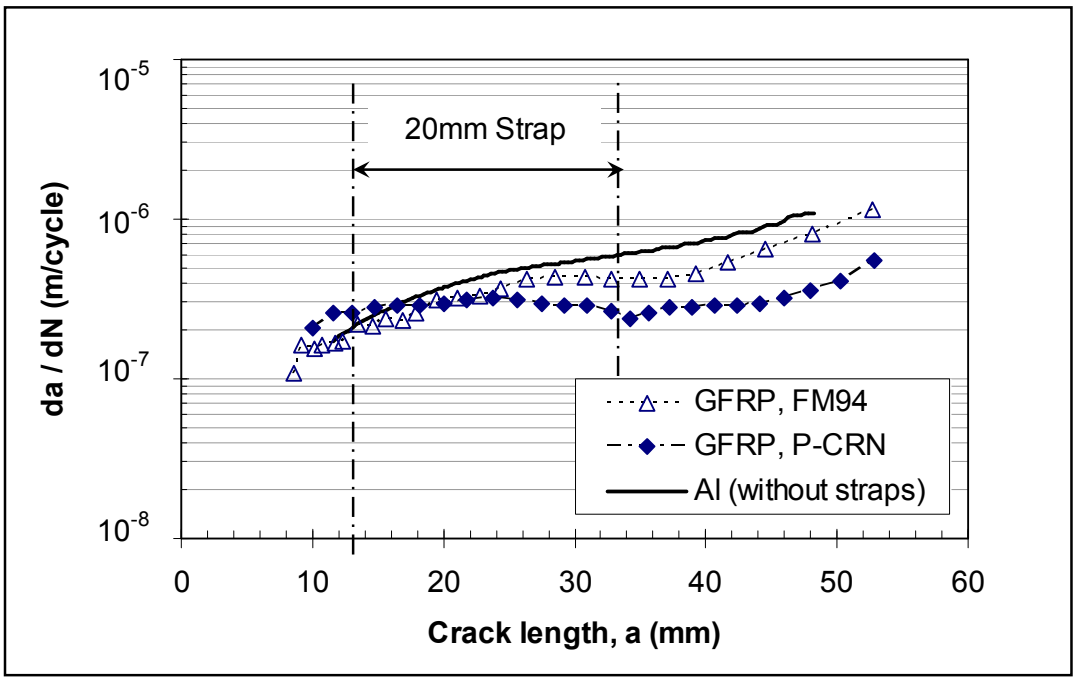

Figure 7.22 – Crack growth rate vs. crack length for the Al without straps, the Al with straps bonded with FM® 94K and the Al with straps bonded with the novel adhesive film

Figure 7.23 shows the fracture surfaces for the aluminium alloy plate and straps bonded with FM® 94K adhesive. In this structure the adhesion was good and homogeneous all over and a cohesive failure was observed.

Figure 7.23 – Fracture surfaces images for the Al structure with FM® 94K adhesive film after fatigue crack propagation

The images in Figure 7.24 show the fracture surfaces of the structure bonded with the novel adhesive film. The straps remained attached to the aluminium alloy plate until final fracture. Upon fracture of the plaque, the lower half of both straps dis-bonded whilst the upper half remained bonded. The adhesive showed cohesive failure on both the glass fibre straps and in the aluminium alloy plate surfaces. However, the zoomed detail (bottom left) shows that during the cure process, whilst the strap was bonded in the correct position, the adhesive slipped from under the strap, most likely due to the pull of the applied vacuum. The fracture surfaces show poorer adhesion occurred in these areas. This is the likely cause of the retardation of the crack starting away from the edge of the strap as for the FM® 94K bonded structure. It is necessary to remember that, unlike the FM® 94K adhesive, the novel adhesive film does not contain rheological additives usually employed to control the flow properties [90].

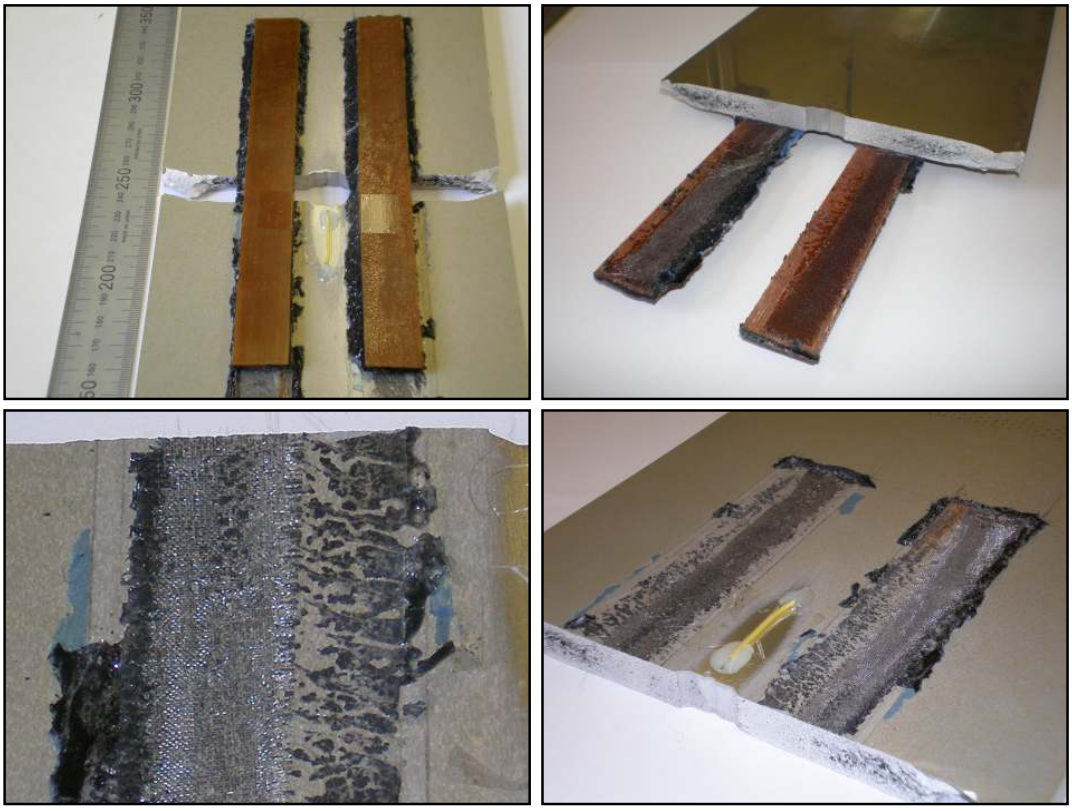

Figure 7.24 – Fracture surfaces images for the Al plate reinforced with the use of the novel adhesive film (P-CRN) after fatigue crack propagation

Figure 7.25 shows an ultrasonic scan taken of the FM® 94K bonded strap that remained attached to the structure after testing. After global failure of the structure the delaminated or dis-bonded area was widespread. Only a small proportion of the strap remained bonded to the aluminium alloy plate.

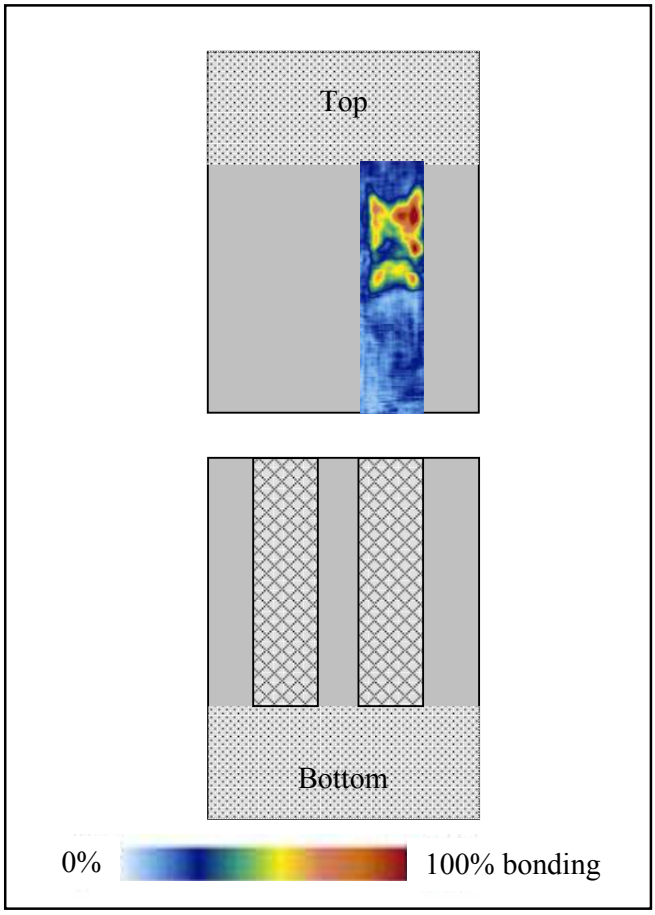

Figure 7.25 – Scans of fatigue crack growth test with the FM® 94K adhesive after failure

Figure 7.26 shows ultrasonic scans taken from the straps bonded with the novel adhesive film before and after fatigue crack growth testing. Well bonded regions indicated by the scans are in good agreement to those observed visually (see Figure 7.24) as well as the poor adhesion and the slippage of the film mentioned above. Comparing the scans after failure for the novel adhesive film and the commercial one it can be concluded that the increased life is due to the novel adhesive film enabling the straps to remain adhered to the structure right up until final fracture.

Even though an apparent increase in fatigue life by the novel adhesive film has been observed compared to the commercial FM® 94K adhesive film, there remain questions. These include for example, the performance of both adhesives on mode I and mode II fatigue and high rate delamination behaviour, beside the interpretation of the data.

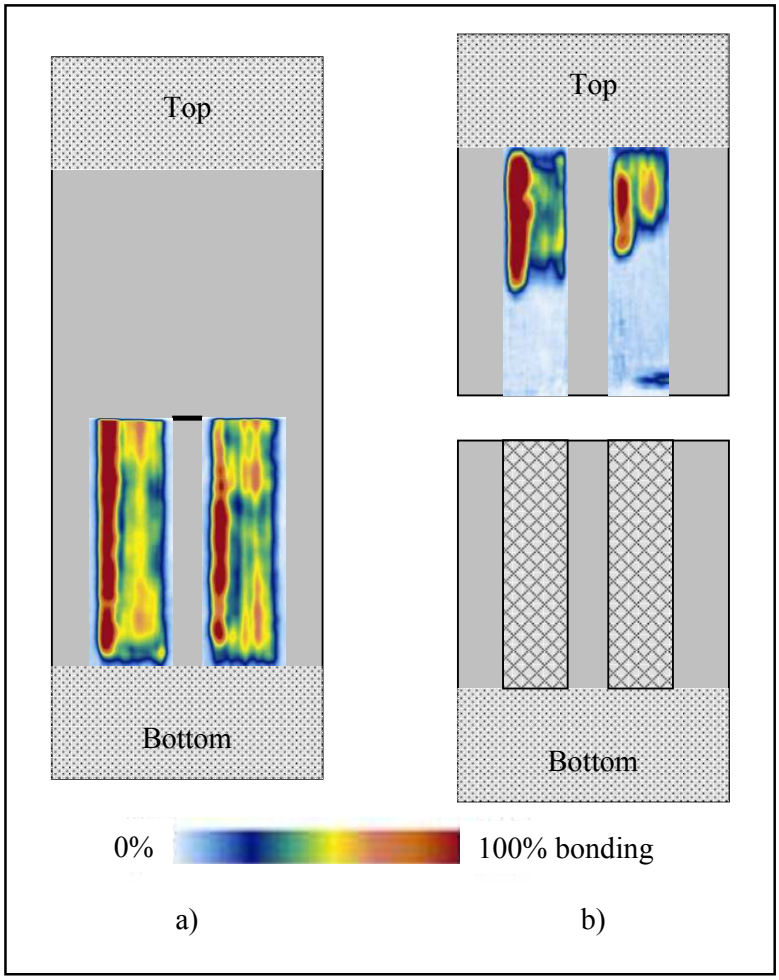

Figure 7.26 – Scans of fatigue crack growth test with the novel adhesive film, a) before and b) after failure

Summary

The novel adhesive formulation in bonded specimens has shown a good overall performance when tested mechanically under mode I, mode II and fatigue conditions. Moreover, its behaviour compared well against commercially available adhesive films when bonded to both composite and metal.

Chapter 8

Overall discussion

This chapter draws together some of the points of discussion raised during this work. Attention is given to the state of the art in the literature at this early stage in the research of carbon nanotubes incorporated in epoxy resins. The production of the novel adhesive film brought additional challenges to this work and these are summarised here also. Discussion on the effects of adding carbon nanotubes to the toughened epoxy used in this work is also made. Finally, the author suggests the most promising direction for future research for this attractive ternary blend of epoxy, CTBN rubber and commercial carbon nanotubes.

8.1 Literature outlook of carbon nanotubes in epoxy resins

The discovery of carbon nanotubes, nearly two decades ago, opened the door to the world of nanoscience and nanotechnology. Since the 1990s, there has been extensive publication by a large number of researchers around the world in this field and thus it has become extremely evident that carbon nanotubes are an important component of the future of material science.

However, some statements in the literature seem to have inflated the potential of nanotechnology. Stating that carbon nanotubes are 100 times stronger at one-sixth the weight of steel is misleading, because nanotubes are nanoscale orthotropic molecules and steel is an isotropic bulk material and the two are not directly interchangeable [51,210]. Another seeming overstatement appeared in a New York Times article: "Today's vision of the science tomorrow", January 2003 [184]. In this article it was predicted that nanotechnology will lead to aerospace vehicles with 98% less structural mass. It is interesting to speculate how long it will take the aerospace companies to meet this prediction.

From virtually the moment nanotubes were discovered it was expected that they would display superlative mechanical properties by analogy with graphite [51] (see Figure 8.1). Therefore, initially the most promising area of composites research involved the mechanical enhancement of polymers using carbon nanotubes as reinforcing fillers. Since it was found that the properties of the resulting nanocomposites were not as expected the research community started efforts on improving the degree of dispersion, impregnation with matrix and the interfacial adhesion. However, enhancement of the mechanical properties of advanced composites materials will require much further investigation and this is definitely a challenging area for the composite community.

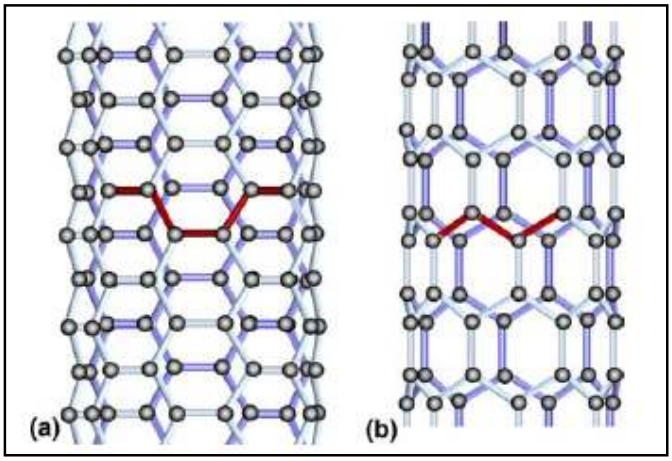

Figure 8.1 – Illustrations of the atomic structure of (a) armchair and (b) ziz-zag carbon nanotubes [50]

The initial disappointment with the poor mechanical reinforcement achieved by the inclusion of carbon nanotubes turned the research towards their exceptional electrical and thermal properties. Later studies encountered that the processing requirements necessary to enhance the electrical conductivity in the resulting nanocomposite contradict those which are employed to promote mechanical reinforcement.

After almost 20 years, the diversity in scientific investigations, technology advancements, processing innovations and product development is staggering. A significant number of excellent review papers [4,50,51,64,211] and books [210,212-214] are available that chronicle and summarise the status of carbon nanotubes reinforcing epoxy resins. However, there is still the need to assemble the interdisciplinary research in order to understand, tailor and optimise properties and avoid making false statements.

Carbon nanotubes have recently become a part of the established modern technology portfolio, but the most significant accomplishments of these nanomaterials are still ahead.

8.2 Design and manufacture of the novel adhesive film

An iterative process of trial and error processing studies together with an increased understanding of the materials science relating to the adhesive constituents has been the basis of the development of the novel adhesive film in this work. The requirement of the adhesive to be processed in film form took the development process far beyond the fundamental mixing of the constituents and was a major challenge throughout the work. The filming process itself needed to be fine-tuned over time as the author's experience and skill level developed in order to achieve high quality, reproducible and homogeneous adhesive films. Similar processes of development are still applied by the main adhesive film manufacturers today. In industrial manufacturing environments hundreds of adhesive formulations may be formulated from which only a few will pass preliminary manufacturing trials leading into production.

The overall design process of the novel adhesive formulation looked at different variants and concentrations of carbon nanotubes and CTBN rubber, as explained in Chapter 4. Preliminary tests carried out in parallel to the design process aided the decision making process. The trial and error based manufacturing development focused on the physical characteristics of the adhesive paste in order for the final adhesive film to be handled.

The filming process was improved by the use of the veil which assisted the homogeneous dispersion of the adhesive paste and improved the handling characteristics of the final film. However, it was also learned that both the veil fibre type and architecture were of considerable importance, alongside the physical characteristics of the adhesive paste, in order for the final product to bind together into a homogeneous film.

Another important issue was the lab-scale 'filming line' used in this work. This consisted of a hotplate, an aluminium carrier plate covered with silicone coated release paper and a doctor blade. This lab-scale 'filming line', whilst consisting of the same

manufacturing stages, was very basic in comparison to the complex industrial adhesive manufacturing equipment (see Figure 8.2 compared to Figure 4.17). One difficulty was holding the veil under tension to keep it flat whilst applying the adhesive paste in order to avoid wrinkles in the resulting film.

Figure 8.2 – Industrial adhesive film manufacturing line [215]

After identification of interfacial failure during the early stages of the adhesive joint testing, a decision was taken to improve the wetting of the substrates through the use of a primer. The idea was to use a similar formulation to the novel adhesive with reduced viscosity before applying the adhesive film. The primer formulation chosen was CR, equivalent to the CRN formulation without the carbon nanotubes. The CR primer formulation, applied using a razor blade as a very thin layer on the substrate surface, prevented the occurrence of interfacial failure.

In summary, the design and lab-scale manufacture of the novel adhesive film produced a good prototype product that compares well to the commercial adhesives used in this work in terms of appearance, quality and the ability to be handled.

8.3 Effects of carbon nanotubes on an epoxy / CTBN system

One of the characteristics of epoxy resins toughened with CTBN rubber is the high viscosity of the resulting blends. When carbon nanotubes were dispersed into these systems, especially at the required filler weight fractions of 0.3 wt%, a further increase in the viscosity of the mixture was obtained. The processing conditions for these ternary samples were different as documented in this work. The carbon nanotubes have a tendency to form agglomerates and to disperse these in the high viscosity mixtures required the use of sonication and higher shear-mixing rates. Moreover, in order to manufacture homogeneous samples without air bubbles from these highly viscous systems, a degassing technique needed to be developed (see Section 4.2.2).

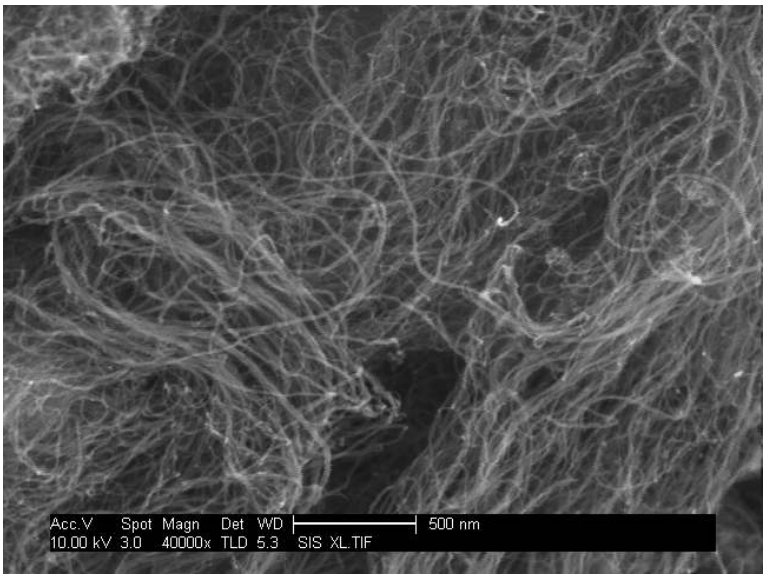

Figure 8.3 – SEM micrograph of the NC-7000 multi-walled carbon nanotubes as supplied, showing a highly-entangled structure

The high viscosity of the CTBN rubber was an initial drawback when trying to add and disperse the carbon nanotubes into the formulation. However, this high starting viscosity of the CRN mixture was beneficial in maintaining the quality of the carbon nanotube dispersion, by preventing the re-agglomeration during cure that is otherwise often observed in thermosetting nanocomposites [4,78].

The addition of CTBN rubber to an epoxy resin leads to the formation of a two-phase morphology of an epoxy matrix with imbedded glassy rubber particles. As previously explained in Chapter 2, considerable work has shown that the separation of the elastomer into a separate phase is necessary for significant toughening to occur and to retain the bulk properties of the epoxy system. Thus, particle size and distribution of the elastomer phase is very important. Figure 8.4 indicates the distribution and size of the rubber particles for the CR formulation of this work.

When carbon nanotubes were added to the epoxy / CTBN system the most notable effect found in this work was a reduction of the mean rubber particle size in the resulting system. As discussed in Chapter 6, this decrease in size with the addition of the carbon nanotubes is thought to be associated with the increase in viscosity of the system caused by the dispersed nanotubes, which may inhibit the growth of the rubbery domains in the pre-gel phase. The possibility of particle nucleation being enhanced by the nanotubes cannot be discounted either, but has not been demonstrated. Recent research has shown carbon nanotubes acting as seeds for nucleation and growth of large thermoset-rich domains when added to an epoxy-thermoplastic resin system [106,216].

The synergistic effect in toughness found in the ternary system of this work along with the good overall balance of properties presented are believed to be associated to the specific morphology of these systems. Figure 8.4 and Figure 8.5 show the distribution and size of the rubber particles for the CR and CRN formulation of this work. Whilst difficult to quantify, the mean size of the rubber particles was demonstrably larger in the CR formulation than in the CRN sample.

To date, the processing of these ternary blends still remains a challenge and small amounts of clusters could not be avoided in this work. However, this ternary system provided a significant electrical conductivity at a low level of carbon nanotube inclusion without a compromise in the thermo-mechanical performance of the blend. The resulting properties along with the specific morphology of these systems make them extremely attractive for future research.

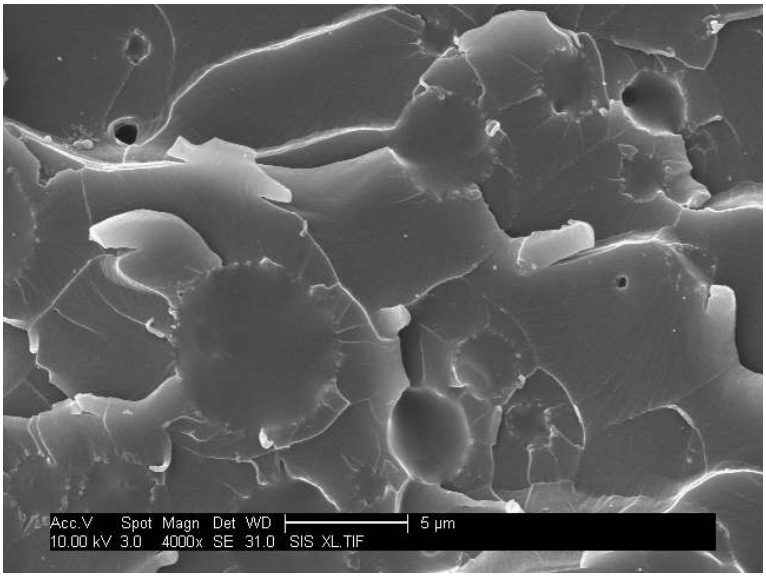

Figure 8.4 – SEM micrographs of etched fracture surfaces of CR formulation

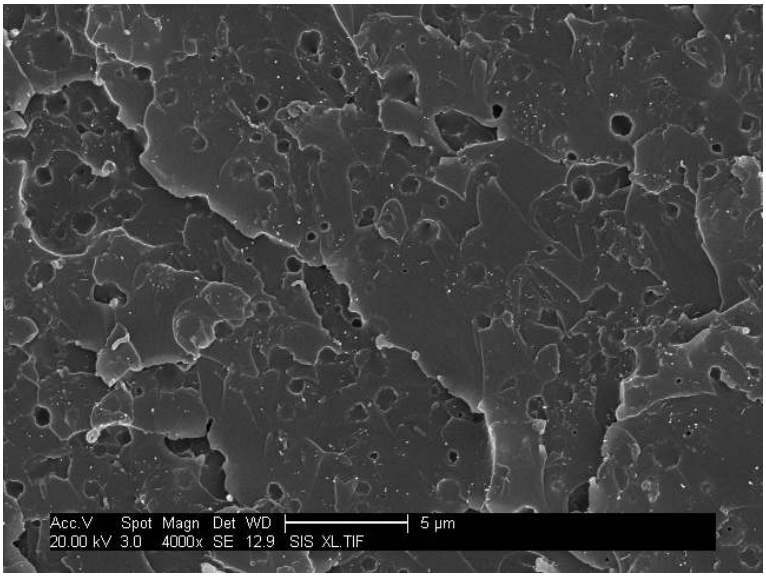

Figure 8.5 – SEM micrographs of etched fracture surfaces of CRN formulation

8.4 Reinforcement or conductivity – the way forward?

Neat carbon nanotubes were included in this novel adhesive formulation as they were believed to be capable of reducing the coefficient of thermal expansion as well as

toughening the formulation considerably. Ultimately, a negligible reduction in the CTE has been obtained so the inclusion of carbon nanotubes fails to deliver on the initial promise. In terms of the mechanical performance, the addition of nanotubes alone showed no significant effect. However, the inclusion of nanotubes and rubber provides a further increase in fracture energy that, accompanied by an increase in the electrical conductivity, gives the solid CRN formulation an attractive overall balance of properties. The hypothesised increase in electrical conductivity was originally considered to be of secondary importance for the intended application but has now become the most attractive functionality of neat carbon nanotube use.

As mentioned in Chapter 2, the very high conductivity of carbon nanotubes makes them excellent candidates for the production of conductive epoxy adhesives, capable of dissipating electro-static charge build-up [18,79,81] and the present work shows that the required conductivity levels conductivity exceeding 10^{-6} S/m can be achieved without compromising mechanical properties such as flexural modulus or compressive yield strength.

Recent research has shown the attainment of a high level of electrical conductivity at low carbon nanotube concentrations in epoxy resins, 0.005 phr being the lowest critical filler content reported so far [64]. This work has shown that the carbon nanotube contribution to reducing the coefficient of thermal expansion cannot be considered significant and that their effect on enhancing toughness was not as expected. Therefore, the carbon nanotubes' role in the adhesive formulation should be increasingly focused on electrical properties. In this context the author's recommendation is to decrease the carbon nanotube content in the adhesive formulation. Electrical conductivity can be maintained at lower carbon nanotube contents and the resulting decrease in the viscosity of the adhesive paste will allow for increasing the rubber content to levels such as those used in commercially available toughened adhesives, typically 15-20 wt% [137,217].

However, attention must be given to a possible reduction in the electrical conductivity by the high amount of CTBN rubber which can change the resulting adhesive morphology. Previous research has shown an increase in the concentration of the rubber

could lead to phase inversion, with discrete epoxy particles separated by a continuous rubber phase [195,218-220]. Figure 8.6 illustrates the change in morphology through increasing the rubber concentration. In the 'normal' structure the electrical conductivity has been shown to increase with the inclusion of rubber particles. The higher conductivity is explained by the higher concentration of the carbon nanotubes in the epoxy phase which provides the conductive pathway. However, in the phase-inverted structure the carbon nanotubes can remain localised within the discrete epoxy particles and thus the conductivity is expected to be lower as a conductive pathway cannot be formed. This could be changed if the carbon nanotubes were localised at the boundaries between the two phases [106,216], as shown in Figure 8.7.

It is essential to know the final morphology of the ternary system, as well as the position of the carbon nanotubes within the structure, in order to get the greatest benefit from the electrical conductivity of these nanofillers.

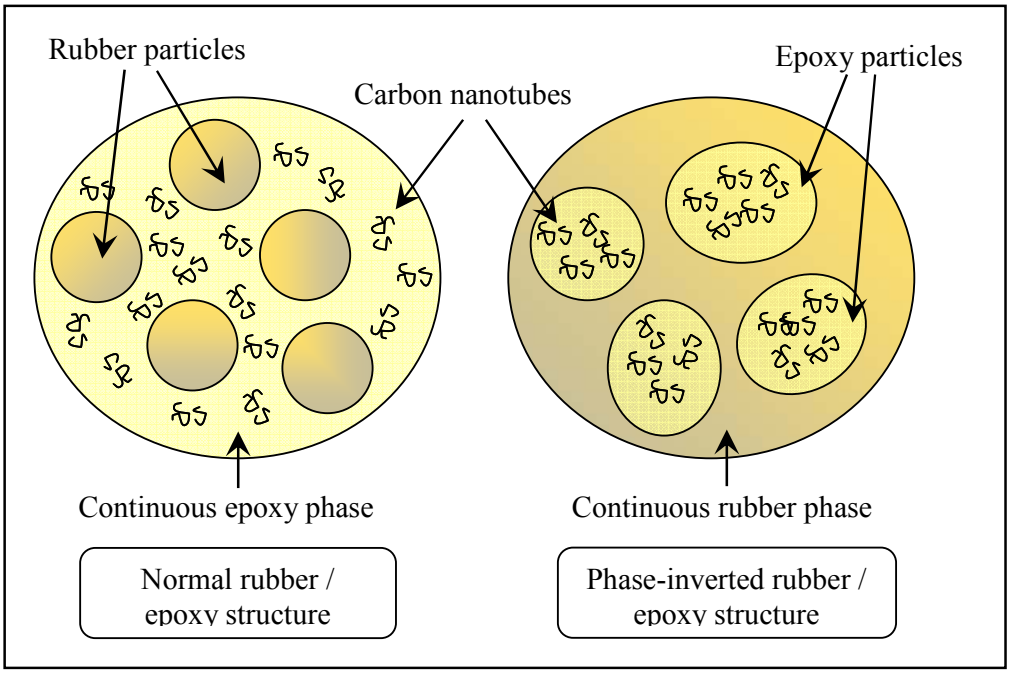

Figure 8.6 – Possible morphology change in the thermosetting ternary blend with an increase in the rubber concentration

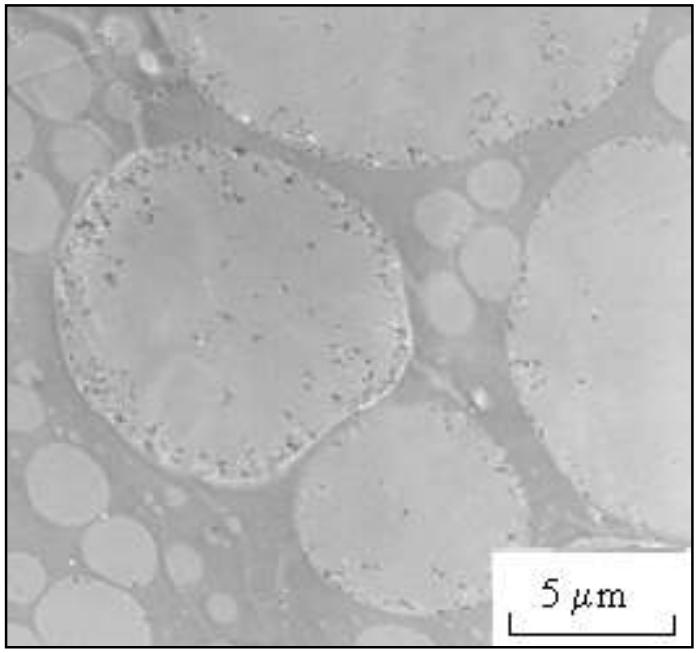

Figure 8.7 – TEM micrographs of an epoxy-thermoplastic system containing 2 wt% of carbon black showing selective localisation of the nanoparticles between the two phases [216]

Summary

This discussion has been focused on the ternary blend of epoxy, CTBN rubber and commercial carbon nanotubes which is the centre of the present study. The good overall balance of properties along with the significant electrical conductivity reported makes them attractive blends for future research.

Chapter 9

Conclusions and suggestions for further work

9.1 Conclusions

1. Microscopy studies have shown a reduction of the mean rubber particle size from 3μm to below 1μm with the addition of the carbon nanotubes in the CRN ternary blend. The synergistic effect on toughness found is believed to be associated to the specific morphology of this system as toughening is enhanced by small rubber particles.

2. The cure kinetics of the novel adhesive formulation, CRN, follows autocatalytic behaviour. The 10% reduction in the CRN total reactivity compared to CR indicated that the presence of the carbon nanotubes reduced the final crosslinking density under dynamic conditions.

3. The expected toughening effect of the phase separated rubber particles is observed, from 144 to 317 J/m^2, with a further increase to 551 J/m^2 in the presence of the carbon nanotubes. In the absence of the rubber, the nanotubes alone produce a minimal effect upon the thermo-mechanical and mechanical characteristics of the resin.

4. Characterization of the cast samples has shown that the base formulations, C and CR, are pure capacitive materials whilst the formulations containing carbon nanotubes, CN and CRN, are conductive materials. The electrical conductivity has been found to increase by six orders of magnitude, up to 1.6 $x10^{-3}$ S/m in the CN and 3.6 $x10^{-3}$ S/m in the CRN ternary blend for a 0.3 wt% concentration of carbon nanotubes.

5. Initial findings of interfacial failure occurred for the films containing carbon nanotubes due to their high viscosity which inhibited wetting of the substrate surfaces while bonding. The use of a 'home-made' surface primer proved to be successful in achieving cohesive or mixed failure.

6. A 'bonded crack retarder' fatigue test has been performed to show the behaviour of the novel adhesive film in an application where damage tolerance is required. The novel adhesive film provided a 30% increase in the structure life compared to the FM® 94K commercial adhesive film.

9.2 Suggestions for further work

9.2.1 Improving the filming process

The manufacture of supported adhesive films was reported in Chapter 4. The processing consisted of spreading the adhesive paste over the veil which was carried out on a hot plate. This was followed by cooling and 'warming plus pressure' periods to form the adhesive into thin film sheets.

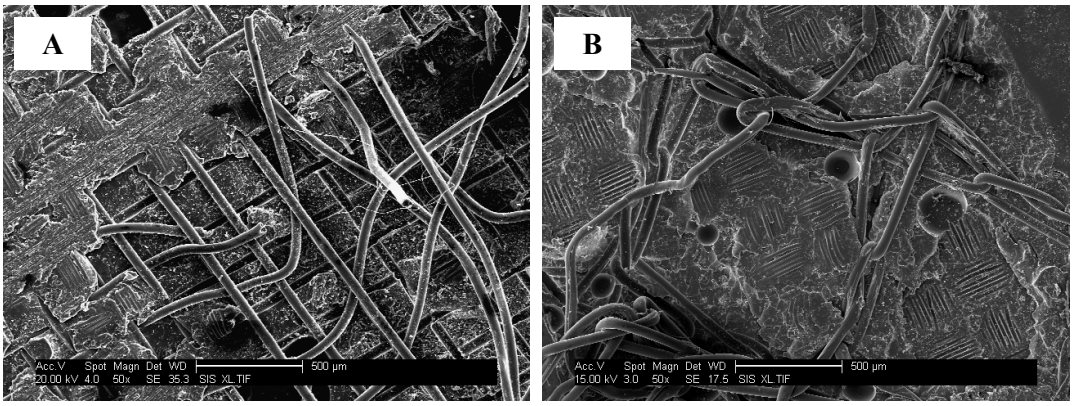

Figure 9.1 – SEM micrographs of mode I fracture surfaces for (A) the novel adhesive film joint GFRP-P-CRN and (B) the commercial adhesives film joint GFRP-FM94

Microscope investigation of the failure surfaces obtained in this work suggested a weak interface between the veils and the adhesive pastes. The micrographs in Figure 9.1 show regions where the veil fibres are not fully wetted out.

A possible area for improvement, although it was never the main focus of this work, is the adhesion between the veil and the adhesive via improved wetting of the veil fibres. It is not possible to reduce the viscosity of the adhesive paste by increasing its

temperature, in order to improve wetting of the veil, as the paste contains hardener. The only viable option is to pass the veil through a heated bath of resin which is compatible with the adhesive system (see Figure 9.2) prior to applying the adhesive paste. Figure 9.2 shows the author's proposal for an improved adhesive filming line.

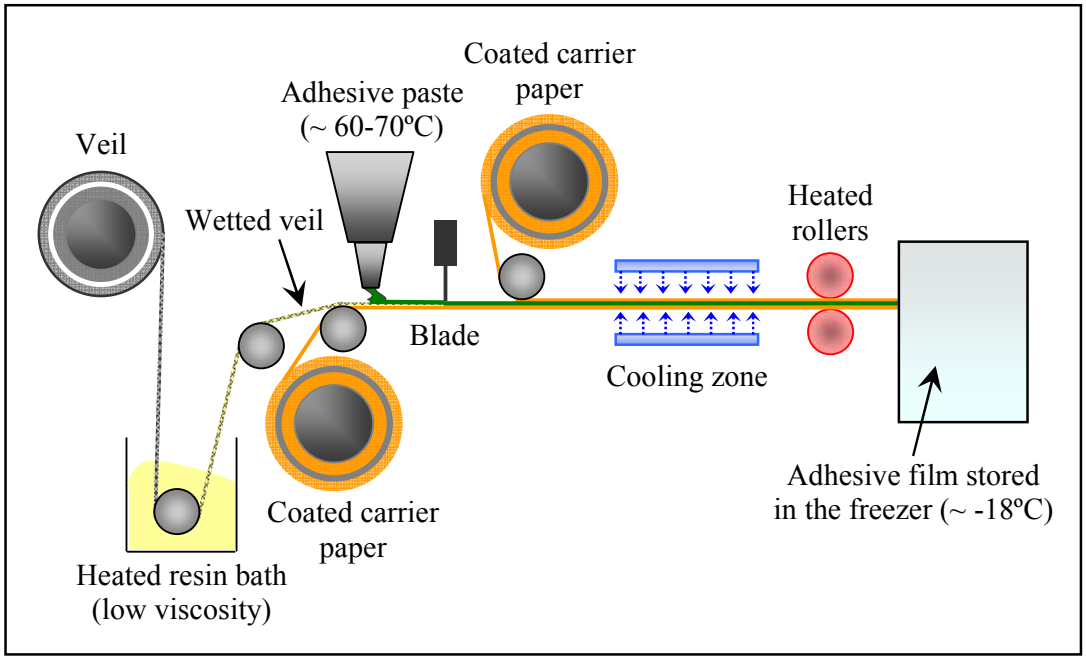

Figure 9.2 – Proposal for the manufacture of adhesive films

The veil from the heated resin bath is drawn onto coated carrier paper, with the adhesive paste poured over these two materials and spread evenly by the blade. The adhesive is then covered with a second sheet of coated carrier paper and drawn through a cooling zone to help solidification. The hot rollers are included to provide a uniform and controlled film thickness in the final product. The final product can then be rolled and placed in frozen storage.

9.2.2 Improving interfacial adhesion

The issues regarding interfacial failure of the adhesive joints were introduced in Chapter 4 and Chapter 7. The main purpose of surface preparation is to ensure that adhesion develops to the extent that the weakest link in the joint is either within the adhesive or

within the substrate. With an optimal surface treatment, failure should not occur at the interface because of a weak boundary layer or insufficient wetting.

Chapter 7 discussed the interfacial failure obtained for the unsupported films containing carbon nanotubes. This was attributed to poor wetting of the substrate surfaces due to the high viscosity of these formulations. In Chapter 4 the author's idea of improving adhesion through the use of a surface primer was introduced. The primer was applied as a thin layer on the substrate so as to help the wetting of the surface without unduly altering the overall adhesive formulation. Testing results reported in Chapter 7 showed this to be a successful method for improving the interfacial adhesion.

It was shown in Chapter 7 that the adhesive joint strength is dependent on the type of substrate as previously reported in published literature [204,205]. Further studies have related the substrate dependence to the cured adhesive in the different joints possessing different glass transition temperatures [206]. Additional possibilities in this specific work for G_{IC} being higher for the aluminium alloy substrates than with GFRP are attributed to the better cohesive mode of failure and are discussed hereafter. The performance of the joint has been proved to be dependent on the surface preparation too [221]. Taking the commercially available adhesive film FM® 94K as an example, the mode of failure was mixed (cohesive and interfacial) when bonded to GFRP but cohesive when bonded to aluminium alloy. Figure 9.3 shows the failed fracture surfaces. That the aluminium alloy substrates showed no evidence of interfacial failure would explain the measured G_{IC} being higher than for the GFRP substrate.

Properties of bonded composites have been shown to be even more dependent on surface preparation than metals [9,221]. Most of these materials have complex formulations and their surfaces are often contaminated with mould-release agents or additives that can migrate to the surface during processing. These contaminants must be removed before bonding to achieve an effective joint. Microscope investigations during this work showed evidence of debris on the GFRP surface after the surface preparation process was completed. In an attempt to remove this contamination, an ultrasonic cleaning process was trialled. The GFRP substrate was immersed in methyl ethyl ketone

[150] and sonicated for one hour using an Elmasonic S120H ultrasonic bath. The high frequency vibrations of this equipment (37 kHz) were intended to dislodge the contaminants.

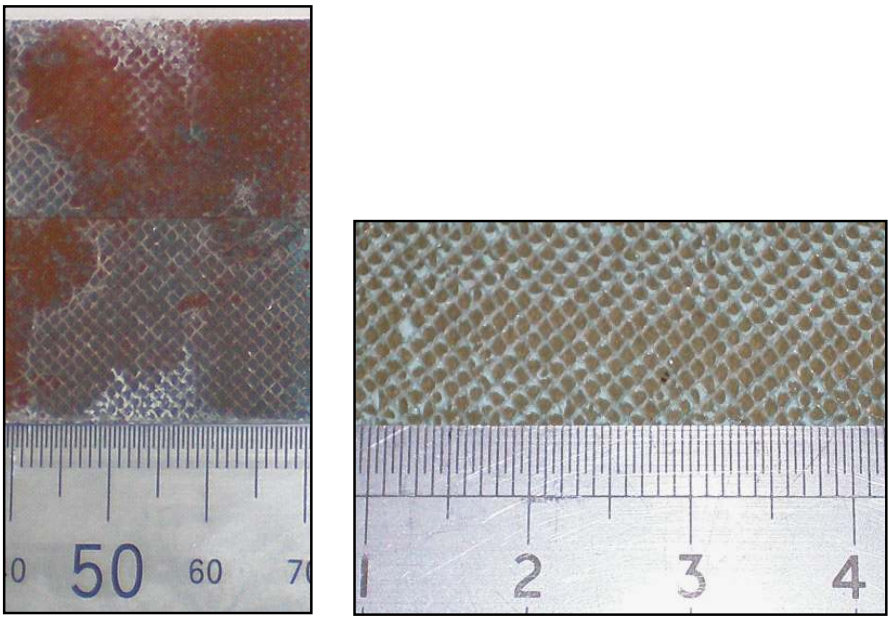

Figure 9.3 – Fracture surfaces of the mixed mode failed GFRP-FM94 (left) and the cohesively failed Al-FM94 (right)

Figure 9.4 shows SEM micrographs of the surface of the GFRP substrate, prepared as detailed in Section 4.3.2.2, prior to sonication (A) and after ultrasonic cleaning (B). The images show the features created on the surface which are negatives from the nylon fibre texture in the peel ply. Examination of the micrographs shows the ultrasonic cleaning process as an ideal technique for removing the loosely held particulates from the composite substrate surface.

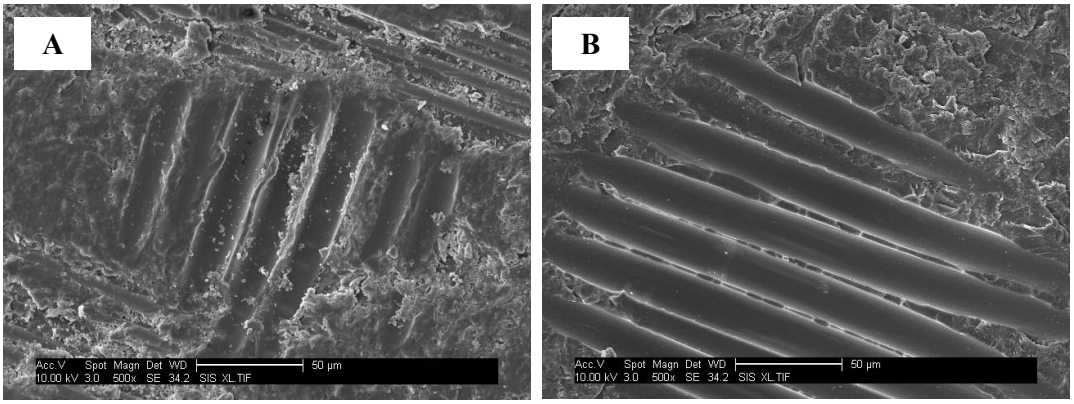

Figure 9.4 – SEM micrographs of the GFRP surface prior to bonding (A) before ultrasonication and (B) after ultrasonication

The author proposes the following extended surface preparation procedure for composite bonding:

- Use of a peel ply during cure and subsequent removal after cure
- Gentle abrasion (P1200 silicon carbide polishing paper)
- Rinse with methyl ethyl ketone (MEK) solvent
- Ultrasonic cleaning whilst immersed in the MEK solvent
- Final rinse with MEK solvent

This extended surface preparation process has not been trialled as yet. However, it is expected that the strength of an adhesive joint would be increased significantly when the loose deposits observed in Figure 9.4-A are removed from the surface, enabling the adhesive to wet the substrate more easily.

This ultrasonic cleaning approach is feasible for small scale components. It is questionable whether such an approach could be adapted for large scale components such as bonded aero structures.

9.2.3 Further work on the novel adhesive formulation

In the thermosetting ternary blends of this work, micro-phase separation has taken place to form dispersed rubber particles in an epoxy matrix phase containing carbon nanotubes. The most noticeable effect has been the reduction of the mean rubber

particle size in the ternary blend compared to the rubber toughened epoxy blend with no carbon nanotubes. The good overall balance of properties found in this study is believed to be associated with the specific morphology of these systems, providing an efficient toughening mechanism as well as a conductive network. Further study on the morphology of these ternary blends is needed and should involve the determination of the particle volume fraction and whether or not the carbon nanotubes act as nucleation sites for the rubber particles.

A glass transition temperature difference of ~30ºC has been measured between the fully cured blends and the 73-75% conversion specimens cured at 120ºC. This suggests that the durability of the blends should be considered in future studies. Since they are capable of undergoing high levels of post-cure this may be detrimental in terms of their hot-wet properties.

After considering the overall balance of properties obtained from the thermosetting ternary system the author suggests further study into decreasing the content of the nanofillers in the adhesive formulation. The decrease in the viscosity of the adhesive paste that this would provide will allow the rubber content to be increased to the higher levels used in commercial adhesives, 15-20 wt%. Characterisation will be needed to analyse the effects on toughness and on the electrical conductivity of the resulting quantitative variant of the ternary blend.

However, as previously discussed, an increase in the concentration of the rubber could lead to phase inversion in the blend. It would be interesting to study the content of CTBN rubber that leads to the phase-inverted morphology in the epoxy without carbon nanotubes. Following this, a more in-depth study could analyse where the nanofillers are positioned within the material for different CTBN rubber concentrations. The nanotubes will either be within the epoxy rich phase, the rubber rich phase or at the boundaries between these two. Furthermore, this study could correlate the changes in morphology with the mechanical and electrical properties.

9.2.4 Further work on bonded joints

Regarding the adhesives in bonded specimens, investigation of the new surface preparation for GFRP substrates is still open. The dislodging of loosely held particulates from the substrate surface through use of an ultrasonic cleaning process is expected to help the adhesive wetting of the substrate, resulting in an increased adhesive joint strength.

Further study on the specialist BCR structure, which provided a background to this PhD work, requires further testing of the adhesives under mode I and mode II fatigue loading conditions and at high strain rates.

Composites and structural adhesives intended for use in primary aerospace structures must avoid moisture uptake and / or solvent swelling. In this respect, bubbles or voids contained within the cured adhesive joint are undesireable. Environmental testing of the novel adhesive in the joint following moisture uptake and/or solvent swelling is needed and future attention should be focussed to this subject.

Appendices

Appendix A – 3PB fracture testing – Correction factors and data analysis

Evaluation of the correction factors f and ϕ for for single edge-notched bending (SENB) test specimens from [145]:

Geometry calibration factor:

$$f = 6\alpha^{1/2}\frac{1.99-\alpha(1-\alpha)(2.15-3.93\alpha+2.7\alpha^2)}{(1+2\alpha)(1-\alpha)^{3/2}}$$

Energy calibration factor: $$\phi = \frac{A+18.64}{dA/d\alpha}$$

$$A = \frac{16\alpha^2}{(1-\alpha)^2}\left(8.9-33.717\alpha+79.616\alpha^2-112.952\alpha^3+84.815\alpha^4-25.672\alpha^5\right)$$

$$\frac{dA}{d\alpha} = \frac{16\alpha^2}{(1-\alpha)^2}\left(-33.717+159.232\alpha-338.856\alpha^2+339.26\alpha^3-128.36\alpha^4\right)+$$
$$+16\frac{\left[2\alpha(1-\alpha)+2\alpha^2\right]}{(1-\alpha)^3}\begin{pmatrix}8.9-33.717\alpha+79.616\alpha^2-112.952\alpha^3+\\+84.815\alpha^4-25.672\alpha^5\end{pmatrix}$$

Where:

$$\alpha = a/w$$

a is the crack length

w is the specimen width.

The following table includes the data obtained from SENB testing:

Specimen ID	***w*** **(mm)**	***h*** **(mm)**	***a*/*w*** **(mm)**	F_Q ***(N)***	C_Q-C_{corr} **(m/N)**	***f***	ϕ
C1	15.3	4.1	0.42	51.8	2.0×10^{-6}	8.50	0.29
C2	15.1	4.0	0.46	47.4	2.6×10^{-6}	9.30	0.27
C3	15.5	4.2	0.46	40.7	2.3×10^{-6}	9.37	0.27
CR1	15.4	4.5	0.47	67.6	3.1×10^{-6}	9.79	0.26
CR2	15.6	4.5	0.51	56.3	3.1×10^{-6}	11.13	0.24
CR3	15.2	4.5	0.46	65.2	2.6×10^{-6}	9.29	0.27
CR4	15.4	4.5	0.45	68.8	2.6×10^{-6}	9.27	0.27
CR5	15.4	4.5	0.49	62.6	2.7×10^{-6}	10.23	0.25
CN1	11.5	3.1	0.44	37.2	2.9×10^{-6}	8.76	0.28
CN2	11.3	3.2	0.44	29.0	3.9×10^{-6}	8.99	0.28
CN3	12.4	3.1	0.40	40.0	2.7×10^{-6}	8.02	0.30
CN4	11.1	3.1	0.45	28.0	4.3×10^{-6}	9.16	0.27
CN5	11.5	3.2	0.43	31.9	3.3×10^{-6}	8.72	0.29
CRN1	12.4	3.7	0.40	72.2	2.9×10^{-6}	8.03	0.30
CRN2	10.5	3.7	0.48	45.0	5.8×10^{-6}	9.91	0.26
CRN3	11.2	3.7	0.45	52.4	4.3×10^{-6}	9.05	0.28
CRN4	11.0	3.7	0.45	50.4	4.8×10^{-6}	9.25	0.27

Appendix B – DCB test correction factors

Evaluation of the correction factors F and N for the double cantilever beam (DCB) geometry from [151]:

Large displacement correction: $$F = 1 - \frac{3}{10}\left(\frac{\delta}{a}\right)^2 - \frac{3}{2}\left(\frac{\delta l_1}{a^2}\right)$$

Load-block correction: $$N = 1 - \left(\frac{l_2}{a}\right)^3 - \frac{9}{8}\left[1 - \left(\frac{l_2}{a}\right)^2\right]\frac{\delta l_1}{a^2} - \frac{9}{35}\left(\frac{\delta}{a}\right)^2$$

Where l_1 and l_2 are load-block dimensions defined in the protocol [171].

Appendix C – ELS test correction factors

Evaluation of the correction factors F and N for the end loaded split (ELS) geometry from [180]:

Large displacement correction: $$F = 1 - \theta_1 \left(\frac{\delta}{L} \right)^2 - \theta_2 \left(\frac{\delta l_1}{L^2} \right)$$

Load-block correction: $$N = 1 - \theta_3 \left(\frac{l_2}{L} \right)^3 - \theta_4 \left(\frac{\delta l_1}{L^2} \right) - \theta_5 \left(\frac{\delta}{L} \right)^2$$

$$\theta_1 = \frac{3}{20} \left[\frac{15 + 50 \left(\frac{a}{L} \right)^2 + 63 \left(\frac{a}{L} \right)^4}{\left[1 + 3 \left(\frac{a}{L} \right)^3 \right]^2} \right]$$

$$\theta_2 = \frac{-3 \left(\frac{L}{a} \right) \left(1 + 3 \left(\frac{a}{L} \right)^2 \right)}{1 + 3 \left(\frac{a}{L} \right)^3}$$

$$\theta_3 = \frac{4}{1 + 3 \left(\frac{a}{L} \right)^3}$$

$$\theta_4 = \frac{-9\left[\left(1-\left(\frac{a}{L}\right)\right)\left(1+3\left(\frac{a}{L}\right)^3\right)+4\left(\frac{a}{L}\right)^2\left(1-\left(\frac{l_2}{a}\right)^2\right)\left(1+3\left(\frac{a}{L}\right)^2\right)\right]}{4\left(1+3\left(\frac{a}{L}\right)^3\right)^2}$$

$$\theta_5 = \frac{36}{35}.\frac{1+\frac{3}{8}\left(\frac{a}{L}\right)^3\left(35+70\left(\frac{a}{L}\right)^2+63\left(\frac{a}{L}\right)^4\right)}{\left(1+3\left(\frac{a}{L}\right)^3\right)^3}$$

References

1. Kwon, Y. K., Berber, S., and Tomanek, D. (2004), 'Thermal Contraction of Carbon Fullerenes and Nanotubes', *Physical Review Letters*, Vol. 92, No. 1, pp. 1-4.

2. Maniwa, Y., Fujiwara, R., Kira, H., Tou, H., Kataura, H., Suzuki, S., Achiba, Y., Nishibori, E., Takata, M., Sakata, M., Fujiwara, A., and Suematsu, H. (2001), 'Thermal Expansion of Single-Walled Carbon Nanotube (SWNT) Bundles: X-Ray Diffraction Studies', *Physical Review B. Condensed Matter and Materials Physics*, Vol. 64, No. 24, pp. 241402.1-241402.3.

3. Xu, Y., Ray, G., and Abdel-Magid, B. (2006), 'Thermal Behavior of Single-Walled Carbon Nanotube Polymer–Matrix Composites', *Composites: Part A*, Vol. 37, No. 1, pp. 114-121.

4. Fiedler, B., Gojny, F. H., Wichmann, M. H. G., Nolte, C. M., and Schulte, K. (2006), 'Fundamental Aspects of Nano-Reinforced Composites', *Composites Science and Technology*, Vol. 66, No. 16, pp. 3115-3125.

5. Martin, C. A., Sandler, J. K. W., Shaffer, M. S. P., Schwarz, M. K., Bauhofer, W., Schulte, K., and Windle, A. H. (2004), 'Formation of Percolating Networks in Multi-Wall Carbon-Nanotube-Epoxy Composites', *Composites Science and Technology*, Vol. 64, No. 15, pp. 2309-2316.

6. Schliekelmann, R. J. (1985), 'Introduction', in Thrall, E. W. and Shannon, R. W. *Adhesive Bonding of Aluminum* Alloys, Marcell Dekker, New York, USA.

7. Engineering and Physical Sciences Research Council (EPSRC) Grant *The Application of Fracture Mechanics to Engineering Adhesive Joints: An Investigation into Mode II and High Rate Loading*, available at: http://gow.epsrc.ac.uk (accessed 2008).

8. Aerospaceweb.org *Airbus A380 Long-Range Jetliner Image*, available at: http://www.aerospaceweb.org/ (accessed 2008).

9. Petrie, E. M. *Important Considerations Regarding Adhesion to Plastics - Part I - Thermosetting Plastics*, available at: http://www.specialchem4adhesives.com (accessed 2007).

10. Petrie, E. M. *Reducing Internal Stresses*, available at: http://www.specialchem4adhesives.com (accessed 2007).

11. Patrick, R. L. (1976), 'Structural Adhesives, With Emphasis on Aerospace Applications', in *Treatise on Adhesion and Adhesives*, Vol. 4, Marcel Dekker, New York, USA.

12. Djokic, D., Johnston, A., Rogers, A., Lee-Sullivan, P., and Mrad, N. (2002), 'Residual Stress Development during the Composite Patch Bonding Process: Measurement and Modelling', *Composites Part A: Applied Science and Manufacturing*, Vol. 33, No. 2, pp. 277-288.

13. Kim, H. S., Park, S. W., Hwang, H. Y., and Lee, D. G. 'Effect of the Smart Cure Cycle on the Performance of the Co-Cured Aluminium/Composite Hybrid Shaft', in *ICCS/13*: *International Conference on Composite Structures N^{o}13* at Melbourne, Australia.

14. Marzocca, A. J., Somoza, A., Goyanes, S. N., Salgueiro, W., and König, P. (2002), 'Characterization of Free Volume in Particulate-Filled Epoxy Resin by Means of Dynamic Mechanical Analysis and Positron Annihilation Lifetime Spectroscopy', *Polymer International*, Vol. 51, Issue 11, pp. 1277-1284.

15. Nishino, T., Airu, X., Matsumoto, T., Matsumoto, K., and Nakamae, K. (1992), 'Residual Stress in Particulate Epoxy Resin by X-Ray Diffraction', *Journal of Applied Polymer Science*, Vol. 45, Issue 7, pp. 1239-1244.

16. Hamerton, I. (1996), *Recent Developments in Epoxy Resins*, Rapra Technology Limited, Shawbury, Shropshire, UK.

17. Petrie, E. M. *Additives for High Temperature Structural Adhesives*, available at: http://www.specialchem4adhesives.com (accessed 2007).

18. Baur, J. and Silverman, E. (2007), 'Challenges and Opportunities in Multifunctional Nanocomposite Structures for Aerospace Applications', *MRS Bulletin*, Vol. 32, pp. 328-333.

19. Wichmann, M. H. G., Sumfleth, J., Gojny, F. H., Quaresimin, M., Fiedler, B., and Schulte, K. (2006), 'Glass-Fibre-Reinforced Composites with Enhanced Mechanical and Electrical Properties - Benefits and Limitations of a Nanoparticle Modified Matrix', *Engineering Fracture Mechanics*, Vol. 73, No. 16, pp. 2346-2359.

20. Chodák, I. and Krupa, I. (1999), 'Percolation Effect and Mechanical Behavior of Carbon Black Filled Polyethylene', *Journal of Materials Science Letters*, Vol. 18, No. 18, pp. 1457-1459.

21. Novák, I., Krupa, I., and Chodák, I. (2002), 'Relation between Electrical and Mechanical Properties in Polyurethane/Carbon Black Adhesives', *Journal of Materials Science Letters*, Vol. 21, No. 13, pp. 1039-1041.

22. Manson, J. A. and Sperling, L. H. (1976), *Polymer Blends and Composites*, Plenum Press, New York, USA.

23. Zhang, X., Boscolo, M., Figueroa-Gordon, D., Allegri, G., and Irving, P. E. (2009), 'Fail-Safe Design of Integral Metallic Aircraft Structures Reinforced by Bonded Crack Retarders', *Engineering Fracture Mechanics*, Vol. 76, Issue 1, pp. 114-133.

24. Irving, P. E. and Figueroa, D. 'Routes to Improved Damage Tolerance; Prediction of Damage Tolerant Performance of High Strength and Hybrid Structures', in *First International Conference on Damage Tolerance of Aircraft Structures* at TU Delft, The Netherlands.

25. Zhang, X., Boscolo, M., Figueroa-Gordon, D., Allegri, G., and Irving, P. E. 'Improving Fail Safety of Aircraft Integral Structures Through Use of Bonded Crack Retarders', in *Proceedings 24th ICAF Symposium* at Naples, Italy.

26. Baldan, A. (2004), 'Review - Adhesively-Bonded Joints and Repairs in Metallic Alloys, Polymers and Composite Materials: Adhesives, Adhesion Theories and Surface Pretreatment', *Journal of Materials Science*, Vol. 39, No. 1, pp. 1-49.

27. SpecialChem Adhesives and Sealants *Adhesion Guide*, available at: http://www.specialchem4adhesives.com (accessed 2007).

28. Petrie, E. M. *New Epoxy Adhesives Are Flexible and Tough*, available at: http://www.specialchem4adhesives.com (accessed 2007).

29. Petrie, E. M. *Improving the Toughness of Structural Adhesives*, available at: http://www.specialchem4adhesives.com (accessed 2007).

30. Kinloch, A. J. (2003), 'Toughening Epoxy Adhesives to Meet Today's Challenges', *MRS Bulletin*, Vol. 28, pp. 445-448.

31. Verchere, D., Sautereau, H., Pascault, J. P., Moschiar, S. M., Riccardi, C. C., and Williams, R. J. J. (1989), 'Miscibility of Epoxy Monomers With Carboxyl-Terminated Butadiene Acrylonitrile Random Copolymers', *Polymer*, Vol. 30, No. 1, pp. 107-115.

32. Pearson, R. A. and Yee, A. F. (1986), 'Toughening Mechanisms in Elastomer-Modified Epoxies. Part 2 - Microscopy Studies', *Journal of Materials Science*, Vol. 21, No. 7, pp. 2475-2488.

33. Kinloch, A. J., Shaw, S. J., Tod, D. A., and Hunston, D. L. (1983), 'Deformation and Fracture Behaviour of a Rubber-Toughened Epoxy. I. Microstructure and Fracture Studies', *Polymer*, Vol. 24, No. 10, pp. 1341-1354.

34. Verchere, D., Sautereau, H., Pascault, J. P., Moschiar, S. M., Riccardi, C. C., and Williams, R. J. J. (1990), 'Rubber-Modified Epoxies. I, Influence of Carboxyl-Terminated Butadiene-Acrylonitrile Random Copolymers (CTBN) on the Polymerization and Phase Separation Processes', *Journal of Applied Polymer Science*, Vol. 41, Issues 3-4, pp. 467-485.

35. Kinloch, A. J., Shaw, S. J., and Hunston, D. L. (1983), 'Deformation and Fracture Behaviour of a Rubber-Toughened Epoxy. II. Failure Criteria', *Polymer*, Vol. 24, No. 10, pp. 1355-1363.

36. Pearson, R. A. (1990), *Sources of Toughness in Modified Epoxies* (PhD thesis), The University of Michigan, Materials Science and Engineering.

37. Kinloch, A. J. and Young, R. J. (1983), *Fracture Behavior of Polymers*, Applied Science Publishers: London, London, UK.

38. Bucknall, C. B. (2007), 'Private Communication', *Cranfield University*, Cranfield, UK.

39. Kinloch, A. J. 'Adhesives in Engineering', in *Proceedings of the Institution of Mechanical Engineers. Part G - Journal of Aerospace Engineering,* Vol. 211 pp. 307-335.

40. Lee, S. M. (1985), 'An in-Situ Failure Model for Adhesive Joints', *The Journal of Adhesion*, Vol. 18, Issue 1, pp. 1-15.

41. Kinloch, A. J. and Shaw, S. J. (1981), 'The Fracture Resistance of a Toughened Epoxy Adhesive', *The Journal of Adhesion*, Vol. 12, Issue 1, pp. 59-77.

42. May, C. A. (1988), *Epoxy Resins: Chemistry and Technology* (2nd Edition), Marcel Dekker, New York, USA.

43. Pardoen, T., Ferracin, T., Landis, C. M., and Delannay, F. (2005), 'Constraint Effects in Adhesive Joint Fracture', *Journal of the Mechanics and Physics of Solids*, Vol. 53, pp. 1951-1983.

44. Yang, Q. D., Thouless, M. D., and Ward, S. M. (1999), 'Numerical Simulations of Adhesively-Bonded Beams Failing With Extensive Plastic Deformation', *Journal of the Mechanics and Physics of Solids*, Vol. 47, Issue 6, pp. 1337-1353.

45. Yang, Q. D. and Thouless, M. D. (2001), 'Mixed-Mode Fracture Analyses of Plastically Deforming Adhesive Joints', *International Journal of Fracture*, Vol. 110, No. 2, pp. 175-187.

46. Mohammed, I. and Liechti, K. M. (2000), 'Cohesive Zone Modelling of Crack Nucleation in Mixed-Mode Interfacial Corners', *Journal of the Mechanics and Physics of Solids*, Vol. 48, pp. 735-764.

47. Sorensen, B. F. (2002), 'Cohesive Law and Notch Sensitivity of Adhesive Joints', *Acta Materialia*, Vol. 50, No. 5, pp. 1053-1061.

48. Ferracin, T., Landis, C. M., Delannay, F., and Pardoen, T. (2003), 'On the Determination of the Cohesive Zone Properties of an Adhesive Layer from the Analysis of the Wedge Peel Test', *International Journal of Solids and Structures*, Vol. 40, No. 11, pp. 2889-2904.

49. Kawashita, L. F., Kinloch, A. J., Moore, D. R., and Williams, J. G. (2008), 'The Influence of Bond Line Thickness and Peel Arm Thickness on Adhesive Fracture Toughness of Rubber Toughened Epoxy–Aluminium Alloy Laminates', *International Journal of Adhesion and Adhesives*, Vol. 28, No. 4-5, pp. 199-210.

50. Thostenson, E. T., Ren, Z., and Chou, T. W. (2001), 'Advances in the Science and Technology of Carbon Nanotube and Their Composites: a Review', *Composites Science and Technology*, Vol. 61, No. 13, pp. 1899-1912.

51. Coleman, J. N., Khan, U., Blau, W. J., and Gun'ko, Y. K. (2006), 'Small but Strong: A Review of the Mechanical Properties of Carbon Nanotube–Polymer Composites', *Carbon*, Vol. 44, No. 9, pp. 1624-1652.

52. Biercuk, M. J., Llaguno, M. C., Radosavljevic, M., Hyun, J. K., and Johnson, A. T. (2002), 'Carbon Nanotube Composites for Thermal Management', *Applied Physics Letters*, Vol. 80, No. 15, pp. 2767-2769.

53. Alexandre, M. and Dubois, P. (2000), 'Polymer-Layered Silicate Nanocomposites: Preparation, Properties and Uses of a New Class of Materials', *Materials Science and Engineering R*, Vol. 28, Issues 1-2, pp. 1-63.

54. Jordan, J., Jacob, K. I., Tannenbaum, R., Sharaf, M. A., and Jasiuk, I. (2005), 'Experimental Trends in Polymer Nanocomposites - A Review', *Materials Science and Engineering A*, Vol. 393, Issues 1-2, pp. 1-11.

55. Dean, D., Abdalla, M., and Ganguli, S. (2003), 'Big Things in Small Packages: Opportunities and Challenges Await Nano-Engineered Adhesives, Sealants and Coatings', *Adhesives Age*, pp. 12-19.

56. Kinloch, A. J. and Taylor, A. C. (2002), 'The Toughening of Cyanate-Ester Polymers - Part I - Physical Modification Using Particles, Fibres and Woven-Mats', *Journal of Materials Science*, Vol. 37, No. 3, pp. 433-460.

57. Faber, K. T. and Evans, A. G. (1983), 'Crack Deflection Processes - I. Theory', *Acta Metallurgica*, Vol. 31, pp. 565-576.

58. Faber, K. T. and Evans, A. G. (1983), 'Crack Deflection Processes - II. Experiment', *Acta Metallurgica*, Vol. 31, pp. 577-584.

59. Kinloch, A. J., Maxwell, D., and Young, R. J. (1985), 'Micromechanisms of Crack Propagation in Hybrid-Particulate Composites', *Journal of Materials Science Letters*, Vol. 4, No. 10, pp. 1276-1279.

60. Hull, D. and Clyne, T. W. (2001), *An Introduction to Composite Materials* (2nd Edition), Cambridge University Press, Cambridge, UK.

61. Johnsen, B. B., Kinloch, A. J., Mohammed, R. D., Taylor, A. C., and Sprenger, S. (2007), 'Toughening Mechanisms of Nanoparticle-Modified Epoxy Polymers', *Polymer*, Vol. 48, No. 2, pp. 530-541.

62. Gojny, F. H., Wichmann, M. H. G., Fiedler, B., and Schulte, K. (2005), 'Influence of Different Carbon Nanotubes on the Mechanical Properties of Epoxy Matrix Composites - A Comparative Study', *Composites Science and Technology*, Vol. 65, Issues 15-16, pp. 2300-2313.

63. Gojny, F. H., Wichmann, M. H. G., Kopke, U., Fiedler, B., and Schulte, K. (2004), 'Carbon Nanotube-Reinforced Epoxy-Composites: Enhanced Stiffness and Fracture Toughness at Low Nanotube Content', *Composites Science and Technology*, Vol. 64, Issue 15, pp. 2363-2371.

64. Gojny, F. H., Wichmann, M. H. G., Fiedler, B., Kinloch, I. A., Bauhofer, W., Windle, A. H., and Schulte, K. (2006), 'Evaluation and Identification of Electrical and Thermal Conduction Mechanisms in Carbon Nanotube/Epoxy Composites', *Polymer*, Vol. 47, No. 6, pp. 2036-2045.

65. Iijima, S. (1991), 'Helical Microtubules of Graphitic Carbon', *Nature*, Vol. 354, pp. 56-58.

66. Royal Society of Chemistry available at: http://www.rsc.org/ (accessed 2007).

67. Penumadu, D., Dutta, A., Pharr, G. M., and Files, B. (2003), 'Mechanical Properties of Blended Single-Wall Carbon Nanotube Composites', *Journal of Materials Research*, Vol. 18, No. 8, pp. 1849-1853.

68. Schulte, K., Gojny, F. H., Fiedler, B., Broza, G., and Sandler, J. K. W. (2005), 'Carbon Nanotube Reinforced Polymers. A State of the Art', in Friedrich, K. *Polymer-Composites – From Nano to Macro Scale*, Springer Science and Business Media, Inc., USA, pp. 3-23.

69. Zhu, J., Kim, J. D., Peng, H., Margrave, J. L., Khabashesku, V. N., and Barrera, E. V. (2003), 'Improving the Dispersion and Integration of Single-Walled Carbon Nanotubes in Epoxy Composites Through Functionalization', *Nanoletters*, Vol. 3, No. 8, pp. 1107-1113.

70. Zhu, J., Peng, H., Rodriguez-Macias, F., Margrave, J. L., Khabashesku, V. N., Imam, A. M., Lozano, K., and Barrera, E. V. (2004), 'Reinforcing Epoxy Polymer Composites Through Covalent Integration of Functionalized Nanotubes', *Advanced Functional Materials*, Vol. 14, Issue 7, pp. 643-648.

71. Zyvex available at: http://www.zyvex.com (accessed 2006).

72. McCarthy, B., Coleman, J. N., Curran, S. A., Dalton, A. B., Davey, A. P., Konya, Z., Fonseca, A., Nagy, J. B., and Blau, W. J. (2000), 'Observation of Site Selective Binding in a Polymer Nanotube Composite', *Journal of Materials Science Letters*, Vol. 19, No. 24, pp. 2239-2241.

73. Lu, K. L., Lago, M., Chen, Y. K., Green, M. L. H., Harris, P. J. F., and Tsang, S. C. (1996), 'Mechanical Damage of Carbon Nanotubes by Ultrasound', *Carbon*, Vol. 34, Issue 6, pp. 814-816.

74. Miyagawa, H., Rich, M. J., and Drzal, L. T. (2006), 'Thermo-Physical Properties of Epoxy Nanocomposites Reinforced by Carbon Nanotubes and Vapor Grown Carbon Fibers', *Thermochimica Acta*, Vol. 442, No. 1-2, pp. 67-73.

75. Lau, K. T., Lu, M., Lam, C. K., Cheung, H. Y., Sheng, F. L., and Li, H. L. (2005), 'Thermal and Mechanical Properties of Single-Walled Carbon Nanotube Bundle-Reinforced Epoxy Nanocomposites: the Role of Solvent for Nanotube Dispersion', *Composites Science and Technology*, Vol. 65, No. 5, pp. 719-725.

76. Schmid, C. F. and Klingenberg, D. J. (2000), 'Mechanical Flocculation in Flowing Fiber Suspensions', *Physical Review Letters*, Vol. 84, No. 2, pp. 290-293.

77. Schmid, C. F. and Klingenberg, D. J. (2004), 'Flocculation in Simulations of Sheared Fiber Suspensions', *International Journal of Multiphase Flow*, Vol. 30, No. 1, pp. 67-87.

78. Sandler, J. K. W. , Kirk, J. E., Kinloch, I. A., Shaffer, M. S. P., and Windle, A. H. (2003), 'Ultra-Low Electrical Percolation Threshold in Carbon Nanotube–Epoxy Composites', *Polymer*, Vol. 44, No. 19, pp. 5893-5899.

79. Sandler, J., Shaffer, M. S. P., Prasse, T., Bauhofer, W., Schulte, K., and Windle, A. H. (1999), 'Development of a Dispersion Process for Carbon Nanotubes in an Epoxy Matrix and the Resulting Electrical Properties', *Polymer* , Vol. 40, No. 21, pp. 5967-5971.

80. Fiedler, B., Gojny, F. H., Wichmann, M. H. G., Bauhofer, W., and Schulte, K. (2004), 'Carbon Nanotubes Be Used to Sense Damage in Composites? ', *Annales De Chimie-Science Des Materiaux*, Vol. 29, No. 6, pp. 81-94.

81. Martin, C. A., Sandler, J. K. W., Windle, A. H., Schwarz, M. K. , Bauhofer, W., Schulte, K., and Shaffer, M. S. P. (2005), 'Electric Field-Induced Aligned Multi-Wall Carbon Nanotube Networks in Epoxy Composites', *Polymer*, Vol. 46, Issue 3, pp. 877-886.

82. Schuler, R., Petermann, J., Schulte, K., and Wentzel, H. P. (1996), 'Percolation in Carbon Black Filled Epoxy Resin', *Macromolecular Symposia*, Vol. 104, pp. 261-268.

83. Schuler, R., Petermann, J., Schulte, K., and Wentzel, H. P. (1997), 'Agglomeration and Electrical Percolation Behavior of Carbon Black Dispersed in Epoxy Resin', *Journal of Applied Polymer Science*, Vol. 63, Issue 13, pp. 1741-1746.

84. M.C. Gill Corporation *Alcore's StrikegridT CEAF Composite Protection against Lighting Strikes Showcased at International Conference on Lightning and Static Electricity*, available at: http://www.mcgillcorp.com (accessed 2008).

85. Kirkpartick, S. (1973), 'Percolation and Conduction', *Review of Modern Physics*, Vol. 45, Issue 4, pp. 574-588.

86. Yu, M. F., Lourie, O., Dyer, M. J., Moloni, K., Kelly, T. F., and Ruoff, R. S. (2000), 'Strength and Breaking Mechanism of Multiwalled Carbon Nanotubes under Tensile Load', *Science*, Vol. 287, No. 5453, pp. 637-640.

87. Yu, M. F., Files, B. S., Arepalli, S., and Ruoff, R. S. (2000), 'Tensile Loading of Ropes of Single Wall Carbon Nanotubes and Their Mechanical Properties', *Physical Review Letters*, Vol. 84, No. 24, pp. 5552-5555.

88. Li, C. and Chou, T. W. (2003), 'Elastic Moduli of Multi-Walled Carbon Nanotubes and the Effect of Van Der Waals Forces', *Composites Science and Technology* , Vol. 63, No. 11, pp. 1517-1524.

89. Electronic Development Labs, I. *Typical Linear Coefficient of Expansion for Common Plastics*, available at: http://www.edl-inc.com (accessed 2008).

90. Petrie, E. M. *Non-Sag Additives for Adhesives and Sealants*, available at: http://www.specialchem4adhesives.com (accessed 2007).

91. Petrie, E. M. (1999), *The Handbook of Adhesives and Sealants*, McGraw-Hill, USA.

92. Peigney, A., Laurent, C., Flahaut, E., Bacsa, R. R., and Rousset, A. (2001), 'Specific Surface Area of Carbon Nanotubes and Bundles of Carbon Nanotubes', *Carbon*, Vol. 39, No. 4, pp. 507-514.

93. Battisti, A., Skordos, A. A., and Partridge, I. K. (2009), 'Monitoring Dispersion of Carbon Nanotubes in a Thermosetting Polyester Resin', *Composites Science and Technology*, Vol. 69, No. 10, pp. 1516-1520.

94. Vlot, A. (2001), *Fibre Metal Laminates. An Introduction*, Kluwer Academic Publisher, The Netherlands.

95. Gou, J., Blanco, R., Khan, A., and Appalla, A. 'Synthesis of Nickel-Coated Carbon Nanopaper Sheets by Pulse Laser Deposition ', in *Symposium R: Transport Behavior in Heterogeneous Polymeric Materials and Composites* at San Francisco, USA.

96. Azomaterials *Galvanic Corrosion - Galvanic Corrosion of Metal and Alloys in Sea Water*, available at: http://www.azom.com (accessed 2008).

97. Pascault, J. P., Sautereau, H., Verdu, J., and Williams, R. J. J. (2003), *Thermosetting Polymers*, Marcel Dekker, New York, USA.

98. Turi, E. A. (1981), *Thermal Characterization of Polymeric Materials*, New York: Academic Press, New York, USA.

99. Song, Y. S. and Youn, J. R. (2005), 'Influence of Dispersion States of Carbon Nanotubes on Physical Properties of Epoxy Nanocomposites', *Carbon*, Vol. 43, Issue 7, pp. 1378-1385.

100. Miyagawa, H. and Drzal, L. T. (2004), 'Thermo-Physical and Impact Properties of Epoxy Nanocomposites Reinforced by Single-Wall Carbon Nanotubes', *Polymer*, Vol. 45, Issue 15, pp. 5163-5170.

101. Puglia, D., Valentini, L., Armentano, I., and Kenny, J. M. (2003), 'Effects of Single-Walled Carbon Nanotube Incorporation on the Cure Reaction of Epoxy Resin and Its Detection by Raman Spectroscopy', *Diamond and Related Materials*, Vol. 12, Issues 3-7, pp. 827-832.

102. Puglia, D., Valentini, L., and Kenny, J. M. (2003), 'Analysis of the Cure Reaction of Carbon Nanotubes/Epoxy Resin Composites through Thermal Analysis and Raman Spectroscopy', *Journal of Applied Polymer Science*, Vol. 88, Issue 2, pp. 452-458.

103. Tao, K., Yang, S., Grunlan, J. C., Kim, Y. S., Dang, B., Deng, Y., Thomas, R. L., Wilson, B. L., and Xin W. (2006), 'Effects of Carbon Nanotube Fillers on the Curing Processes of Epoxy Resin-Based Composites', *Journal of Applied Polymer Science*, Vol. 102, Issue 6, pp. 5248-5254.

104. Xie, H., Liu, B., Yuan, Z., Shen, J., and Cheng, R. (2004), 'Cure Kinetics of Carbon Nanotube/Tetrafunctional Epoxy Nanocomposites by Isothermal Differential Scanning Calorimetry', *Journal of Polymer Science, Part B: Polymer Physics*, Vol. 42, Issue 20, pp. 3701-3712.

105. Gojny, F. H. and Schulte, K. (2004), 'Functionalisation Effect on the Thermo-Mechanical Behaviour of Multi-Wall Carbon Nanotube/Epoxy-Composites', *Composites Science and Technology*, Vol. 64, No. 15, pp. 2303-2308.

106. Dimopoulos, A., Skordos, A. A., and Partridge, I. K. 'Cure of a Carbon Nanotube Modified Multiphase Epoxy-Thermoplastic Resin System', in *49th AIAA Structures, Structural Dynamics, and Materials Conference* at Schaumburg, USA.

107. Wise, C. W., Cook, W. D., and Goodwin, A. A. (1997), 'Chemico-Diffusion Kinetics of Model Epoxy-Amine Resins', *Polymer*, Vol. 38, No. 13, pp. 3251-3261.

108. Um, M. K., Daniel, I. M., and Hwang, B. S. (2002), 'A Study of Cure Kinetics by the Use of Dynamic Differential Scanning Calorimetry', *Composites Science and Technology*, Vol. 62, Issue 1, pp. 29-40.

109. Schawe, J. E. K. (2002), 'A Description of Chemical and Diffusion Control in Isothermal Kinetics of Cure Kinetics', *Thermochimica Acta*, Vol. 388, Issues 1-2, pp. 299-312.

110. Karkanas, P. I. and Partridge, I. K. (2000), 'Cure Modelling and Monitoring of Epoxy/Amine Resin Systems. I. Cure Kinetics Modelling', *Journal of Applied Polymer Science*, Vol. 77, No. 7, pp. 1419-1431.

111. O'Brien, D. J. and White, S. R. (2003), 'Cure Kinetics, Gelation and Glass Transition of a Bisphenol F Epoxide', *Polymer Engineering and Science*, Vol. 43, Issue 4, pp. 863-874.

112. Rosu, D., Cascaval, C. N., Mustata, F., and Ciobanu, C. (2002), 'Cure Kinetics of Epoxy Resins Studied by Non-Isothermal DSC Data', *Thermochimica Acta*, Vol. 383, Issues 1-2, pp. 119-127.

113. Skordos, A. A. and Partridge, I. K. (2001), 'Cure Kinetics Modelling of Epoxy Resins Using a Non-Parametric Numerical Procedure', *Polymer Engineering and Science*, Vol. 41, No. 5, pp. 793-805.

114. Huntsman *Araldite® MY750 - Data Sheet*, available at: www.resins-online.com (accessed 2008).

115. Grillet, A. C., Galy, J., Gérard, J. F., and Pascault, J. P. (1991), 'Mechanical and Viscoelastic Properties of Epoxy Networks Cured With Aromatic Diamines', *Polymer*, Vol. 32, No. 10, pp. 1885-1891.

116. Petrie, E. M. *Solid Epoxy Adhesive Systems*, available at: http://www.specialchem4adhesives.com (accessed 2007).

117. Jones, F. R., Zhang, W., and Hayes, S. A. (2007), 'Thermally Induced Self Healing of Thermosetting Resins and Matrices in Smart Composites', in *Self Healing Materials. An Alternative Approach to 20 Centuries of Materials Science*, Springer, The Netherlands, pp. 69-93.

118. Emerald Performance Materials *Hycar® Reactive Liquid Polymers CTBN 1300x8 and CTBN 1300x8F*, available at: http://www.emeraldmaterials.com (accessed 2008).

119. Emerald Performance Materials *Hypox™ RK84 - Technical Bulletin*, available at: http://www.emeraldmaterials.com (accessed 2008).

120. Emerald Performance Materials *Hypox™ RA840 - Technical Bulletin*, available at: http://www.emeraldmaterials.com (accessed 2008).

121. Treverton, J. A. and Paul, A. J. (1995), 'A TOF-SIMS Study of an Acid-Terminated Butadiene-Acrylonitrile Copolymer Used As a Toughening Agent in Modern Adhesive Formulations ', *International Journal of Adhesion and Adhesives*, Vol. 15, Issue 4, pp. 237-248.

122. Hyperion Catalysis *MB1215-00 Multi-Walled Carbon Nanotube-Epoxy Masterbatch*, available at: http://www.fibrils.com (accessed 2008).

123. Nanocyl *Nanocyl® 7000 Series - Datasheet*, available at: http://www.nanocyl.com (accessed 2008).

124. Pyrograf Products Inc. *Pyrograf®-III Carbon Nanofibers (PR-24-XT-LHT-OX)*, available at: http://pyrografproducts.com (accessed 2008).

125. Cytec Engineered Materials Ltd. *FM® 94 Modified Epoxy Film*, available at: http://www.cytec.com (accessed 2007).

126. Cytec Engineered Materials Ltd. *FM® 1515-3 Film Adhesive*, available at: http://www.cytec.com (accessed 2007).

127. Huntsman *Araldite® 420 A/B - Two Component Epoxy Adhesive*, available at: http://secure.silmid.com (accessed 2007).

128. Hexcel Composites *Hexply® 913 Product Data*, available at: http://www.hexcel.com (accessed 2006).

129. Hexcel Composites *HexPly® 913 - 125°C Curing Epoxy Matrix*, available at: http://www.hexcel.com (accessed 2007).

130. Chakrabarti, D. J., Liu, J., Sawtell, R. R., and Venema, G. B. 'New Generation High Strength High Damage Tolerance 7085 Thick Alloy Product with Low Quench Sensitivity', in Nie, J. F. et al. *Materials Forum,* Vol. 28 Institute of Materials Engineering Australasia Ltd, Australia.

131. Cytec Engineered Materials Ltd. *BR® 127 Corrosion Inhibiting Primer*, available at: http://www.cytec.com (accessed 2007).

132. Petrie, E. M. *The Importance of Glass Transition Temperature in Formulating Adhesives and Sealants*, available at: www.specialchem4adhesives.com (accessed 2007).

133. Min, B. G., Stachurski, Z. H., and Hodgkin, J. H. (1993), 'Cure Kinetics of Elementary Reactions of a DGEBA/DDS Epoxy Resin: 1. Glass Transition Temperature versus Conversion', *Polymer*, Vol. 34, No. 23, pp. 4908-4912.

134. Resolution Performance Products LLC (2001), *Physical properties guide for epoxy resins and related products*, Houston, USA.

135. Zhou, Y., Pervin, F., Lewis, L., and Jeelani, S. (2007), 'Experimental Study on the Thermal and Mechanical Properties of Multi-Walled Carbon Nanotube-Reinforced Epoxy', *Materials Science and Engineering A*, Vol. 452-453, pp. 657-664.

136. Gouri, C., Ramaswamy, R., and Ninan, K. N. (2000), 'Studies on the Adhesive Properties of Solid Elastomer-Modified Novolac Epoxy Resin', *International Journal of Adhesion and Adhesives*, Vol. 20, No. 4, pp. 305-314.

137. Farris, R. D. and Steward, S. L. (Resolution Performance Products LLC) (*New Epoxy Toughners Widen the Adhesive Formulation Window*, available at: http://www.specialchem4adhesives.com (accessed 2007).

138. Branson Ultrasonics *Branson S-450D Ultrasonic Cell Disruptor / Homogenizers*, available at: http://www.bransonultrasonics.com/ (accessed 2007).

139. Yun, M. S. and Lee, W. I. (2008), 'Analysis of Bubble Nucleation and Growth in the Pultrusion Process of Phenolic Foam Composites', *Composites Science and Technology* , Vol. 68 , No. 1, pp. 202-208.

140. Zhao, L. and Gao, L. (2003), 'Stability of Multi-Walled Carbon Nanotubes Dispersion with Copolymer in Ethanol', *Colloids and Surfaces. A, Physicochemical and Engineering Aspects*, Vol. 224, No. 1-3, pp. 127-134.

141. Nadler, M., Mahrholz, T., Riedel, U., Schilde, C., and Kwade, A. (2008), 'Preparation of Colloidal Carbon Nanotube Dispersions and Their Characterisation Using a Disc Centrifuge ', *Carbon*, Vol. 46, Issue 11, pp. 1384-1392.

142. Weisenberger, M. C., Andrews, R., and Rantell, T. (2007), 'Carbon Nanotube Polymer Composites: Recent Developments in Mechanical Properties', in *Physical Properties of Polymers Handbook* (2^{nd} Edition), Vol. VI, Springer, New York, pp. 585-598.

143. Matthews, F. L. and Rawlings, R. D. (1999), *Composite Materials: Engineering and Science*, Woodhead Publishing Limited, Cambridge, UK.

144. Costa, E. (2008), 'Private Communication', *Cranfield University*, Cranfield, UK.

145. International Standards Organisation (ISO) (2000), *Plastics - Determination of Fracture Toughness (G_{IC} and K_{IC}) - Linear Elastic Fracture Mechanics (LEFM) Approach*, ISO 13586:2000, British Standards Institute (BSI), London, UK.

146. Crouch, B. A., Bender, R. G., and Williams, J. G. (1992), 'An Investigation of Notching Techniques for Fracture Toughness Measurement in Amorphous Nylon', *Engineering Fracture Mechanics*, Vol. 41 , No. 1, pp. 49-57.

147. International Standards Organisation (ISO) (2003), *Plastics - Determination of Flexural Properties*, ISO 178:2003, British Standards Institute (BSI), London, UK.

148. International Standards Organisation (ISO) (2003), *Plastics - Determination of Compressive Properties*, ISO 604:2003, British Standards Institute (BSI), London, UK.

149. American Society for Testing and Materials (ASTM) (2004), *Standard Test Method for D-C Resistance or Conductance of Moderately Conductive Materials*, ASTM D 4496-2004, ASTM International, USA.

150. Dillard, J. G. (1990), 'Adhesives and Sealants', in Brinson, H. F. *Engineered Materials Handbook*, Vol. 3, ASM International, Metals Park, OH, USA,

151. Blackman, B. R. K., Kinloch, A. J., Paraschi, M., and Teo, W. S. (2003), 'Measuring the Mode I Adhesive Fracture Energy, G_{IC}, of Structural Adhesive Joints: the Results of an International Round-Robin', *International Journal of Adhesion and Adhesives*, Vol. 23, No. 4, pp. 293-305.

152. Blackman, B. R. K., Kinloch, A. J., and Paraschi, M. (2005), 'The Determination of the Mode II Adhesive Fracture Resistance, G_{IIC}, of Structural Adhesive Joints: an Effective Crack Length Approach', *Engineering Fracture Mechanics*, Vol. 72, Issue 6, pp. 811-812.

153. Höhne, G. W. H., Hemminger, W. F., and Flammersheim, H. J. (2003), *Differential Scanning Calorimetry* (2nd Edition), Springer-Verlag, New York, USA.

154. Kazilas, M. C. (2002), *Acquisition and Interpretation of Dielectric Data for Thermoset Cure Monitoring* (PhD thesis), Cranfield University, Cranfield, UK.

155. Skordos, A. A. (2000), *Modelling and Monitoring of Resin Transfer Moulding* (PhD thesis), Cranfield University, Cranfield, UK.

156. Gill, P. S., Saurbrunn, S. R., and Reading, M. (1993), 'Modulated Differential Scanning Calorimetry', *Journal of Thermal Analysis*, Vol. 40, pp. 931-939.

157. Simon, S. L. and McKenna, G. B. (1997), 'The Effects of Structural Recovery and Thermal Lag in Modulated DSC Measurements', *Thermochimica Acta*, Vol. 307, No. 1, pp. 1-10.

158. Weyer, S., Merzlyakov, M., and Schick, C. (2001), 'Application of an Extended Tool – Narayanaswamy – Moynihan Model Part 1. Description of Vitrification and Complex Heat Capacity Measured by Temperature – Modulated DSC', *Thermochimica Acta*, Vol. 377, No. 1-2, pp. 85-96.

159. Dawkins, J. V. (1978), *Developments in Polymer Characterisation*, Elsevier Applied Science Publishers, Barking, Essex, UK.

160. Menard, K. P. (1999), *Dynamic Mechanical Analysis: A Practical Introduction*, CRC Press LLC, Florida, USA.

161. Cheremisinoff, N. P. (1993), *Elastomer Technology Handbook*, CRC Press, Inc., Florida, USA.

162. Brown, R. (1999), *Handbook of Polymer Testing: Physical Methods*, Marcel Dekker, Inc., New York, USA.

163. TA Instruments *Thermomechanical Analyzer*, available at: http://www.tainstruments.com (accessed 2008).

164. Haines, P. J. (2002), *Principles of Thermal Analysis and Calorimetry*, Royal Society of Chemistry, Cambridge, UK.

165. International Standards Organisation (ISO) (99), *Plastics - Thermomechanical Analysis (TMA) - Part 2: Determination of Coefficient of Linear Thermal Expansion and Glass Transition Temperature*, ISO 11359-2:1999, British Standards Institute (BSI), London, UK.

166. Kapton® Polyimide Films *Summary of Properties*, available at: http://www2.dupont.com (accessed 2009).

167. Keithley Instruments Inc. *Model 6517A Electrometer / High-Resistance Meter*, available at: http://www.keithley.com (accessed 2008).

168. Keithley Instruments Inc. *Models 6220/2182A Delta Model System with DC Current Source and Nanovoltmeter*, available at: http://www.keithley.com (accessed 2008).

169. Solartron Analytical *1260A Impedance/Gain-Phase Analyzer*, available at: http://www.solartronanalytical.com (accessed 2008).

170. International Standards Organisation (ISO) (98), *Fibre-Reinforced Plastic Composites - Determination of Flexural Properties*, ISO 14125: 1998, British Standards Institute (BSI), London, UK.

171. British Standards (BS) (2001), *Determination of the Mode I Adhesive Fracture Energy G_{IC} of Structure Adhesives Using the Double Cantilever Beam (DBC) and Tapered Double Cantilever Beam (TDCB) Specimens*, BS 7991:2001, British Standards Institute (BSI), London, UK.

172. Turmel, D., Szpicak, J., Singh, S., and Partridge, I. (1995), 'Crack Initiators and Pre-Cracking Techniques for Fracture Testing of Polymer Matrix Composites', in *Deformation and Fracture of Composites (DFC-3)* at Guildford, UK.

173. Kinloch, A. J. (1987), *Adhesion and Adhesives: Science and Technology*, Chapman and Hall, London, UK.

174. Hashemi, S., Kinloch, A. J., and Williams, J. G. (1990), 'The Analysis of Interlaminar Fracture in Uniaxial Fibre-Polymer Composites', in *Proceedings of the Royal Society of London. Series A, Mathematical and Physical Sciences,* Vol. 427 pp. 173-199.

175. Blackman, B. R. K., Dear, J. P., Kinloch, A. J., and Osiyemi, S. (1991), 'The Calculation of Adhesive Fracture Energies From Double-Cantilever Beam Test Specimens', *Journal of Materials Science Letters*, Vol. 10, No. 5, pp. 253-256.

176. European Structural & Integrity Society (ESIS) (2002), *Fibre-Reinforced Plastic Composites - Determination of Apparent Mode II Interlaminar Toughness, G_{IIc}, for Unidirectionally Reinforced Materials*, Version 01-04-02, Task Committee 4 (TC4) on fracture of composites and polymers,

177. Turmel, D., Szpicak, J., Singh, S., and Partridge, I. (1995), 'Crack Initiators and Pre-Cracking Techniques for Fracture Testing of Polymer Matrix Composites', in *Deformation and Fracture of Composites (DFC-3)* at Guildford, UK.

178. Blackman, B. R. K., Kinloch, A. J., and Paraschi, M. (2003), 'On the Mode II Loading of Adhesive Joints', *European Structural Integrity Society*, Vol. 32, pp. 293-304.

179. Blackman, B. R. K., Brunner, A. J., and Davies, P. (2001), 'Delamination Fracture of Continuous Fibre Composites: Mixed-Mode Fracture', in *Fracture Mechanics Testing Methods for Polymers, Adhesives and Composites* , Vol. 28, Elsevier, Oxford, UK, pp. 335-359.

180. Blackman, B. R. K., Brunner, A. J., and Williams, J. G. (2006), 'Mode II Fracture Testing of Composites: a New Look at an Old Problem', *Engineering Fracture Mechanics*, Vol. 73, Issue 16, pp. 2443-2455.

181. American Society for Testing and Materials (ASTM) (2000), *Standard Test Method for Measurement of Fatigue Crack Growth Rates*, ASTM E 647-2000, ASTM International, USA.

182. Samprovalakis, M. (2007), *Fatigue Crack Growth Rate Reduction in Aircraft Using Bonded Crack Retarders* (MSc thesis), Cranfield University, Cranfield, UK.

183. Sitaras, I. (2008), *Effect of Aluminium Strap Strength Differences on Crack Retarder Performance* (MSc thesis), Cranfield University, Cranfield, UK.

184. The New York Times *Today's Visions of the Science of Tomorrow*, available at: http://www.nytimes.com (accessed 2008).

185. Sourour, S. and Kamal, M. R. (1976), 'Differential Scanning Calorimetry of Epoxy Cure: Isothermal Cure Kinetics', *Thermochimica Acta*, Vol. 14, pp. 41-59.

186. Chern, C. S. and Poehlein, G. W. (1987), 'A Kinetics Model for Curing Reactions of Epoxides With Amines', *Polymer Engineering and Science*, Vol. 27, No. 11, pp. 788-795.

187. Skordos, A. A. and Partridge, I. K. (2004), 'Inverse Heat Transfer for Optimisation and on-Line Thermal Properties Estimation in Composites Curing', *Inverse Problems in Science and Engineering*, Vol. 12, Issue 2, pp. 157-172.

188. Fox, T. G. (1956), 'Glass Transitions of Mesophase Macromolecules', *Bulletin of the American Physical Society*, Vol. 1, pp. 123-129.

189. Kinloch, A. J. and Taylor, A. C. (2003), 'Mechanical and Fracture Properties of Epoxy/Inorganic Micro- and Nano-Composites ', *Journal of Materials Science Letters*, Vol. 22, No. 20, pp. 1439-1441.

190. Burton, B. L. and Bertram, J. L. (1996), 'Design of Tough Epoxy Thermosets', in Arends, C. B. *Polymer Toughening*, Marcel Dekker, New York, USA.

191. Sumita, M., Sakata, K., Hayakawa, Y., Asai, S., Miyasaka, K., and Tanemura, M. (1992), 'Double Percolation Effect on the Electrical Conductivity of Conductive Particles Filled Polymer Blends', *Colloid and Polymer Science*, Vol. 270, No. 2, pp. 134-139.

192. Ci, L. and Bai, J. (2006), 'The Reinforcement Role of Carbon Nanotubes in Epoxy Composites with Different Matrix Stiffness', *Composites Science and Technology*, Vol. 66, Issues 3-4, pp. 599-603.

193. Miyagawa, H. and Drzal, L. T. (2004), 'Thermophysical and Impact Properties of Epoxy Nanocomposites Reinforced by Single-Wall Carbon Nanotubes', *Polymer*, Vol. 45, Issue 5, pp. 5163-5170.

194. Meincke, O., Kaempfer, D., Weickmann, H., Friedrich, C., Vathauer, M., and Warth, H. (2004), 'Mechanical Properties and Electrical Conductivity of Carbon-Nanotube Filled Polyamide-6 and its Blends with Acrylonitrile/Butadiene/Styrene', *Polymer*, Vol. 45, Issue 3, pp. 739-748.

195. Thomas, R., Durix, S., Sinturel, C., Omonov, T., Goossens, S., Groeninckx, G., Moldenaers, P., and Thomas, S. (2007), 'Cure Kinetics, Morphology and Miscibility of Modified DGEBA-Based Epoxy Resin - Effects of a Liquid Rubber Inclusion', *Polymer*, Vol. 48, No. 6, pp. 1695-1710.

196. Sayre, J. A., Assink, R. A., and Lagasse, R. R. (1981), 'Characterization of the Phase Structure of an Amine Cured Rubber Modified Epoxy', *Polymer*, Vol. 22, pp. 87-94.

197. Taylor, A. C., Kinloch, A. J., Masania, K., Mohammed, R. D., and Sprenger, S. 'Toughness of Nanoparticle-Modified Epoxy and Fibre Composites', in *Proceedings of 31st Annual Meeting of the Adhesion Society* at Texas, USA.

198. Kinloch, A. J., Mohammed, R. D., Taylor, A. C., Eger, C., Sprenger, S., and Egan, D. (2005), 'The Effect of Silica Nano Particles and Rubber Particles on the Toughness of Multiphase Thermosetting Epoxy Polymers ', *Journal of Materials Science*, Vol. 40, No. 18, pp. 5083-5086.

199. Imperial College - Research: Adhesion and adhesives *DCB Analysis Spreadsheets*, available at: http://www3.imperial.ac.uk (accessed 2008).

200. Tzetzis, D. and Hogg, P. J. (2006), 'Bondline Toughening of Vacuum Infused Composite Repairs', *Composites: Part A*, Vol. 37, No. 9, pp. 1239-1251.

201. Cartié, D. D. R. (2000), *Effect of Z-Fibres™ on the Delamination Behaviour of Carbon Fibre / Epoxy Laminates* (PhD thesis), Cranfield University, Cranfield, UK.

202. Partridge, I. K. and Cartié, D. D. R. (2005), 'Delamination Resistant Laminates by Z-Fiber® Pinning. Part I Manufacture and Fracture Performance', *Composites: Part A*, Vol. 36, Issue 1, pp. 55-64.

203. Steinbrecher, G., Buchman, A., Sidess, A., and Sherman, D. (2006), 'Characterization of the Mode I Fracture Energy of Adhesive Joints', *International Journal of Adhesion and Adhesives*, Vol. 26, No. 8, pp. 644-650.

204. Bell, A. J. and Kinloch, A. J. (1997), 'The Effect of the Substrate Material on the Value of the Adhesive Fracture Energy, G_{IC} ', *Journal of Materials Science Letters*, Vol. 16, pp. 1450-1453.

205. Yan, C., Mai, Y. W., Yuan, Q., Ye, L., and Sun, J. (2001), 'Effects of Substrate Materials on Fracture Toughness Measurement in Adhesive Joints', *International Journal of Mechanical Sciences*, Vol. 43, No. 9, pp. 2091-2102.

206. Blackman, B. R. K., Kinloch, A. J., and Paraschi, M. (2001), 'The Effect of the Substrate Material on the Value of the Adhesive Fracture Energy, Gc: Further Considerations', *Journal of Materials Science Letters*, Vol. 20, No. 3, pp. 265-267.

207. Imperial College - Research: Deformation and fracture of polymers and composites *ELS Analysis Spreadsheets*, available at: http://www3.imperial.ac.uk (accessed 2008).

208. Lee, S. M. (1997), 'Mode II Delamination Failure Mechanisms of Polymer Matrix Composites', *Journal of Materials Science*, Vol. 32, No. 5, pp. 1287-1295.

209. O'Brien, T. K. (1998), 'Composite Interlaminar Shear Fracture Toughness, G_{IIC}: Shear Measurement or Sheer Myth?', in *Composite Materials: Fatigue and Fracture* , ASTM STP 1330, Philadelphia, PA, USA, pp. 3-18.

210. Schulz, M. J., Kelkar, A., and Sundaresan, M. J. (2006), *Nanoengineering of Structural, Functional, and Smart Materials*, CRC Press, Florida, USA.

211. Thostenson, E. T., Li, C., and Chou, T. W. (2005), 'Nanocomposites in Context', *Composites Science and Technology*, Vol. 65, Issues 3-4, pp. 491-516.

212. Krishnamoorti, R. and Vaia, R. A. (2001), *Polymer Nanocomposites: Synthesis, Characterization, Modeling*, ACS symposium series, American Chemical Society, Washington, DC, USA.

213. Ray, S. S. and Bousmina, M. (2006), *Polymer Nanocomposites and Their Applications*, American Scientific, Stevenson Ranch, CA, USA.

214. Mai, Y. W. and Yu, Z. Z. (2006), *Polymer Nanocomposites CRC*, Woodhead Publishing, Cambridge, UK.

215. Nantong Sanxin *Stretch Adhesive Film Machine*, available at: http://www.ntsanxin.com/ (accessed 2008).

216. Dimopoulos, A. (2007), *Effect of Carbon Nanoparticle Addition on Epoxy Cure* (PhD thesis), Cranfield University, Cranfield, UK.

217. Hexcel Composites Ltd. (2008), 'Private Communication', Duxford, Cambridge, UK.

218. Ratna, D. and Banthia, A. K. (2000), 'Epoxidized Soybean Oil Toughened Epoxy Adhesive', *Journal of Adhesion Science and Technology*, Vol. 14, No. 1, pp. 15-25.

219. Siebert, A. R. (1984), 'Rubber Modified Thermoset Resins', in Riew, C. K. and Gillham, J. K. *Advances in Chemistry Series, 208*, American Chemical Society, Washington, DC, USA , pp. 179.

220. Lin, K. F. and Chung, U. L. (1994), 'Phase-Inversion Investigations of Rubber-Modified Epoxies by Electron Microscopies and X-Ray Diffraction', *Journal of Materials Science*, Vol. 29, No. 5, pp. 1198-1202.

221. Petrie, E. M. *Cleaning Processes for Improving Adhesion*, available at: http://www.specialchem4adhesives.com (accessed 2007).